

The mechanics of crack-tip dislocation emission and twinning

Thèse N° 7110

Présentée le 25 avril 2019

à la Faculté des sciences et techniques de l'ingénieur
Laboratoire de modélisation mécanique multi-échelle
Programme doctoral en mécanique

pour l'obtention du grade de Docteur ès Sciences

par

Predrag ANDRIC

Acceptée sur proposition du jury

Prof. J.-F. Molinari, président du jury

Prof. W. Curtin, directeur de thèse

Dr R. Janisch, rapporteuse

Dr G. Moras, rapporteur

Prof. J. M. Kolinski, rapporteur

2019

*To my wife, Dragana
and my children, Ekaterina, and Nikola*

Acknowledgements

The present thesis summarizes my research carried out during the previous four years at École Polytechnique Fédérale de Lausanne (EPFL), in the Laboratory for Multiscale Mechanics Modeling (LAMMM). Financial support was provided by the European Research Council (ERC) through the Advanced Grant "Predictive Computational Metallurgy", ERC Grant agreement No. 339081 - PreCoMet. At the end of this very interesting and life-changing scientific journey, I would like to address a few words of thanks.

First of all, I would like to thank to my PhD thesis advisor, Professor Bill Curtin, who gave me an opportunity to be a part of the world leading group in the field of mechanics of materials. He guided me with patience through various scientific problems, provided me with valuable knowledge, and transferred to me some of his excellent teaching skills. Moreover, I am thankful for his understanding and support during challenging moments I experienced in everyday life.

I would also like to thank the jury members for being willing to participate in my PhD exam. I am also thankful to the current and former members of LAMMM: Till Junge, Francesco Maresca, Aitor Luque, Wolfram Nöhring, Max Hodapp, Nikolas Bouklas, Ali Tehrani, Markus Stricker, Binglun Yin, Xiao Zhou, Rasool Ahmad, Ali Falsafi, Alireza Ghafarollahi, Ankit Gupta, Hu Yi, Eleanor Mak, Daniel Marchand, Shankha Nag, Mostafa Khosrownejad, Céline Varvenne, Fabio Pavia, Kris Baker, Mike Francis, Zhaoxuan Wu, Varun Rajan, Satish Rao, Ben Szajewsky, and Vladimir Dorodnitsyn. Furthermore, many thanks to always smiling LAMMM secretary, Ms. Géraldine Palaj, for her assistance with everyday issues. It has been a wonderful experience working with such a great group of people.

I am grateful to Aitor for introducing me to atomistic simulations. I thank to Francesco for his help and support in finding a new career opportunity. I always enjoyed social events and discussions about computational mechanics organized by Till. I thank to Aitor, Wolfram and Max for many meetings followed by *Le jus de pomme*. Thank you Ali Tehrani and Eleanor for fruitful discussions about fundamentals of Fracture Mechanics. Moreover, I am thankful to Binglun for introducing me to *very careful* DFT calculations.

I would also like to thank Professor Bosko Rasuo and Professor Mirko Dinulovic, from University of Belgrade, and Professor Branimir Krstic from University of Defense in Belgrade, for giving me the necessary scientific foundation to tackle with my PhD studies. I am grateful to the unreserved help I got from my numerous cousins and relatives living in Switzerland. Moreover, a special thank goes to Sladjana Andric for finding me a place to live in Lausanne, twice.

I express my deepest thanks to my parents, Petar and Vera, and my brother Stefan, for their love,

Acknowledgements

support and encouragement during my whole life. I also thank to my parents in law, Dragan and Saja Dragic, who took the time to help with my children.

Finally, I would like to dedicate this work to my wife Dragana, and my children Ekaterina and Nikola, the most important persons in my life. They were always with me, in good and hard times, giving me an unconditional support, love, and assistance in innumerable ways. I am sure that without their patient and encouragement this thesis would have never been written.

Lausanne, April 2019

P. A.

Abstract

Dislocation emission from a crack tip is a necessary mechanism for crack tip blunting and toughening. A material is intrinsically ductile under Mode I loading when the critical stress intensity K_{Ie} for dislocation emission is lower than the critical stress intensity K_{Ic} for cleavage. In intrinsically ductile fcc metals, a first partial dislocation is emitted, followed either by a trailing partial dislocation (“ductile” behavior) or a twinning partial dislocation (“quasi-brittle”).

K_{Ie}^{first} for the first partial dislocation emission is usually evaluated using the approximate Rice theory, which predicts a dependence on the elastic constants and the unstable stacking fault energy γ_{usf} . Here, atomistic simulations across a wide range of fcc metals show that K_{Ie}^{first} is systematically larger (10–30%) than predicted. However, the critical crack-tip shear displacement is up to 40% smaller than predicted. The discrepancy arises because Mode I emission is accompanied by the formation of a surface step that is not considered in the Rice theory. A new theory for Mode I emission is presented based on the ideas that (i) the stress resisting step formation at the crack tip creates “lattice trapping” against dislocation emission such that (ii) emission is due to a mechanical instability at the crack tip. The new theory naturally includes the energy to form the step, and reduces to the Rice theory (no trapping) when the step energy is small. The new theory predicts a higher K_{Ie}^{first} at a smaller critical shear displacement, rationalizing deviations of simulations from the Rice theory.

The twinning tendency is estimated using the Tadmor and Hai extension of the Rice theory. Atomistic simulations reveal that the predictions of the critical stress intensity factor K_{Ie}^{twin} for crack tip twinning are also systematically lower (20–35%) than observed. Energy change during nucleation reveal that twinning partial emission is not accompanied by creation of a surface step while emission of the trailing partial creates a step. The absence of the step during twinning motivates a model for twinning nucleation that accounts for the fact that nucleation does not occur directly at the crack tip. New predictions are in excellent agreement with all simulations that show twinning. A second mode of twinning is found wherein the crack first advances by cleavage and then emits the twinning partial at the new crack tip.

The stacking fault stress dependence is analyzed through (i) the generalized stacking fault potential energy (GSFE) and (ii) the generalized stacking fault enthalpy (GSFH). At an imposed shear displacement, there is also an associated inelastic normal displacement Δ_n around the fault. Atomistic simulations with interatomic potentials and/or first principle calculations reveal that

Abstract

GSFE and Δ_n both increase with tensile stress. An increasing GSFE contradicts long-standing wisdom and previous studies. Positive Δ_n coupled to the applied normal stress decreases the GSFH, but GSFH is not useful for general mechanics problems. "Opening softening" effects are not universal, and so the analysis of any particular nanomechanics problem requires precise implementation of the combination of GSFE and Δ_n rather than the GSFH.

Key words: Fracture mechanics, Dislocation nucleation and emission, Ductile to brittle transition, Molecular statics, First principle calculations

Zusammenfassung

Die Versetzungsemission von einer Rissspitze ist ein notwendiger Mechanismus für das Abstumpfen der Rissspitze und die Bruchzähigkeit. Man bezeichnet ein Material als intrinsisch duktil bezüglich der Rissöffnungsart I, wenn der kritische Spannungsintensitätsfaktor K_{Ie} für Versetzungsemission niedriger ist als der kritische Spannungsintensitätsfaktor K_{Ic} für Trennbruch. Bei intrinsisch duktilen kfz Metallen wird zuerst eine Partialversetzung emittiert, gefolgt von einer nachlaufenden Partialversetzung ("duktilen" Verhalten) oder einer Zwillingspartialversetzung ("quasi spröde").

K_{Ie}^{first} für die erste Emission einer Partialversetzung wird normalerweise näherungsweise anhand der Theorie von Rice bewertet, die von den elastischen Konstanten und der instabilen Stapelfehlerenergie γ_{usf} abhängt. Atomistische Simulationen für ein breites Spektrum an kfz Metallen zeigen allerdings, dass K_{Ie}^{first} systematisch größer ist (10–30%) als vorhergesagt. Die kritische Scherverschiebung der Rissspitze ist jedoch um bis zu 40% kleiner als vorhergesagt. Die Diskrepanz entsteht, weil die Emission bezüglich der Rissöffnungsart I mit der Bildung einer Oberflächenstufe einhergeht, die in der Theorie von Rice nicht berücksichtigt wird. Es wird eine neue Theorie für die Emission bezüglich der Rissöffnungsart I vorgestellt, die darauf basiert, dass (i) die spannungsresistente Stufenbildung an der Rissspitze "Gitterfallen" erzeugt, die der Versetzungsemission entgegenwirkt, so dass (ii) die Emission durch eine mechanische Instabilität an der Rissspitze hervorgerufen wird. Die neue Theorie beinhaltet die Stufenbildungsenergie und reproduziert die Theorie von Rice (keine Gitterfallen), wenn die Stufenenergie klein ist. Die neue Theorie sagt einen höheren Spannungsintensitätsfaktor K_{Ie}^{first} bei einer geringeren kritischen Scherverschiebung voraus, was die Abweichungen zwischen den Simulationen und der Theorie von Rice erklärt.

Die Zwillingsbildung wird mithilfe der Erweiterung der Theorie von Rice durch Tadmor und Hai abgeschätzt. Atomistische Simulationen zeigen, dass die Vorhersagen des kritischen Spannungsintensitätsfaktors K_{Ie}^{twin} für Zwillingsbildung an der Rissspitze ebenfalls systematisch niedriger sind (20–35%) als vorhergesagt. Die Änderungsenergie aufgrund der Versetzungsbildung zeigt, dass die Emission der Zwillingspartialversetzung nicht mit der Erzeugung einer Oberflächenstufe einhergeht, während die Emission einer nachlaufenden Versetzung eine solche erzeugt. Das Fehlen der Oberflächenstufe während der Zwillingsbildung motiviert ein neues Modell, das berücksichtigt, dass Zwillingsbildung nicht direkt an der Rissspitze auftritt. Die Vorhersagen anhand dieses Modells stimmen hervorragend mit allen Simulationen überein in denen Zwillingsbildung

Zusammenfassung

beobachtet wird. Darüber hinaus wurde eine zweite Form der Zwillingsbildung gefunden, bei der sich der Riss zunächst ausbreitet und erst danach die Zwillingspartialversetzung an der neuen Rissspitze emittiert.

Die Abhängigkeit des Stapelfehlers von der Spannung wird mithilfe (i) der generalisierten Stapelfehlerenergie (GSFE) und (ii) der generalisierten Stapelfehlerenthalpie (GSFH) analysiert. Bei einer angelegten Schubverschiebung entsteht zusätzlich eine nicht elastische Normalverschiebung Δ_n um den Stapelfehler. Atomistische Simulationen mit interatomaren Potentialen und/oder ab initio Verfahren zeigen, dass sowohl die GSFE als auch Δ_n unter einer angelegten Zugspannung zunehmen. Eine zunehmende GSFE widerspricht allen früheren Untersuchungen. Ein positives Δ_n , gekoppelt mit einer angelegten Normalspannung, verringert die GSFH, die aber für allgemeine Mechanikprobleme nicht nützlich ist. "Öffnungs-ErweichungsEffekte sind nicht universell und erfordern daher für die Analyse eines bestimmten Problems in der Nanomechanik die Berücksichtigung der Kombination aus GSFE und Δ_n , anstelle der GSFH.

Schlagwörter: Bruchmechanik, Versetzungsbildung und -emission, Spröd-duktil Übergang, Molekular-Statik, Ab initio Verfahren

Contents

Acknowledgements	v
Abstract (English/Deutsch)	vii
List of figures	xiii
List of tables	xxiii
1 Introduction	1
1.1 Fracture toughness as the main concern of fracture mechanics	1
1.2 Motivation: Intrinsic ductility as a precursor to ductile fracture	3
1.3 Outline of the thesis	6
2 Modeling fracture across different length scales	9
2.1 Linear Elastic Fracture Mechanics	9
2.1.1 Crack stress fields in Plane Strain	10
2.1.2 Asymptotic near-tip stress fields	12
2.1.3 K-dominance zone	16
2.1.4 Crack tip processes: the fracture process zone	16
2.1.5 Crack tip processes: stress intensity and energetic perspectives	17
2.1.6 Modeling crack growth: Implementation and issues	18
2.2 Cohesive zone model	19
2.2.1 The Barenblatt model	19
2.2.2 Cohesive zone modeling of fracture	21
2.3 Modeling fracture in metals	23
2.3.1 Continuum Plasticity-Cohesive Zone (CP-CZ) modeling of fracture	23
2.3.2 Discrete Dislocation-Cohesive Zone (DD-CZ) modeling of fracture	24
2.4 Atomistic modeling of fracture	26
2.4.1 Size of the K-dominant zone in atomistic modeling of fracture	27
2.4.2 Atomistic crack-tip processes: cleavage versus dislocation emission	28
2.4.3 Simulation methods and issues	30
2.4.3.1 Creating cracks in atomistic systems	30
2.4.3.2 Center-crack and other finite-crack geometries	31
2.4.3.3 K-controlled simulation framework	33

Contents

2.4.4	Illustrative examples	35
2.4.4.1	Brittle fracture	35
2.4.4.2	Crack-tip dislocation emission	41
2.4.5	Discussion and concluding remarks	48
3	Continuum theories of crack-tip dislocation emission	53
3.1	Introduction	53
3.2	Rice theory for dislocation emission	53
3.3	Tadmor-Hai theory for crack-tip twinning	56
3.4	Shielding effect on second partial dislocation emission	57
4	New theory for Mode I crack-tip dislocation emission	59
4.1	Introduction	59
4.2	Rice theory versus atomistic simulations	60
4.2.1	Materials studied	60
4.2.2	Mode II loading	62
4.2.3	Mode I loading	64
4.3	Energy due to surface step creation during dislocation emission	67
4.4	New theory for crack tip dislocation emission	70
4.5	Validation of the new theory	76
4.6	Approximate model for prediction of the crack-tip dislocation emission	78
4.7	Discussion and concluding remarks	80
5	New theory for crack-tip twinning in fcc metals	83
5.1	Introduction	83
5.2	Tadmor-Hai theory versus atomistic simulations	85
5.3	Energy changes near the crack-tip during second partial dislocation emission	88
5.4	New theory for crack-tip twinning	91
5.5	Trailing partial emission: why twinning is observed in all simulations	93
5.6	Forward twinning and twin thickening in fcc metals	95
5.7	Concluding remarks	97
6	Stress-dependence of generalized stacking fault energies	99
6.1	Introduction	99
6.2	GSFE under normal stress: simulation methods	102
6.3	GSFE under normal stress: results	104
6.4	GSFE under normal applied loading: boundary conditions and size effects	108
6.5	Applications of the GSFE	111
6.5.1	GSFE: An analysis based on the Eshelby method	111
6.5.2	Shockley partial dislocation dissociation under applied normal stress	113
6.5.3	Crack-tip dislocation emission under mixed Mode II/I loading	118
6.6	Concluding remarks	120

7	Conclusion	123
A	Appendix	127
A.1	Effective elastic constants	127
A.2	Shearing of the triangular crack tip structural unit	129
A.3	Comparison of shear displacement profiles in Mode I and Mode II	130
A.4	Computation of the crack-tip parameter β	131
A.5	Assessment of the theory for K_{Ie}^{first} and different slip plane orientations	131
A.6	Assessment of the theory for K_{Ie}^{twin} and different slip plane orientations	134
A.7	GSFE under uniaxial tension	134
A.8	Partials dissociation d and stress dependence of isotropic elastic properties	136
	Bibliography	149
	Curriculum Vitae	151

List of Figures

1.1	Historical overview of catastrophic failure of structures: a) Versailles train crash in 1842 caused by fatigue fracture of a locomotive axle, b) Schenectady ship that broke into two in 1943, c) The Comet airplane lost in 1953 due to fracture from a rectangular window, d) Japan Air Lines Boeing 747 lost due to fatigue fracture in 1984, and e) Morandi Bridge collapsed in 2018.	2
1.2	Schematic representation showing various processes that contribute to materials fracture toughness across different length scales: a) fiber bridging in composites [10], b) crazing in polymers [11], c) interatomic forces across crack surfaces in extremely brittle materials, and d) plastic deformation, characterized by discrete dislocations, around the crack-tip in metals [14]. A particular length scale is identified by length units in parentheses.	3
1.3	Evolution of an atomically sharp crack in a dislocation-free fcc single crystal: a) Initial configuration at the applied load prior to dislocation emission or cleavage. b) the crack geometry after dislocation emission for which $K_{Ie} < K_{Ic}$ requirement is satisfied; c) the crack geometry after cleavage for which $K_{Ie} < K_{Ic}$ requirement is not satisfied. Note that the crack geometry stays self-similar in cleavage. Atoms are visualized using OVITO [15].	4
1.4	Schematic representation of how intrinsic ductility enables, or intrinsic brittleness inhibits, pronounced plasticity around the crack-tip: a) Initial configuration with an atomically sharp crack; b) Fracture in an intrinsically brittle material where the crack remains sharp during the loading; c) Fracture in an intrinsically ductile material where the crack is blunted by emission of dislocations. In both examples, there is some far-field plasticity that can contribute to the materials fracture toughness.	5
2.1	a) Centrally positioned finite crack in an infinite plate under biaxial stress σ^{app} . Stresses in the outer zone (sufficiently far from the crack) are strongly influenced by the boundary conditions (B.C.) and sample geometry. b) Stress zones in a cracked body with the fracture process zone (FPZ) in the vicinity of the crack-tip, surrounded by the K-dominance zone where the asymptotic fields given by Eq. 2.8 are accurate. The size of the K-dominant zone is much smaller than the crack size.	10

List of Figures

2.2	a) Asymptotic singular opening stress $\sigma_{22}(x)$ (blue line) computed using Eq. 2.9 along with more realistic non-linear stress profile in the crack tip vicinity (red line) which depends on a material considered and fracture processes. b) Cohesive zone with tractions $T(x)$ over the length u_c , $u_c \ll a$. Note that the crack surfaces change their shape to satisfy the condition of the zero stress intensity at the tip. c) The nonlinear cohesive tractions T as a function of the crack-tip opening displacement δ . The maximum stress σ_c corresponds to the crack-tip opening displacement δ^* with $\delta^* \ll u_c$. The area under the curve is the fracture energy G_c .	20
2.3	Modeling the crack-tip plasticity from the continuum scale where plastic deformations are governed by the power-law plasticity, over the dislocation scale plasticity where discrete dislocations interact with the crack-tip, down to atomic scale where a single dislocation is emitted from the crack-tip. The left figure is taken from [39], while the middle figure is taken from [40].	22
2.4	Steady-state toughness as a function of σ_c/σ_Y for three different strain hardening exponents. Overall, fracture toughness goes towards infinity when plastic deformation around the crack tip starts being dominant. Figure is taken from [41].	24
2.5	a) Contours of local average plastic strain, along with the crack tip opening displacement ($\times 10$) obtained from DD-CZ modeling of fracture at the far-field energy release rate $G = 5.25G_c$. Position of actual dislocations are shown as symbols and the dislocation density in the region is $2 \times 10^{14}/m^2$. b) Fracture toughness G/G_c versus σ_c/σ_Y . Both figures are taken from [14]	25
2.6	Atomic opening stress $\sigma_{22}(x_1 > 0, x_2 = 0)$ versus distance from the crack tip, for crack sizes considered here as observed in simulations within the "brittle" crystal orientation. The asymptotic singular stress given by Eq. 2.18 is also shown (black line). The use of a log-log reveals the K -field singularity of $(-\frac{1}{2})$	28
2.7	Closing and opening of a) an atomistically sharp crack when the applied K_I is b) below, and c) above the Griffith value, respectively. Atoms are visualized using OVITO [15].	30
2.8	Far field applied stress at the cleavage point with $K_{Ic} = 1\text{MPa}\sqrt{\text{m}}$, as a function of the half crack size a	32
2.9	Tangent elastic moduli as a function of the applied normal stress in fcc Nickel. .	33
2.10	Absolute difference in x_2 atomic positions between the elastic solution given by Eq. 2.19 (K-field) and relaxed structure for the same applied K_I within the box size of $21 \times 21 \times 1\text{nm}^3$. Atoms are colored according to x_2 absolute displacement difference shown by the scale. Displacement difference in the red zone is off-scale with the maximum displacement of 0.012 \AA	34
2.11	K-test geometry used to simulate a) brittle fracture and b) dislocation emission from the crack-tip. Blue color indicate domain of atoms where boundary conditions are applied.	37
2.12	CCT test geometry used to simulate centrally positioned finite crack under uniaxial (only black arrows) or biaxial (black and gray arrows) applied strain ϵ^{app} . Blue color indicates domain of atoms where boundary conditions are applied. .	38

2.13	<p>K-test geometry for blunted cracks created by deletion of a) two, b) three and c) four atomic layers. In each case, the left figure shows the crack tip morphology at the applied $K_I = K_{Ic} = 0.91\text{MPa}\sqrt{\text{m}}$, the middle figure shows the crack-tip at the applied K_I immediately before the cleavage, while the right figure shows the crack after brittle fracture started. Atoms in this figure are colored based on Common Neighbor Analysis [15]; green for fcc and white for surface.</p>	39
2.14	<p>Critical stress intensity factor for cleavage K_{Ic} as observed in the K-test simulations for different simulation cell sizes (red diamonds), along with the predictions of LEFM based theoretical prediction (Eq. 2.32) (blue line). The black dashed line represents minimum cell size for converged results.</p>	40
2.15	<p>Computed critical stress intensity factor for cleavage $K_{Ic} = \sigma_{22}^{cr}\sqrt{\pi a}$ versus crack size a in the CCT test simulations (cf. Fig. 2.12) under uniaxial (purple solid lines) and biaxial (orange dashed lines) loading. Squares corresponds to results computed using σ_{22}^{cr} directly from simulations while diamonds corresponds to results computed using $\sigma_{22}^{cr} = C_{22ij}\epsilon_{ij}^{cr}$. Solid red line: K-test result.</p>	41
2.16	<p>Critical stress intensity factor for crack-tip dislocation emission K_{Ie} as observed in the K-test simulations for different simulation cell sizes (red diamonds), along with the predictions of LEFM based theoretical prediction (Eq. 2.49) (blue line). The black dashed line represents minimum cell size for converged results. . . .</p>	42
2.17	<p>Computed critical stress intensity factor for crack-tip dislocation emission $K_{Ie} = \sigma_{22}^{cr}\sqrt{\pi a}$ versus crack size a in the CCT test simulations under uniaxial (purple solid lines) and biaxial (orange dashed lines) loading. Squares correspond to result computed using σ_{22}^{cr} directly from simulations while diamonds correspond to results computed using $\sigma_{22}^{cr} = C_{22ij}\epsilon_{ij}^{cr}$. Solid red line: K-test results.</p>	43
2.18	<p>Equilibrium position r of the first partial dislocation after nucleation using a) the K-test geometry and b) the CCT-test geometry under uniaxial and biaxial tension. The distance between the crack-tip and the outer CCT boundary along the slip plane (green circles) is shown for reference.</p>	44
2.19	<p>K-test results for the critical stress intensity factor for crack-tip twinning versus simulation cell size (red diamonds) along with the predictions of the LEFM based theory (blue squares).</p>	47
2.20	<p>Computed critical stress intensity factor for crack-tip twinning $K_{Ie}^{twin} = \sigma_{22}^{cr}\sqrt{\pi a}$ versus crack size a in the CCT test simulations under uniaxial (purple solid lines) and biaxial (orange dashed lines) loading. Squares correspond to results computed using σ_{22}^{cr} directly from simulations, while diamonds correspond to results computed using $\sigma_{22}^{cr} = C_{22ij}\epsilon_{ij}^{cr}$. Solid red line: K-test results obtained using the largest simulation cell.</p>	48

List of Figures

3.1	Generalized stacking fault (GSF) energy along the direction of the first partial dislocation (the solid line), GSF energy along the direction of the trailing partial dislocation (the dashed line), and generalized twinning fault (GTF) energy along the direction of the twinning partial dislocation (dotted line) computed in fcc Ni [81].	54
4.1	Crack geometry in Mode II loading formed by a) deleting the interatomic interactions between the crack surfaces (yellow and blue atoms, respectively) and denoted as “screening” and b) removing one layer of atoms and then screening the remaining atoms (yellow and blue, respectively) and denoted as “blunting”. For both (a) and (b), the crack geometry is shown (i) at zero load, (ii) at the critical load for dislocation emission, and (iii) after dislocation emission. The triangles are the basic structural units through which the shear displacement along the plane of emission are analysed, as indicated. Atoms are visualized using OVITO [15].	63
4.2	Results of simulations under Mode II loading for both “screening” and “blunting” models: a) Critical stress intensity factor K_{IIe} for crack-tip dislocation emission; b) Relative shear displacement of the structural units at the crack tip and, for “screening” only, immediately behind the crack tip. In both (a) and (b), light blue symbols show the predictions of the Rice model.	64
4.3	Crack geometry in Mode I loading formed by a) deleting the interatomic interactions between the crack surfaces (yellow and blue atoms, respectively) and denoted as “screening” and b) removing three layer of atoms and denoted as “blunting”. For both (a) and (b), the crack geometry is shown (i) at zero load, (ii) at the critical load for dislocation emission, and (iii) after dislocation emission. The triangles are the basic structural units through which the shear displacement along the plane of emission are analyzed, as indicated.	65
4.4	Results of simulations in Mode I for both “screening” and “blunting” models: a) Critical stress intensity factor K_{Ie} for crack-tip dislocation emission; b) Relative shear displacement of the structural units at the crack tip. In both (a) and (b), light blue symbols show the predictions of the Rice theory.	66
4.5	Computation of the nucleation energy a) for “blunting” crack geometry; b) for “screening” crack geometry; and c) atom-by-atom energy change in the blunting case after full slip (one partial Burgers vector) for Nickel.	67
4.6	Slip energy change versus slip displacement, for successive atomic structural units along the slip plane computed for fcc Ni [81]; only the energy for the structural unit at the crack tip deviates significantly from the bulk GSF energy.	69
4.7	GSF energy (red lines) and nucleation energy (blue lines) versus relative slip for all fcc materials studied here: a) screening; b) blunting. GSF energies are identical in both figures.	70

4.8	a) Linear elastic body with semi-infinite crack under pure Mode I loading surrounding the dislocation emission plane that is characterized by atomic structural units along the slip plane; b) Local stresses acting on the crack tip structural unit: an applied stress due to the remote applied K_I load and a restoring stress due to the shear resistance of the crack tip structural unit, which together determine the local equilibrium shear deformation (dashed lines).	71
4.9	Graphical construction for the equilibrium shear displacement Δ_1 of the crack tip unit in Mode II loading or in Mode I loading when no step is present, for several different far-field loadings. Solid blue line: crack tip restoring stress versus crack tip shear displacement due to GSF energy only; Red lines: crack tip applied shearing stress versus shear displacement. b) Critical shear displacements $\Delta_1, \Delta_2, \dots$ along the slip plane at the point of dislocation emission, with critical energy release rate corresponding to the shaded area.	72
4.10	Graphical construction for the equilibrium shear displacement Δ_1 of the crack tip unit when a step is created during emission in Mode I loading and all other displacements $\Delta_2, \Delta_3, \dots$ remain in the linear regime, for several different far-field loadings. Solid blue line: crack tip restoring stress versus shear displacement including the step energy; Red lines: crack tip applied shearing stress versus shear displacement; for reference, dashed blue line shows the crack tip restoring stress versus shear displacement due only to the stacking fault energy.	74
4.11	a) Critical shear displacements $\Delta_1, \Delta_2, \dots$ along the slip plane at the point of dislocation emission, for the realistic case corresponding to some non-linearity in $\Delta_2, \Delta_3, \dots$ beyond the crack-tip structural unit. b) Critical shear displacements $\Delta_1, \Delta_2, \dots$ along the slip plane at the point of dislocation emission, when the crack tip restoring stress is skewed toward higher displacement. In both figures the associated critical energy release rate corresponds to the shaded area.	75
4.12	a) Critical stress intensity factor for dislocation emission (Theory: orange; Simulation: red; Rice: blue line) for a) cracks formed by “screening”; b) cracks formed by “blunting”. Orange dashed line computed with Δ_1^c crack tip displacement.	77
4.13	Crack tip restoring stress for crack formed by screening (solid lines) and for crack formed by blunting (dashed lines) in Ni, Cr50 and Cu.	77
4.14	Critical stress intensity factor for dislocation emission for all materials studied here; Simulations (red), full theory (orange); approximate model (purple) for a) screening and b) blunting.	78
4.15	Critical energy release rate G_{Ie} as a function of the materials surface energy γ_s normalized by γ_{usf} for all materials studied here; Simulations - screening (red diamonds), Simulations - blunting (orange squares), Simulation results from [132] (open red diamonds), Analytical model Eq. 4.7 (purple line); Rice theory (black dashed line).	80

List of Figures

5.1	<p>Partial dislocations emitted from a crack tip in a fcc metal: a) First partial dislocation at some equilibrium distance with the stacking fault behind it; b) First and trailing partial dislocation forming the full dislocation with the stacking fault between them; c) Twinning fault formed by the emission of the twinning partial dislocation; c) Region of two stacking faults formed by the second dislocation emission on the nonadjacent slip plane. Only non-fcc atoms are presented and colored according to Common Neighbour Analysis [15]; red for hcp and white for other.</p>	84
5.2	<p>a) Geometry used to simulate second partial dislocation emission using a semi-infinite crack with the first partial dislocation removed to infinity, achieved by displacing the region marked by the red line by the first partial Burgers vector. Blue color indicates boundary atoms. b) Atomic scale crack-tip geometry at zero loading. Atoms are colored based on Common Neighbour Analysis [15]; green for fcc, red for hcp and white for surface.</p>	86
5.3	<p>a) Crack geometry in Mode I at the critical load for the emission of the twinning partial dislocation. b) Crack geometry after “back” twinning emission. c) Crack geometry after “forward” twinning emission. The same atom at the original crack tip is indicated in all figures to show the two different mechanisms.</p>	87
5.4	<p>Critical stress intensity factor for emission as observed in the simulations (red diamonds), along with the predictions of continuum theories based on the Peierls model (blue circles) for the “back” twinning partial dislocation</p>	87
5.5	<p>a) Linear elastic body with semi-infinite crack under Mode I loading with embedded slip planes for analysis of the emission of the trailing and twinning partial dislocations. The slip planes are characterized by atomic structural units. b) The three structural units that control emission of the second partial dislocation. . . .</p>	88
5.6	<p>a) Initial configuration of the computational domain used to compute atom-by-atom energy changes due to relative shear displacement along the trailing or twinning slip plane. Energy change per atom after subtraction of the energy changes per atom corresponding to the bulk GSF and GTF energies per atom, showing the energy changes due to surface effects near the crack tip for b) the twinning partial and c) the trailing partial, at relative slip . Atoms in (a) are colored by Common Neighbour Analysis [15] (green for fcc, red for hcp and white for surface); Atoms in (b) and (c) are colored according to energy change shown by the scale. Energies of atoms near the crack tip are off scale, and indicated in each figure.</p>	89
5.7	<p>Slip energy change (per unit area) vs. shear displacement of the first trailing unit (solid line), first twinning unit (dashed-dotted line), second twinning unit (dashed line), and second trailing unit (dotted line), computed for fcc Ni [81]. The second twinning unit and second trailing unit are negligibly different from the bulk GSF and GTF energies.</p>	91

5.8	Critical stress intensity factor for emission as observed in the simulations (red diamonds), along with the predictions of continuum theories based on the Peierls model (blue circles), and the Andric-Curtin theory (orange squares) for the “back” twinning partial dislocation.	92
5.9	Critical stress intensity factor for the emission of the “back” twinning partial dislocation including the effect of shielding due to the first partial dislocation, as observed in the simulations (red diamonds) and as computed by the new twinning theory (orange squares).	93
5.10	a) Critical stress intensity factor for Griffith cleavage K_{Ic} (purple diamonds) and predicted “back” twinning partial emission $K_{Ie,tip}^{twin}$ (orange squares); forward emission is predicted when $K_{Ic} < K_{Ie,tip}^{twin}$ and the cases where forward twinning is observed in simulations are indicated. b) Critical stress intensity factor for Griffith cleavage K_{Ic} (purple diamonds) and simulated value of the critical stress intensity at the onset of “forward” twinning (red circles), showing that forward twinning starts at K_{Ic} . The number of “back” twinning events prior to “forward” twinning is indicated for each material, as observed in simulation and, in parentheses, as predicted by Eq. 5.6	96
6.1	Generalized stacking fault energy with full normal relaxation (blue squares) and relaxation only across the slip plane (red diamonds) computed in Aluminum [81] at $T = 0K$	100
6.2	a) Typical simulation cell for computing the GSFE under applied normal stress, with the lower and upper domains indicated by red and blue, and atoms on which forces are applied indicated in green. b) Stacking fault region for describing the local constitutive behavior for rigid block sliding under applied tractions T_n . c) Inter-planar spacing around the stacking fault for a given shear displacement Δ_s and applied tractions T_n . Atoms are visualized using OVITO [15].	102
6.3	(i) The GSFE Ψ_{gsf} , and ii) total inelastic normal displacement Δ_n across the slip plane for different applied normal stresses T_n ; (iii) The GSFE Ψ_{gsf} for different applied inelastic displacements Δ_n ; (iv) GSFH versus shear displacement Δ_s for different applied normal stresses T_n . All values are computed with interatomic potentials at $T = 0K$ in a) nickel, b) copper and c) aluminum.	105
6.4	Normalized stable γ_{ssf} and unstable stacking fault γ_{usf} energies in Ni (blue color), Cu (red color) and Al (green color) versus applied normal tensile stress.	106
6.5	Atom-by-atom energy change during rigid block shear displacement at the point of the unstable stacking energy γ_{usf} and stable stacking fault energy γ_{ssf} in fcc Ni under a) zero applied stress, and b) at the applied stress $T_n = 10GPa$. Note that contributions to the energy are confined to a few layers of atoms around the fault. Energies of atoms exceeding the energy scale are indicated.	106
6.6	(i) The GSFE Ψ_{gsf} , (ii) total inelastic normal displacement Δ_n across the slip plane, and (iii) GSFH versus shear displacement Δ_s for different applied normal stresses as computed in DFT in a) copper, b) aluminum and c) magnesium {0001}.	107

List of Figures

6.7 The size dependence of a) γ_{usf}^{disp} and b) γ_{ssf}^{disp} using displacement boundary conditions along with γ_{usf}^{enth} and γ_{ssf}^{enth} computed using Eq. 6.3 and shown on the right axis, at the applied strain of $\epsilon_{22} = 0.045$ in nickel (blue diamonds), copper (red squares) and aluminum (green circles). 110

6.8 Geometry used to simulate the equilibrium separation d between Shockley partial dislocations under normal stress applied that is perpendicular to the slip plane (along x_2 axis). Red color indicates partial dislocations and dislocation lines along x_1 axis, while the grey color represents the stacking fault. Orange color indicates the elliptic cylinder that undergoes some eigenstrain $\epsilon^T = \epsilon_{22}^T = \Delta_n(\Delta_s, T_n)$. Blue color indicates boundary atoms. 114

6.9 Inelastic vertical displacement at the stable stacking fault position ($\Delta_s = b_p$) in a) Ni and b) Al between atomic planes immediately across the slip plane ($\Delta_n^{(0)}$) (red color), and between atomic planes just above and below the slip plane ($\Delta_n^{(1)}$) (blue color). The inelastic vertical displacement is zero everywhere else, as shown here for ($\Delta_n^{(2)}$) (orange color). 115

6.10 Equilibrium separation between partial dislocations in a) Ni and b) Al at different applied stress that is perpendicular to the slip plane, normalized with its value at zero applied load, as predicted by Eq. 6.17 with γ_{ssf}^{enth} (black line), or by Eq. 6.24 (blue color), and as observed in atomistic simulations (orange squares). 116

6.11 a) Crack geometry in mixed Mode II/I loading formed by removing one layer of atoms and then by artificially canceling the interaction between the atoms marked with black circles. b) Crack geometry after dislocation emission. Opening stress just before the emission is measured between atoms marked with stars. Atoms are colored based on Common Neighbor Analysis [15]; green for fcc, red for hcp and white for surface atoms. 119

6.12 Molecular statics results of the critical stress intensity factor K_{IIe} as a function of the applied K_I in mixed Mode II/I loading in nickel (blue diamonds), copper (red squares) and aluminum (green circles). Crack-tip opening stresses just before the emission are indicated for every applied K_I . Solid symbols correspond to the emission along the upper (initial) slip plane, while the open symbols correspond to the emission along the lower slip plane. 120

A.1 Tangent elastic Shear moduli μ and Poisson's ratios ν in Ni and Al computed using molecular statics at $T = 0K$ as a function of the applied far-field normal stress T_n 128

A.2 Studied crack tip triangular structural unit: a) initial geometry; b) the crack tip unit under pure shear; c) the crack tip unit under shear and normal stresses. . . . 129

A.3 The shear displacement distribution along the slip plane in Mode II (screening) and Mode I (blunting) at different far-field K in Ni. 130

A.4 Restoring stress τ_{res} of the crack tip structural with the surface step creation (the blue line) and without the surface step creation (the red line) and the family of applied stresses τ_{app} (green lines) for different applied K_I in Nickel. 131

A.5 a) The shear displacement distribution along the slip plane in Mode I for different inclination angles θ ; b) The effective Mode II stress intensity factor as a function of the inclination angle θ which causes the same crack tip shear displacements. 132

A.6 a) Nucleation energy as a function of the relative slip for different inclination angles θ ; b) The shear resistance, computed from the nucleation energy, for different inclination angles θ . These curves are computed for fcc Ni. 133

A.7 a) Critical stress intensity factor for dislocation emission as a function of the slip plane inclination angle θ in fcc Ni; Simulation (red diamonds); Analytical model Eq. 4.7 (purple circles); Rice theory (black squares); dashed line shows the simulation result when constraining deformation of the symmetric slip plane that exists at the lowest angle. b) Crack tip geometry when $\theta = 35.3^\circ$ and definition of the structural units along two symmetric slip planes. 133

A.8 GSFE versus slip displacement, for various applied normal tensile stresses under uniaxial strain (solid line) and uniaxial stress (dashed line) as computed using interatomic potentials at $T = 0K$ in a) nickel, b) copper and c) aluminum 136

A.9 Equilibrium separation between partial dislocations in a) Ni and b) Al at different applied stress that perpendicular to the slip plane, normalized with its value at zero applied load, as predicted by equation by Eq. 6.24 when stress dependence of elastic properties is (blue color)/is not (red color) taken into account, and as observed in atomistic simulations (orange squares). 137

List of Tables

2.1	Material properties of fcc Ni used to compute its critical stress intensity factors for Griffith cleavage K_{Ic} (Eq. 2.32) and dislocation emission K_{Ie} (Eq. 2.43). Model orientations are defined by the crack plane normal (\mathbf{n}), and the crack front direction [l].	36
4.1	Material elastic properties, unstable stacking fault energies γ_{usf} , stable stacking fault energies γ_{ssf} , unstable twinning fault energies γ_{utf} , surface energies for (111) slip plane, and material parameters $f^{(1)}$ and $f^{(2)}$ for predicting the crack-tip twinning. All the values are computed using standard methods and molecular statics simulations [103, 129]	61
4.2	Positions of the γ_{usf} , along with the simulation results in Mode I for screening and blunting given as the ratios of simulation K_{Ie} and Rice prediction for K_{Ie} , and measured shear displacements of the first and second structural units at the point of emission (see Figure 4.3).	66
4.3	Ratio of critical stress intensity factors with ($K_{Ie,step}$) and without ($K_{Ie,Rice}$) the surface step, for various values of the $g = \tau_{res}/\tau_{gsf}$ and crack tip Green's function parameter β , as computed using the Peierls model of Figure 4.10.	74
4.4	Crack tip cleavage/emission competition in magnesium as predicted from (i) Rice theory, (ii) The new theory for dislocation emission, and (iii) as observed in atomistic simulations. The values of material properties and simulations results are taken from [58].	82
5.1	Predicted critical stress intensities for twinning (Eq. 5.2) and trailing (Eq. 5.5) partial dislocation emission, for 17 fcc materials. The ratio of surface energy to unstable minus stable stacking fault energy is shown, and the Rice theory is applicable when this value is below 6.9, as indicated for those materials marked by an asterisk.	94
6.1	Stable stacking fault energy γ_{ssf} and inelastic normal displacement Δ_n computed in copper via DFT using stress boundary conditions along with the stable stacking fault enthalpy γ_{ssf}^{enth} computed using Eq. 6.3, and γ_{ssf}^{disp} computed using displacement boundary conditions.	111
A.1	Values of the parameter β computed in various fcc systems.	131

List of Tables

- A.2 Critical stress intensity factor for twinning partial dislocation emission for different slip plane inclination angles θ as predicted by the Andric-Curtin twinning theory and as observed in the simulations. The observed and predicted twinning mode is shown, along with the Griffith K_{Ic} and the parameter $f^{(1)}(C_{ijkl})$ 135

1 Introduction

1.1 Fracture toughness as the main concern of fracture mechanics

Fracture Mechanics is an absolutely necessary tool in a design process of various structures (airplanes, cars, bridges, ...) that require high reliability during their lifetime performance. A constant demand for lower cost, lower weight, and improved energy efficiency across different industries requires much faster development of new materials. The science of fracture mechanics is therefore intended to illuminate materials and structural fracture toughness, and their resistance to fatigue and embrittlement (e.g. stress corrosion cracking or hydrogen embrittlement), as key properties for preventing fracture of structures and catastrophic failure.

In spite of the engineering appearance to be systematic in using available design methods, the lack of physics-based understanding of phenomena that control fracture and fatigue has led to numerous (catastrophic) failures (see Figure 1.1). It was noted in the mid 19th century that steel structures are very sensitive to fracture and fatigue [1]. The Versailles train crash in 1842 (see Figure 1.1a), caused by fatigue fracture of a leading locomotive axle, raised an awareness about the connection between stress concentration sites and crack growth [2]. The pioneering works from the late 19th century provided momentum for further development of fracture mechanics. It was Griffith with his seminal paper [3] who made established foundations of modern fracture mechanics [4]. Using the concept of total energy variation, he showed that a certain amount of work (surface energy) is necessary to drive the crack growth in linearly elastic and brittle materials. Griffith was the first one who realized the size effects in fracture problems. However, Griffith's work was not properly recognized until the mid 20th century, when the works of Orowan [5] and Irwin [6, 7] appeared; they provided a more complete analysis in understanding fracture, and Linear Elastic Fracture Mechanics (LEFM) was born. The methods of LEFM were used for understanding the brittle fracture of large welded structures, as illustrated in Figure 1.1b by a photography of the Schenectady ship that broke in two. LEFM was/is used on a daily basis for estimating reliability assessment of various structures. However, problems associated with fracture of structures were/are reappearing. Two Comet airplanes, presented in Figure 1.1c, were lost due to a fast fatigue crack nucleated from a rectangular window in 1953 and 1954. The next

Chapter 1. Introduction

picture in Figure 1.1d is the Japan Air Lines Boeing 747 that has been lost in 1984 due to an ejection of the aircraft's vertical stabilizer caused by a fracture of the rear pressure bulkhead. The final picture in Figure 1.1e, but definitely not the last example, is the Morandi Bridge that has collapsed in Italy in 2018. Systematic analysis of different structural failures can be found in papers such as Ref. [8, 9] published in *Engineering Failure Analysis*. It is materials failure, due to crack growth, that has led to the catastrophic result in every case listed. Therefore, fracture of structures is mostly a material problem.

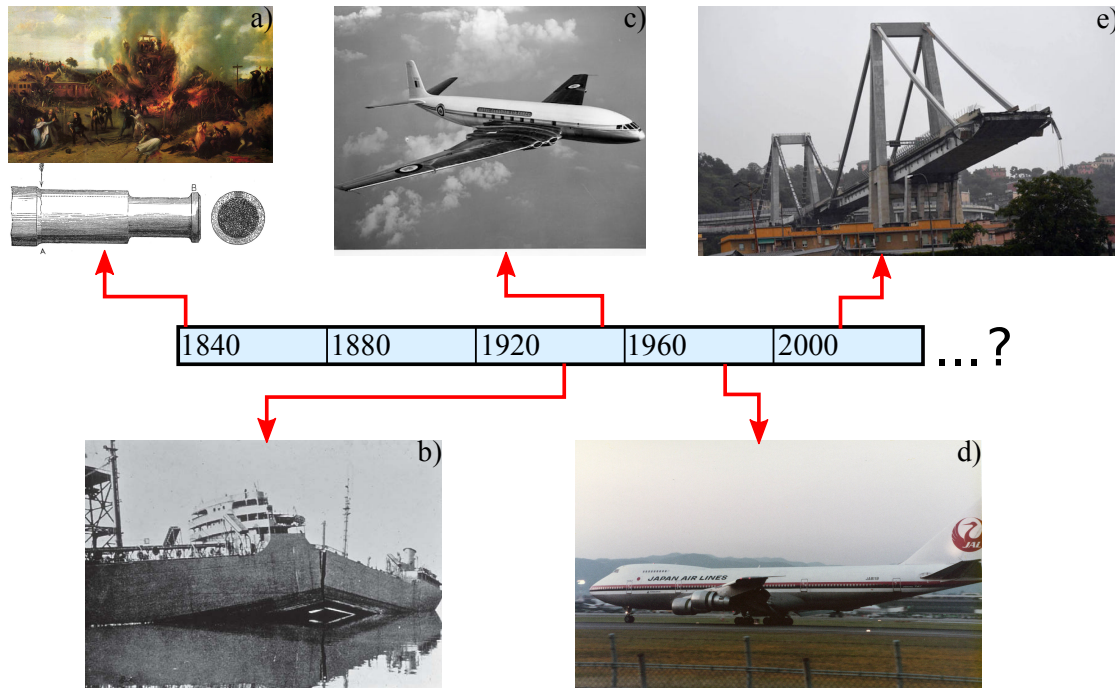


Figure 1.1 – Historical overview of catastrophic failure of structures: a) Versailles train crash in 1842 caused by fatigue fracture of a locomotive axle, b) Schenectady ship that broke into two in 1943, c) The Comet airplane lost in 1953 due to fracture from a rectangular window, d) Japan Air Lines Boeing 747 lost due to fatigue fracture in 1984, and e) Morandi Bridge collapsed in 2018.

Systematic design of materials that possess *high fracture toughness* is essential for structural performance and reliability. A widely accepted definition for fracture toughness is the material resistance to growth of a pre-existing crack. Therefore, fracture toughness can be closely related to the energy that is dissipated in the crack-tip vicinity [fracture process zone (FPZ)]. As illustrated in Figure 1.2, the dissipated energy depends on the material under consideration, and it is governed by various processes across different length scales. Figure 1.2a shows the fiber bridging between crack surfaces, as a macroscale process at the mm scale, that contributes to the fracture toughness in fiber-reinforced composites [10]. A similar process, but at the micron scale, that costs energy for crack growth in polymers is crazing (see Figure 1.2b) [11]. Crazes consist of parallel fibrils and voids, that spans the entire deformed region in front of a crack-tip, and are responsible for the large fracture toughness [12]. In extremely brittle materials, e.g. in silicon, fracture toughness is controlled only by nanoscale processes associated with cutting of

1.2. Motivation: Intrinsic ductility as a precursor to ductile fracture

interatomic forces (see Figure 1.2c). Fracture energy that is dissipated in metals and their alloys is mainly controlled by the pronounced plasticity around the crack-tip. Plastic deformations, described in Figure 1.2d by discrete dislocations [13], dissipate the energy and provide extremely high fracture toughness. A successful design of materials that possess high fracture toughness is fulfilled only if processes that contribute to the fracture toughness are completely understood. Therefore, as will be discussed later in this manuscript, *the methods of Fracture Mechanics are primarily used in finding the fracture energy.*

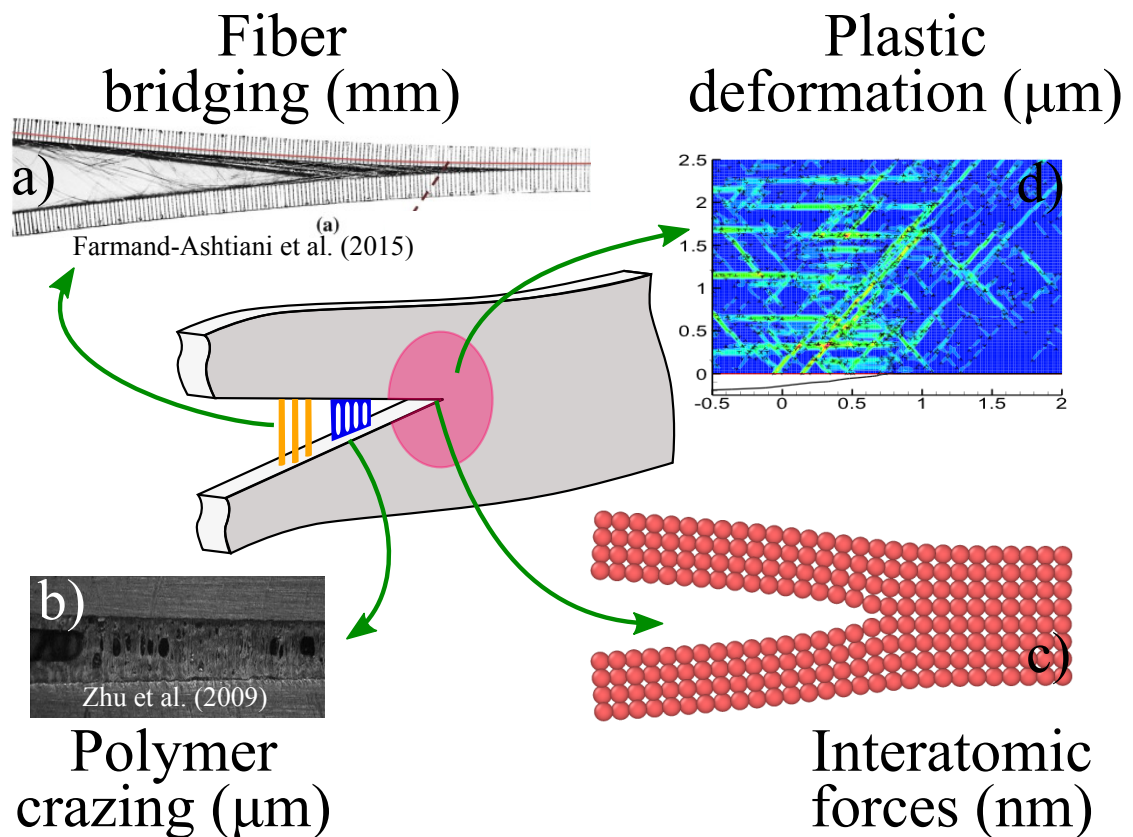


Figure 1.2 – Schematic representation showing various processes that contribute to materials fracture toughness across different length scales: a) fiber bridging in composites [10], b) crazing in polymers [11], c) interatomic forces across crack surfaces in extremely brittle materials, and d) plastic deformation, characterized by discrete dislocations, around the crack-tip in metals [14]. A particular length scale is identified by length units in parentheses.

1.2 Motivation: Intrinsic ductility as a precursor to ductile fracture

Metals and their alloys are the most widely used structural materials across many applications. They are integral constituents of many components that are used in failure-critical applications (e.g. aerospace and automotive industry, civil engineering, medicine, ...). Due to their practical importance, it is essential to understand processes that enable their high fracture toughness. The

previous section shortly discussed that the plastic deformations around a crack-tip are responsible for high fracture toughness in metals.

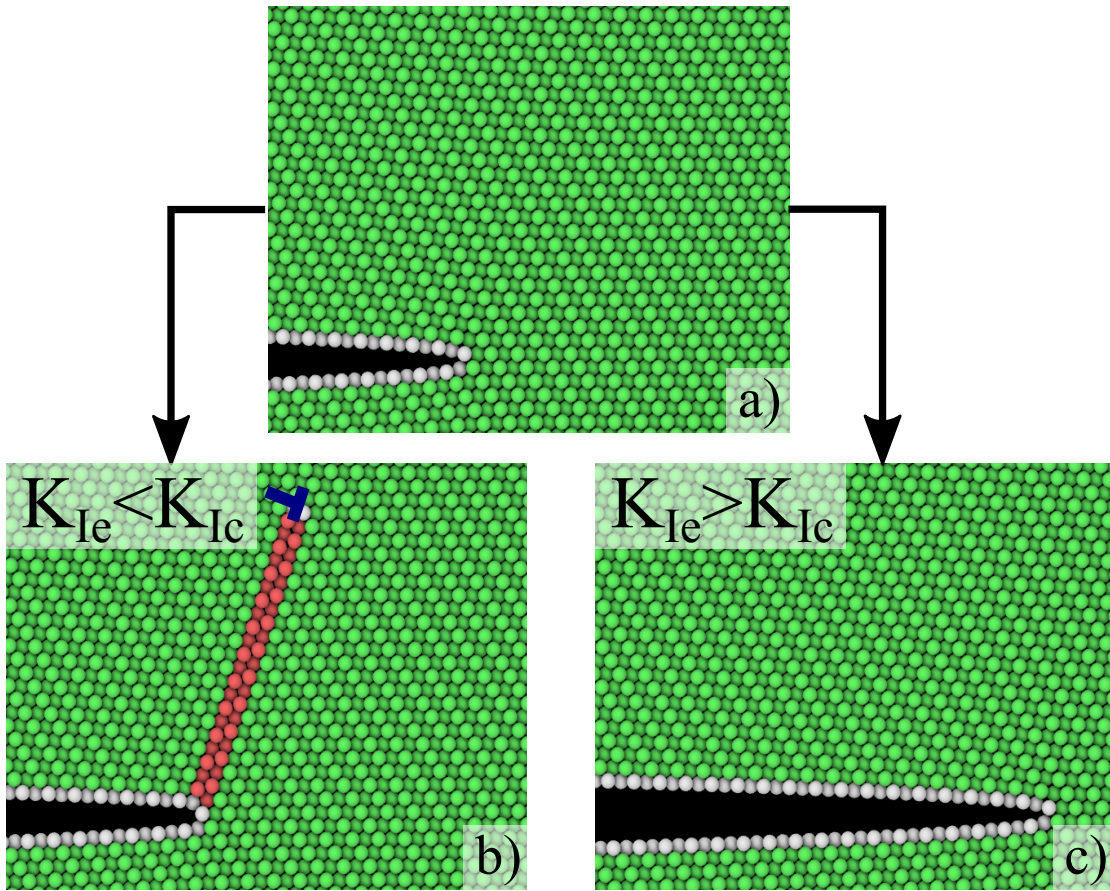


Figure 1.3 – Evolution of an atomically sharp crack in a dislocation-free fcc single crystal: a) Initial configuration at the applied load prior to dislocation emission or cleavage. b) the crack geometry after dislocation emission for which $K_{Ie} < K_{Ic}$ requirement is satisfied; c) the crack geometry after cleavage for which $K_{Ie} < K_{Ic}$ requirement is not satisfied. Note that the crack geometry stays self-similar in cleavage. Atoms are visualized using OVITO [15].

In this work, a fundamental requirement for achieving extensive plasticity around the crack tip (high fracture toughness) is addressed. *A fundamental requirement for achieving high fracture toughness in crystalline metals is that a material be intrinsically ductile, which is opposite from an intrinsically brittle material.* A crystalline metal is intrinsically ductile if an atomically sharp crack in a loaded material emits dislocation(s) and blunts rather than cleaving and remaining sharp (see Figure 1.3). Specifically, if the critical stress intensity factor for emission K_{Ie} is smaller than the critical stress intensity factor for Griffith cleavage K_{Ic} [3], then the material will emit dislocations, blunt, and eventually fail by mechanisms that absorb considerable energy (see Figure 1.3b and c). A schematic representation of how intrinsic ductility enables, or intrinsic brittleness inhibits, pronounced plasticity around the crack-tip is shown in Figure 1.4 [16].

1.2. Motivation: Intrinsic ductility as a precursor to ductile fracture

Figure 1.4a shows an initial configuration of a single crystal with a pre-existing atomically sharp crack. In an intrinsically brittle material, the crack is unable to emit dislocations. With increasing of the applied load, the crack remains sharp and eventually starts growing in a cleavage-like manner leading to a very low fracture toughness (see Figure 1.4b). In an intrinsically ductile material, as illustrated in Figure 1.4c, the crack naturally emits dislocations and blunts, therefore changes the singularity at the tip and enables pronounced plasticity to develop. Eventually, a large hydrostatic pressure develops in front the tip, leading to void nucleation, growth and coalescence, and eventually to a large energy dissipation; this process is known as ductile fracture in metals. In both examples shown, the usual far-field plasticity is present and contributes to the measured fracture toughness. However, the overall fracture behavior and toughness is completely different in the two cases.

Dislocation emission from the crack tip is thus a necessary precursor to crack tip blunting and toughening. It also represents one of the fundamental problems in mechanics of materials. In light of its practical importance, the present manuscript provides a theoretical physics-based framework for computing the critical stress intensity factor for crack tip dislocation emission and twinning.

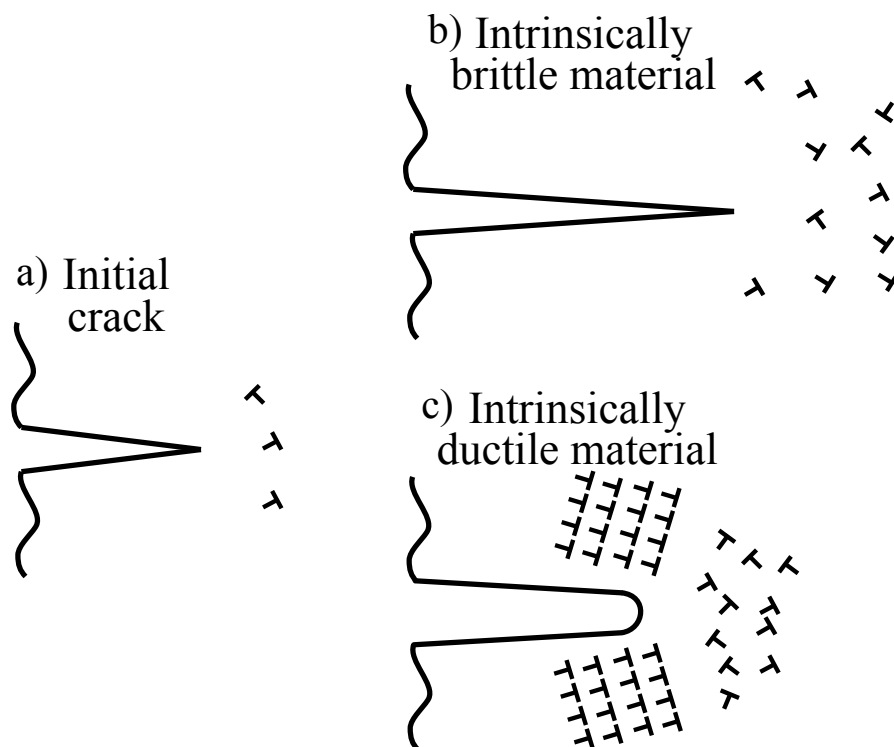


Figure 1.4 – Schematic representation of how intrinsic ductility enables, or intrinsic brittleness inhibits, pronounced plasticity around the crack-tip: a) Initial configuration with an atomically sharp crack; b) Fracture in an intrinsically brittle material where the crack remains sharp during the loading; c) Fracture in an intrinsically ductile material where the crack is blunted by emission of dislocations. In both examples, there is some far-field plasticity that can contribute to the materials fracture toughness.

1.3 Outline of the thesis

The remainder of this thesis is organized as follows:

Chapter 2 discuss methods for modeling fracture across different length scale. The basic equations of Linear Elastic Fracture Mechanics are introduced in Section 2.1, with a focus on the asymptotic stress and displacement fields around a crack-tip, the scale of the K-dominant zone, and energetic perspectives associated with the crack-tip processes. Section 2.2 presents the Cohesive zone model for describing the non-linear behavior in front the tip. Section 2.3 discuss available methods for modeling energy dissipation due to plastic deformations in metals using either Continuum Plasticity-Cohesive Zone (CP-CZ) or Discrete Dislocation-Cohesive Zone (DD-CZ) modeling of fracture. Finally, Section 2.4 critically analyze methods used for atomistic modeling of fracture.

In Chapter 3, we give a brief presentation of the continuum theories for predicting the critical stress intensity factors for various crack-tip dislocation emission processes. Section 3.2 gives a more detailed exposition of the Rice theory and its predictions for critical stress intensity factors for the first partial emission K_{Ie}^{first} , trailing partial emission K_{Ie}^{trail} and the critical slip Δ_c for elastically isotropic and anisotropic materials. Section 3.3 provides an overview of the Tadmor-Hai theory for predicting the critical stress intensity for crack-tip twinning K_{Ie}^{twin} . Finally, in Section 3.4 we discuss the shielding effect of the first partial dislocation on further nucleation processes.

In Chapter 4, we present a new theory for Mode I crack-tip dislocation emission. In Section 4.2, we first introduce 17 fcc materials that are studied here, after which we carefully validate the Rice model for Mode II loading for these materials, and finally we present results for Mode I loading, with a slip plane inclined at an angle $\theta = 70.53^\circ$ with respect to the crack plane, and show clear deviations from the Rice theory. In Section 4.3, we show that the energy change at the crack tip during the emission/slip process has contributions from the surface step energy as well as the stacking fault energy. In section 4.4, we developed the new theory for crack tip dislocation emission based on a mechanical instability at the crack tip. In Section 4.5, we compare the new theoretical model for dislocation emission to simulations across a wide range of fcc materials. In section 4.6, we introduce an analytic criteria and show it to be in good agreement with the full model results. Implications of the new model are then discussed and our main results reiterated in Section 4.7.

In Chapter 5, we present a new theory for crack-tip twinning in fcc metals. In Section 5.2, we evaluate the accuracy of the Tadmor-Hai twinning theory against atomistic simulations for 17 fcc metals introduced in Section 4.2, and show the quantitative failures of the theory. To better understand the controlling crack-tip phenomena, in Section 5.3 we investigate the energy changes at the crack tip during the emission processes and show that twinning partial emission is not accompanied by step creation while trailing partial emission does involve step creation. In Section 5.4, we introduce a modified Tadmor-Hai theory for predicting crack-tip twinning

and show excellent agreement with the simulations. Then, in Section 5.5, we apply the theory presented in Chapter 4 to predict K_{Ie}^{trail} and resolve the discrepancy between the Tadmor-Hai trends and simulations. In Section 5.6 we introduce and analyze “forward” twinning as a new twinning mode. Finally, in Section 5.7, we present concluding remarks.

In Chapter 6, we analyze stress dependence of generalized stacking fault energies (GSFE). In Section 6.2, we introduce methods for computing the GSFE $\Psi_{gsf}(\Delta_s, T_n)$ and inelastic normal displacement $\Delta_n(\Delta_s, T_n)$ under an applied normal tensile stress T_n . Section 6.3 presents our results for the GSFE and inelastic normal displacement, as computed using interatomic potentials and first-principles methods, and the subsequent determinations of $\Psi_{gsf}(\Delta_s, \Delta_n)$ and generalized stacking fault enthalpy (GSFH) $\Psi_{gsf}^{enth}(\Delta_s, T_n)$. In Section 6.4, we show the errors that arise in the computation of the GSFE and GSFH when computed using displacement boundary condition; these rationalize previous literature results. Section 6.5 discuss which thermodynamics quantity is most appropriate to use for describing different mechanics problems.

The main results of the thesis are then reiterated in Section 7. The main implications of the work are analyzed and directions for further research are discussed.

2 Modeling fracture across different length scales

This chapter is partly extracted from the following publication:

- (1) Andric P, Curtin WA. Atomistic modeling of fracture. *Modelling and Simulation in Materials Science and Engineering*. 2018 Nov 16;27(1):013001.

The contemporary design process of materials is intimately coupled to modeling of fracture across different length scales, from macro- and continuum scale, down to meso- and atomic scale. Neglecting fracture behavior associated with one of the length scales can lead to poor understanding of the different phenomena that contribute to the overall fracture toughness of a material. Comprehensive understanding of the phenomena that control fracture is necessary to prevent catastrophic failure. The process of understanding first begins with describing the state of the cracked body using Linear Elastic Fracture Mechanics.

2.1 Linear Elastic Fracture Mechanics

Linear Elastic Fracture Mechanics (LEFM), as one of the most successful sub-fields of Solid Mechanics, is used for describing and predicting different fracture phenomena, such as: (i) Brittle fracture under (quasi)-static and dynamic loading, (ii) Stress-corrosion cracking, (iii) Fatigue crack growth, or (iv) Atomic scale fracture. Understanding of LEFM is a crucial requirement for modeling fracture, from continuum scale, down to atomic scale. In LEFM, the entire body behaves according to linear elasticity, and then the local crack tip phenomena at distances from the crack tip $r \ll a$ are occurring within the asymptotic field very near to the crack tip. When the non-linear/non-convex behavior is confined to a region $r \ll a$ (to be more carefully specified below), conditions known as "small scale yielding" (SSY), the loading is entirely controlled by the magnitude of the asymptotic fields predicted by LEFM [17, 18]. This framework is captured schematically in Figure 2.1, which indicates the full domain of interest containing a crack, the region near the crack tip where the asymptotic fields dominate (the so-called K-dominant zone $r < r_K$), and the domain of non-linear/non-convex behavior (the so-called Fracture Process

Chapter 2. Modeling fracture across different length scales

Zone (FPZ), occurring over a scale $r_{FPZ} \ll r_K$. When small scale yielding is satisfied, i.e. $r_{FPZ} \ll r_K \ll a$, the crack tip behavior depends only on the asymptotic crack tip fields and not on the macroscopic loading conditions. This confers a huge generality to studies focused on the crack tip region. When SSY conditions are satisfied, phenomena observed and quantified in the FPZ as a function of the magnitude of the asymptotic field are relevant to all macroscopic fracture problems independent of loading and geometry. Before launching into details, one can already conclude that all the beauty and simplicity of LEFM is in its one-parameter dependence. LEFM is well-established in a vast literature [19, 20, 21, 22] but we revisit the key results here since they form the fundamental theoretical basis for modeling fracture across different length scales.

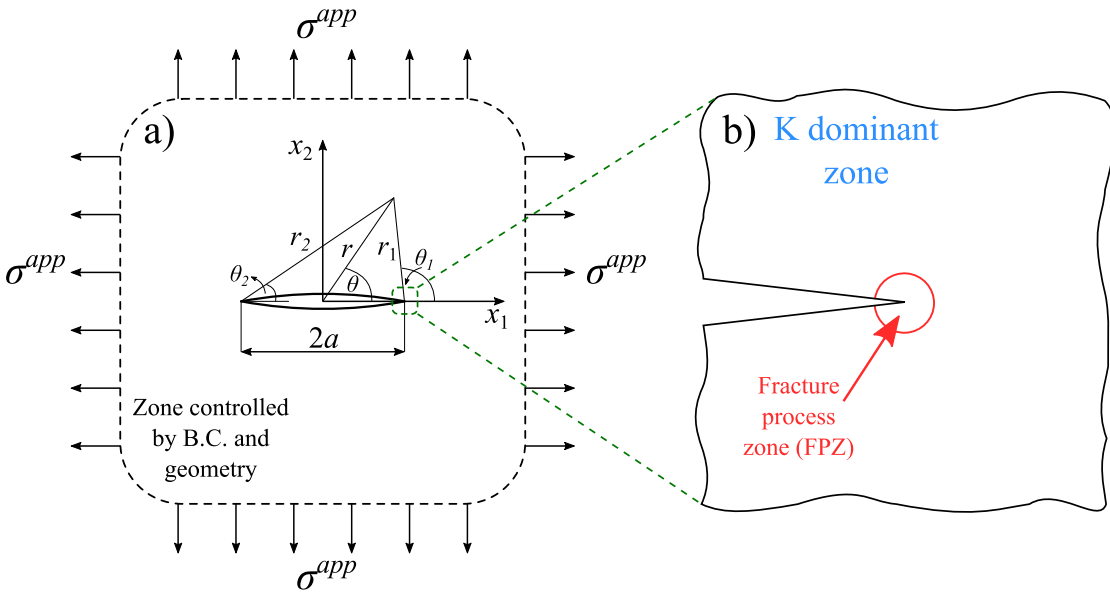


Figure 2.1 – a) Centrally positioned finite crack in an infinite plate under biaxial stress σ^{app} . Stresses in the outer zone (sufficiently far from the crack) are strongly influenced by the boundary conditions (B.C.) and sample geometry. b) Stress zones in a cracked body with the fracture process zone (FPZ) in the vicinity of the crack-tip, surrounded by the K-dominance zone where the asymptotic fields given by Eq. 2.8 are accurate. The size of the K-dominant zone is much smaller than the crack size.

2.1.1 Crack stress fields in Plane Strain

We consider a large plate of lateral dimensions $-L/2 < x_1 < L/2$, $-L/2 < x_2 < L/2$ made of a linear isotropic material and subject to plane strain loading so that results are independent of the out-of-plane x_3 dimension. The plate contains a finite crack of a size $2a$ in the center $-a < x_1 < a$, $x_2 = 0$ with $a \ll L$. The crack is defined by the imposition of traction-free boundary conditions on both the upper and lower crack surfaces. Here, we analyze the plate subjected to a biaxial stress σ^{app} applied on the outer boundaries with $L \rightarrow \infty$ (see Fig. 2.1a).

This loading scenario corresponds to the so-called Mode I fracture mode, where the crack is

opened by a perpendicular tensile load. Mode II (in-plane shear) and Mode III (anti-plane strain) are the other two independent modes of loading, but the general conclusions from the theory for Mode I apply equally to Mode II and Mode III loading, and so these are not discussed here. Although the Mode I biaxial loading may appear to be a special case even for Mode I, it will be shown below that the asymptotic singular stresses in the crack-tip vicinity do not depend on the geometry or the far-field loading. The outer boundary conditions for the problem are then

$$\begin{aligned}\sigma_{12} = \sigma_{22} = 0 \text{ at } |x_1| \leq a \text{ and } x_2 = 0 \\ \sigma_{11} = \sigma_{22} = \sigma^{app} \text{ at } x_i^2 \rightarrow \infty.\end{aligned}\tag{2.1}$$

In linear elasticity, components of the small strain tensor are related to components of the displacement field u_i as $\epsilon_{ij} = (u_{i,j} + u_{j,i})/2$, where $(\cdot)_{,i}$ denotes partial differentiation with respect to x_i . The stress tensor is related to the strain tensor via Hooke's law $\sigma_{ij} = C_{ijkl}\epsilon_{kl}$ where C_{ijkl} is the material stiffness tensor. We will start with isotropic elasticity and later generalize to anisotropic elasticity, since nearly all single crystal materials are anisotropic to some degree. The two independent elastic constants in isotropic elasticity are then taken as the shear modulus μ and Poisson ratio ν . The solution to the equilibrium equation in linear elasticity and the given boundary conditions can be obtained using different methods such as complex potential method [23] or Eshelby inclusion method [24]. In this work, the solutions for a cracked plane are obtained using the complex potential method following the Kolosov-Muskhelishvili formulation [23]. The stress and displacement fields are given in terms of complex potentials as

$$\begin{aligned}\sigma_{11} + \sigma_{22} &= 4\text{Re}\{\psi(z)_{,1}\} \\ \sigma_{22} - \sigma_{11} + 2i\sigma_{12} &= 2\{\bar{z}\psi(z)_{,2} + \chi(z)_{,2}\} \\ 2\mu(u_1 + iu_2) &= (3 - 4\nu)\psi(z) - \overline{z\psi(z)_{,1}} - \overline{\chi(z)_{,1}}\end{aligned}\tag{2.2}$$

where $z = x_1 + ix_2$, and $\psi(z)$ and $\chi(z)$ are analytical complex functions to be determined. Since the crack fields will be singular at the crack tips, the complex functions must have the appropriate singularities. Note that $(\cdot)_{,1}$ and $(\cdot)_{,2}$ in Eq. 2.2 are the first and second derivative with respect to z , respectively. The solution of the unknown complex function $\psi(z)$ for the crack problem was introduced by Westergaard [25] as

$$\begin{aligned}\psi &= \frac{1}{2}\sigma^{app}\sqrt{z^2 - a^2} + Az \\ \psi_{,1} &= \frac{\sigma^{app}z}{\sqrt{z^2 - a^2}} + A\end{aligned}\tag{2.3}$$

where A is a real valued constant. Since the far-field loading is symmetric with respect to the x_1 axis, the shear stress $\sigma_{12} = 0$ along $x_2 = 0$. This leads to the unique relation between $\psi(z)$ and $\chi(z)$ as

$$\chi(z)_{,2} + \bar{z}\psi(z)_{,2} + A = 0.\tag{2.4}$$

Chapter 2. Modeling fracture across different length scales

For the present case of biaxial tension $A = 0$ while for uniaxial tension $A = \sigma^{app}/2$. The stress field associated with A does not contribute to the crack-tip singularity. Substituting Eqs. 2.3 and 2.4 into Eq. 2.2 yields a solution for the unknown stress field that is most conveniently expressed in terms of the polar coordinates (see Fig. 2.1a) with

$$\begin{aligned} z &= r e^{i\theta} \\ z - a &= r_1 e^{i\theta_1} \\ z + a &= r_2 e^{i\theta_2}. \end{aligned} \quad (2.5)$$

With this notation, the stress field is

$$\begin{aligned} \sigma_{11} &= \frac{\sigma^{app} r}{\sqrt{r_1 r_2}} \left[\cos \left(\theta - \frac{1}{2} \theta_1 - \frac{1}{2} \theta_2 \right) - \frac{a^2}{r_1 r_2} \sin \theta \sin \frac{3}{2} (\theta_1 + \theta_2) \right] \\ \sigma_{22} &= \frac{\sigma^{app} r}{\sqrt{r_1 r_2}} \left[\cos \left(\theta - \frac{1}{2} \theta_1 - \frac{1}{2} \theta_2 \right) + \frac{a^2}{r_1 r_2} \sin \theta \sin \frac{3}{2} (\theta_1 + \theta_2) \right] \\ \sigma_{12} &= \frac{\sigma^{app} r}{\sqrt{r_1 r_2}} \left[\frac{a^2}{r_1 r_2} \sin \theta \cos \frac{3}{2} (\theta_1 + \theta_2) \right]. \end{aligned} \quad (2.6)$$

2.1.2 Asymptotic near-tip stress fields

The stress fields close to the crack tip are of fundamental importance in fracture mechanics. These asymptotic fields are obtained by taking the limits $\sigma_{ij} \rightarrow \infty$ as $r_i \rightarrow 0$, with various terms above reducing to

$$\begin{aligned} \frac{r_1}{a} &\ll 1, \quad \theta \approx 0, \quad \theta_2 \approx 0 \\ r &\approx a, \quad r_2 \approx 2a \\ \sin \theta &\approx \frac{r_1}{a} \sin \theta_1 \\ \sin \frac{3}{2} (\theta_1 + \theta_2) &\approx \sin \frac{3}{2} \theta_1 \\ \cos \left(\theta - \frac{1}{2} \theta_1 - \frac{1}{2} \theta_2 \right) &\approx \cos \frac{1}{2} \theta_1 \\ \cos \frac{3}{2} (\theta_1 + \theta_2) &\approx \cos \frac{3}{2} \theta_1 \end{aligned} \quad (2.7)$$

and thus leading to the asymptotic near-tip stress state

$$\begin{aligned} \sigma_{11} &= \frac{\sigma^{app} a}{\sqrt{2a r_1}} \cos \frac{1}{2} \theta_1 \left(1 - \sin \frac{1}{2} \theta_1 \sin \frac{3}{2} \theta_1 \right) \\ \sigma_{22} &= \frac{\sigma^{app} a}{\sqrt{2a r_1}} \cos \frac{1}{2} \theta_1 \left(1 + \sin \frac{1}{2} \theta_1 \sin \frac{3}{2} \theta_1 \right) \\ \sigma_{12} &= \frac{\sigma^{app} a}{\sqrt{2a r_1}} \sin \frac{1}{2} \theta_1 \cos \frac{1}{2} \theta_1 \cos \frac{3}{2} \theta_1. \end{aligned} \quad (2.8)$$

Shifting the coordinate system to be centered on the crack tip ($r, \theta_1 \equiv \theta$), the near-tip can be expressed in terms of the Mode I *stress intensity factor* K_I as

$$\begin{aligned}\sigma_{11} &= \frac{K_I}{\sqrt{2\pi r}} \cos \frac{1}{2}\theta \left(1 - \sin \frac{1}{2}\theta \sin \frac{3}{2}\theta\right) \\ \sigma_{22} &= \frac{K_I}{\sqrt{2\pi r}} \cos \frac{1}{2}\theta \left(1 + \sin \frac{1}{2}\theta \sin \frac{3}{2}\theta\right) \\ \sigma_{12} &= \frac{K_I}{\sqrt{2\pi r}} \sin \frac{1}{2}\theta \cos \frac{1}{2}\theta \cos \frac{3}{2}\theta\end{aligned}\tag{2.9}$$

with K_I for this problem defined as [6]

$$K_I = \sigma^{app} \sqrt{\pi a} .\tag{2.10}$$

The asymptotic stress field is thus independent of the particular applied stress, or crack length, and only depends on the combination through the Mode I stress intensity factor K_I .

Eq. 2.9 reveals the well-known inverse square root singularity at the crack-tip, with the magnitude of the singularity controlled by the stress intensity factor K_I . Although Eq. 2.9 has been derived for a very specific loading case (see Fig. 2.1a), the asymptotic near-tip stress fields are *independent* of the geometry and boundary conditions. K_I uniquely characterizes the singular stress field near the crack tip, and does not depend on the material properties. The value of K_I is determined by the entire problem geometry and crack shape, but the crack tip behavior can be entirely characterized in terms of phenomena occurring as a function of the single loading parameter K_I . For complex geometries and loadings, the crack tip field depends on the three loading parameters K_I , K_{II} , and K_{III} ; we focus on K_I for simplicity and because it is usually more important than the other loading modes.

The asymptotic displacement fields around the crack tip can be derived in a similar manner, leading to

$$\begin{aligned}u_1 &= \frac{K_I}{\mu} \sqrt{\frac{r}{2\pi}} \cos \frac{\theta}{2} \left(1 - 2\nu + \sin^2 \frac{\theta}{2}\right) \\ u_2 &= \frac{K_I}{\mu} \sqrt{\frac{r}{2\pi}} \sin \frac{\theta}{2} \left(2 - 2\nu - \cos^2 \frac{\theta}{2}\right).\end{aligned}\tag{2.11}$$

Note that Eq. 2.11 is only valid for the plane-strain approximation.

The isotropic results of Eqs. 2.9 and 2.11 can be generalized to full anisotropic elasticity [26]. Atomistic simulations often deal with crystalline materials that are elastically anisotropic. Macroscopic isotropy only emerges in aggregates of polycrystals. Thus, detailed simulation and interpretation of atomistic simulation results requires the application of anisotropic elasticity and/or a quantitative understanding of the differences created by using isotropic models to understand anisotropic materials. A very detailed and complete description of the general formalism developed by Stroh [27] and its application to fracture problems can be found in Chapters 5 and

11, respectively, of "*Anisotropic elasticity: Theory and Application*", T. C. T. Ting [26], and hence we only summarize the major results here. The anisotropic stress fields are

$$\begin{aligned} [\sigma_{11}, \sigma_{21}, \sigma_{31}]^T &= -\frac{K_I}{\sqrt{2\pi r}} \operatorname{Re} \left\{ \mathbf{B} \left\langle \frac{v_\alpha}{\sqrt{\cos \theta + v_\alpha \sin \theta}} \right\rangle \mathbf{B}^{-1} \right\} \\ [\sigma_{12}, \sigma_{22}, \sigma_{32}]^T &= -\frac{K_I}{\sqrt{2\pi r}} \operatorname{Re} \left\{ \mathbf{B} \left\langle \frac{1}{\sqrt{\cos \theta + v_\alpha \sin \theta}} \right\rangle \mathbf{B}^{-1} \right\} \end{aligned} \quad (2.12)$$

for the near tip stress state. The angle bracket notation in Eq. 2.12 and subsequently below is used to represent elements of an diagonal matrix. The corresponding near tip displacement fields are

$$\mathbf{u} = K_I \sqrt{\frac{2r}{\pi}} \operatorname{Re} \left\{ \mathbf{A} \left\langle \sqrt{\cos \theta + v_\alpha \sin \theta} \right\rangle \mathbf{B}^{-1} \right\} \quad (2.13)$$

where v , \mathbf{A} and \mathbf{B} satisfy the following eigenvalue equation

$$\mathbf{N} \begin{bmatrix} \mathbf{A} \\ \mathbf{B} \end{bmatrix} = v \begin{bmatrix} \mathbf{A} \\ \mathbf{B} \end{bmatrix}. \quad (2.14)$$

In Eq. 2.14 $v = \langle v_\alpha \rangle = \operatorname{diag}[v_\alpha]$ are the eigenvalues defined in the Stroh formalism, $\mathbf{A} = [\mathbf{a}_1, \mathbf{a}_2, \mathbf{a}_3]$ and $\mathbf{B} = [\mathbf{b}_1, \mathbf{b}_2, \mathbf{b}_3]$ are complex matrices composed of eigenvectors \mathbf{a} and \mathbf{b} , and \mathbf{N} is the *fundamental elasticity matrix* [28] defined as

$$\mathbf{N} = \begin{bmatrix} \mathbf{N}_1 & \mathbf{N}_2 \\ \mathbf{N}_3 & \mathbf{N}_1^T \end{bmatrix} \quad (2.15)$$

with

$$\mathbf{N}_1 = -\mathbf{T}^{-1} \mathbf{R}^T, \quad \mathbf{N}_2 = \mathbf{T}^{-1}, \quad \mathbf{N}_3 = \mathbf{R} \mathbf{T}^{-1} \mathbf{R}^T - \mathbf{Q} \quad (2.16)$$

and

$$\mathbf{Q} = \begin{bmatrix} C_{11} & C_{16} & C_{15} \\ C_{16} & C_{66} & C_{56} \\ C_{15} & C_{56} & C_{55} \end{bmatrix}, \quad \mathbf{R} = \begin{bmatrix} C_{16} & C_{12} & C_{14} \\ C_{66} & C_{26} & C_{46} \\ C_{56} & C_{25} & C_{45} \end{bmatrix}, \quad \mathbf{T} = \begin{bmatrix} C_{66} & C_{26} & C_{46} \\ C_{26} & C_{22} & C_{24} \\ C_{46} & C_{24} & C_{44} \end{bmatrix}. \quad (2.17)$$

C_{ij} in Eq.2.17 are the components of the material stiffness tensor written in the contracted (Voigt) notation. A closed form analytical solution can be derived when the material properties are

symmetric about the crack line [20], leading to

$$\begin{aligned}\sigma_{11} &= \frac{K_I}{\sqrt{2\pi r}} \operatorname{Re} \left[\frac{a_1 a_2}{a_1 - a_2} \left(\frac{a_2}{\sqrt{\cos \theta + a_2 \sin \theta}} - \frac{a_1}{\sqrt{\cos \theta + a_1 \sin \theta}} \right) \right] \\ \sigma_{22} &= \frac{K_I}{\sqrt{2\pi r}} \operatorname{Re} \left[\frac{1}{a_1 - a_2} \left(\frac{a_1}{\sqrt{\cos \theta + a_2 \sin \theta}} - \frac{a_2}{\sqrt{\cos \theta + a_1 \sin \theta}} \right) \right] \\ \sigma_{12} &= \frac{K_I}{\sqrt{2\pi r}} \operatorname{Re} \left[\frac{a_1 a_2}{a_1 - a_2} \left(\frac{1}{\sqrt{\cos \theta + a_1 \sin \theta}} - \frac{1}{\sqrt{\cos \theta + a_2 \sin \theta}} \right) \right]\end{aligned}\quad (2.18)$$

for the near-tip stress state and

$$\begin{aligned}u_1 &= K_I \sqrt{\frac{2r}{\pi}} \operatorname{Re} \left[\frac{1}{a_1 - a_2} \left(a_1 p_2 \sqrt{\cos \theta + a_2 \sin \theta} - a_2 p_1 \sqrt{\cos \theta + a_1 \sin \theta} \right) \right] \\ u_1 &= K_I \sqrt{\frac{2r}{\pi}} \operatorname{Re} \left[\frac{1}{a_1 - a_2} \left(a_1 q_2 \sqrt{\cos \theta + a_2 \sin \theta} - a_2 q_1 \sqrt{\cos \theta + a_1 \sin \theta} \right) \right]\end{aligned}\quad (2.19)$$

for the near tip displacement fields, where p_1 , p_2 , q_1 and q_2 depend on the material elastic properties. These constants can be found from

$$\begin{aligned}p_1 &= S_{11}^p a_1^2 + S_{12}^p - S_{16}^p a_1 \\ p_2 &= S_{11}^p a_2^2 + S_{12}^p - S_{16}^p a_2 \\ q_1 &= S_{12}^p a_1 + S_{22}^p / a_1 - S_{26}^p \\ q_2 &= S_{12}^p a_2 + S_{22}^p / a_2 - S_{26}^p\end{aligned}\quad (2.20)$$

where a_1 and a_2 are roots of the following characteristic equation

$$S_{11}^p a^4 - 2S_{16}^p a^3 + (2S_{12}^p + S_{66}^p) a^2 - 2S_{26}^p a + S_{22}^p = 0 \quad (2.21)$$

and $S_{ij}^p = S_{ij} - S_{i3}S_{3j}/S_{33}$, where $\mathbf{S} = \mathbf{C}^{-1}$, are components of the material compliance tensor for the plane strain approximation, when expressed in the Voigt notation. The above equations are slightly unwieldy, but easily computed. Thus, there is little impediment to the application of full anisotropic elasticity in simulations and their interpretation when using the K -test methodology (see below). For the center-crack tensions (CCT) specimen, which involves only traction boundary conditions, the simulation method is independent of the anisotropy. However, the crack tip fields follow the anisotropic results since the material is anisotropic; interpretation thus still requires knowledge of the anisotropic fields.

In addition to Eq. 2.19, we also introduce the final solution for Mode II displacement field as

$$\begin{aligned}u_1 &= K_{II} \sqrt{\frac{2r}{\pi}} \operatorname{Re} \left[\frac{1}{a_1 - a_2} \left(p_2 \sqrt{\cos \theta + a_2 \sin \theta} - p_1 \sqrt{\cos \theta + a_1 \sin \theta} \right) \right] \\ u_1 &= K_{II} \sqrt{\frac{2r}{\pi}} \operatorname{Re} \left[\frac{1}{a_1 - a_2} \left(q_2 \sqrt{\cos \theta + a_2 \sin \theta} - q_1 \sqrt{\cos \theta + a_1 \sin \theta} \right) \right].\end{aligned}\quad (2.22)$$

Eq. 2.22 is used later in the manuscript for setting displacement boundary conditions in simulations of a crack-tip dislocation emission in Mode II (see Chapter 4).

2.1.3 K-dominance zone

The asymptotic crack tip fields are controlled by the stress intensity factor K_I . However, the domain over which the asymptotic fields dominate the non-asymptotic fields depends on the crack size. Since we have the entire stress field for the center-crack problem (Eq. 2.6) and the asymptotic fields (Eq. 2.9), we can examine the relative contributions of the asymptotic and non-asymptotic fields.

The *degree of K-dominance* is usually assessed using the opening stress σ_{22} along the x_1 line ahead of the crack. The degree of K -dominance Λ is then defined as [20]

$$\Lambda = \frac{\sigma_{22}^{singular}}{\sigma_{22}^{singular} + \sigma_{22}^{nonsingular}} \quad (2.23)$$

where $\sigma_{22}^{singular} = K_I/\sqrt{2\pi x_1}$, ($x_1 > 0$, $\theta = 0$), is the singular opening stress ahead of the crack tip and

$$\sigma_{22}^{singular} + \sigma_{22}^{nonsingular} = \frac{(x_1 + a)\sigma^{app}}{\sqrt{x_1(x_1 + 2a)}}, \quad (x_1 > 0, \theta = 0) \quad (2.24)$$

is the total stress ahead of the crack-tip derived from Eq. 2.6, and rewritten for the coordinate system positioned at the right tip. Recalling that $K_I = \sigma^{app}\sqrt{\pi a}$, Eq. 2.23 can be rewritten as

$$\Lambda = \frac{\sqrt{1 + x_1/2a}}{(1 + x_1/a)} \approx 1 - 3x_1/4a. \quad (2.25)$$

A typical estimate of the radius r_K within which the asymptotic field dominates is obtained by setting $\Lambda \geq 0.90$, leading to $r_K = x_K \approx 0.15a$ for $\Lambda = 0.90$. Other choices for Λ yield different estimates but the major outcome is that the domain of K -dominance is always much smaller than the half-crack size a .

2.1.4 Crack tip processes: the fracture process zone

The diverging stresses at the crack tip that are predicted by linear elastic fracture mechanics are, of course, resolved to finite values due to non-linear response of the real material at very high stresses. The local failure of linear elastic fracture mechanics does not, however, negate the role of K_I as the relevant loading parameter. The deviations from linear behavior can be thought of as perturbations that are self-equilibrating locally. The deviations do not generate additional long-range fields but are only dipolar ($1/r^2$ in 2d). Therefore, all of the energetic changes in the system are also localized around the region of non-linear behavior, and this domain

is termed the "fracture process zone (FPZ)" with characteristic scale r_{FPZ} around the tip. As long as the non-linear behavior is well-confined within the K -dominant domain, $r_{FPZ} \ll r_K$, the asymptotic fields at $r \approx r_K$ are unchanged, and the fields beyond r_K are also unchanged. The present qualitative discussion is formally proven by Rice [29] and Willis [18].

The major quantity of interest in modeling of fracture across different scales is the effective fracture toughness, i.e. the resistance of the material to crack growth including all of the near-tip energy-dissipating processes that may occur in the FPZ. Since loading is determined entirely by K_I , the fracture toughness is equal to the critical stress intensity K_{Ic} at which the crack extends. The critical stress intensity K_{Ic} may evolve as the crack grows, due to an evolving size of the FPZ and associated increase in energy dissipation by FPZ processes. This is captured through the notion of a crack-resistance curve, or R-curve, $K_{Ic} = K_{Ic}(\Delta a)$ where Δa is the extent of crack growth. During crack growth, it remains necessary that the entire evolving FPZ stays within the K -dominant regime.

2.1.5 Crack tip processes: stress intensity and energetic perspectives

Since the fracture toughness is determined by energy-dissipating processes in the FPZ, it is also convenient to formulate the fracture problem in an energetic framework. To this end, one can define the mechanical *energy release rate* G [6, 7, 5] that is equal to the change in total mechanical energy of the body that would occur if the crack were to extend by an increment da . The mechanical energy release rate thus represents the amount of mechanical energy available in the entire body for paying the energetic cost of the dissipative processes. In other words, G provides the energy to drive the crack. The energy release rate G per unit da of crack extension is defined as

$$G = -\frac{d\Pi}{da} \quad (2.26)$$

where Π is the total mechanical free energy

$$\Pi = \frac{1}{2} \int_V \sigma_{ij} \epsilon_{ij} dV - \int_S T_i u_i dS . \quad (2.27)$$

The first term in Eq. 2.27 is the elastic energy stored in the loaded body while the second term is the work done by external tractions acting on the boundaries of the body.

There is then a unique relation between the energy release rate G and the stress intensity factor K_I , as shown by Irwin [6, 7], and by Rice [17, 19] using the path independence of the so-called J-integral since the stress and displacement fields depend only on the applied K_I (see Eqs. 2.9 and 2.11). Based on the results presented here, a unique relationship between G and K_I is not immediately obvious. However, for the special case of the center-crack specimen in the isotropic material, with all the fields given in Eqs. 2.9 and 2.11, we can explicitly show this relationship.

The energy release rate under plane-strain Mode I loading is

$$G = \frac{(1 - \nu)}{2\mu} K_I^2. \quad (2.28)$$

The fracture criterion $K_I = K_{Ic}$ thus also corresponds to the energetic fracture criterion $G = G_{Ic}$ where G_{Ic} is the energetic cost of the inelastic energy-dissipating processes per increment of crack growth. The fracture toughness K_{Ic} can then be computed from knowledge of the energy cost G_{Ic} due to dissipative processes as

$$K_{Ic} = \sqrt{\frac{2\mu}{1 - \nu} G_c}. \quad (2.29)$$

The isotropic results of Eq. 2.28 can be generalized to full anisotropic elasticity as [26, 27]

$$G = \mathbf{K}^T \mathbf{\Lambda} \mathbf{K} \quad (2.30)$$

where $\mathbf{\Lambda}$ is the Stroh energy tensor [27] and $\mathbf{K} = [K_{II}, K_I, K_{III}]^T$ is the stress intensity factor for a mixed mode of loading. We compute the Stroh energy tensor as

$$\mathbf{\Lambda} = \frac{1}{2} \text{Re}(i \mathbf{A} \mathbf{B}^{-1}) \quad (2.31)$$

with \mathbf{A} and \mathbf{B} computed using Eq. 2.14.

In a purely brittle material, the energy-dissipating process under quasi-static loading (no dynamics) is solely the creation of new surfaces upon extension of the crack. The critical energy release rate is thus $G_c = 2\gamma_s$ where γ_s is the surface energy of the cleavage plane and the Mode I fracture toughness is then

$$K_{Ic} = \sqrt{2\gamma_s \Lambda_{22}^{-1}}. \quad (2.32)$$

Any inelastic process can be characterized by the value of K_I or G at which the process occurs. The subscript c is reserved for the critical process of crack growth.

2.1.6 Modeling crack growth: Implementation and issues

Modeling fracture using the concept of continuum mechanics is a challenging process. Recall that the standard formulation of continuum mechanics is based on the solution of Navier's 2nd order partial differential equation (PDE) in which the displacement of all points in space is uniquely defined by material properties and applied boundary conditions. The reader is redirected to Ref. [30] for further detail about the fundamental elasticity equations. In fracture, creation of new surfaces caused by crack growth requires one point in space to divide into two. This then leads to a severe situation where the relation between points in space is lost and an unique solution does not exist. Therefore, modeling fracture at the continuum scale requires the explicit introduction

of a crack with traction free crack surfaces.

The Finite Element Method is commonly used for simulating crack growth at the continuum scale. More details on FEM can be found in Ref. [31, 32]. Here, we only point out the most important steps in modeling fracture using FEM, and to issues that can arise. As discussed above, a pre-existing crack is defined with traction free crack surfaces within the computational domain. As well, appropriate elements that are used for a more accurate description of the singular crack tip fields ($\sim r^{-1/2}$) are defined. Next, the crack-tip stress intensity factor K_I is computed with either stress or displacement fields in front of the tip, using appropriate methods based on the superposition principle [19, 20]. The condition for crack growth is satisfied if $K_I > K_{Ic}$, where K_{Ic} is the material fracture toughness calibrated to experiments. Similarly, the problem can be addressed energetically by computing the J-integral and comparing it with an experimental value J_c . If the crack propagates, the crack-tip is moved by some distance Δa . However, despite its simplicity, the FEM is not used since: (i) it is based on crack growth Δa which is not specified, (ii) the crack-growth criterion depends on the experimental values of either K_{Ic} or J_{Ic} (valid only for one material), and (iii) it is computationally very inefficient since a new mesh is required after each increment of crack growth by Δa . These issues can be circumvented using additional information from smaller scales such as meso- or atomic scale. Meso- and atomic scale modeling of fracture is discussed in detail in the following sections.

2.2 Cohesive zone model

2.2.1 The Barenblatt model

Section 2.1 provides a detailed overview of LEFM solutions for the stress field around a stationary crack as

$$\sigma_{ij} \sim \frac{K_I}{\sqrt{x}} f(C_{ijkl}, \theta) \quad (2.33)$$

which is singular at the crack-tip ($x \rightarrow 0$) (see Fig. 2.2a). The paradox associated with the crack-tip stresses being infinite arises from the linear elastic continuum representation of a material and the assumption of a perfectly sharp crack. In reality, stresses around the crack tip have some finite values which can be visualized as the red line in Fig 2.2a. The exact shape of the actual opening stress is not known a priori since it depends on fracture processes, and materials used. Several mechanics based methods have been proposed to remove the crack-tip singularity which, at least conceptually, might lead to a better physical description of the crack-tip stresses.

An independent criterion was proposed by Barenblatt [33] in which the cohesive forces between the crack surfaces were analyzed. Conceptually, Barenblatt divided the crack length into the two regions, the cohesive zone region u_c over which the cohesive forces are strong, and the remainder of the crack with length $a - u_c$ over which the cohesive forces are negligible (see Fig. 2.2b). Furthermore, the theory is based on the following two hypotheses:

Chapter 2. Modeling fracture across different length scales

- (i) The length of the section of the crack on which cohesive forces act can be assumed negligibly small in comparison with the total length of the crack or $u_c \ll a$, and
- (ii) The crack shape, and consequently the local distribution of cohesive forces, in vicinity of the points on the contour of the crack at which cohesive forces are at the maximum intensity does not depend on the applied far-field load.

The two hypothesis are naturally satisfied if the cohesive forces are large and decay rapidly to zero as the separation between crack surfaces increases.

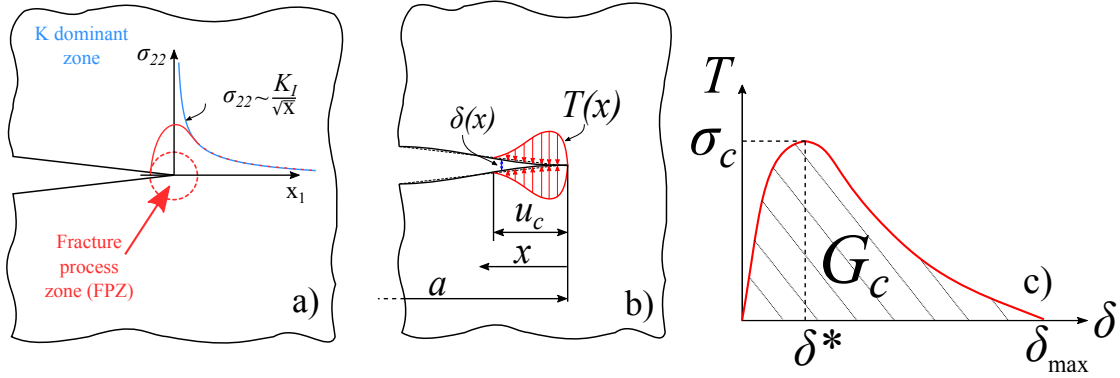


Figure 2.2 – a) Asymptotic singular opening stress $\sigma_{22}(x)$ (blue line) computed using Eq. 2.9 along with more realistic non-linear stress profile in the crack tip vicinity (red line) which depends on a material considered and fracture processes. b) Cohesive zone with tractions $T(x)$ over the length u_c , $u_c \ll a$. Note that the crack surfaces change their shape to satisfy the condition of the zero stress intensity at the tip. c) The nonlinear cohesive tractions T as a function of the crack-tip opening displacement δ . The maximum stress σ_c corresponds to the crack-tip opening displacement δ^* with $\delta^* \ll u_c$. The area under the curve is the fracture energy G_c .

The cohesive forces eliminate the crack-tip singularity by generating an additional inelastic opening displacement; this then leads to a shape change of the crack surfaces. The additional crack-tip displacement, beyond that predicted by elasticity, leads to a finite stress at the tip since the *crack-tip stress intensity* K_I^{tip} is reduced to zero, or

$$K_I^{tip} = K_I^{far} - B = 0 \quad (2.34)$$

where K_I^{far} is the far-field applied stress intensity, and B is the Barenblatt's stress intensity factor computed using the following expression [20]

$$B = 2\sqrt{\frac{a}{\pi}} \int_{a-u_c}^a \frac{T(x)dx}{\sqrt{a^2 - x^2}}. \quad (2.35)$$

The preceding equation is derived using the superposition principle and the distribution of Green's functions in half-space. Note that in LEFM $K_I^{far} = K_I^{tip}$ if there are no other stress-sources (e.g. dislocations, cohesive forces, ...) in the crack-tip vicinity. Eventually, sufficiently high K_I^{far} will lead to the condition in which the cohesive forces $T(x)$ are not any more capable to balance

K_I^{far} . This leads to the Barenblatt's criterion for the crack growth defined as:

$$K_I^{far} \geq B. \quad (2.36)$$

If the above assumptions are satisfied, the Barenblatt's theory agrees with the predictions based on LEFM. The formal details regarding agreement between LEFM and Barenblatt's theory are discussed and proved by Willis [18].

2.2.2 Cohesive zone modeling of fracture

Barenblatt's theory attracted the significant attention in the continuum mechanics community since it provides a physics-based approach for modeling the crack growth. However, aside from the general description that the cohesive tractions are related to separation of atomic layers, the specific definition of them has not been given. The present author agrees with the Barenblatt's approach since there is no need to provide such descriptions in the general theory. Beauty of the Barenblatt's model is in its generality associated with description of the crack-tip dissipating processes.

The cohesive law is supposed to describe the nonlinear traction separation of a material across the crack surfaces. A fracture problem can then be solved by collapsing the cohesive law onto a surface which is then embedded in an elastic material. *There is no uniform form for the cohesive law*, since it is material and scale dependent. An example for the nonlinear cohesive tractions T as a function of the crack opening δ is presented in Fig 2.2c. As the crack opens (δ increases), the tractions will reach the maximum stress σ_c , after which they enter in the softening regime up to the point where the tractions go to zero leading to the traction free crack surfaces. The SSY applies (crack-tip fields governed by K_I) if the lateral length of the cohesive zone u_c is much smaller than the crack size, $u_c \ll a$, and crack growth is uniquely controlled by the fracture energy G_c which is computed as

$$G_c = \int_0^{\delta_{max}} T(\delta) d\delta. \quad (2.37)$$

The above integral is simply the area under the traction versus separation curve. The maximum stress σ_c is essentially irrelevant if $u_c \ll a$; crack growth only depends on G_c . However, if the crack size is on the order of the cohesive length, $u_c \sim a$, then the maximum stress σ_c is important, and the problem becomes geometrically dependent. Eventually, once the crack is sufficiently short, the concept of fracture mechanics stop being useful.

Due to obvious practical importance, a number of cohesive laws were introduced for modeling fracture across different length scale. Dugdale cohesive zone model [34] is usually employed for simulating fracture process zone in polymers where crazing dissipates the energy. The cohesive zone model can be employed for simulating fiber pullout in composites, as previously done by Xia et al. [35]. The cohesive law for atomic separation in brittle fracture is usually described by

Chapter 2. Modeling fracture across different length scales

the so-called "Universal Binding Energy" which can be fitted to

$$T(\delta) = e \frac{\sigma_c}{\delta^*} \delta e^{-\frac{\delta}{\delta^*}} \quad (2.38)$$

where $\int_0^{\delta^{max}} T(\delta) d\delta = \gamma_s$. Universal Binding Energy of a material can be computed directly from atomistic simulations using either interatomic potentials or first principle calculations [36].

Finally, the cohesive zone model can be implemented in the finite element method using the cohesive elements. The model implementation is rather straight forward from the conceptual point of view. An additional component, due to work of the cohesive tractions over the crack surfaces S_{coh} , is simply added to the Principle of Virtual Work, leading to

$$\int_V \sigma_{ij} \delta \epsilon_{ij} dV - \int_S T_i \delta u_i dS - \int_{S_{coh}} T_i \delta u_i dS = 0. \quad (2.39)$$

However, actual implementation of the model requires a special care. First, the mesh size needs to resolve the cohesive behavior properly over the length u_c . Therefore, the minimum mesh size d in the cohesive zone needs to be at least three times smaller than the cohesive zone length, or $d < u_c/3$. Second, using the cohesive elements in a whole computational domain can lead to the artificial loss of a material stiffness. This problem is resolved either by (i) inserting the cohesive elements in a zone where the crack is expected to grow, or (ii) inserting the cohesive elements dynamically [37, 38]. Overall, the cohesive zone modeling of fracture is a powerful tool for simulating the crack growth naturally. The main advantage of the model is in introduction of the length scale through the cohesive length u_c . Finally, the model provides a connection between different scales since the cohesive model is usually derived from the smaller scale.

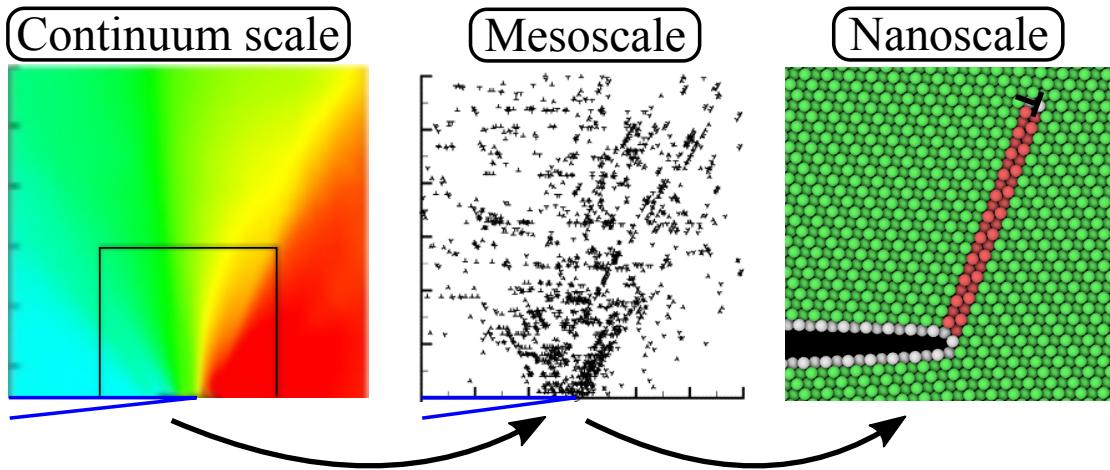


Figure 2.3 – Modeling the crack-tip plasticity from the continuum scale where plastic deformations are governed by the power-law plasticity, over the dislocation scale plasticity where discrete dislocations interact with the crack-tip, down to atomic scale where a single dislocation is emitted from the crack-tip. The left figure is taken from [39], while the middle figure is taken from [40].

2.3 Modeling fracture in metals

Two mechanisms that control the fracture toughness of metals, especially in early stages of crack growth, are: (i) atomic decohesion in front of the tip, and (ii) plastic deformation around the crack-tip. Even though the both processes are fundamentally important to achieve the high toughness, it is the energy dissipation due to plasticity that dominates. The method that is commonly used for modeling atomic decohesion in front of the tip is introduced in the previous section (Cohesive zone model). We now discuss available methods for simulating plasticity around the quasi-static growing crack in metals.

Plasticity in metals is scale-dependent. Therefore, the methods used for modeling plasticity can be grouped into: (i) the continuum scale and power-law plasticity, (ii) the mesoscale and discrete dislocation plasticity, and (iii) the atomic scale and motion of individual dislocations. Same methods apply for simulating plastic deformation around growing cracks in metals (see Figure 2.3).

2.3.1 Continuum Plasticity-Cohesive Zone (CP-CZ) modeling of fracture

Continuum Plasticity-Cohesive Zone (CPCZ) modeling of fracture was introduced by Tvergaard and Hutchinson [41] for studying crack growth resistance in an elastic-plastic solid. The cohesive law used to model decohesion in front of the tip has a trapezoidal shape with the fracture energy G_c defined as:

$$G_c = \int_0^{\delta_{max}} T d\delta = \frac{1}{2} \sigma_c [\delta_{max} + \delta_2 - \delta_1]. \quad (2.40)$$

The parameters δ_1 and δ_2 are "shape" parameters since the separation law is completely defined by G_c , σ_c , δ_1/δ_{max} and δ_2/δ_{max} . Generally, the separation law can be of any shape if the cohesive zone size is much smaller than the crack size; it is the fracture energy G_c which controls the crack growth. The trapezoidal cohesive model is commonly used since it is very convenient for numerical implementation.

A material constitutive model under uniaxial tension is described using

$$\epsilon = \begin{cases} \sigma/E, & \sigma \leq \sigma_Y \\ (\sigma_Y/E)(\sigma/\sigma_Y)^{1/N}, & \sigma \geq \sigma_Y \end{cases} \quad (2.41)$$

where σ_Y is the material yield strength, E is Young's modulus, and N corresponds to the strain hardening coefficient. A material behaves as elastic-perfectly plastic when $N=0$. The problem is then solved using the FEM with the cohesive elements used in the zone where crack growth is expected.

Figure 2.3a shows the stress field around the crack-tip in the elastic-plastic material. The stress zones in Figure 2.3a appear due to the accumulated plastic deformations along directions with

Chapter 2. Modeling fracture across different length scales

the highest resolved shear stress. Crack growth initiation is found to be in a complete agreement with Barenblatt's theory; steady-state crack growth occurs at the point where the crack opening reaches δ_{max} . The critical stress intensity factor for the steady-state crack growth K_{SS} as a function of σ_c/σ_Y and N is shown in Figure 2.4. Overall, the CP-CZ model provides reasonable qualitative trends since the simulated fracture toughness tends to be bigger if (i) there is less hardening (smaller N), and (ii) σ_c/σ_Y is sufficiently high. However, the model predicts an unrealistically high toughness (infinite) in materials with $\sigma_c/\sigma_Y > 5$ and/or $N \rightarrow 0$. Note that in metallic materials we find $\sigma_c/\sigma_Y > 10$ when the cohesive law is supposed to describe actual atomic separation ("Universal Binding Energy").

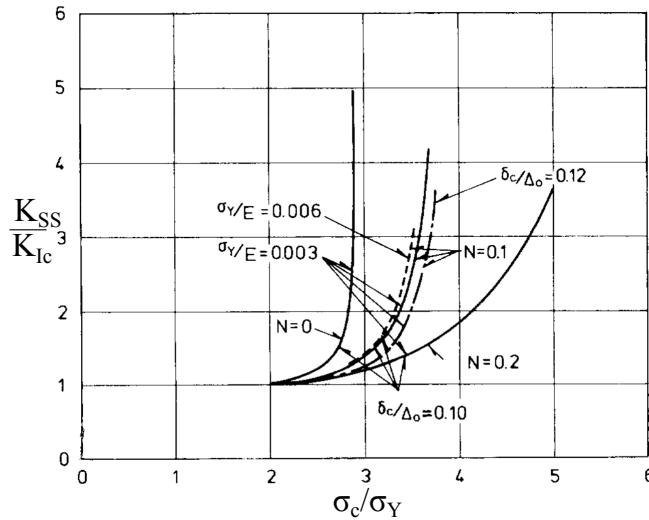


Figure 2.4 – Steady-state toughness as a function of σ_c/σ_Y for three different strain hardening exponents. Overall, fracture toughness goes towards infinity when plastic deformation around the crack tip starts being dominant. Figure is taken from [41].

The above model fails for $\sigma_c/\sigma_Y > 5$ and $N \rightarrow 0$ since the continuum plasticity is the *homogenized representation of plastic deformations caused by movement of individual dislocations*. As a consequence, complex phenomena associated with the actual interactions between the crack-tip and dislocations is lost. The above model can be improved using the strain gradient plasticity [42], or by actual description of dislocations and their interactions with the crack-tip stress field. The following section shortly describes the later approach for simulating the crack-tip plasticity within the discrete dislocation formulation [13].

2.3.2 Discrete Dislocation-Cohesive Zone (DD-CZ) modeling of fracture

It is now well-known that dislocations are the main carriers of plasticity in metals and other crystalline materials [43]. Plastic strain is controlled by collective motion of dislocations since their movement generates an additional slip in materials. Overall, plastic deformations are governed by nucleation and movement of dislocations, their various interactions and their annihilation.

The Discrete Dislocation-Cohesive Zone (DD-CZ) modeling of fracture was introduced by Van

der Giessen et al. [40]. The method is then extensively used for studying the fracture properties of short cracks [44], fatigue crack growth [45, 46], and the origin of plasticity length scales in fracture [14, 47, 48]. As in CP-CZ modeling of fracture, the atomic decohesion is modeled using the cohesive law. Further, the energy dissipated around the crack tip is modeled using the discrete dislocation formulation [13] (see Fig. 2.3). Examination of Figures 2.3a and b shows that DD-CZ has characteristics of the continuum-like plasticity over a representative volume. However, DD enables us to model actual dislocation response in highly stressed regions such as the crack-tip; this feature is, by definition, absent in the continuum crystal plasticity. The slip generated by dislocation movements close to the tip is different than predicted by the power-law plasticity. Actual modeling of discrete dislocations in the crack-tip vicinity allows us to simulate the evolution of plasticity (dislocation density) around the crack-tip (see Figure 2.5a). More importantly, Figure 2.5b shows that DD-CZ method enables for evaluating the fracture toughness in cases for which $\sigma_c/\sigma_Y > 5$.

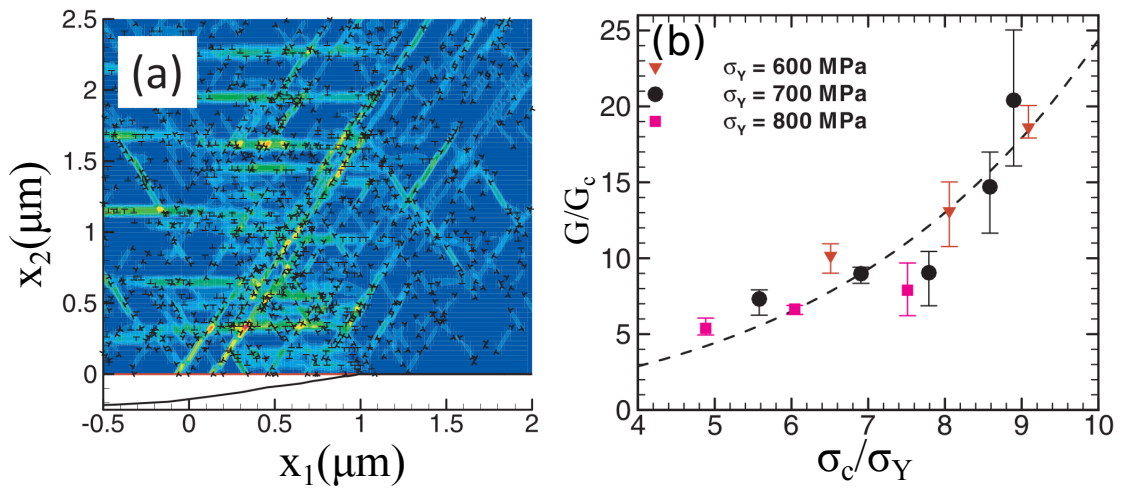


Figure 2.5 – a) Contours of local average plastic strain, along with the crack tip opening displacement ($\times 10$) obtained from DD-CZ modeling of fracture at the far-field energy release rate $G = 5.25G_c$. Position of actual dislocations are shown as symbols and the dislocation density in the region is $2 \times 10^{14}/\text{m}^2$. b) Fracture toughness G/G_c versus σ_c/σ_Y . Both figures are taken from [14]

DD-CZ modeling of fracture is shown to be a very powerful method for simulating the evolution of plasticity around the crack-tip. However, there are challenges that still need to be addressed. First, the method is computationally inefficient once a high number of dislocations is generated around the crack-tip; simulating crack growth in materials with a very low yield strength σ_Y quickly becomes infeasible. Second, interaction between dislocations and the cohesive tractions can introduce an additional uncertainty. It is noted that the crack opening due to the dislocation stress field can be significantly affected by the shape of the cohesive law [47]. Finally, the crack remains sharp as it grows through a material, while in reality the crack-tip usually blunts by dislocations emitted from the tip. The crack-tip dislocation emission is an atomistic process.

Therefore, atomistic modeling of fracture needs to be employed for simulating crack-tip blunting due to dislocation emission. More details on atomistic modeling of fracture is presented in the following section.

2.4 Atomistic modeling of fracture

A number of important phenomena in fracture are connected with atomistic/nanoscale behavior around a crack. The intrinsic nature of a material - is it brittle or ductile? - is dictated by whether an initial sharp crack will cleave (intrinsically brittle) or blunt by dislocation emission (intrinsically ductile) [3, 49, 50]. The attack of embrittling species at the crack tip, as in hydrogen embrittlement [51], involves detailed chemical interactions at the atomic scale. The behavior of cracks along, parallel to, or approaching grain boundaries, and the influence of chemical segregation to grain boundaries on fracture toughness are similarly intrinsically atomic-scale issues. The interactions of cracks with nanoscale microstructure and defects (solutes, precipitates, dislocations, voids,...) also plays a role in establishing macroscopic fracture behavior.

Given the range of important nanoscale fracture phenomena that might be of interest in different situations, it is then natural to analyze problems using atomistic simulations so as to gain mechanistic, qualitative, and/or quantitative understanding. Such simulations encompass molecular statics or dynamics using either semi-empirical classical interatomic potentials or first-principles methods. The latter require advanced multiscale techniques and so will only be addressed at the end of this section. Pioneering work on atomistic modeling of fracture started almost five decades ago with studies on the influence of crystallographic orientation on crack propagation [52], and the effects of lattice trapping of cracks [53]. Due to the limited computational power, these early simulations were limited to a very small number of atoms, although work of Thomson and coworkers [53] using Greens function methods presaged modern multiscale modeling. Increasing computer power has led to a concomitant increase in atomistic studies of fracture covering many of the topics mentioned above. We point to a few representative references for intrinsic brittle/ductile behavior [54, 55, 56, 57, 58], grain boundary fracture [59, 60, 61, 62], H and other chemical embrittlement [62, 63, 64, 65, 66, 67], and crack/defect interactions [36, 68, 69, 70, 71]. In this large literature, various simulation methods have been used to probe phenomena qualitatively or quantitatively.

Not all simulation methods are equally useful for obtaining an accurate understanding of the phenomena. The broad focus of this section addresses the advantages and disadvantages of different methodologies, in terms of their ability to extract quantitatively accurate results that are faithful to the principles of fracture mechanics. Unfortunately, many publications (specific citations are omitted) use methods that strongly influence the outcomes of the simulations, and thus leading to inaccurate, if not incorrect, conclusions about fracture phenomena. The main point is that certain simulation methods for nanoscale cracks are often not directly relevant to the real behavior of larger cracks. Specifically, as we will show, the simulation of a nanoscale center-crack tension specimen often precludes satisfying the conditions for the application of linear elastic

fracture mechanics; other finite crack geometries have the same problem. We advocate, and show directly the advantages of, the use of simulations specifically designed to correctly capture the nanoscale crack tip region of, essentially, semi-infinite cracks, where the loading variable is precisely the stress intensity factor K that controls the crack-tip deformation. Such " K -test" simulations avoid many artifacts that arise in finite-crack simulations, and enable quantitative computation of the critical stress intensities for various phenomena, the overall material fracture toughness, and, equally importantly, detailed quantitative comparison with theories.

To be a bit more precise, but before launching into detailed analysis, the atomistic study of cracks is usually intended to reveal the complex response of atoms in the very high stress region just ahead of a sharp crack. Except in explicit problems of nanoscale materials or structures, the crack sizes (characteristic crack length a) of interest are usually envisioned to be quite large on an atomic scale (1 micron or larger). Thus, the nanoscale crack tip region is only a very small portion of the entire crack. Under a macroscopic load, phenomena at the crack tip are driven by the local stresses around the crack tip. Due to the high enhancement of the stress near the crack tip, non-linear and non-convex behavior can occur near the crack tip even though the far-field load levels are quite low. Thus, *the default analysis of atomic scale fracture mechanics is Linear Elastic Fracture Mechanics (LEFM)*. That LEFM indeed describes fracture at atomic scale has also been demonstrated experimentally using nanoscale fracture tests in Silicon [72, 73].

As already discussed in Section 2.1, the concept of LEFM applies only if the "small scale yielding" condition is satisfied, i.e. $r_{FPZ} \ll r_K \ll a$. One can now immediately comprehend that problems wherein the typical crack size a itself is on the nanoscale cannot easily satisfy the SSY condition, or only satisfy the SSY condition at the scale of the atomic spacing, where the material response is intrinsically discrete. This introductory discussion presages our analyses below: failure to satisfy SSY conditions in nanoscale simulation studies invalidates the generality of the observed/measured results, making them non-transferable to the true problems of interest. Thus, atomistic simulation methods must be designed to satisfy SSY, and the applicability of SSY must be continually assessed as complex non-linear/non-convex crack tip phenomena evolve under increasing load.

2.4.1 Size of the K-dominant zone in atomistic modeling of fracture

A size of the K-dominant zone in atomistic modeling of fracture can be estimated directly from simulations by examining the virial atomic opening stresses in front the crack tip. As an explicit example, Fig. 2.6 shows the stress field $\sigma_{22}(x_1, x_2 = 0)$ obtained from an atomistic simulation of a center crack specimen in Ni, for various crack sizes a and loads having the same K_I ; details of such simulation are explained in Sec. 2.4.4.1. When presented in double-log form, the asymptotic square root singularity appears nicely and the deviations from the asymptotic field with increasing distance from the crack tip (whose location is itself not exact) are easily identified. For a crack of size $a_{min} \approx 18\text{\AA}$, notable deviations appear at distances $\approx 3\text{\AA}$. For the largest crack, $a = 140\text{\AA}$, requiring a simulation domain of $L \approx 300nm$ containing ~ 7.7 million

atoms at $T = 0K$, deviations from the asymptotic field are evident at a distance of $\approx 40\text{\AA}$. The simulation results are thus fully consistent with the analytic estimate for $r_K = \frac{4}{3}(1 - \Lambda)a$, and hence this estimate can be used to design relevant simulation sizes.

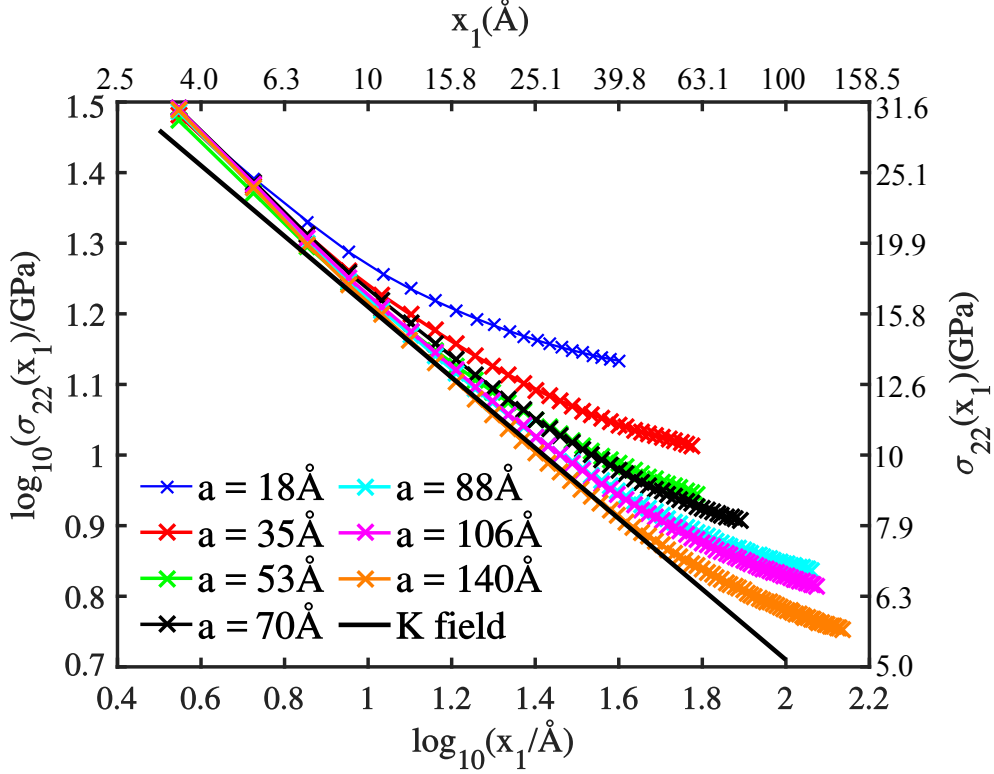


Figure 2.6 – Atomic opening stress $\sigma_{22}(x_1 > 0, x_2 = 0)$ versus distance from the crack tip, for crack sizes considered here as observed in simulations within the "brittle" crystal orientation. The asymptotic singular stress given by Eq. 2.18 is also shown (black line). The use of a log-log reveals the K -field singularity of $(-\frac{1}{2})$.

2.4.2 Atomistic crack-tip processes: cleavage versus dislocation emission

In Section 2.1.5 we have derived the expression for computing the critical stress intensity factor for Griffith cleave in anisotropic materials as

$$K_{Ic} = \sqrt{2\gamma_s \Lambda_{22}^{-1}}. \quad (2.42)$$

where the crack-tip dissipating process is associated with creation of two new surfaces, and it is quantified by the value of a material surface energy γ_s . Another atomistic process that leads to energy dissipation is the crack-tip dislocation emission. The critical stress intensity factor for crack-tip dislocation emission in Mode I K_{Ie} can be computed, as well. Various details on existing and new methods for computing the K_{Ie} are discussed in Chapter 4. Briefly, for emission of a dislocation with Burgers vector at an angle ϕ with respect to the crack front direction and occurring along a slip plane at angle θ to the crack plane, the critical Mode I stress intensity for

emission is [50, 74]

$$K_{Ie} = \sqrt{G_{Ie} o(\theta, \phi)} / F_{12}(\theta) \cos \phi \quad (2.43)$$

where G_{Ie} is a critical energy release rate for dislocation emission, $F_{12}(\theta)$ is a geometrical factor

$$\frac{K_I}{\sqrt{2\pi r}} F_{12}(\theta) = (\sigma_{22} - \sigma_{11}) \sin \theta \cos \theta + \sigma_{12} (\cos^2 \theta - \sin^2 \theta) \quad (2.44)$$

with σ_{ij} defined by Eq. 2.18, and $o(\theta, \phi)$ is an elasticity coefficient given by

$$o(\phi, \theta) = s_i(\phi) \Lambda_{ij}^{(\theta)-1} s_j(\phi) \quad (2.45)$$

with

$$s(\phi) = (\cos \phi, 0, \sin \phi) \quad (2.46)$$

and

$$\Lambda_{ij}^{(\theta)} = \Omega_{ik} \Lambda_{kl} \Omega_{jl}. \quad (2.47)$$

In the last equation Ω is the rotation matrix given by

$$\Omega = \begin{bmatrix} \cos \theta & \sin \theta & 0 \\ -\sin \theta & \cos \theta & 0 \\ 0 & 0 & 1 \end{bmatrix}. \quad (2.48)$$

The value of G_{Ie} for emission is not known a priori, and must be estimated based on theoretical analyses of the emission process. The critical energy release rate for the crack-tip dislocation emission G_{Ie} can be computed using, for example, the following expression [75]:

$$G_{Ie} = \begin{cases} 0.145\gamma_s^e + 0.5\gamma_{usf}, & \gamma_s^e > 3.45\gamma_{usf} \\ \gamma_{usf}, & \gamma_s^e < 3.45\gamma_{usf} \end{cases} \quad (2.49)$$

where γ_{usf} is the unstable stacking fault energy for slip along the slip plane and γ_s^e is the surface energy for the emission plane. Derivation of Eq. 2.49 is discussed in Chapter 4 of this manuscript.

The two cases above, brittle failure and dislocation emission, are important because they establish the intrinsic ductility of a crystalline material. A material is *intrinsically ductile* if $K_{Ic} < K_{Ie}$ (dislocation emission precedes fracture) and is *intrinsically brittle* if $K_{Ic} > K_{Ie}$ (brittle cleavage precedes dislocation emission). In Sec. 2.4.4 we analyze the competition between Griffith cleavage and crack-tip dislocation emission to elucidate important issues in the atomistic modeling of fracture.

2.4.3 Simulation methods and issues

2.4.3.1 Creating cracks in atomistic systems

The LEFM-envisioned crack, as a slit of zero elastic modulus consisting of upper and lower *traction free crack surfaces*, often cannot be created naturally in atomistic simulations. A traction free condition cannot be simply imposed on atoms due to atomic interactions across the crack surfaces. As a consequence, an atomically sharp crack is unstable to closure at loads below the Griffith K_{Ic} , or it is unstable to propagation at loads above the K_{Ic} . However, in extremely brittle materials (no crack-tip dislocation emission prior to cleavage), it is possible to simulate an atomically sharp and stable crack at $K_{Ic} \pm \Delta K$ with ΔK being very small but having some finite value [58, 76, 77, 78]. Stability of the crack at loads $\sim K_{Ic}$ is due to effect known as "lattice trapping" [53, 79]. This effect arises because of the discrete nature of an atomic system in which precise force law, that characterizes atomic interactions, can restrain crack opening until the crack tip bond is mechanically unstable. At this point, the applied stress intensity factor exceeds the thermodynamic Griffith value K_{Ic} . Similarly, in the case of unloading, the applied load for crack to close falls behind the Griffith K_{Ic} . The lattice trapping is usually very small in metals, where the critical stress intensity for crack to grow is only few percents above K_{Ic} . However, it can be considerably larger in fracture along grain boundaries [62], or in materials such as silicon [77, 80]. The crack stability as a function of the applied K_I has been examined explicitly using atomistic simulations and the K-test geometry in fcc Ni [81] (see Fig. 2.7).

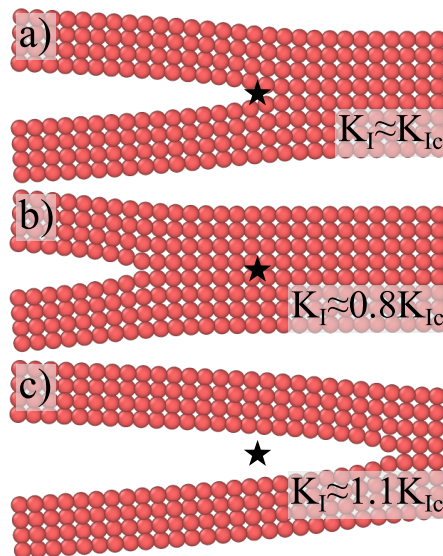


Figure 2.7 – Closing and opening of a) an atomistically sharp crack when the applied K_I is b) below, and c) above the Griffith value, respectively. Atoms are visualized using OVITO [15].

For describing the intrinsic nature (intrinsic ductility/brittleness) of a material we usually explore some competitive crack-tip processes that occur at loads below Griffith K_{Ic} . Therefore, to prevent the crack from closure we have to use one of the following approximate methods for creating a traction free crack:

- (i) "Screening", where we artificially delete interactions between atoms on either side of the initial crack surfaces. However, since interatomic potentials are typically many-body (long-range), the screening can slightly change the behavior of all the atoms at/near the crack tip;
- (ii) "Blunting", where we delete a few layers of atoms to create crack surfaces. The finite distance between the crack surfaces prevents atomistic interactions across the crack faces and leads to the desired traction free condition. However, a slightly blunted crack is created and so deviations from the ideally sharp crack can arise (the crack-tip singularity is removed).

The quantitative difference between a truly sharp crack, "screening", and "blunting" will be explored in Sec. 2.4.4.1.

2.4.3.2 Center-crack and other finite-crack geometries

Simulations using finite-size cracks appear convenient - they are easy to construct, the loading is simple, and the geometries are similar to macroscopic test specimens. Thus, the results from fracture mechanics are often used for interpretation without detailed investigation of the applicability of LEFM. Here, we highlight a few of the general issues that make these finite-size crack tests undesirable for atomistic simulations.

We emphasize the conditions for a valid transferable measure of crack tip fracture processes: $r_{FPZ} \ll r_K \ll a$. The size of r_{FPZ} for a sharp crack can be estimated using the non-linear/non-convex energy versus separation curve obtained from the separation of two rigid blocks of material starting from the zero-stress equilibrium configuration [82]. This traction separation curve often follows the so-called Universal Binding Energy curve [83]. Approximating the actual curve by the Dugdale model of a constant cohesive stress σ_c acting over a maximum crack opening of δ_{max} yields the fundamental cohesive length $u_c \approx 3E\delta_{max}/8\sigma_c$ [34, 84], and $u_c \approx r_{FPZ}$. With the typical ratio $\sigma_c/E = 1/10$ and maximum opening $\delta_{max} \approx a_0/5$, the cohesive length is $u_c \sim a_0$. Thus, the minimum crack size to satisfy $r_{FPZ} \ll r_K \ll a$ with $r_{FPZ} = a_0$, $r_K = 2r_{FPZ}$, and $r_K = 0.15a$, is $2a = 26a_0 \approx 100\text{\AA}$. A total system size should usually be $10\times$ larger to avoid boundary effects. Plane-strain simulations at this scale ($1000\text{\AA} \times 1000\text{\AA} \times a_0$) involve approximately 360,000 atoms and are computationally quite feasible. However, this scale is at the absolute minimum level and only satisfies one general requirement of LEFM.

For more complex problems, much larger cracks are necessary to ensure K -dominance. For instance, a crack along a grain boundary has an intrinsic scale associated with the periodic length of the grain boundary structure l_{gb} . Even for relatively simple grain boundaries, this structure has a length of multiple lattice constants. Study of fracture along or near a grain boundary then requires that at least a length l_{gb} exist within the K -dominant region, so $l_{gb} < r_K$ sets an absolute minimum on r_K and hence the allowable crack size a and, consequently a minimum total system size. Again, cracks at this scale can be simulated, but the problems become computationally more

Chapter 2. Modeling fracture across different length scales

demanding and with many atoms in the non-asymptotic domain.

A more serious problem is that the applied stress levels needed to drive crack tip phenomena are very high in finite-crack specimens. The applied stress necessary to generate a stress intensity K_I is $\sigma^{app} = K_I/\sqrt{\pi a}$. Taking a typical stress intensity factor at which crack-tip phenomena arise as $K_I = 1\text{MPa}\sqrt{\text{m}}$, the applied stress versus crack length is shown in Fig. 2.8. These stress levels are on the order of 1-15GPa for cracks up to $a \approx 320\text{nm}$. At this magnitude of the far-field stresses, the stresses in the non-asymptotic region are at this level or larger, and this creates two severe problems.

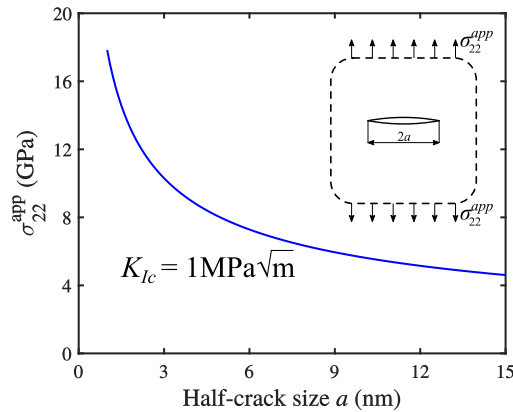


Figure 2.8 – Far field applied stress at the cleavage point with $K_{Ic} = 1\text{MPa}\sqrt{\text{m}}$, as a function of the half crack size a .

The first problem is that the entire material is no longer linearly elastic, violating the basic premise of LEFM. Fig. 2.9 shows the tangent elastic moduli for single crystal Ni using the well-established Mishin EAM potential for Ni [81]. Computational details are presented in Appendix A. The elastic constants vary notably at high stresses, so that predictions based on LEFM become invalid. Often, simulations are performed with applied displacements rather than stresses, with the stresses computed from linear elasticity and then used in LEFM to determine the operative K_I in the simulation. Such simulations can be partially corrected by using the measured stress obtained from simulations, but the entire material is still behaving non-linearly and so care must be taken in subsequent application of LEFM (although some aspects of LEFM are preserved for non-linear (hyper-) elastic materials).

The second problem is that the high stresses well ahead of the crack drive non-linear/inelastic/damage phenomena that are outside the intended FPZ. Conversely, these high stresses create an FPZ that has $r_{FPZ} > r_K$, violating LEFM. This can be especially problematic for the study of crack/defect interactions, because the defects can respond to the high non-asymptotic stress fields while still far ahead of the crack, initiating processes that would not occur until much higher load levels or for defects only much closer to the crack tip. Study of grain boundaries is particularly prone to this problem, since grain boundaries can emit dislocations at stresses well below the cohesive strength of the material. Thus, in finite-crack specimens, grain boundary emission may occur

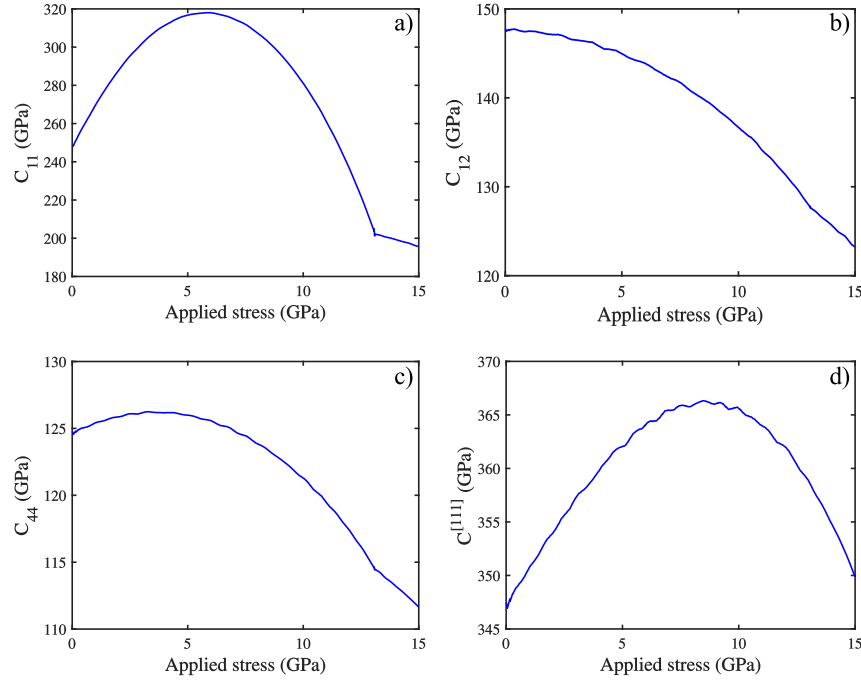


Figure 2.9 – Tangent elastic moduli as a function of the applied normal stress in fcc Nickel.

unrealistically far ahead of the crack. The study of dislocation/crack interactions is another case where the high stresses are problematic. The Peierls stress for a dislocation is often rather low (1-100 MPa, especially in fcc metals and alloys, and some hcp slip systems). Thus, dislocations near the crack tip can move very far from the crack - outside of r_K due to the high far-field stresses. Dislocations can also be driven toward the crack by the same high stresses. In both cases, the dislocations are moving in response to fields generated by the specimen geometry, and not solely by the crack tip field. We will show this explicitly below.

2.4.3.3 K-controlled simulation framework

We have highlighted the importance of maintaining the length scale hierarchy $r_{FPZ} \ll r_K \ll a$ and some of the challenges in doing so within the center-crack specimen, which extends to any other finite-crack test specimens. These challenges can be entirely circumvented by using a different test geometry corresponding to a semi-infinite crack. The K -controlled geometry forgoes modeling of an entire finite specimen and instead explicitly studies only the asymptotic crack tip region. Specifically, a simulation cell is created in which an edge crack (traction-free surface) extends in toward the middle of the specimen. The boundary conditions on all outer cell boundaries are the displacement fields of the asymptotic near-crack fields of Eqs. 2.11, 2.13 or 2.19 (depending on materials anisotropy and symmetry) with respect to the crack tip position. By construction, the entire simulation domain is then within the asymptotic K field. The loading parameter is then precisely K_I (and can be extended to include K_{II} and K_{III}). The response of the material is then also precisely the intrinsic crack tip response under the stress intensity

loading.

In this K -test geometry, there is no crack size; a is essentially infinite. The entire specimen is within the K -dominant zone by construction. The only requirement for a valid fracture test is then that $r_{FPZ} \ll r_{sim}$ where r_{sim} is a characteristic simulation cell radius (although the cell can be of any shape). For the same total number of atoms in a simulation cell, the K -test geometry ensures that all the atoms are within the K -dominant zone and maximizes the number of atoms in the FPZ. Furthermore, the simulation cell size needed is determined entirely by the FPZ of the process under study, and can be quite small for phenomena that are highly localized to the crack tip. These assumptions have been verified explicitly via simulations; other specific details are presented in Sec. 2.4.4.1. Fig. 2.10 shows the absolute displacement difference $\Delta u_2 = |u_2 - u_2^{\text{relaxed}}|$ computed in fcc Ni [81] at the applied $K_I = 0.85 \text{MPa}\sqrt{\text{m}}$, where u_2 is the elastic solution given by Eq. 2.19, while u_2^{relaxed} are atomic positions after energy minimization is performed. The non-linear atomic displacements, generated during the energy minimization, are present only in the zone close to the tip (FPZ). We find $\Delta u > 0.005 \text{\AA}$ within the radius of $\sim 2 \text{nm}$, and $\Delta u > 0.001 \text{\AA}$ within the radius of $\sim 10 \text{nm}$, around the crack tip. The maximum displacement difference is at the tip with the magnitude $\Delta u = 0.012 \text{\AA}$. Atoms outside the FPZ thus preserve their elastic positions as given by Eq. 2.19 (K -dominance zone) although they are allowed to move freely. Thus, the " K -test" completely satisfies the concept of LEFM. Unlike the finite-crack specimens, the stress fields are the correct asymptotic fields and there are no artificially high stresses far ahead of the crack tip. All defects inside the simulation domain thus also experience the correct stress fields.

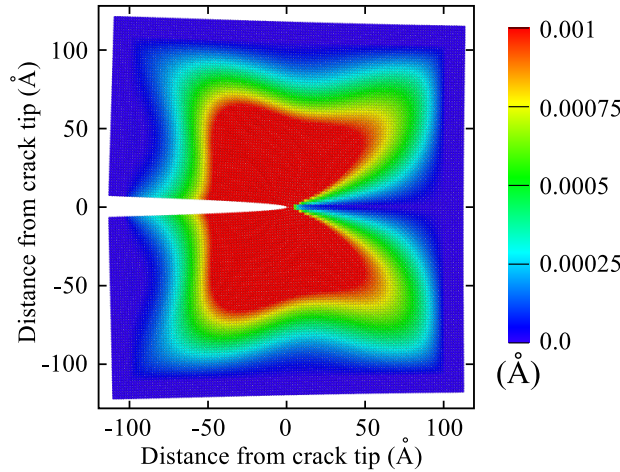


Figure 2.10 – Absolute difference in x_2 atomic positions between the elastic solution given by Eq. 2.19 (K -field) and relaxed structure for the same applied K_I within the box size of $21 \times 21 \times 1 \text{nm}^3$. Atoms are colored according to x_2 absolute displacement difference shown by the scale. Displacement difference in the red zone is off-scale with the maximum displacement of 0.012\AA .

There are very few disadvantages to the K -test geometry. One disadvantage is the need for the correct asymptotic displacement fields in complex problems. For instance, for a sample with a grain boundary where the crystalline material is elastically anisotropic, the single-crystal anisotropic fields are not appropriate. Anisotropic solutions can be created for some geometries,

especially with reflection symmetry across the crack plane, but there are no general solutions. In contrast, a CCT specimen does not require imposition of any displacement boundary conditions and so the consequences of the change in crystalline orientation across the grain boundary are automatically incorporated. However, the CCT specimen remains problematic for other reasons. Another apparent disadvantage of the K -test is that the boundary conditions are specific to the position of the crack tip so that the boundary conditions become inaccurate as the crack extends. This issue is, however, easily rectified by updating the crack tip position as the simulation proceeds so that the boundary conditions always correspond to the actual crack tip position [85, 86].

The K -test geometry has been used for decades in continuum-level finite element simulations of fracture problems. It has been employed precisely to maintain SSY conditions at all times. Its adoption in atomistic simulations has, unfortunately, been more sporadic.

2.4.4 Illustrative examples

In the following subsections, we analyze several basic fracture problems using molecular statics to highlight the general points made above. For each of the first few problems, we use single-crystal Ni as the test material and examine both the K -test and CCT test geometries, examine convergence, and compare them against one another and against theoretical predictions. Simulations are executed using the Large-scale Atomistic/Molecular Massively Parallel Simulator (LAMMPS) [87]. Key material properties computed with the Ni EAM interatomic potential [81] are shown in Table 2.1. The fcc elastic properties reveal a Zener anisotropy of $A = 2C_{44}/(C_{11} - C_{12}) = 2.5$ ($A = 1$ for isotropy) and so we use anisotropic analyses to set boundary conditions in the K -test and also use Eqn. 2.32 to compute K_{Ic} for Griffith cleavage and Eqn. 2.43 to compute K_{Ie} for crack-tip dislocation emission (see Table 2.1). Similar analysis can be applied to examine the fracture processes and crack-growth in amorphous materials such as Li-Si system. For more details on atomistic modeling fracture in amorphous systems, the reader is redirected to [85, 86].

2.4.4.1 Brittle fracture

Brittle fracture: Simulation set-up. As the first illustrative example we analyze brittle fracture in fcc Ni single crystal under plane strain loading conditions. A minimum requirement for simulating Griffith cleavage, as already discussed in Sec. 2.1.5, is $K_{Ic} < K_{Ie}$. To achieve this condition, we use a single crystal oriented with $X_1 = [1\ 0\ 0]$, $X_2 = [0\ 1\ 0]$ and $X_3 = [0\ 0\ 1]$ for which, by using material properties presented in Table 2.1 and Eq. 2.32, we compute $K_{Ic} = 0.91\text{MPa}\sqrt{\text{m}}$. The crack front then intersects an oblique $\langle 1\ 1\ 1 \rangle$ slip plane making dislocation emission to difficult ($K_{Ic} \ll K_{Ie}$); therefore, we do not show K_{Ie} . We further present specific simulation details that have not been discussed in Sections 2.4.3.2 and 2.4.3.3. In both test geometries, the crack is lying in the $x_1 - x_3$ plane with crack front along x_3 . Periodic boundary conditions are applied along x_3 while traction free boundaries are imposed in x_1 and x_2 directions. Since the simulations are performed in a homogeneous material at $T = 0\text{K}$, results are independent of cell thickness in x_3 direction; therefore, for both test geometries we set the

a_0	C_{11}	C_{12}	C_{44}	γ_{usf}	γ_{utf}	$\gamma_s^{[100]}$	$\gamma_s^{[111]}$	$K_{Ic}^{(010)[001]}$	$K_{Ic}^{(111)[\bar{1}10]}$	$K_{Ic}^{(111)[\bar{1}\bar{1}0]}$
(Å)	(GPa)	(GPa)	(GPa)	(J/m ²)	(J/m ²)	(J/m ²)	(J/m ²)	(MPa√m)	(MPa√m)	(MPa√m)
3.52	247.9	147.8	124.8	0.367	0.428	1.882	1.631	0.91	0.92	0.80

Table 2.1 – Material properties of fcc Ni used to compute its critical stress intensity factors for Griffith cleavage K_{Ic} (Eq. 2.32) and dislocation emission K_{Ie} (Eq. 2.43). Model orientations are defined by the crack plane normal (n), and the crack front direction [l].

simulation cell thickness to be $\sim 1\text{nm}$.

In the K -test geometry (see Fig 2.11a), the simulated crack tip of a semi-infinite crack is at $x_1 = 0$ and $x_2 = 0$, and the cell size has dimensions of approximately $120 \times 120\text{nm}^2$ in $x_1 - x_2$ plane. We perform three different simulations using cracks created by the three possible methods: truly sharp crack, screening, and blunting (see Sec. 2.4.3.1). Since the $[001]$ is one of the mirror planes in fcc metals, we load the crack corresponding to the applied K_I by imposing atomic displacements using Eq. 2.19. After each loading increment of $\Delta K = 0.01\text{MPa}\sqrt{\text{m}}$, atoms within $2r_c$ ($r_c =$ cut-off distance of the interatomic potential) of the simulation outer boundary are held fixed (see Fig. 2.11), while all other atoms are relaxed to minimize the total energy of the system using the "fire" method [88] with the force tolerance of 10^{-6} eV/\AA on every atom. However, within the material studied here we find no difference in the simulated results with the force tolerance of 10^{-5} eV/\AA and 10^{-4} eV/\AA on every atom. This is not a surprising since the crack-tip stresses are on the order of several GPa before any interesting event occurs. The simulation is terminated once the crack starts to propagate.

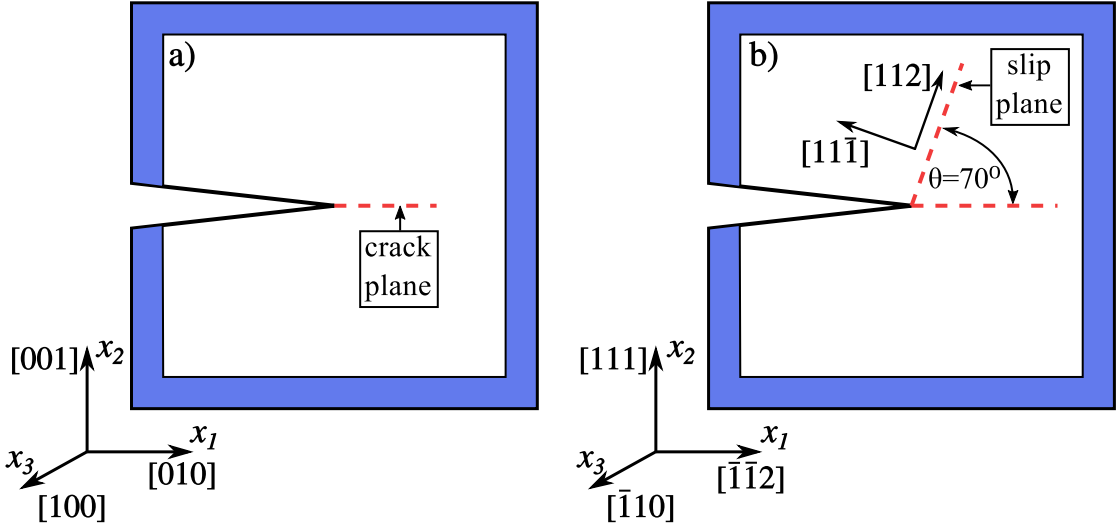


Figure 2.11 – K-test geometry used to simulate a) brittle fracture and b) dislocation emission from the crack-tip. Blue color indicate domain of atoms where boundary conditions are applied.

In the CCT test geometry (see Fig. 2.12), we simulate a centrally positioned crack having a finite size $2a$ with two tips at $x_1 = \pm a$ and $x_2 = 0$. The simulation box has size of $22a \times 20a$ in the $x_1 - x_2$ plane. To investigate the effects of size and non-linearity we vary the half crack size a approximately between 2nm and 15nm . We analyze both uniaxial and biaxial loading using displacement boundary conditions. After each loading increment of $\Delta\epsilon^{app} = 0.001$, the boundary atoms within $2r_c$ of the simulation cell outer boundary are held fixed at the imposed displacement corresponding to the applied strain ϵ^{app} while all other atoms are relaxed to minimize the total energy of the system using the fire method [88]. Since we need to simulate several million atoms for $a > 5\text{nm}$ we use a force tolerance of 10^{-5} eV/\AA in biaxial tension and 10^{-4} eV/\AA in uniaxial tension. We terminate the simulation when cleavage begins. We compute K_{Ic} for the slit crack

using $K_{Ic} = \sigma_{22}^{cr} \sqrt{\pi a}$, where the critical applied stress σ_{22}^{cr} corresponds to the critical applied strain ϵ^{cr} , and is computed either (i) directly from simulations $\sigma_{22}^{cr} = \sigma_{22}^{cr, sim}$, or (ii) from Hooke's law $\sigma_{22}^{cr} = C_{22ij} \epsilon_{ij}^{cr}$. A traction free crack is formed using "screening."

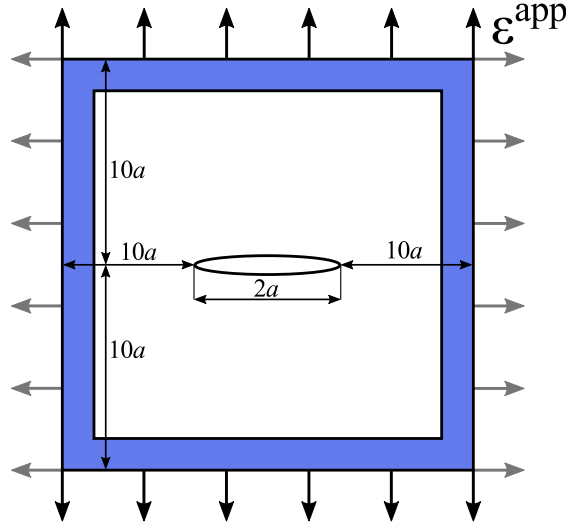


Figure 2.12 – CCT test geometry used to simulate centrally positioned finite crack under uniaxial (only black arrows) or biaxial (black and gray arrows) applied strain ϵ^{app} . Blue color indicates domain of atoms where boundary conditions are applied.

Brittle fracture: Simulation results. The observed crack tip behavior in both the K -test and the CCT test geometries is cleavage, as planned. We now focus on quantitative results observed using the K -test geometry. The simulated critical stress intensity factor for Griffith cleavage is $K_{Ic} = 0.93 \text{MPa}\sqrt{\text{m}}$ when the truly sharp crack configuration is used, and $K_{Ic} = 0.92 \text{MPa}\sqrt{\text{m}}$ when "screening" is used. A slightly lower K_{Ic} in "screening" arises due to deletion of atomic interactions across the crack surfaces that affects the response of the crack-tip atoms. However, both simulated K_{Ic} values are only slightly higher than the K_{Ic} predicted by LEFM (see Table 2.1). This is expected due to small lattice trapping, as discussed in Sec. 2.4.3.1. We further examine the simulated behavior when the crack is formed by deletion of two, three and four atomic layers, respectively (see Fig. 2.13). In every case we find a considerable increase in K_{Ic} since the "blunting" changes the singularity at the tip [55]. The lowest K_{Ic} is obtained for a crack formed by deletion of three atomic layers because this configuration preserves the morphology that most closely resembles the sharp crack (see Fig. 2.13b). Note that the distinct steps and the void in Fig. 2.13c(2) and c(3) are generated by the non-linear atomic rearrangements and not due to dislocation activity. Using "blunting" for crack formation is useful since the crack tip can be blunted by different real physical processes that may occur at the atomic scale. However, soon after the crack starts to propagate, its growth is mainly controlled by the condition for a truly sharp crack. Thus, the sharp crack should always be considered as a fundamental starting point in evaluation of intrinsic brittleness/ductility.

We next investigate the influence of the simulation cell size on fracture toughness using the

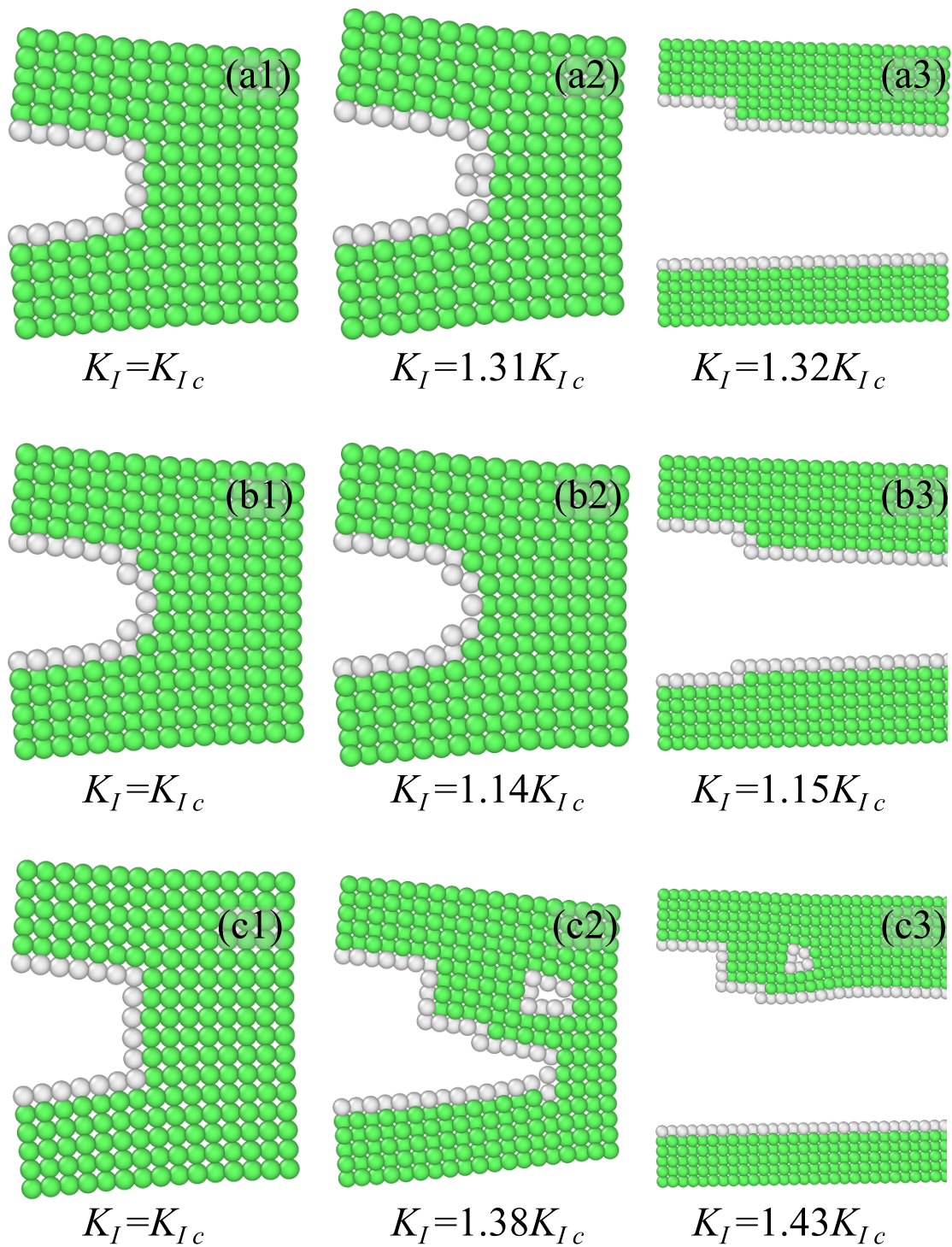


Figure 2.13 – K -test geometry for blunted cracks created by deletion of a) two, b) three and c) four atomic layers. In each case, the left figure shows the crack tip morphology at the applied $K_I = K_{Ic} = 0.91\text{MPa}\sqrt{\text{m}}$, the middle figure shows the crack-tip at the applied K_I immediately before the cleavage, while the right figure shows the crack after brittle fracture started. Atoms in this figure are colored based on Common Neighbor Analysis [15]; green for fcc and white for surface.

truly sharp crack configuration. For the material considered here we find that a cell size of $21 \times 21 \times 1 \text{ nm}^3$, with the crack tip $\sim 10 \text{ nm}$ far from the boundary, is sufficiently big for converged results (see Fig. 2.14). Decreasing the simulation cell size leads to only a modest increase in simulated K_{Ic} . This is expected because the non-linear/non-convex atomic behavior (the FPZ) exists only in the crack tip vicinity, as discussed above (see Fig. 2.10). Overall, the K -test geometry is shown to be, quantitatively and qualitatively, a very well controlled model for simulating brittle fracture at atomic scale.

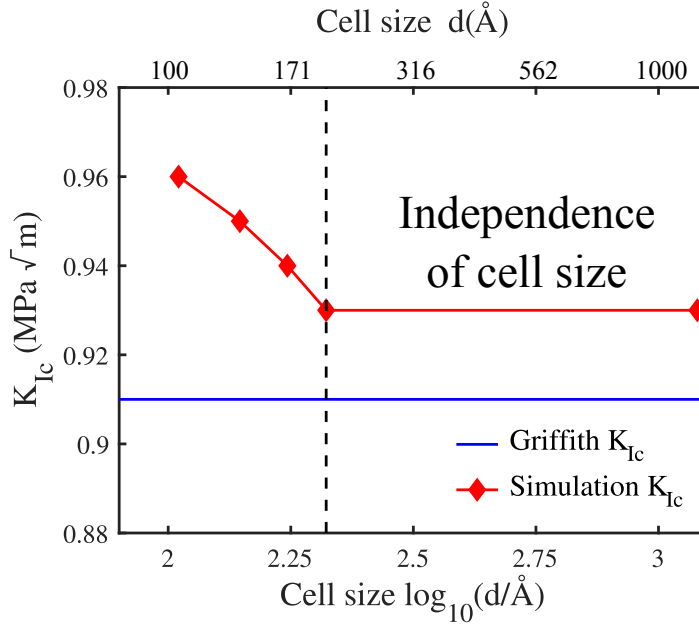


Figure 2.14 – Critical stress intensity factor for cleavage K_{Ic} as observed in the K -test simulations for different simulation cell sizes (red diamonds), along with the predictions of LEFM based theoretical prediction (Eq. 2.32) (blue line). The black dashed line represents minimum cell size for converged results.

We now explore results obtained using the CCT test geometry under uniaxial and biaxial tension. Fig. 2.15 shows the critical stress intensity factor for cleavage computed as $K_{Ic} = \sigma_{22}^{cr} \sqrt{\pi a}$. The σ_{22}^{cr} is obtained from the measured critical applied strain ϵ_{ij}^{cr} in two ways. First, we use Hooke's Law $\sigma_{22}^{cr} = C_{22ij} \epsilon_{ij}^{cr}$ with the small-strain elastic constants. Second, we use the measured stress in the simulation, $\sigma_{22}^{cr} = \sigma_{22}^{cr,sim}$ computed from the average virial stress of the entire atomic system in x_2 direction; this method is commonly used in the vast literature publish to date. However, this method for evaluating $\sigma_{22}^{cr,sim}$ can introduce some uncontrolled errors which mainly arise due to nonlinear behavior and elastic relaxations. A more precise method for estimating $\sigma_{22}^{cr,sim}$ is to use the same simulation cell without a crack but loaded at the same critical applied strain ϵ^{cr} . In addition, for comparison, Fig. 2.15 shows the converged K -test simulation results obtained using the truly sharp crack. Note that we do not compare the simulated results with the Griffith value for K_{Ic} since the nanoscale CCT test geometry violates the basic concept of LEFM (see below). Several crucial features emerge from Fig. 2.15. First, the deduced K_{Ic} varies with crack size a . This result should immediately preclude any further application of the nanoscale CCT test since

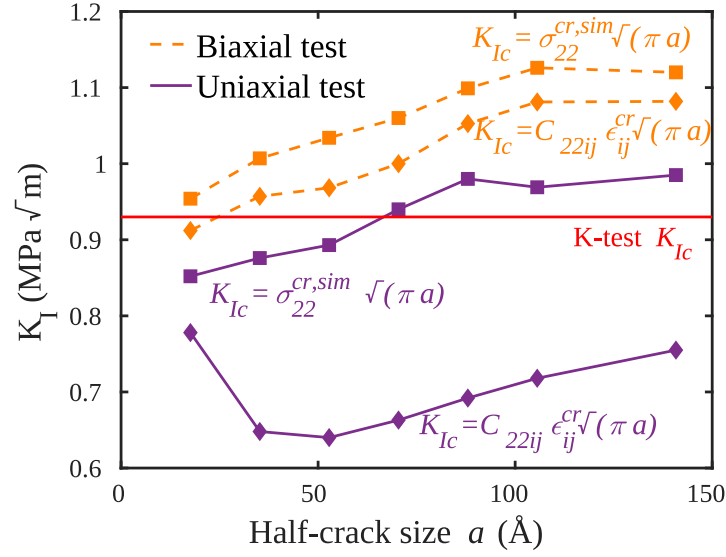


Figure 2.15 – Computed critical stress intensity factor for cleavage $K_{Ic} = \sigma_{22}^{cr} \sqrt{\pi a}$ versus crack size a in the CCT test simulations (cf. Fig. 2.12) under uniaxial (purple solid lines) and biaxial (orange dashed lines) loading. Squares corresponds to results computed using σ_{22}^{cr} directly from simulations while diamonds corresponds to results computed using $\sigma_{22}^{cr} = C_{22ij} \epsilon_{ij}^{cr}$. Solid red line: K-test result.

K_{Ic} is a material property independent of the crack size. Second, the estimated K_{Ic} is either far above or far below the K -test result, with no tendency toward convergence with increasing a . Third, since the elastic moduli increase with applied stress (see Fig. 2.9), the computed K_{Ic} is higher when σ_{22}^{cr} is used directly from simulations. Finally, the simulated K_{Ic} depends on whether we apply biaxial or uniaxial tension, even though σ_{11}^{app} does not contribute to the crack-tip singularity. All these differences arise due to (i) material nonlinearity associated with extremely high applied stresses, and (ii) violation of the length scale hierarchy $r_{FPZ} \ll r_k \ll a$ (see Sec. 2.1.3). The above results clearly confirm our previous conclusions that atomistic simulation of a finite size crack are not a reliable approach for obtaining quantitative insights into material fracture characteristics at nanoscale.

2.4.4.2 Crack-tip dislocation emission

First partial dislocation emission. As the second illustrative example we analyze dislocation emission from the crack-tip using both the K -test and CCT test geometries again. A fundamental requirement for observing the emission is $K_{Ie} < K_{Ic}$. To achieve this, we orient the crystal with $X_1 = [\bar{1} \bar{1} 2]$, $X_2 = [1 1 1]$ and $X_3 = [\bar{1} 1 0]$, forming a crack with a single $(11\bar{1})$ slip plane inclined at the angle $\theta = 70.53^\circ$ to the crack. Using this orientation, material properties presented in Table 2.1, and Eqs. 2.32 and 2.43, we compute $K_{Ie} = 0.80 \text{ MPa}\sqrt{\text{m}}$ and $K_{Ic} = 0.92 \text{ MPa}\sqrt{\text{m}}$, satisfying the condition for intrinsic ductility. One of the approximate methods for creating traction free crack surfaces must now be used since emission should occur at a load below the

Griffith K_{Ic} (see Sec. 2.4.3.1) where the sharp crack would be closing from the start of the simulation [16]. In the K -test geometry we use both "screening" and "blunting" by deletion of three atomic layers while in the CCT test geometry we only use "screening". All other simulation details are as presented in Sec. 2.4.4.1.

The observed crack tip event in both geometries studied here is the emission of a partial dislocation prior to Griffith cleavage. We again first discuss results observed in the K -test simulations. The simulated critical stress intensity factor for crack tip dislocation emission, for both "screening" and "blunting", is $K_{Ie} = 0.77\text{MPa}\sqrt{\text{m}}$. While for the material studied here we find no difference between "screening" and "blunting", in the majority of other materials studied we find "screening" better represents the truly sharp crack. The reader is redirected to Chapter 4 for more details on how crack formation affects dislocation emission. In this section, we only use "screening" for all subsequent studies. The theoretical predictions computed using Eqs. 2.43 and 2.49 are slightly higher than the simulations (see Table 2.1) but the agreement remains very good. The difference arises because the theory assumes existence of non-linear slip only along a single slip plane while in reality there is some other non-linear behavior around the crack tip. Similarly to the brittle fracture, a simulation cell size of $18 \times 18\text{nm}^2$ is sufficient for converged results (see Fig. 2.16). Overall, the K -test geometry is again shown to be an accurate and computationally-efficient method for simulating the crack-tip dislocation emission.

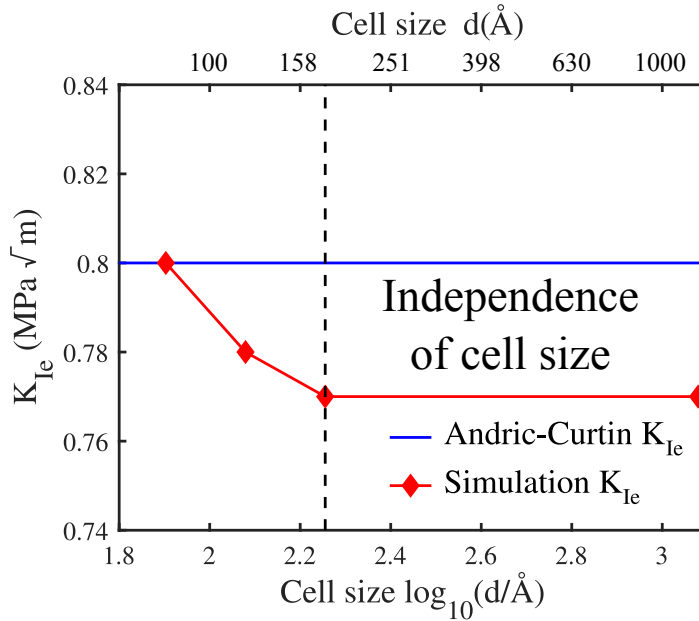


Figure 2.16 – Critical stress intensity factor for crack-tip dislocation emission K_{Ie} as observed in the K -test simulations for different simulation cell sizes (red diamonds), along with the predictions of LEFM based theoretical prediction (Eq. 2.49) (blue line). The black dashed line represents minimum cell size for converged results.

We now show results on crack tip dislocation emission observed using the CCT test geometry. Fig. 2.17 shows K_{Ie} , computed using both $K_{Ie} = \sigma_{22}^{cr,sim} \sqrt{\pi a}$ and $K_{Ie} = C_{22ij} \epsilon_{ij}^{cr} \sqrt{\pi a}$, in uniaxial and biaxial tension tests. The converged K -test result is also shown. Once again we

find a dependence of K_{Ie} on the crack size, loading scenario, and method used to evaluate σ_{22}^{cr} . However, the quantitative difference between the K -test and CCT test geometries, especially in biaxial tension, is smaller for dislocation emission than in brittle fracture. The fairly good agreement between the two test geometries is due to the smaller nonlinear behavior of the crystal oriented with (111)[$\bar{1}10$] (see Fig. 2.9d) and the lower applied stresses. However, the material response versus applied stress is not known a priori unless specifically measured in advance.

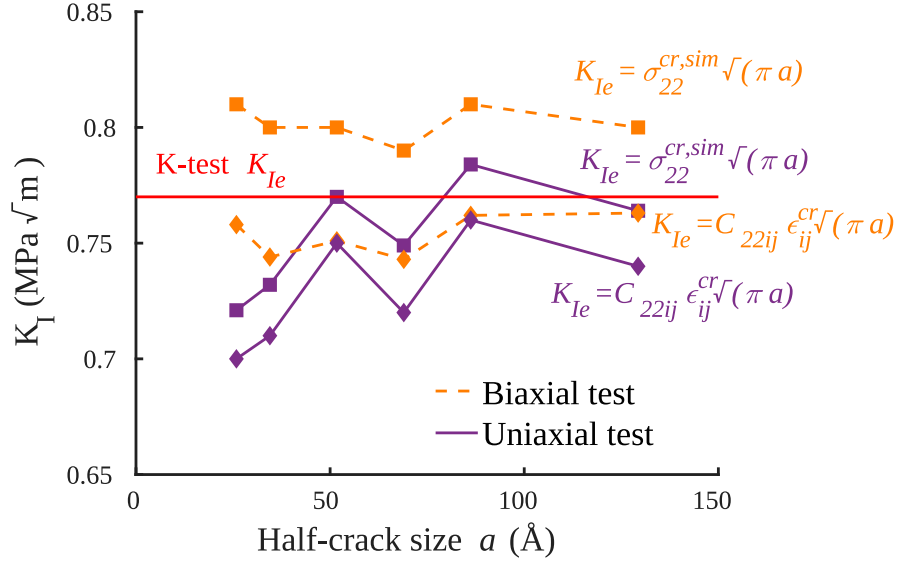


Figure 2.17 – Computed critical stress intensity factor for crack-tip dislocation emission $K_{Ie} = \sigma_{22}^{cr} \sqrt{\pi a}$ versus crack size a in the CCT test simulations under uniaxial (purple solid lines) and biaxial (orange dashed lines) loading. Squares correspond to result computed using σ_{22}^{cr} directly from simulations while diamonds correspond to results computed using $\sigma_{22}^{cr} = C_{22ij} \epsilon_{ij}^{cr}$. Solid red line: K-test results.

Dislocation/crack interaction: Equilibrium position of the first partial dislocation. After nucleation, the first partial dislocation moves to an equilibrium distance r along the slip plane ahead of the crack, at which point the total Peach-Koehler (P-K) force is zero [50]. For a partial dislocation emitted from a semi-infinite crack, the total P-K force has the following form

$$\frac{K_I F_{12}(\theta) b_p}{\sqrt{2\pi r}} - \gamma_{ssf} - \frac{b_p^2 o(\theta, \phi)}{8\pi r} = 0 \quad (2.50)$$

where b_p is the partial dislocation Burgers vector, and γ_{ssf} is the stable stacking fault energy. The three terms in this equation are (i) the force due to the applied K_I , resolved for a particular slip plane inclination angle, that moves the dislocation away from the crack tip, (ii) the stacking fault that drives dislocation back toward the tip, and (iii) the image force due to crack free surface, which also attracts the dislocation back toward the crack tip. We neglect the intrinsic Peierls stress of the partial dislocation moving through the lattice because it is small. A simple manipulation

yields the equilibrium distance r as a function of the applied K_I given by

$$r = \frac{(K_I F_{12}(\theta))^2 b_p^2}{8\pi\gamma_{ssf}^2} \left(1 + \sqrt{1 - \frac{\gamma_{ssf} o(\theta, \phi)}{(K_I F_{12}(\theta))^2}} \right)^2 \quad (2.51)$$

where the exact solution is the largest root. The preceding equation is valid in an infinite medium. In a finite size cell there is an additional contribution to the P-K force due to the fixed boundary that repels the dislocation from the boundary back toward the tip. The boundary effect on r has been evaluated explicitly using atomistic simulations in the K -test geometry. Fig. 2.18a shows the equilibrium position of the first partial dislocation immediately after nucleation using different simulation cell sizes. While the difference between Eq. 2.51 and simulated r is rather small in the largest simulation cell, a considerable difference emerges with decreasing cell size. The importance of this distance between the dislocation(s) (far-field plasticity) and the crack-tip is discussed in the following section.

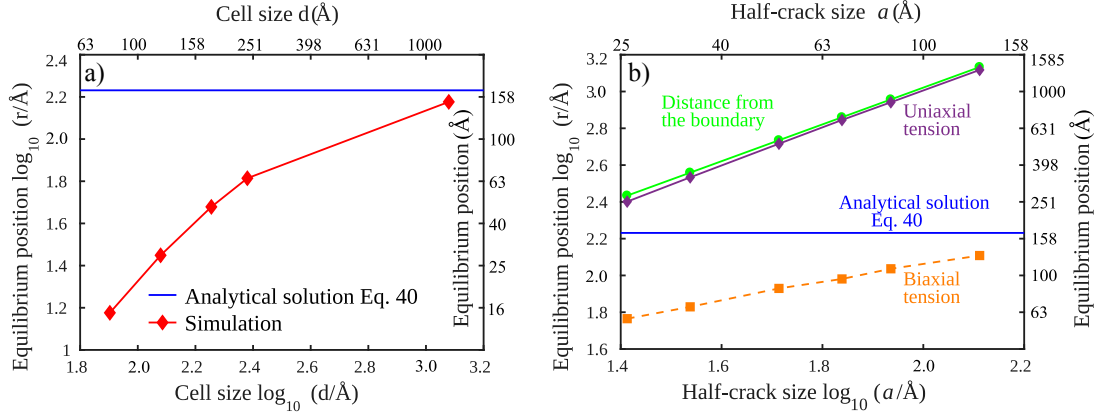


Figure 2.18 – Equilibrium position r of the first partial dislocation after nucleation using a) the K-test geometry and b) the CCT-test geometry under uniaxial and biaxial tension. The distance between the crack-tip and the outer CCT boundary along the slip plane (green circles) is shown for reference.

We next examine the equilibrium position of the first partial dislocation simulated in the CCT-test geometry. The problematic contribution of the high far-field stress to the equilibrium distance can be easily assessed by comparing results in uniaxial and biaxial tension. Neglecting the contribution of the asymptotic crack-tip field, and recalling that the resolved shear stress along the slip plane inclined at an angle θ is $\tau_r(\theta) = (\sigma_{22}^{app} - \sigma_{11}^{app}) \sin \theta \cos \theta + \sigma_{12}^{app} (\cos^2 \theta - \sin^2 \theta)$, we expect that the equilibrium distance r of the first partial dislocation to be much larger in uniaxial tension. This is shown clearly in Fig. 2.18b. Due to the very low Peierls stress for dislocations in fcc metals, the first partial dislocation under uniaxial loading always moves nearly to the simulation cell boundary. The asymptotic crack tip stress field does not contribute to the final position r in the CCT test under uniaxial tension. Instead, the dislocation position is controlled by the non-asymptotic stress field. In biaxial tension the far-field resolved shear stress along the slip

plane is effectively zero. The equilibrium position of the first partial dislocation is then controlled only by the K -dominance zone, which itself depends on the crack size a . Therefore, the first partial dislocation is much closer to the crack tip (smaller r) ahead of short cracks, converging toward Eq. 2.51 for the largest crack size a . The huge difference in the partial position r between uniaxial and biaxial loading conditions shows clearly how the far-field (non-asymptotic) stresses lead to significant differences in behavior. For uniaxial tension, the partial dislocation has moved far outside the K -dominance domain, thus obviously violating the application of LEFM for any subsequent crack tip behavior, as discussed further below.

Dislocation/crack interaction: Shielding effect. The stress field of the first partial dislocation at distance r on a slip plane inclined at angle θ creates additional crack-tip stress intensity factors k_j^d ($j = I, II, III$). Crack-tip shielding corresponds to $k_j^d < 0$ and anti-shielding to $k_j^d > 0$. In other words, the dislocation within the asymptotic crack-tip field generates an additional stress intensity factor at the crack tip that subtracts/adds to the far-field applied stress intensity. For the coordinate system centered at the crack tip, and when the first partial is an edge dislocation, the shielding of a semi-infinite crack can be computed using LEFM [49, 89, 90] as

$$\begin{aligned} k_I^d = k_2^d &= -\frac{1}{2\sqrt{2\pi r}} \sum_{j=1}^3 \Lambda_{2j}^{-1} D_{2k}^j(\theta) b_k \\ k_{II}^d = k_1^d &= -\frac{1}{2\sqrt{2\pi r}} \sum_{j=1}^3 \Lambda_{1j}^{-1} D_{2k}^j(\theta) b_k \end{aligned} \quad (2.52)$$

with \mathbf{b} being the dislocation Burgers vector, $\mathbf{\Lambda}$ the Stroh tensor, and $\mathbf{D}^j(\theta)$ related to the angular distribution of stresses near the crack tip for the particular j mode of loading given in polar coordinates by

$$\sigma_{kl}(r, \theta) = \sum_{j=1}^3 \frac{1}{\sqrt{2\pi r}} K_j D_{kl}^j(\theta). \quad (2.53)$$

Note that Eq. 2.52 is expressed with respect to the coordinate system positioned at the tip where $j = 1$ corresponds to Mode II, and $j = 2$ corresponds to Mode I, or $[k_1^d \ k_2^d]^T = [k_{II}^d \ k_I^d]^T$. The author is taking an opportunity to point out to this uncertainty that has appeared in the original papers (see Ref. [86, 91]). In addition, note that an edge dislocation does not generate any k_{III}^d . Although the dislocation is an additional stress source that acts over the crack surfaces, the length scale requirement $r_{FPZ} \ll r_K \ll a$ is preserved. The FPZ for subsequent crack-tip events is again only the atomistic region around the tip, aside from the residual stacking fault that is ignored due to elasticity purposes. Thus, the K -test geometry is again suitable model for obtaining insights into dislocation shielding effects. Since we deal with linear elasticity, the same model applies in the presence of multiple dislocations around the tip, as well. Therefore, the well-posed K -test enables investigation of the effects of far-field plasticity on overall fracture toughness [92].

The k_I^d and k_{II}^d , computed using Eq. 2.52, are exact solutions for semi-infinite cracks; therefore, we cannot use Eq. 2.52 for evaluating dislocation shielding of finite size cracks. Shielding of cracks having size of few nm is generally small, often negligible, as compared to semi-infinite cracks [93]. Thus, the nanoscale CCT test is not a quantitatively reliable approach for evaluating the shielding of cracks due to preexisting dislocations. Furthermore, under uniaxial loading where the first partial dislocation has moved far from the entire crack, any remaining shielding is sample size and geometry dependent.

Second partial dislocation emission. In fcc metals, such as Ni, further increase of the far-field applied stress intensity factor generates emission of a second partial dislocation. Details about possible processes for the emission of a second partial dislocation are discussed in Chapter 5. Within the (111)[$\bar{1}10$] crystal orientation and at $T = 0\text{K}$, the only possible process is the emission of the twinning partial dislocation, which has the same character as the first partial but gliding on an immediately adjacent slip plane [94]. Simulated values of K_{Ie}^{twin} for crack-tip twinning are compared with the theoretical predictions based on the theory derived and analyzed in Chapter 5 of this manuscript. The remote critical stress intensity factor for crack-tip twinning K_{Ie}^{twin} in the presence of the first partial dislocation is

$$K_{Ie}^{twin} = f^{(1)}(C_{ijkl}) \left(\sqrt{(\gamma_{utf} - \gamma_{ssf})o(\theta, \phi)}/F_{12}(\theta) + k_I^d + \frac{F_{22}(\theta)}{F_{12}(\theta)} k_{II}^d \right) \quad (2.54)$$

where γ_{utf} is the unstable twinning fault energy, $f^{(1)}(C_{ijkl})$ is a material constant that correlates the far-field applied K_I and the stress intensity along the twinning slip plane, and $F_{22}(\theta)$ corrects for the resolved shear stress along the slip plane due to k_{II}^d . Twinning partial dislocation emission can be examined without the shielding by effectively moving the first partial dislocation to infinity; in this special case Eq. 2.54 does not quite reduce to Eq. 2.43 since the stacking fault remains in the crack tip vicinity. The reader is redirected to Chapter 5 for more details on this specific problem. Here, we examine the crack-tip twinning in the presence of the first partial dislocation.

We thus investigate crack-tip twinning using both the K -test and CCT test geometries. Fig. 2.19 shows the K_{Ie}^{twin} for different cell sizes as measured in K -test atomistic simulations and as predicted by Eq. 2.54 in the presence of the first partial dislocation. As input in Eq. 2.52 we use the simulated position of the first partial dislocation r immediately before twinning occurs. Fig. 2.19 shows K_{Ie}^{twin} increases as the simulation cell size decreases, which is due to (i) boundary effects as discussed above and, more importantly, (ii) the change in shielding since the equilibrium separation r is strongly affected by the sample boundary (see Fig. 2.18a). Note that fully converged results on crack-tip twinning require considerably larger simulation sizes. Decreasing the simulation cell size, we further observe a change of the twinning plane from behind the crack tip to ahead of the crack tip. More details on different twinning modes can be found in Chapter 5. Overall, the K -test is shown to be a well-controlled, quantitatively and qualitatively precise approach to simulating atomic scale crack-tip events in the presence

of far-field plasticity. However, when all dislocations are fully retained in the simulation, it is necessary that the simulation size be such that all dislocations are in their true (infinite material, infinite crack) positions so that their shielding/unshielding contributions are accurate. This size can be computationally infeasible, motivating the development of multiscale methods to capture the dislocation plasticity away from the immediate crack tip (see Sec. 2.4.5).

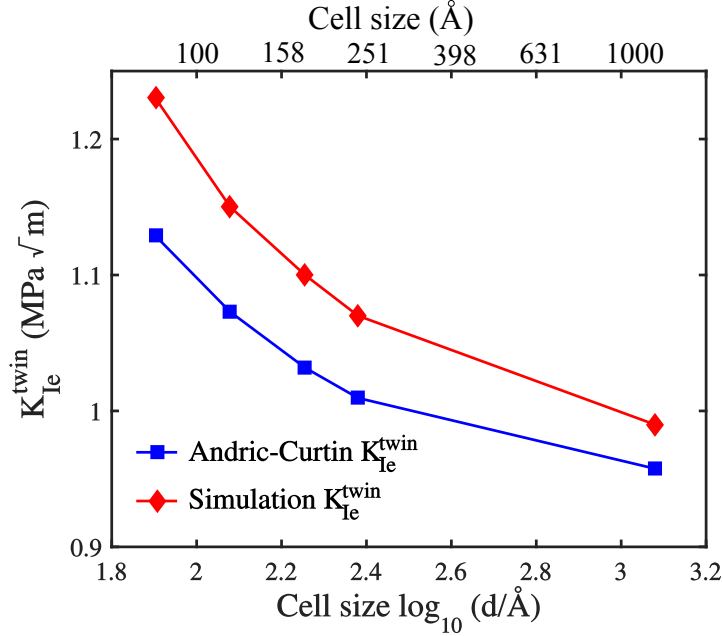


Figure 2.19 – K -test results for the critical stress intensity factor for crack-tip twinning versus simulation cell size (red diamonds) along with the predictions of the LFM based theory (blue squares).

Fig. 2.20 shows the CCT test results for the critical stress intensity factor for crack tip twinning computed using (i) uniaxial and (ii) biaxial tension tests along with the K -test results obtained using the largest simulation cell (however not fully converged due to reasons discussed above). Note, once again, that we do not compare simulation results with the LFM based theoretical predictions due to reasons that are discussed several times so far. We find K_{Ie}^{twin} depends on crack size, loading scenario, and calculation of σ^{cr} , as in every other case studied above. We notice K_{Ie}^{twin} to be much higher in biaxial than uniaxial tension; in other words twinning partial emission is much easier under uniaxial tension. The difference between two cases is due to (i) nonlinear response of the system and (ii) different shielding, since the first partial is much farther from the crack tip in uniaxial tension (see Fig. 2.18 and Sec. 2.4.4.2). Finally, good agreement between $K_{Ie}^{twin} = \sigma_{22}^{cr,sim} \sqrt{\pi a}$ and $K_{Ie}^{twin} = C_{22ij} \epsilon_{ij}^{cr} \sqrt{\pi a}$ in uniaxial tension is essentially a simulation artifact associated with $\sigma_{22}^{cr,sim}$ and the overall stress reduction due to emission of the first partial dislocation. As already discussed in Sec. 2.4.4.1, the more precise method for estimating the $\sigma_{22}^{cr,sim}$ is to use the simulation cell without a crack and loaded at the critical applied strain ϵ^{cr} . All these results suggests that the nanoscale CCT test is not a suitable method for assessing fundamental material fracture properties, although the correct phenomena may be reproduced. What seems to be more important is that plasticity in front of a finite size crack is

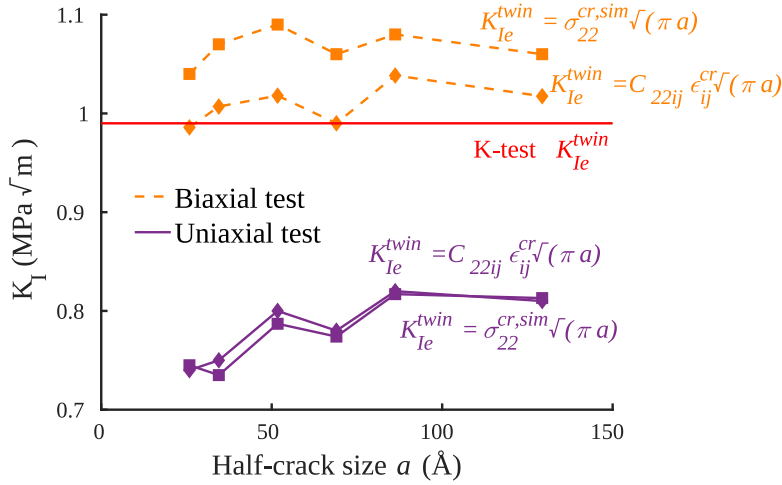


Figure 2.20 – Computed critical stress intensity factor for crack-tip twinning $K_{Ie}^{twin} = \sigma_{22}^{cr} \sqrt{\pi a}$ versus crack size a in the CCT test simulations under uniaxial (purple solid lines) and biaxial (orange dashed lines) loading. Squares correspond to results computed using σ_{22}^{cr} directly from simulations, while diamonds correspond to results computed using $\sigma_{22}^{cr} = C_{22ij} \epsilon_{ij}^{cr}$. Solid red line: K-test results obtained using the largest simulation cell.

more easily triggered by phenomena outside of the FPZ, and therefore outside the domain of LEFM.

2.4.5 Discussion and concluding remarks

Atomistic modeling of fracture is now frequently being used to explore the behavior of crack-tip atoms in crystalline metals, alloys, ceramics, amorphous materials, and including the presence of different nanoscale defects. Here, we have critically analyzed several common simulation methods based on linear elastic fracture mechanics LEFM based methods. We have demonstrated that the atomic-scale center-crack geometry often violates the basic concepts of Small Scale Yielding that is at the heart of the application of LEFM. These tests violate the length scale hierarchy $r_{FPZ} \ll r_K \ll a$ and often introduce far field (non-crack tip) non-linear response and damage/plasticity due to the very high far-field applied stress needed to drive the desired crack-tip events. As a consequence, results obtained in the CCT test are not quantitative or general, and usually do not agree well with theoretical predictions. The problems that arise with the CCT test geometry are circumvented by the "K-test" which uses a semi-infinite crack geometry controlled by an applied stress intensity K . By construction, the "K-test" satisfies the concept of SSY, and provides results that are well-converged even at fairly small cell sizes, and results that generally agree well with the theoretical predictions. The advantages of the K-test have been demonstrated for both crystalline and amorphous materials.

We now discuss more advanced K-test simulation methods for investigating different processes associated with the atomically sharp crack tip. In the illustrative example shown in Sec. 2.4.4.2

we investigated the emission of the first and second (twinning) partial dislocation from a crack tip, respectively, but not further emission. The first emission is a vital process for crack blunting and toughening, but the overall fracture toughness is also governed (i) by the interaction between the crack tip and far-field plasticity (dislocations created by sources away from the crack tip itself) and (ii) continued (multiple) emission from the crack. The K -test atomistic model becomes computationally infeasible because the size of the real plastic zone would contain too many atoms. However, dislocations sufficiently far from the crack tip interact with the crack through elastic interactions only and, as we saw in the simple case of shielding of the crack by the first emitted partial dislocation, the elastic shielding/anti-shielding of cracks by dislocations can be computed analytically using elasticity theory, for plane-strain problems, and need not be directly simulated [36]. This then leads to the application of multiscale methods such as the coupled atomistic discrete dislocation (CADD) method [95, 96]. In CADD, the zone around the crack-tip is modeled with full resolution and so dislocation emission and fracture processes occurs naturally. Away from the crack tip, the material is described by the discrete dislocation (DD) plasticity model [13] in which continuum dislocations glide and interact with each other and with the crack via their elastic fields. The direct coupling of atomistics to continuum in CADD also enables the motion of dislocations into and out of the atomistic region in a seamless manner, such that the only approximation is, in principle, the elimination of the dislocation core structure for dislocations sufficiently far from the crack tip region. With such an approach, the K -test geometry is used in an identical manner, but effectively with two process zones, FPZ_{DD} and FPZ_{At} with FPZ_{DD} spanning the domain of the continuum dislocation plasticity and the much smaller FPZ_{At} contained within FPZ_{DD} ensuring proper atomistic response around the very high stress crack tip region.

Using interatomic potentials for simulating the atomistic region around the crack-tip is convenient if the potentials are sufficiently accurate. However, most of available interatomic potentials are not suitable for accurate description of real chemical effects on either brittle fracture or dislocation nucleation. These problems can again be circumvented by using a multiscale strategy in which the crack tip region is fully described by quantum mechanics while elasticity is used at further distances. The K -test method is applied with the K boundary conditions applied on the outer elasticity domain, enabling the use of a small quantum domain, and thus making the problem computationally tractable. Such a quantum-mechanical coupled atomistic discrete dislocation (QM-CADD) framework within the K -test geometry was developed to study the effects of hydrogen and oxygen on dislocation emission in aluminum [97, 98]. The K -test geometry has also been used in quantum mechanical/ molecular mechanical (QM/MM) multiscale coupling method in silicon [99] and in aluminum [100]. In QM/MM, the region around the crack tip is again simulated with quantum accuracy but coupled to a surrounding material domain simulated using classical interatomic potentials.

The present section provides the theoretical analysis followed by atomistic simulations of a semi-infinite cracks with periodic boundary conditions applied along the crack front under plane strain loading. Plane strain is not identical to 2d, however, and so the K -test can be applied to study some fully 3-dimensional effects. Specifically, by using simulation cells having a

Chapter 2. Modeling fracture across different length scales

sufficient length along the crack line direction it is possible to analyze problems such as (i) crack-tip dislocation emission on oblique slip planes, (ii) crack interactions with preexisting 3D dislocation loops [101], (iii) crack-tip dislocation emission in alloys and multicomponent solid solutions, and (iv) cleavage/dislocation emission from a crack-tip by kinks. Furthermore, the fracture simulations presented in this work were performed at $T = 0\text{K}$. However, dislocation emission and other processes are thermally-activated with some K -dependent 3d nucleation (or transition) state. Nonetheless, the K -test geometry enables study of such 3d nucleation problems, eg. [102, 103, 104].

Recent attention has also been given to the investigation of fully-embedded nanosize cracks (3d cracks), and the effects of crack front curvature on crack motion [105, 106]. It has been found that such embedded cracks are more prone to develop plastic zones ahead of the crack tip as compared to cracks with straight fronts under plane strain loading. However, special care must be taken in dealing with 3D cracks because they are finite sized and must be modeled in the 3D equivalent of CCT (a penny-crack geometry). 3D simulations thus suffer from the same challenges as 2D CCT tests. First, as in semi-infinite cracks, the fundamental length scale hierarchy $r_{FPZ} \ll r_K \ll a$ must be preserved, and the K-dominant zone remains comparable to that of 2D plain strain cracks. Embedded cracks of several nm diameter will quickly violate SSY after the first dislocation emission event. Secondly, as in the CCT case, the far-field applied stresses necessary to induce crack tip events are again extremely high, which introduces nonlinearities as noted also in Ref. [106]. Third, a high applied uniaxial stress generates high resolved shear stresses along different slip planes which act to drive dislocations far from the crack and generally to assist in creating plastic activity around the crack over sizes that may exceed the crack size itself. The pronounced plastic zone is thus not necessarily due to the nanocrack itself. Finally, nanoscale 3D cracks have high crack curvature that is not realistic for larger-scale cracks and which can introduce additional artificial effects. Therefore, the atomistic-scale simulation of fully 3D cracks must be approached with considerable care, and the present authors do not recommend such studies. The emergence of new fully-3D multiscale methods, specifically the generalization of CADD to 3D [107, 108, 109, 110] may alleviate some of the above issues and expand our ability to study realistic 3D cracks both qualitatively and quantitatively.

As noted above, in many fracture problems the FPZ is immensely larger than the atomic scale so that direct MD simulations in the presence of a semi-infinite crack remain infeasible. In such cases, the variations in the stress field are then slow over atomistic scales, and local regions of material ahead of the crack can be envisioned as under some homogeneous loading state (uniaxial tension, triaxial stress, etc.). In such cases, atomistic simulations can be used to study the FPZ response itself without the explicit crack tip. These studies are carried out on "representative" volumes of material under a suitable stress state for the problem of interest. The work of Robbins et al. [12, 111] on polymers, mentioned earlier, is one such example. Falk et al. [112] and Khosrownejad et al. [85] have carried out studies of the FPZ in amorphous metals and amorphous Li-Si, respectively. Tensile separation studies of crystalline materials and grain boundaries, with and without chemical segregation, have also been studied [82]. A full discussion and analysis of such methods is beyond the scope of the present manuscript. However, as with explicit-crack

fracture tests, care must be taken to obtain quantitative results. For instance, the size of the "representative" volume is often unknown a priori, and the energy dissipation in a 3D simulation cell must be appropriately related to the expected dissipated energy in the actual fracture specimen. Size effects and boundary conditions also enter in subtle ways. Nonetheless, such studies are less problematic than explicit crack studies although less quantitative for relating to the true fracture problem.

To conclude, the examples presented in this section demonstrate that accurate atomistic modeling of fracture should be based on the K -test geometry if possible. As a consequence, the K -test simulations are used in Chapters 4 and 5 for more detailed studies of crack-tip dislocation emission and twinning in metals. The use of finite-size embedded cracks, such as the center-crack tension test, should be examined carefully in advance to ensure that none of the various issues/problems/artifacts identified here would strongly influence the results. In general, we do not recommend tests such as the CCT due to the difficulties in remaining within the limits of small scale yielding and LEFM, but recognize that the K -test may not be useful for all problems of interest. Overall, use of the K -test demonstrates that a range of atomic-scale fracture phenomena can be studied both qualitatively and quantitatively, providing valuable insight into the fundamental fracture of materials.

3 Continuum theories of crack-tip dislocation emission

3.1 Introduction

Fundamental importance of the crack-tip dislocation emission has been conceptually discussed in the introductory section of the manuscript. Due to its practical importance, a number of continuum mechanics models have been introduced to predict various critical stress intensity factors for crack tip dislocation emission [49, 113, 114, 115, 116]. However, the most widely-used model is that given by Rice, which is based on a cohesive model for slip displacement ahead of the crack [50]. Under Mode II (in-plane shear) loading, Rice showed that emission is controlled by an energy criterion involving the unstable stacking fault (USF) energy γ_{usf} . The USF is a saddle point on the generalized stacking fault energy surface associated with relative shear displacements of two rigid blocks of material. Under Mode I loading, the Mode II analysis does not apply directly, but Rice postulated that, at the point of emission, the slip profile along the slip plane is the same as that in Mode II. This yields a dependence of K_{Ie} on γ_{usf} and on the orientation of the slip plane relative to the crack front.

The Rice analysis is equally applicable for predicting the critical stress intensity factors for the emission of the first partial K_{Ie}^{first} and trailing partial K_{Ie}^{trail} dislocations in fcc metals [50]. However, many molecular statics (MS) simulations revealed that fcc metals usually show crack-tip twinning at $T = 0K$ [117]. This observation inspired Tadmor and Hai to propose an extension of the Rice theory for predicting the critical stress intensity factor for crack-tip twinning [94], showing that K_{Ie}^{twin} depends on the unstable twinning fault energy γ_{utf} . By comparing the critical stress intensity factor for the emission of the trailing partial K_{Ie}^{trail} and the emission of the twinning partial dislocation K_{Ie}^{twin} , twinning is preferred if $K_{Ie}^{twin} < K_{Ie}^{trail}$.

3.2 Rice theory for dislocation emission

Rice formulated a criterion for crack tip dislocation emission based on the Peierls concept [43]. This concept assumes the existence of a periodic energy functional $\Psi(\Delta)$ that is a function of

Chapter 3. Continuum theories of crack-tip dislocation emission

the relative slip Δ between two rigid crystal blocks. The energy is the so-called generalized stacking fault energy (GSF energy) evaluated at relative slip Δ , with $0 \leq \Delta \leq b$ where b is the Burgers vector of the emitted dislocation. For fcc materials, the focus of the work here, the emitted dislocation is composed of partial dislocations with Burgers vector b_p . A typical GSF energy function $\Psi_{gsf}(\Delta)$ for an fcc material is shown in Fig. 3.1, obtained from an atomistic simulation at $T = 0K$ in Ni described with EAM potential [81]. The GSF curve is a material property, independent of any crack geometry or mode of loading in a crack problem. The reader is referred to Chapter 6 for more details about the GSF energy.

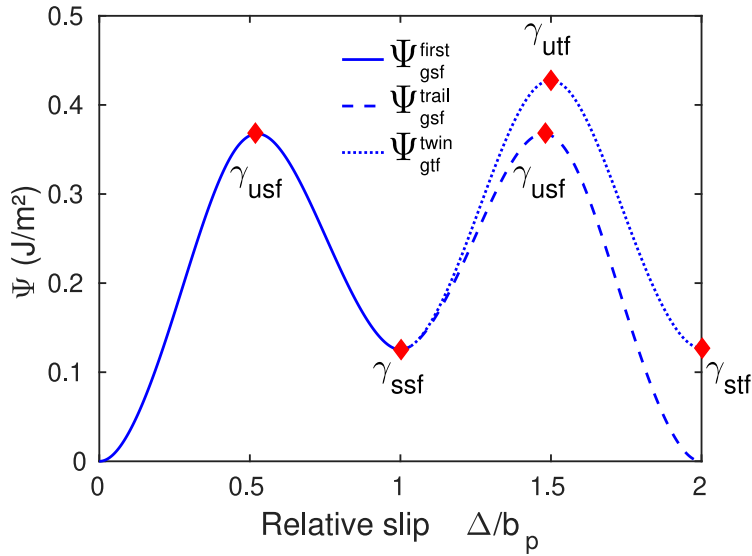


Figure 3.1 – Generalized stacking fault (GSF) energy along the direction of the first partial dislocation (the solid line), GSF energy along the direction of the trailing partial dislocation (the dashed line), and generalized twinning fault (GTF) energy along the direction of the twinning partial dislocation (dotted line) computed in fcc Ni [81].

Once nucleated, the first partial moves to an equilibrium distance from the crack tip and leaves the stacking fault behind it. Since the first partial dislocation stays relatively close to the tip, it imposes an additional shielding mixed-mode stress intensity acting at the crack tip. The crack tip responds to the total stress intensity at the crack tip, independent of how that stress intensity is established. Thus, the important physics of the problem remains at the crack tip, independent of the shielding due to the first partial. Therefore, in our restatements of the Rice and Tadmor-Hai theories here and in Section 3.3, we first neglect the effects of the first partial. Then in Section 3.4 we show that the shielding effect is the same for both processes and so does not influence which process is more favorable.

Rice solved the problem of dislocation emission ahead of a semi-infinite crack under pure Mode II loading as a Mode II cohesive zone problem where the GSF energy defines the (continuum) cohesive response ahead of the crack tip via the material shear resistance as $\tau_{gsf} = d\Psi_{gsf}^{first}(\Delta)/d\Delta$.

3.2. Rice theory for dislocation emission

The cohesive model eliminates the elastic stress singularity at the crack tip in analogy to a cohesive/bridging/Dugdale zone in the Mode I fracture problem. Since the GSF curve includes the elastic response of the material that is already contained in the elastic field, Rice introduced the displacement discontinuity δ , which is the inelastic slip, i.e. the additional slip beyond that predicted by elasticity. He then showed that $\delta = \Delta - h\tau_{gsf}(\Delta)/\mu$, where h is the atomic inter-planar spacing and μ is the shear modulus (along the plane of sliding). Rice then introduced the inelastic potential $\Phi(\delta)$ for the energy associated with the inelastic slip, given by

$$\Phi(\delta) = \Psi_{gsf}^{first} - h\tau^2/2\mu. \quad (3.1)$$

which differs from $\Psi_{gsf}^{first}(\Delta)$ but has the same maximum value at the unstable stacking fault energy, $\max(\Psi_{gsf}^{first}(\Delta)) = \max(\Phi_{gsf}^{first}(\delta)) = \gamma_{usf}$.

Within the framework of the cohesive model, the path-independent J-integral can be applied [17]. In isotropic elasticity, the J-integral along a contour far from the crack is $J_{far} = (1 - \nu)K_{II}^2/2\mu = G$ where G is the macroscopic energy release rate. The J-integral along a crack face contour around the cohesive zone is given by

$$J = - \int_0^\infty \tau_{gsf} \frac{\partial \delta}{\partial x} dx = \int_0^{\delta_{tip}} \tau_{gsf}(\delta) d\delta \equiv \Phi(\delta_{tip}). \quad (3.2)$$

Path independence of the J-integral leads to the result

$$G \equiv (1 - \nu)K_{II}^2/2\mu = \Phi(\delta_{tip}). \quad (3.3)$$

An incipient dislocation (partial slip distribution along the slip plane) loses stability when the slip discontinuity at the crack tip reaches the critical unstable stacking fault position, $\delta_c^{tip} = \Delta_{usf}$, at which point δ and Δ are equal, $\delta_c^{tip} = \Delta_c^{tip} = \Delta_{usf}$. At this point, the inelastic slip energy is a maximum and equal to γ_{usf} , and so G is also a maximum and corresponds to the point of dislocation emission. Within isotropic elasticity, the corresponding critical stress intensity factor for dislocation emission is then

$$K_{IIe} = \sqrt{2\mu\gamma_{usf}/(1 - \nu)}. \quad (3.4)$$

For Mode I loading, where the slip plane is inclined at some angle θ to the crack plane, there is no exact solution. The crack tip geometry is not self-similar and the J-integral concept does not apply. Rice proposed that, at the point of emission, the distribution of shear slip along the slip plane is the same in Modes I and II. This allows the result for Mode II to be used to estimate emission for Mode I by computing the effective Mode II loading along the slip plane, leading to

$$K_{Ie} = \sqrt{2\mu\gamma_{usf}/(1 - \nu) / \cos^2(\theta/2) \sin(\theta/2)} \quad (3.5)$$

with emission again occurring when $\Delta_c^{tip} = \Delta_{usf}$. The isotropic results of Eqs. 3.4 and 3.5 were

Chapter 3. Continuum theories of crack-tip dislocation emission

generalized to full anisotropic elasticity[74] with the result

$$\begin{aligned} K_{IIe} &= \sqrt{\gamma_{usf} o(\theta, \phi)} \\ K_{Ie} &= \sqrt{\gamma_{usf} o(\theta, \phi) / F_{12}(\theta)} \end{aligned} \quad (3.6)$$

where $o(\theta, \phi)$ is a function of the slip plane angle θ and the angle ϕ between the dislocation Burgers vector and the crack front direction in the slip plane and $F_{12}(\theta)$ is related to the angular distribution of shear stress at the crack tip. Details regarding the computation of $o(\theta, \phi)$ and $F_{12}(\theta)$ are presented in Sec. 2.1.5.

With increasing far-field loading, the first partial dislocation can be followed either by (i) the trailing partial dislocation emission or (ii) the twinning partial dislocation emission. A model for the critical stress intensity factor for the trailing partial emission K_{Ie}^{trail} was also introduced by Rice [50]. While similar to the analysis for the leading partial, additional important aspects enter. As the first partial dislocation moves away from the crack tip, it leaves behind a stacking fault. This causes the energy at the crack tip to be shifted to the intrinsic stacking fault γ_{ssf} (see Figure 3.1). The trailing partial nucleates on the same slip plane as the leading partial, and so the energy barrier for its emission is $\gamma_{usf} - \gamma_{ssf}$ (dashed line in Figure 3.1). The emission of the trailing partial dislocation is also associated with a change in the angle between the partial dislocation Burgers vector and the crack front direction, $\phi_{first} \rightarrow \phi_{trail}$. In fcc metals, the difference is always $|\phi_{trail} - \phi_{first}| = 60^\circ$. By using the constrained path approximation and the same assumption regarding slip profiles in Mode II and Mode I, Rice derived the critical stress intensity factor at the tip for the emission of the trailing partial dislocation in Mode I as

$$K_{Ie,tip}^{trail} = \sqrt{(\gamma_{usf} - \gamma_{ssf}) o(\theta, \phi_{trail}) / F_{12}(\theta) \cos(\phi_{trail})}. \quad (3.7)$$

3.3 Tadmor-Hai theory for crack-tip twinning

The first partial dislocation can also be followed by the emission of the twinning partial dislocation. An analytical model for predicting K_{Ie}^{twin} was proposed by Tadmor and Hai [94] as an extension of the Rice theory with two main differences: (i) the angle between the twinning partial Burgers vector and the crack front direction is same as for the first partial dislocation $\phi_{first} = \phi_{twin}$, and (ii) the twinning partial forms the micro-twin boundary by nucleation on the adjacent slip plane and, therefore, the energy functional describing the shear displacement along the twinning plane is the generalized twinning fault (GTF) energy (the dotted line in Figure 3.1). The energy barrier for the twinning partial emission is then $\gamma_{utf} - \gamma_{ssf}$. Following Rice, Tadmor and Hai derived the critical stress intensity factor at the tip for the emission of the twinning partial dislocation as

$$K_{Ie,tip}^{twin} = \sqrt{(\gamma_{utf} - \gamma_{ssf}) o(\theta, \phi_{first}) / F_{12}(\theta)}. \quad (3.8)$$

At temperature $T = 0K$ a material is predicted to emit the twinning partial dislocation when $K_{Ie,tip}^{twin} < K_{Ie,tip}^{trail}$.

3.4 Shielding effect on second partial dislocation emission

Once emitted, the first partial dislocation moves to some distance r at which the total Peach-Koehler force is equal to zero [50]. Analytical solutions for the equilibrium position r of the first partial dislocation, along with the additional stress intensity factors k_i^d , ($i = I, II, III$), that are generated due to its stress field has been shown and discussed in Section 2.4 (see Eq. 2.52). These additional stress intensity factors then shift the far-field stress intensity factor K_I for the emission of the trailing or twinning partial to

$$\begin{aligned} K_{Ie}^{trail} &= \sqrt{(\gamma_{usf} - \gamma_{ssf})o(\theta, \phi_{trail})/F_{12}(\theta) \cos(\phi_{trail}) + k_I^d + \frac{F_{22}(\theta)}{F_{12}(\theta)} k_{II}^d} \\ K_{Ie}^{twin} &= \sqrt{(\gamma_{utf} - \gamma_{ssf})o(\theta, \phi_{first})/F_{12}(\theta) + k_I^d + \frac{F_{22}(\theta)}{F_{12}(\theta)} k_{II}^d} \end{aligned} \quad (3.9)$$

with $F_{22}(\theta)$ correcting for the resolved shear stress along the slip plane due to k_{II}^d . Eq. 3.9 suggests that the emission of the second partial dislocation is only controlled by the processes in the vicinity of the crack-tip. As noted above, the shielding affects both processes equally through a net stress intensity acting at the crack tip. Shielding is thus not intrinsic to either of the two possible crack-tip processes, and does not affect which process is more favorable.

4 New theory for Mode I crack-tip dislocation emission

This chapter is extracted from the following publication:

- (1) Andric P, Curtin WA. New theory for Mode I crack-tip dislocation emission. Journal of the Mechanics and Physics of Solids. 2017 Sep 1;106:315-37.

4.1 Introduction

Chapter 3 provided a brief overview of the continuum based Rice theory for predicting the critical stress intensity factor for crack-tip dislocation emission. Molecular statics and dynamics simulations provided a means by which to validate the Rice model. Early simulations [118, 119] showed that the Rice criterion gives accurate predictions for K_{IIe} under Mode II loading, where the crack plane is coplanar with the slip plane. However, results for Mode I loading showed varying levels of agreement from material to material. It was recognized that deviations from the Rice criterion could be due to the creation of a surface step (surface ledge) during the Mode I nucleation process. Several authors thus tried to incorporate the additional energy of the surface step [54, 120, 121, 122] into a Rice-type analysis, but usually for one particular material with some approximations, and without achieving significantly better results. In all of these models, the key Rice concept was maintained: the unstable stacking fault energy controls the dislocation nucleation with emission occurring when the slip displacement reaches the displacement corresponding to the unstable stacking fault displacement. Schoeck (2003) [123] considered a related continuum model, but with creation of a step introduced through an additional constant force acting at the crack tip. The resulting energy functional was then solved approximately using a variational method to obtain the slip distribution along the slip plane, and results were shown for simplified slip energy models. One conclusion of the Schoeck analysis is that, for low step energy, dislocation emission could occur below the Rice prediction, which is not generally supported by simulations in Mode II or Mode I for atomically sharp cracks and is difficult to rationalize physically. Schoeck was pursuing a valuable path that is echoed here, but with an approximate

model. Zamora et al. [97] proposed a continuum approach that included extra energy for step formation near the crack tip and proposed a method for computing the step energy contribution, but they presented limited results for a specific system where the role of surface step creation was not clearly identified.

Here, we approach the Mode I emission problem as a mechanical instability governed by a critical crack tip displacement. We show that, in contradiction to a key assumption in the Rice theory, the energy change at the crack tip due to relative slip is monotonically increasing with crack tip displacement, due to the energy cost of creating the step. Thus, the Rice theory simply cannot apply: there is no saddle point in the energy versus slip. We then develop a model that assumes all non-linear response to occur at the crack tip to demonstrate that, in the presence of the step, there exists a critical crack tip displacement at which mechanical instability occurs, i.e. the driving stress at the crack tip due to the applied field can no longer be balanced by the restoring stresses that resist step formation. The simple model rationalizes simulation trends and provides analytic results. We apply the model to 17 different fcc materials where, due to material non-linearities, we use the measured critical crack tip displacement in the theory and then predict K_{Ie} in very good agreement with the simulated values. The new theory captures all key aspects of the Mode I dislocation nucleation process, resolving the discrepancies of the Rice theory. A simplified analytic model is then presented that involves only easily-computable material properties yet shows excellent agreement with the simulations. The simplified model is also used to rectify previous discrepancies between Rice theory and atomistic simulations in other materials.

4.2 Rice theory versus atomistic simulations

4.2.1 Materials studied

The crack tip dislocation emission is analyzed for 17 different fcc materials. To describe Aluminum interatomic interactions we use two different EAM potentials developed by Mishin et al. [81] and Ercolessi and Adams [124]. Mishin EAM potentials were also used to describe Ni [81] and Copper [125] while the Adams et al. [126] EAM potentials were used to describe Gold, Silver and Palladium. A set of effective alloy potentials, labeled Cr10-Cr100, were derived using a homogenization procedure [127] based on an Fe-Ni-Cr EAM ternary system developed by Bonny et al. [128]. The homogenization procedure enables the creation of a set of single-atom materials with continuous property variations by continuous change of the underlying alloy composition. The Cr10-Cr100 materials are a discrete set of materials of compositions $\text{Cr}_x\text{Fe}_{(1-x)/2}\text{Ni}_{(1-x)/2}$ that have a smooth variations in material properties over some range. It so happens that these materials have nearly constant (111) surface energies while the stacking fault energies, GSF curves, slip Δ_{usf} at the unstable stacking fault, and anisotropic elastic properties vary significantly. The relevant properties for each material computed using standard methods and molecular statics simulations [103, 129] are presented in Table 4.1.

Material	a_0 (Å)	C_{11} (GPa)	C_{12} (GPa)	C_{44} (GPa)	$o(\theta = 70, \phi = 0)$ (GPa)	$o(\theta = 70, \phi = 60)$ (GPa)	Λ_{22} (GPa)	γ_{usf} (J/m ²)	γ_{ssf} (J/m ²)	γ_{utf} (J/m ²)	$f^{(1)}$	$f^{(2)}$	γ_s (J/m ²)
AlM [81]	4.050	113.4	61.5	31.6	87.9	64.9	88.7	0.167	0.145	0.220	1.314	1.646	0.871
AlE [124]	4.032	118.0	62.2	36.7	97.0	72.3	98.2	0.119	0.106	0.168	1.313	1.666	0.871
Au [126]	4.080	183.2	158.7	45.3	101.0	60.6	103.7	0.097	0.005	0.099	1.422	1.819	0.796
Ag [126]	4.090	129.1	91.7	56.7	115.4	78.1	120.0	0.119	0.002	0.119	1.349	1.713	0.619
Cu [125]	3.615	169.9	122.6	76.2	152.1	101.7	158.4	0.162	0.044	0.184	1.350	1.729	1.240
Pd [126]	3.890	221.1	183.0	72.6	152.2	93.8	157.4	0.145	0.015	0.152	1.400	1.796	1.301
Ni [81]	3.520	247.9	147.8	124.8	249.8	181.0	260.0	0.368	0.125	0.428	1.299	1.654	1.631
Cr10 [127]	3.497	301.3	171.5	156.7	311.2	229.1	324.1	0.425	0.051	0.451	1.314	1.669	1.445
Cr20 [127]	3.507	276.6	165.6	148.7	287.5	208.2	300.4	0.356	0.049	0.380	1.324	1.681	1.441
Cr33 [127]	3.522	246.6	158.1	138.5	257.8	181.9	270.5	0.288	0.057	0.317	1.338	1.699	1.434
Cr40 [127]	3.529	232.6	154.7	133.7	243.7	169.2	256.3	0.264	0.067	0.298	1.345	1.705	1.430
Cr50 [127]	3.541	213.1	150.8	127.6	223.7	150.5	236.2	0.240	0.089	0.285	1.358	1.726	1.424
Cr60 [127]	3.552	205.5	150.3	124.6	214.7	141.7	227.1	0.232	0.117	0.289	1.367	1.738	1.418
Cr70 [127]	3.563	204.5	152.8	124.6	212.4	138.2	224.8	0.237	0.152	0.308	1.375	1.747	1.413
Cr80 [127]	3.572	211.2	159.0	127.9	218.1	141.2	230.8	0.255	0.190	0.340	1.383	1.751	1.408
Cr90 [127]	3.579	225.6	168.9	139.4	231.8	150.7	245.2	0.287	0.231	0.385	1.390	1.751	1.404
Cr100 [127]	3.584	247.3	182.5	145.5	253.3	166.3	267.5	0.328	0.272	0.441	1.396	1.727	1.400

Table 4.1 – Material elastic properties, unstable stacking fault energies γ_{usf} , stable stacking fault energies γ_{ssf} , unstable twinning fault energies γ_{utf} , surface energies for (111) slip plane, and material parameters $f^{(1)}$ and $f^{(2)}$ for predicting the crack-tip twinning. All the values are computed using standard methods and molecular statics simulations [103, 129]

4.2.2 Mode II loading

To validate the Rice criterion for crack tip dislocation emission in Mode II, we perform molecular statics simulations using the molecular dynamics code LAMMPS [87]. We simulate a semi-infinite crack under plane strain loading conditions using the "K-test" described above (see Section 2.4.4). The crack is loaded incrementally by applying the atomic displacements using Eq. 2.22. To create a crack coplanar with the slip plane, an fcc crystal is oriented with $X_1 = [112]$, $X_2 = [1\bar{1}\bar{1}]$, $X_3 = [\bar{1}10]$ (see Figure 4.1). The simulation cell has dimensions of approximately $120 \times 120 \times 1 \text{ nm}^3$. A traction free crack surfaces are created using both "screening", and "blunting" by removal of one atomic row of atoms plus "screening" of the remaining atoms across the crack surfaces. Even though "blunting" can be modeled by deletion of several atomic layers, simulations show that these two cases give quite similar results for Mode II and also bracket the predictions of the Rice theory. The load is incrementally increased in steps of $\Delta K_{II} = 0.001 \text{ MPa}\sqrt{\text{m}}$. The simulation is terminated when the first partial dislocation is emitted from the crack tip. All other simulation details are identical to those presented in Section 2.4.4.

Figure 4.2 shows the results for the critical stress intensity factor K_{IIe} and crack tip relative slip at the point of emission, as simulated for 17 different EAM potentials [81, 124, 125, 126] and as predicted by the Rice theory [50] (see Section 3.2). Figure 4.2a shows that the Rice prediction for the critical stress intensity K_{IIe} for emission is in a very good quantitative agreement with the simulation values, although there are larger deviations for the "screening" case for the Cr60 - Cr100 potentials, which have rather asymmetric GSF curves (see below). Overall, the Rice prediction for K_{IIe} is generally between the two simulation results, which is the best possible agreement we could expect given the uncertainty in setting the atomistic crack tip conditions.

Furthermore, we measure shear displacements along the slip plane as the *shear deformation of the atomic triangular structural units* indicated in Figure 4.1. The shear displacement Δ of a structural unit $i = 1, 2, \dots$ along the slip plane can be evaluated as $\Delta'_i = u_s^{j+1} - u_s^{j-1}$, or $\Delta_i = u_s^{j+1} - u_s^j$, where u_s^j is the displacement of an atom j along $[112]$ slip direction (see Figure 4.2). Note that u_s^{j+1} and u_s^j are atomic displacements measured on the opposite sides of the slip plane; same holds for u_s^{j+1} and u_s^{j-1} . Under pure shear, two values for the shear displacement are identical, $\Delta'_i = \Delta_i$, and we find only very small differences between Δ_i and Δ'_i in the simulated Mode II loading, as expected. Figure 4.2b shows the crack tip shear displacement just before emission, as measured in the simulations and as predicted by the Rice theory. The shear displacement shown in Figure 4.2b is Δ_1 . In the screening case (Figure 4.1a), the atomic unit immediately behind the crack tip does not fully satisfies the condition of a traction free crack surface and so we also show the shear deformation Δ_0 immediately behind the crack tip, and expect Δ_0 and Δ_1 to bracket the true value. Overall, the Rice prediction is slightly higher than simulation results, but in broad agreement. There are few cases (the Cr70-Cr100 potentials) where the Rice prediction is notably higher than the simulations results, and for the same potentials we find a larger discrepancy in the prediction of the critical K_{IIe} . A possible reason for this discrepancy is mentioned in Section 4.4.

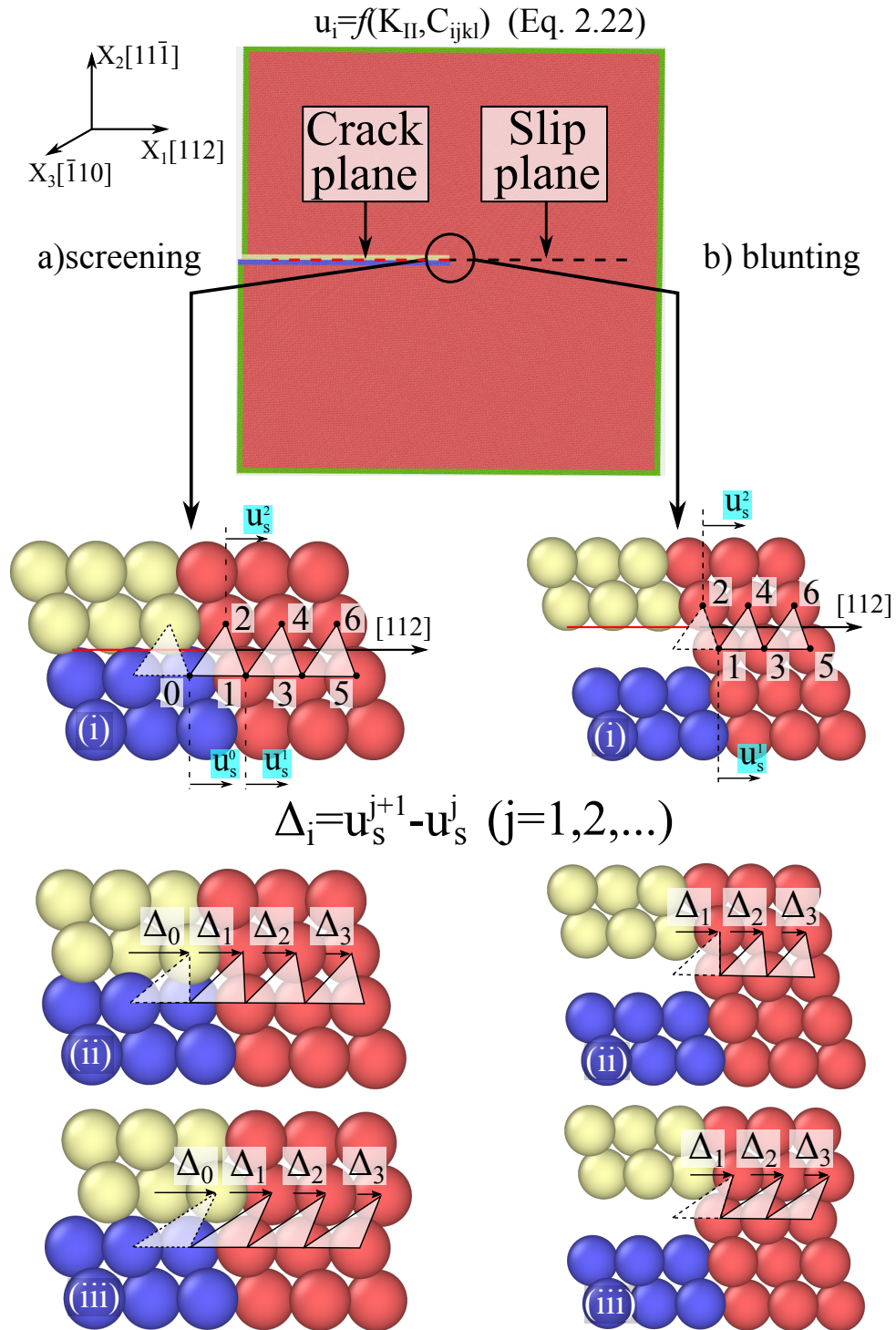


Figure 4.1 – Crack geometry in Mode II loading formed by a) deleting the interatomic interactions between the crack surfaces (yellow and blue atoms, respectively) and denoted as “screening” and b) removing one layer of atoms and then screening the remaining atoms (yellow and blue, respectively) and denoted as “blunting”. For both (a) and (b), the crack geometry is shown (i) at zero load, (ii) at the critical load for dislocation emission, and (iii) after dislocation emission. The triangles are the basic structural units through which the shear displacement along the plane of emission are analysed, as indicated. Atoms are visualized using OVITO [15].

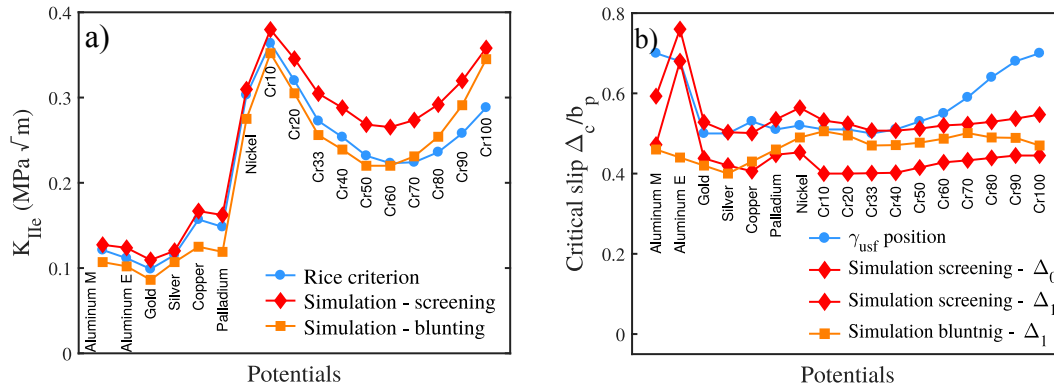


Figure 4.2 – Results of simulations under Mode II loading for both “screening” and “blunting” models: a) Critical stress intensity factor K_{IIe} for crack-tip dislocation emission; b) Relative shear displacement of the structural units at the crack tip and, for “screening” only, immediately behind the crack tip. In both (a) and (b), light blue symbols show the predictions of the Rice model.

We conclude that, within the limitations of the ability to simulate an ideal Mode II crack, the Rice model is accurate, qualitatively and quantitatively, in its prediction of dislocation emission under Mode II. Since the Rice theory is intended for Mode II, and since no step is formed during the emission, the agreement is not surprising. However, it is important to demonstrate this level of agreement between simulation and theory in Mode II because it highlights the clear differences that will arise in Mode I.

4.2.3 Mode I loading

We now examine the Rice criterion for crack tip dislocation emission in Mode I loading performing an additional set of molecular statics simulations. An fcc crystal is oriented with $X_1 = [\bar{1}\bar{1}2]$, $X_2 = [111]$, $X_3 = [\bar{1}10]$, forming a crack with a slip plane inclined at an angle $\theta = 70.53^\circ$ to the crack plane (see Figure 4.3); this is usually the orientation for easiest dislocation emission. The crack is, once again, loaded by applying the increments of atomic displacement using Eq. 2.19 and $\Delta K_I = 0.001\text{MPa}\sqrt{\text{m}}$. A traction free crack surfaces are created using both (i) “screening” between the yellow and blue atoms (Figure 4.3a), or (ii) “blunting” by deletion of three layers of atoms (Figure 4.3b). All other simulation details are identical to those presented in Section 2.4.4.

The critical stress intensity factor K_{Ie} for emission under Mode I loading is shown in Figure 4.4a. The Rice theory gives fair quantitative predictions for K_{Ie} , but is almost always lower than simulations for both “screening” and “blunting”. Some differences are large, up to 20 – 50% (see also Table 4.2). Results here are consistent with other results on specific systems scattered through the literature. The second observation is that, as in Mode II, the simulated K_{Ie} is usually slightly larger for “screening” as compared to “blunting”. There is no clear interpretation of this

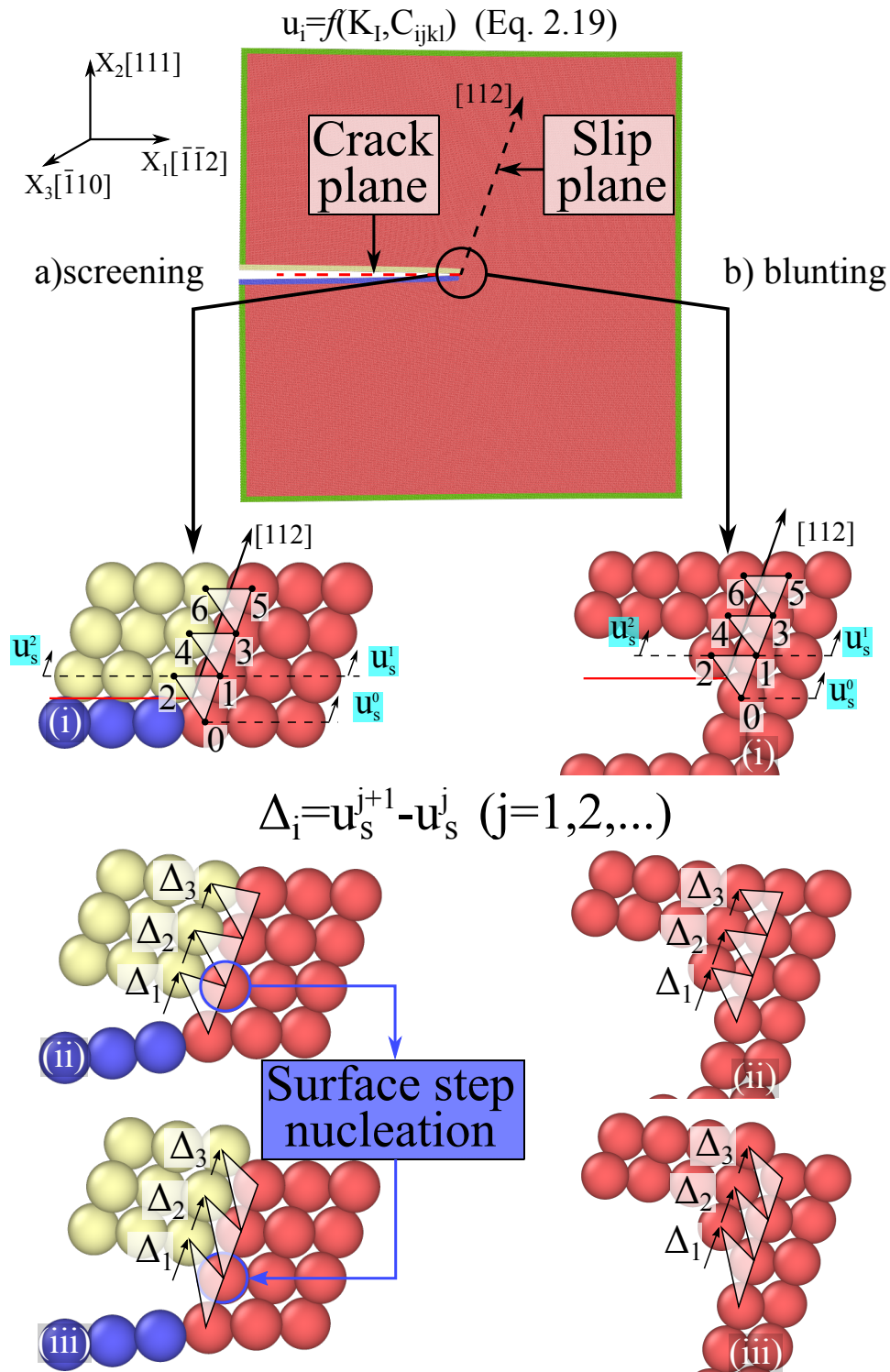


Figure 4.3 – Crack geometry in Mode I loading formed by a) deleting the interatomic interactions between the crack surfaces (yellow and blue atoms, respectively) and denoted as “screening” and b) removing three layer of atoms and denoted as “blunting”. For both (a) and (b), the crack geometry is shown (i) at zero load, (ii) at the critical load for dislocation emission, and (iii) after dislocation emission. The triangles are the basic structural units through which the shear displacement along the plane of emission are analyzed, as indicated.

Chapter 4. New theory for Mode I crack-tip dislocation emission

difference in Rice theory. Sun et al. [130] noted that the Rice theory for Mode I does not account for the opening displacement normal to the slip plane, which is expected to reduce the slip energy and thus reduce K_{Ie} below the Rice theory; such effects would increase the discrepancy between the theory and simulations.

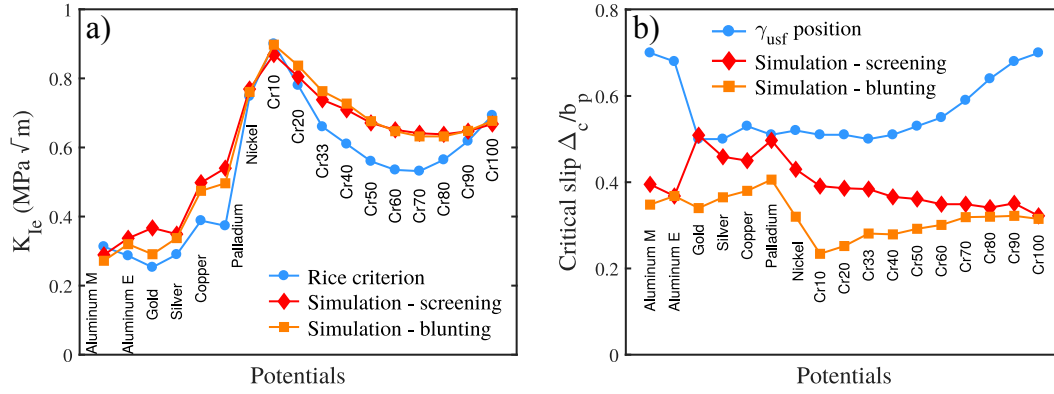


Figure 4.4 – Results of simulations in Mode I for both “screening” and “blunting” models: a) Critical stress intensity factor K_{Ie} for crack-tip dislocation emission; b) Relative shear displacement of the structural units at the crack tip. In both (a) and (b), light blue symbols show the predictions of the Rice theory.

Material	Δ_{usf}/b_p	Screening			Blunting				
		K_{sim}/K_{Rice}	Δ_1/b_p	Δ_2/b_p	K_{sim}/K_{Rice}	Δ_1/b_p	Δ_2/b_p	Δ'_1/b_p	Δ'_2/b_p
Al [81]	0.70	0.92	0.395	0.279	0.87	0.348	0.241	0.461	0.323
Al [124]	0.68	1.18	0.368	0.258	1.12	0.368	0.280	0.484	0.356
Au [126]	0.50	1.45	0.509	0.366	1.07	0.340	0.248	0.398	0.291
Ag [126]	0.50	1.20	0.459	0.334	1.07	0.365	0.268	0.447	0.334
Cu [125]	0.53	1.28	0.450	0.330	1.15	0.380	0.287	0.497	0.349
Pd [126]	0.51	1.45	0.497	0.365	1.19	0.406	0.311	0.483	0.366
Ni [81]	0.52	1.03	0.430	0.302	1.03	0.318	0.226	0.385	0.272
Cr10 [127]	0.51	0.97	0.392	0.267	1.00	0.234	0.165	0.335	0.234
Cr20 [127]	0.51	1.03	0.386	0.269	1.07	0.252	0.182	0.353	0.249
Cr33 [127]	0.50	1.12	0.384	0.277	1.16	0.281	0.209	0.380	0.273
Cr40 [127]	0.51	1.16	0.366	0.266	1.19	0.279	0.211	0.375	0.271
Cr50 [127]	0.53	1.20	0.361	0.266	1.21	0.299	0.232	0.393	0.288
Cr60 [127]	0.55	1.22	0.349	0.259	1.21	0.301	0.237	0.395	0.291
Cr70 [127]	0.59	1.21	0.349	0.261	1.19	0.319	0.255	0.406	0.301
Cr80 [127]	0.64	1.13	0.341	0.257	1.12	0.320	0.256	0.410	0.302
Cr90 [127]	0.68	1.05	0.351	0.267	1.05	0.326	0.258	0.417	0.307
Cr100 [127]	0.70	0.96	0.322	0.243	0.98	0.315	0.249	0.409	0.296

Table 4.2 – Positions of the γ_{usf} , along with the simulation results in Mode I for screening and blunting given as the ratios of simulation K_{Ie} and Rice prediction for K_{Ie} , and measured shear displacements of the first and second structural units at the point of emission (see Figure 4.3).

More importantly, Figure 4.4b and Table 1 show the simulated and predicted results for the critical crack tip shear displacement under Mode I loading. Here, we measure the shear deformation of the crack tip unit as $\Delta_1 = u_s^2 - u_s^1$ (see the initial crack in Figure 4.3). Due to very high normal stresses in the slip direction in Mode I, there can be some difference between Δ_1 and $\Delta'_1 = u_s^2 - u_s^0$ for some materials; physical aspects of this difference are explained in Appendix A.2. In Mode I loading, the difference between the Rice theory and simulation is notable: the

4.3. Energy due to surface step creation during dislocation emission

simulated instability point is often far below the value postulated by Rice, with differences of typically up to 40%. From an energetic point of view, the energy release rate at displacements below $\sim b_p/2$ is simply far too low to provide the unstable stacking fault energy necessary to nucleate a dislocation according to the Rice mechanism. Examining the results in Figure 4.4 further, we see that the screening case shows a critical slip at emission that is closer to the Rice prediction, but these cases also have a critical K_{Ie} that is much larger than the Rice prediction. For instance, in Au, Pd, and Ag, the critical slip at the crack tip in the “screening” case is almost equal to the slip at the unstable stacking fault energy (the Rice prediction), but the K_{Ie} is $\sim 50\%$ higher than the Rice prediction. Since the energy and the crack tip displacement are intimately coupled in the Rice theory, there is a fundamental problem with the Rice theory for Mode I loading. As we show in the next section, the problem lies in the fact that the Rice theory does not account for the creation of the surface step that accompanies dislocation emission in Mode I.

4.3 Energy due to surface step creation during dislocation emission

When a dislocation nucleates under Mode I loading, a surface step is created, as indicated in Figure 4.3. Figures 4.3 a(ii),b(ii) are at the point of nucleation and, while the final state (Figures 4.3 a(iii), b(iii)) clearly shows the creation of a surface step, there is a nascent surface step and an associated partial step energy at the point of emission. The energy to create the emerging surface step is an additional energy cost for dislocation emission. However, as seen previously in Figure 4.4b, the critical displacement at the point of dislocation emission is usually well below the Rice prediction. The energy of the inelastic slip along the stacking fault is therefore much lower than γ_{usf} . The total energy at the critical displacement in Mode I is thus some fraction of γ_{usf} plus some fraction of the step energy. The critical displacement at the emission point is also not at the instability point predicted by the Rice theory and so a simple incorporation of a step energy into the Rice model, as done in early attempts to include the step [54, 120, 121, 122], is not accurate. The dislocation nucleation differs significantly from the mechanism envisioned in the Rice theory, requiring an entirely new theory.

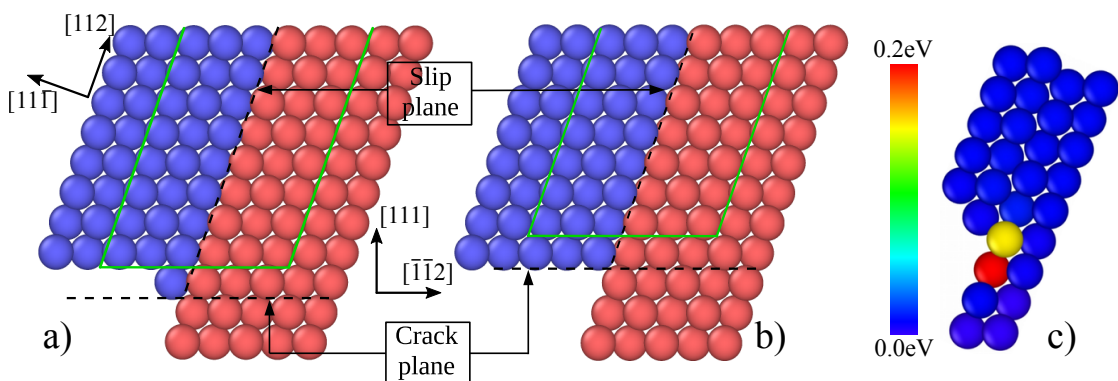


Figure 4.5 – Computation of the nucleation energy a) for “blunting” crack geometry; b) for “screening” crack geometry; and c) atom-by-atom energy change in the blunting case after full slip (one partial Burgers vector) for Nickel.

The first step toward a new theory involves investigation of the energy versus slip displacement as the actual nucleation process takes place, including the energy associated with the emerging surface. We proceed in direct analogy to the usual computation of the GSF curve, using a method similar to that presented by Zamora et al. [97]. First, we create a non-orthogonal simulation cell, oriented with $X = [\bar{1}\bar{1}2]$, $Y = [111]$, $Z = [\bar{1}10]$. The simulation cell size is $6\sqrt{6}a_0 \times 8\sqrt{3}a_0 \times 2\sqrt{2}a_0 \text{Å}^3$. We apply periodic boundary conditions in $[112]$ direction, while in $[1\bar{1}\bar{1}]$ we apply free boundary conditions (see Figure 4.5a, b). Two identical crystal parts are defined and depicted as blue and red atoms, respectively. The interface between the blue and red atoms represents the slip plane. The initial crack tip geometry (blunting or screening) is created by (i) increasing of the simulation box size in $[\bar{1}\bar{1}\bar{2}]$ direction and (ii) deleting extra atoms, as depicted in Figure 4.5a, b. We then rigidly slide the left crystal domain (blue atoms) relatively to the right crystal domain (red atoms). As in a standard GSF computation, relaxation is permitted only in the direction normal to the slip plane. We then compute energy change over a domain which includes three atoms on either side of the slip plane plus the crack tip atoms. The domain size in the $[112]$ direction is sufficiently long so that atoms far from the crack tip are essentially bulk atoms. Figure 4.5c shows atom-by-atom energy change after slip of one partial Burgers vector (the final state after emission); the energy changes of the atoms just at the crack tip dominate the overall energy change. Along the slip plane away from the crack tip atoms, the energy is intrinsic stacking fault γ_{ssf} but this energy is not visible in Figure 4.5c because it is overwhelmed by the energy of the crack tip atoms. At any slip displacement Δ , we measure the energy change *local to the crack tip atoms* by subtracting the energy associated with the bulk GSF over all atoms in the domain except those at the crack tip, as outlined by the green line in Figures 4.5a,b. The remaining energy is the total energy, due to both the stacking fault and the step, associated with the slip of the atoms that define the crack tip structural unit. We divide this energy by the atomic spacing $\sqrt{6}a_0/4$ along the $[112]$ direction, and by $2\sqrt{2}a_0$ to along the $[\bar{1}10]$ direction, to obtain the crack tip slip energy (per unit area), which we call the nucleation energy, defined as

$$\Psi_{nuc}(\Delta) = \Psi_{step}(\Delta) + \Psi_{gsf}(\Delta) \quad (4.1)$$

where $\Psi_{step}(\Delta)$ is the energy associated with step creation at the crack tip and $\Psi_{gsf}(\Delta)$ is the bulk GSF energy contribution in the crack tip unit. Note that the two contributions in Eq. 4.1 are not independently separable in the simulations but we write Eq. 4.1 to indicate that, in the absence of any step, the nucleation energy should still include the GSF energy. Figure 4.6b shows $\Psi_{nuc}(\Delta)$ along with the standard GSF curve for the case of fcc Ni. Figure 4.5 exhibits several crucial features. First and foremost, unlike the GSF curve, there is no maximum in $\Psi_{nuc}(\Delta)$ at any slip $\Delta < b_p$. *The absence of a maximum immediately precludes application of the Rice theory, which is based on a maximum energy (γ_{usf}) at which point the material offers no resistance to further slip.* Second, the total crack tip energy is significantly larger than the GSF energy. This is not surprising because the free surface energy is typically much larger than the unstable stacking fault energy. Third, the final value of the nucleation energy $\Psi_{nuc}(\Delta = b_p)$, which we call the surface step energy γ_{step} , is slightly lower than the flat surface energy γ_s of the exposed

4.3. Energy due to surface step creation during dislocation emission

crystalline facet. This difference is due to the local atomic structure of the crack tip. For all 17 potentials studied here, this ratio is $\gamma_{step}/\gamma_s \approx 0.7 \pm 0.05$.

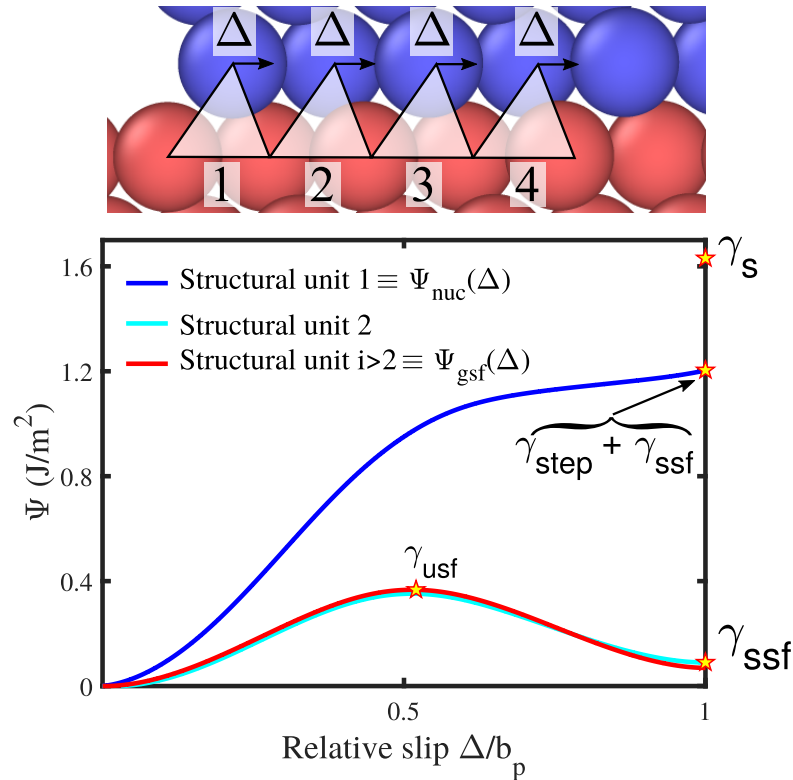


Figure 4.6 – Slip energy change versus slip displacement, for successive atomic structural units along the slip plane computed for fcc Ni [81]; only the energy for the structural unit at the crack tip deviates significantly from the bulk GSF energy.

We can further verify that the surface step creation has no influence further along the slip plane away from the crack tip by analyzing the energy changes of each triangular structural unit along the slip plane as a function of the relative slip Δ (see Figure 4.6a). Figure 4.6b shows that, even in unit 2 adjacent to the crack tip unit, the energy is nearly identical to the GSF energy. Therefore, the step energy is localized to the structural unit at the crack tip. This conclusion holds for every material studied here and will be used to develop a new theory for dislocation emission in the next section. The nucleation energy $\Psi_{nuc}(\Delta)$ and GSF energy $\Psi_{gsf}(\Delta)$ are computed for all materials studied here as shown in Figures 4.7a,b for both “screening” and “blunting” crack geometry; the conceptual points observed for Ni are valid in all cases. The small differences between “screening” and “blunting”, not visible in Figures 4.7a and b, give rise to differences in the simulated K_{Ie} , as we will see below.

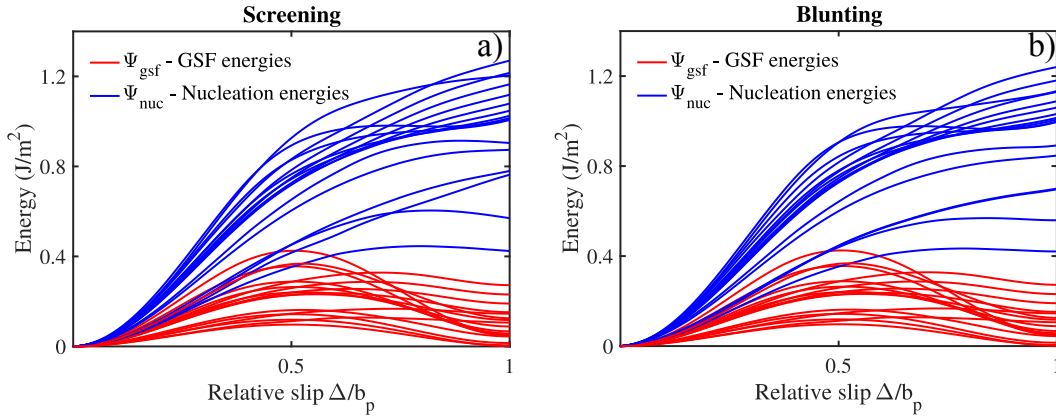


Figure 4.7 – GSF energy (red lines) and nucleation energy (blue lines) versus relative slip for all fcc materials studied here: a) screening; b) blunting. GSF energies are identical in both figures.

4.4 New theory for crack tip dislocation emission

Since the nucleation energy does not have a maximum, we deduce that emission must correspond to a local mechanical instability at the crack tip. Due to the high energy cost of shearing associated with step formation, the dislocation is “trapped” at the crack tip in a manner reminiscent of “lattice trapping” of a cleavage crack [79]. In “lattice trapping” for the cleavage crack problem, the precise force-displacement behavior of the crack-tip bond can restrain crack opening until the crack tip bond is mechanically unstable. At this point, the applied load K_I exceeds the thermodynamic Griffith value K_{Ic} . In the dislocation emission problem here, the shear stress needed to shear the crack tip unit up to the unstable point of dislocation emission is higher than that corresponding to the GSF energy. Once the shear of the crack tip unit reaches a critical level at which the crack tip unit becomes unstable, the dislocation then move away unstably along the slip plane. The weaker restoring stresses further along the slip plane, due only to the GSF energy, are unable to impede the dislocation nucleation.

While the new theory will be fundamentally different from the Rice theory, we retain key assumptions consistent with the Rice analysis (see Figure 4.8). Most importantly, we assume that (i) only the shear resistance along the slip plane controls the nucleation process, (ii) all non-linear behavior is confined to the slip plane, and (iii) that the shear displacement distribution $\Delta_1, \Delta_2, \dots$ along the slip plane is the same in Modes I and II. This last assumption has been explicitly verified as shown in Appendix A.3, where we demonstrate that, for a specified displacement Δ_1 at the crack tip, the remaining displacements $\Delta_2, \Delta_3, \dots$ along the slip plane are essentially the same in Mode I and Mode II loadings. The main difference between the new theory and the Rice theory will be in the crack tip constitutive behavior, i.e. the resistance of the crack tip structural unit to shearing due to the emergence of the step in Mode I but not in Mode II, as shown already in Figure 4.6b. The other difference with Rice analysis will be that we deal only with the total shear displacements Δ ; we find no need to introduce the inelastic slip measure δ and in this aspect we

are consistent with the analysis of Schoeck [123].

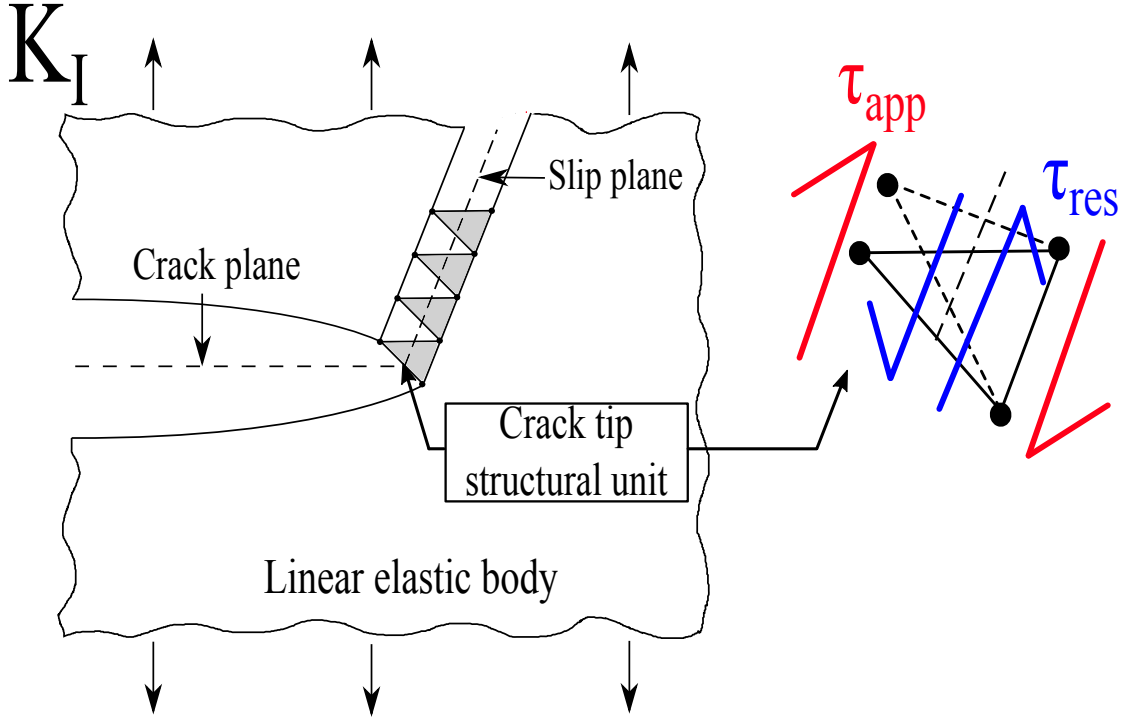


Figure 4.8 – a) Linear elastic body with semi-infinite crack under pure Mode I loading surrounding the dislocation emission plane that is characterized by atomic structural units along the slip plane; b) Local stresses acting on the crack tip structural unit: an applied stress due to the remote applied K_I load and a restoring stress due to the shear resistance of the crack tip structural unit, which together determine the local equilibrium shear deformation (dashed lines).

We start by analyzing the case with zero step energy; this analysis thus also applies to Mode II and will reveal the Rice solution from a different perspective. For zero step energy, the energy versus slip is only the GSF energy. The corresponding GSF "restoring" shear stress τ_{res} across the slip plane is the derivative of the energy. We use a sinusoidal Peierls model so that $\tau_{res} = \tau_{gsf} = (\mu b_p / 2\pi h) \sin(2\pi \Delta / b_p)$, as shown in Figure 4.9a. We now focus on the crack tip structural unit and assume that all non-linear behavior is confined to this crack tip structural unit, i.e. shear deformations further along the slip plane remain in the (nearly) linear domain of the Peierls curve. Then, a remote applied K_I generates a shear stress $\tau_{app,0}$ on the crack-tip unit that is linear in K_I . As the shear displacement Δ of the crack tip unit increases, the applied shear decreases linearly as $\tau_{app} = \tau_{app,0} - \mu \Delta / h(\beta - 1)$, as indicated in Figure 4.9a. Here, the constant β is the crack-tip Green's function for shear in the lattice; $\beta = 2$ for a linear isotropic continuum and varies between 1.4 and 2.3 for the anisotropic fcc materials studied here (see Appendix A.4).

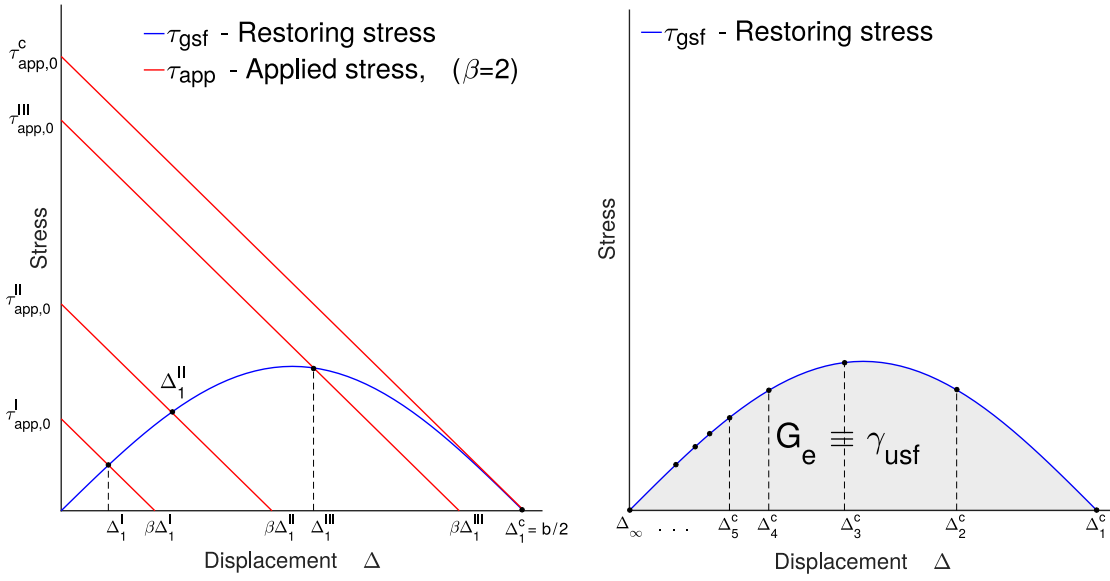


Figure 4.9 – Graphical construction for the equilibrium shear displacement Δ_1 of the crack tip unit in Mode II loading or in Mode I loading when no step is present, for several different far-field loadings. Solid blue line: crack tip restoring stress versus crack tip shear displacement due to GSF energy only; Red lines: crack tip applied shearing stress versus shear displacement. b) Critical shear displacements $\Delta_1, \Delta_2, \dots$ along the slip plane at the point of dislocation emission, with critical energy release rate corresponding to the shaded area.

At any given applied K_I , and thus any given $\tau_{app,0}$, the equilibrium crack tip displacement Δ_1 is given by the condition $\tau_{app} = \tau_{res}$, as shown graphically in Figure 4.9a for several values of $\tau_{app,0}$ with $\beta = 2$. For the sequence of applied stresses ($\tau_{app,0}^I, \tau_{app,0}^{II}, \dots$), the corresponding equilibrium shear displacements ($\Delta_1^I, \Delta_1^{II}, \dots$) are stable equilibrium points because $d\tau_{app}/d\Delta < d\tau_{res}/d\Delta$ for all $0 < \Delta < b_p/2$. There is no mechanical instability until $\Delta_1 = \Delta_1^c = b_p/2$. The stress $\tau_{app,0}^c$ at this instability is then proportional to K_{Ie} . The assumption of linearity for all units ahead of the crack tip unit is not really true: in the more general case, the crack tip units deform stably along the GSF curve until the crack tip unit becomes unstable. The instability could then occur prior to $\Delta_1 < b_p/2$; in other words, some lattice trapping can occur in Mode II even without the step, and this can account for the deviation in predicting K_{IIe} in the Cr60-Cr100 potentials. However, the spatial range of the GSF stress versus displacement corresponds, in the language of the “lattice trapping” cleavage problem [79], to a relative long-range force law with very small lattice trapping. The instability thus usually occurs very near, or at, $\Delta_1 = \Delta_1^c = b_p/2$, with $\Delta_2^c, \Delta_3^c, \dots$ as shown in Figure 4.9b, and hence trapping is generally small in Mode II. At the instability point, all atoms move forward to the next stable position, such that $\Delta_2^c \rightarrow \Delta_1^c, \Delta_3^c \rightarrow \Delta_2^c, \dots$. The total energy required to reach the instability point is then equal to the energy required to take the crack tip unit from $\Delta_1 = 0$ to $\Delta_1 = b_p/2$. This energy is equal to the area under the τ_{gsf} curve, which in turn is precisely γ_{usf} , as indicated in Figure 4.9b. This construction is the discrete analog to the continuous cohesive zone model that is implicit in the

4.4. New theory for crack tip dislocation emission

Rice theory, but using the total shear displacement Δ and GSF energy $\Psi_{gsf}(\Delta)$ rather than the displacement discontinuity δ and energy $\Phi(\delta)$.

We now use the same general analysis to consider the case of dislocation emission when a surface step is created. Again, we assume that only the crack tip deforms non-linearly. Due to the step creation, the energy of the crack tip unit is $\Psi_{nuc}(\Delta) = \Psi_{step}(\Delta) + \Psi_{gsf}(\Delta)$ and the restoring stress is $\tau_{res} = d\Psi_{nuc}/d\Delta$. Figure 11 shows the restoring stress for a Peierls model of the nucleation energy, $\Psi_{nuc}(\Delta)$ and $\tau_{res} = g(\mu b_p/2\pi h) \sin(2\pi\Delta/b_p)$, where $g = \tau_{res}/\tau_{gsf}$ is the factor by which the restoring stress with the step exceeds the restoring stress when there is no step creation. However, the surrounding material remains elastic. *Therefore, the applied stress remains exactly the same as before, $\tau_{app} = \tau_{app,0} - \mu\Delta/h(\beta - 1)$.* With increasing applied stress $\tau_{app,0}$, the stable equilibrium shear displacement Δ_1 of the crack tip unit evolves stably as shown in Figure 11. A mechanical instability, corresponding to dislocation nucleation, then occurs at the applied stress $\tau_{app,0}^{c,step}$ where the equilibrium shear displacement becomes metastable, i.e. when $\tau_{app} = \tau_{res}$ and $d\tau_{app}/d\Delta = d\tau_{res}/d\Delta$, as indicated in Figure 11. When $g > 1.5$, and for $\beta = 2$, the instability occurs at $\Delta_1^c \ll b_p/2$ and the shear displacements $\Delta_2^c, \Delta_3^c, \dots$ ahead of the crack tip remain (nearly) in the linear range of the GSF stress curve, as indicated in Figure 12a. The ratio of the remote applied stress intensity at the instability point for the step case (Mode I) to that of the no-step case (the Rice model) is equal to the ratio of the critical stresses,

$$\tau_{app,0}^{c,step} / \tau_{app,0}^c = K_{Ie,step} / K_{Ie,Rice} \quad (4.2)$$

As seen graphically in Figure 4.10, the fractional increase in the remote stress intensity factor is larger than, but not significantly larger than, the Rice value. The “trapping” of the nucleating dislocation at the crack tip due to the extra energy of the step thus leads to a critical shear displacement instability that is lower than the Rice value but at a K_{Ie} that is larger than the Rice value.

The graphical analysis using the Peierls representation, as shown in Figure 4.10, can be executed numerically for any desired values of the two relevant material parameters β and g . Table 4.3 shows computed results for a range of typical values in real materials. At fixed β , increasing the step energy (increasing g) leads to increasing critical stress intensity for emission and decreasing critical crack tip shear displacement. These results are broadly consistent with the Mode I simulation results. Three important aspects merit comment. First, the theory predicts a continuous transition from emission controlled by γ_{usf} (Rice theory) to emission controlled by the step energy. Second, as seen for the case of $g = 1.5$, the increase in K_{Ie} above the Rice value is quite small even when the step energy is an appreciable fraction of γ_{usf} . Third, the analysis is independent of the slip plane inclination angle θ because the same nominal step is created at any $\theta \neq 0$ and rotation of the stress field accounts for all differences in the “applied” stresses (see Appendix A.5).

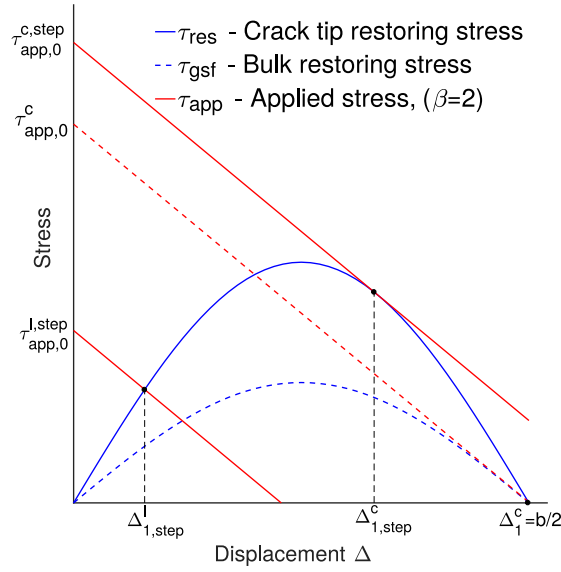


Figure 4.10 – Graphical construction for the equilibrium shear displacement Δ_1 of the crack tip unit when a step is created during emission in Mode I loading and all other displacements $\Delta_2, \Delta_3, \dots$ remain in the linear regime, for several different far-field loadings. Solid blue line: crack tip restoring stress versus shear displacement including the step energy; Red lines: crack tip applied shearing stress versus shear displacement; for reference, dashed blue line shows the crack tip restoring stress versus shear displacement due only to the stacking fault energy.

g	$\beta = 1.5$		$\beta = 1.75$		$\beta = 2.0$	
	$K_{Ie,step}/K_{Ie,Rice}$	Δ_c	$K_{Ie,step}/K_{Ie,Rice}$	Δ_c	$K_{Ie,step}/K_{Ie,Rice}$	Δ_c
1.5	1	0.5	1.01	0.42	1.09	0.36
2	1	0.5	1.09	0.36	1.22	0.33
2.5	1.03	0.4	1.18	0.33	1.36	0.31
3	1.09	0.36	1.29	0.32	1.5	0.3

Table 4.3 – Ratio of critical stress intensity factors with ($K_{Ie,step}$) and without ($K_{Ie,Rice}$) the surface step, for various values of the $g = \tau_{res}/\tau_{gsf}$ and crack tip Green's function parameter β , as computed using the Peierls model of Figure 4.10.

In realistic cases, the slip displacements away from the crack tip can again become (slightly) non-linear. In this case, the system softens and the simple graphical analysis based on non-linearity only at the crack tip is insufficient. However, at the instability point, the shear displacements again simply shift as $\Delta_2^c \rightarrow \Delta_1^c$, $\Delta_3^c \rightarrow \Delta_2^c$, etc. So, even when non-linearity extends beyond the crack tip structural unit, the energy that must be provided by the applied field to reach the point of instability is computed as the area under the curve shown in Figure 4.11a. The critical energy for emission can thus be computed in terms of the critical displacements Δ_1^c , and Δ_2^c . There are two contributions, one from the crack tip unit that follows Ψ_{nuc} and another from all other units

4.4. New theory for crack tip dislocation emission

that follow the Ψ_{gsf} energy function, so that

$$J = \int_{\Delta_2^c}^{\Delta_1^c} \tau_{res} d\Delta + \int_0^{\Delta_2^c} \tau_{gsf} d\Delta \quad (4.3)$$

which yields

$$J = \Psi_{nuc}(\Delta_1^c) - \Psi_{nuc}(\Delta_2^c) + \Psi_{gsf}(\Delta_2^c) \quad (4.4)$$

as shown graphically in Figure 4.11. The critical stress intensity factor is then computed using the standard relationship between K and G ,

$$K_{Ie} = \sqrt{G_{Ie} o(\theta, \phi) / F_{12}(\theta)}. \quad (4.5)$$

The analysis thus resembles the Rice theory, *but emission is controlled by reaching a critical crack tip displacement associated with a mechanical instability due to the step formation.*

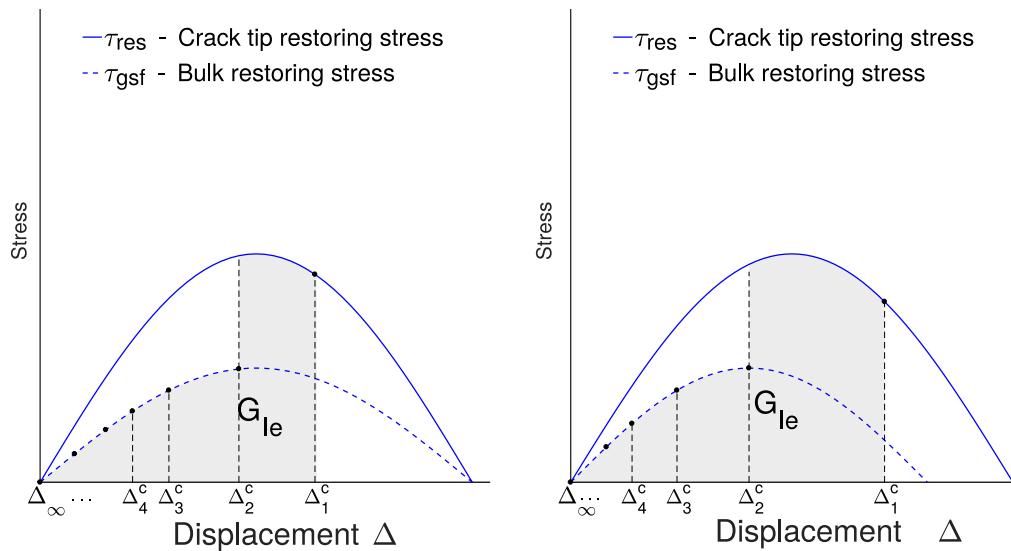


Figure 4.11 – a) Critical shear displacements $\Delta_1, \Delta_2, \dots$ along the slip plane at the point of dislocation emission, for the realistic case corresponding to some non-linearity in $\Delta_2, \Delta_3, \dots$ beyond the crack-tip structural unit. b) Critical shear displacements $\Delta_1, \Delta_2, \dots$ along the slip plane at the point of dislocation emission, when the crack tip restoring stress is skewed toward higher displacement. In both figures the associated critical energy release rate corresponds to the shaded area.

Furthermore, if the maximum crack tip restoring stress is skewed toward higher displacements (see Figure 4.11b), which arises in some of the atomistic systems (derivatives of curves shown in Figure 4.7), then the instability can be shifted toward larger displacements, even reaching $\Delta_1^c \approx b_p/2$, but then with a much greater energy and hence a much greater K_{Ie} . Such a situation

prevails in materials such as Au and Pd (see Figure 4.4). *So, a measurement of emission at $\sim b_p/2$ does not at all imply that the Rice model is applicable.*

4.5 Validation of the new theory

The previous section presented an analytical model that highlights the controlling physics/mechanics of the crack tip dislocation emission, and clearly rationalizes the origins of the deviations from the Rice theory. The analysis predicts the critical crack tip shear displacement Δ_1^c but assumes non-linearity to exist only in the crack tip unit. Even with some non-linearity away from the crack tip unit, the new model can predict the critical shear displacement Δ_1^c and the critical energy release rate G_{Ie} (as shown in Figure 4.11) for some simulated materials (Ni, Cu and Cr10-Cr40) in very good agreement with simulation results. However, in most of the simulated materials, the non-linear shear displacements further along the slip plane do not allow for direct application of the analytic theory. While non-linear behavior in the second structural unit could be included [79], such a complication is beyond the scope of this paper. Instead, we validate the new theory for K_{Ie} by using the simulated values of the critical shear displacement (see Table 4.2) as input to compute G_{Ie} , as shown in Figure 4.11. While not a fully independent prediction of both Δ_1^c and K_{Ie} , this approach nonetheless quantitatively demonstrates key aspects of the theory.

First, we assess the accuracy of the new theory for cracks formed by “screening”. Figure 4.12a shows the critical stress intensity factor K_{Ie} as predicted using the new theory (Eqs. 4.3-4.5); also shown are the simulation results and the Rice predictions. The predictions of the new theory are in excellent agreement with simulations, and generally better than, or comparable to, the Rice predictions. The new theory always predicts slightly higher results than found in the simulations, which likely reflects the limits of all models that use elasticity plus a non-linear slip model only along the slip plane. The overestimation found for Cr10 and Cr20 are cases with high normal stresses at the crack tip, where effects associated with stretching of the crack-tip unit along and normal to the slip plane may be more important (see below).

Next, we examine the accuracy of the new theory for cracks formed by blunting. Note that the Rice theory does not distinguish between these two cases, aside from approximate attempts to deal with elliptical crack tips [131]. Figure 4.12b shows that the predicted K_{Ie} value is very close to the Rice value, with overall comparable agreement (sometimes slightly better, sometimes slightly worse) than the Rice prediction. Only Cr10 and Cr20 are notably off from the simulations. Recall, however, that the critical crack tip shear for blunting is much smaller than the Rice prediction, so that the physical model associated with the new theory is much more accurate overall than the Rice model. The present model thus also accounts for the differences in both K_{Ie} and Δ_1^c between “screening” and “blunting”. As shown in Figure 4.13 for the specific cases of Ni and Cu (and also for both Al, Au, Ag, Pd, Cr100 and Cr90 potentials in Figure 4.7), the restoring stress for “blunting” is shifted to slightly lower shear displacements as compared to “screening”, leading to smaller predicted K_{Ie} and Δ_1^c .

4.5. Validation of the new theory

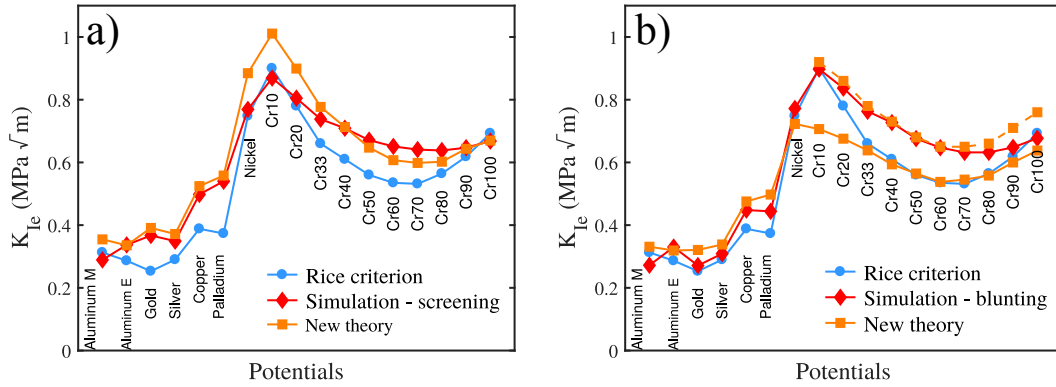


Figure 4.12 – a) Critical stress intensity factor for dislocation emission (Theory: orange; Simulation: red; Rice: blue line) for a) cracks formed by “screening”; b) cracks formed by “blunting”. Orange dashed line computed with Δ_1^c crack tip displacement.

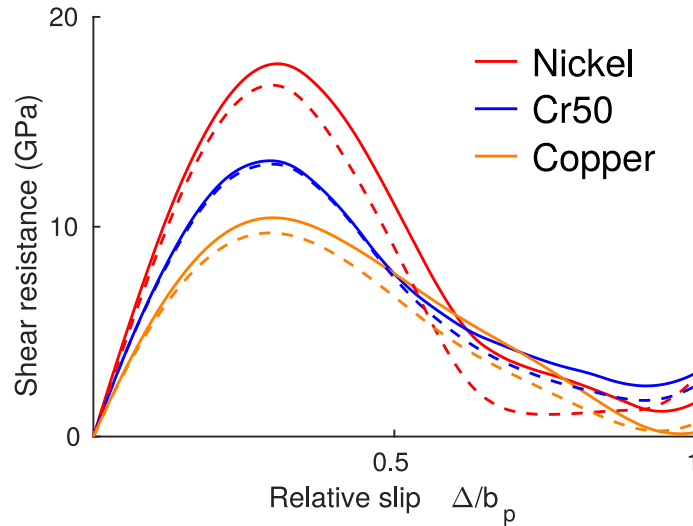


Figure 4.13 – Crack tip restoring stress for crack formed by screening (solid lines) and for crack formed by blunting (dashed lines) in Ni, Cr50 and Cu.

The deviation of the new theory from the simulations for the Cr10-Cr80 potentials lies in the fact that the crack tip shearing energy is strongly affected by the normal stress parallel to the slip plane. The measured critical Δ_1^c for these potentials is actually below the displacement at the maximum restoring stress, and so there cannot be an instability based on Δ_1^c alone. In these cases, the normal stress acting at the crack tip stretches the crack tip unit (see Appendix A.2) so that Δ_1 is not an accurate measure of the average crack tip shear. Instead, the shear displacement Δ_1' better reflects the shearing of the crack tip unit. In addition, the restoring stress for these potentials (shown in Figure 4.13 for the specific case of Cr50) is not affected by the crack geometry and so crack geometry does not influence the simulated K_{Ic} (see Figure 4.4a), and thus Δ_1 in the screening case is very close to Δ_1' in the blunting case (see Table 4.2). As shown in Figure 4.12b by the dashed line, predictions of the theory using the measured Δ_1' and the same $\Psi_{nuc}(\Delta)$ are

in very good agreement with the simulations. This difference shows that the precise deformation at the crack tip structural unit affects the critical stress intensity for emission by modest amounts, but these amounts can explain the differences between sharp “screened” cracks and “blunted” cracks, a feature absent in the Rice theory.

4.6 Approximate model for prediction of the crack-tip dislocation emission

The analysis in the previous section demonstrates the quantitative success of the conceptually new model. However, the predictions in Figures 4.12a,b use the simulation values for the critical shear displacement. Unlike the simple Peierls model (Figures 4.9 and 4.10), the instability point has not been predicted; the effects of non-linearities and the precise shear vs. displacement behavior beyond the maximum shear resistance preclude analytic analysis. Furthermore, we seek an analytic model that does not require direct atomistic simulations of the crack problem since there is no need for a model if one only needs to execute a standard molecular statics crack simulation. Thus, we aim for simplified models that predict K_{Ic} in terms of only the easily-computable (i) GSF curve Ψ_{gsf} and nucleation energy curve Ψ_{nuc} or (ii) unstable stacking fault energy γ_{usf} and surface energy γ_s .

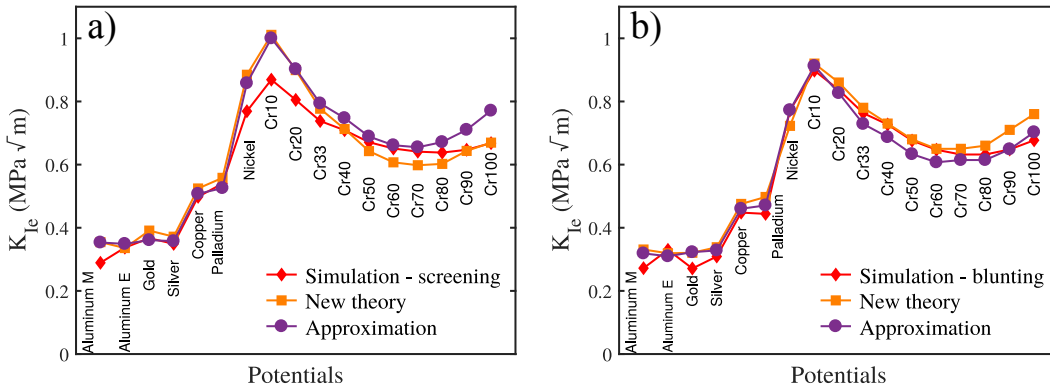


Figure 4.14 – Critical stress intensity factor for dislocation emission for all materials studied here; Simulations (red), full theory (orange); approximate model (purple) for a) screening and b) blunting.

For the simplified model which involves only Ψ_{gsf} and Ψ_{nuc} it is necessary to determine the critical crack tip shear displacements Δ_1^c , Δ_2^c . The analytical model of Section 4.4, along with the results given in Table 4.3, shows that the critical value Δ_1^c is weakly dependent on the step energy once the step energy is somewhat larger than the GSF energy. These results are also consistent with the simulations. Based on these observations we deduce that single value of Δ_1^c is sufficient for any material and can be used in the approximate model. Analyzing the critical crack tip shear displacements shown in Table 4.2, we can estimate $\Delta_1^c \approx 0.39b_p$ for “screening” and $\Delta_1^c \approx 0.33b_p$ for “blunting”, which are the averages across the entire set of simulation results for “screening” and “blunting”, respectively. For both crack configurations we find $\Delta_2^c/\Delta_1^c \approx 0.7$; this is not

4.6. Approximate model for prediction of the crack-tip dislocation emission

surprising because the ratio Δ_2^c/Δ_1^c is determined mainly by elasticity and so is not strongly dependent on Δ_1^c nor crack geometry. Using these pairs of values for all materials, and Ψ_{gsf} and Ψ_{nuc} for each specific material, we compute K_{Ie} via Eqs. 4.4-4.5 and obtain the results shown in Figures 4.14a,b. This approximate solution is again in very good agreement with the simulations across the entire range of materials. This estimate works well even when the Δ_1^c deviates from the above estimated value because (i) there is some cancellation of errors, (ii) $\Delta_2^c/\Delta_1^c \approx 0.7$ is retained, and (iii) K_{Ie} scales only with the square root of the critical energy.

The above approximation still requires computation of $\Psi_{nuc}(\Delta)$ for the specific crack tip geometry. A simpler model that depends only on the unstable stacking fault energy γ_{usf} and surface energy γ_s is very valuable since these quantities are easily computed via first-principles methods using simple periodic-cell geometries. We first recall that $\gamma_{step} \approx 0.7\gamma_s$. Then, the values $\Delta_1^c = 0.36b_p$, $\Delta_2^c/\Delta_1^c = 0.7b_p$ (and so $\Delta_2^c = 0.25b_p$) capture *both* “screening” and “blunting” well, for most of the studied materials. From Eq. 4.4 and a simple Peierls model, the contribution from the GSF energy is then $\Psi_{gsf}(0.25b_p) = 0.5\gamma_{usf}$. Again using a simple Peierls model, the contribution from the crack tip unit is $\Psi_{nuc}(0.36b_p) - \Psi_{nuc}(0.25b_p) = 0.7\gamma_{step} - 0.5\gamma_{step} = 0.14\gamma_s$. Therefore, a good analytic estimate of the critical energy release rate at the point of dislocation emission is $G_{Ie} = 0.14\gamma_s + 0.5\gamma_{usf}$. A small correction to this estimate precisely captures the average G_{Ie} across the entire set of simulations,

$$G_{Ie} = 0.145\gamma_s + 0.5\gamma_{usf} \quad (4.6)$$

Eq. 4.6 applies to systems with high step energies (the dominant case in real materials). The full model reduces to the Rice model as the step energy decreases, $K_{Ie} \rightarrow K_{Ie,Rice}$ as $\gamma_{step} \rightarrow \gamma_{usf}$ with $\gamma_s \approx \gamma_{usf}/0.7$ (see Peierls analysis and Table 4.3). Eq. 4.6 does not capture this limit, and should not be used when the surface energy/step energy are small. An analytic model that captures the correct limit is thus

$$G_{Ie} = \begin{cases} 0.145\gamma_s^e + 0.5\gamma_{usf}, & \gamma_s^e > 3.45\gamma_{usf} \\ \gamma_{usf}, & \gamma_s^e < 3.45\gamma_{usf} \end{cases} \quad (4.7)$$

Figure 4.15 shows the predictions of Eq. 4.7 for G_{Ie} along with the simulation results (screening and blunting). Also included are additional simulations and predictions for a family of pair-potentials having fixed γ_s and varying γ_{usf} [132], using full anisotropy not included in Ref. [132]. The agreement is very good across the entire spectrum of materials. The single analytical formula of Eq. 4.7, with K_{Ie} following from Eq. 4.5, is thus a suitable analytic replacement for the Rice model that incorporates the effect of the step energy and is based on a deeper understanding of the crack tip processes controlling dislocation nucleation.

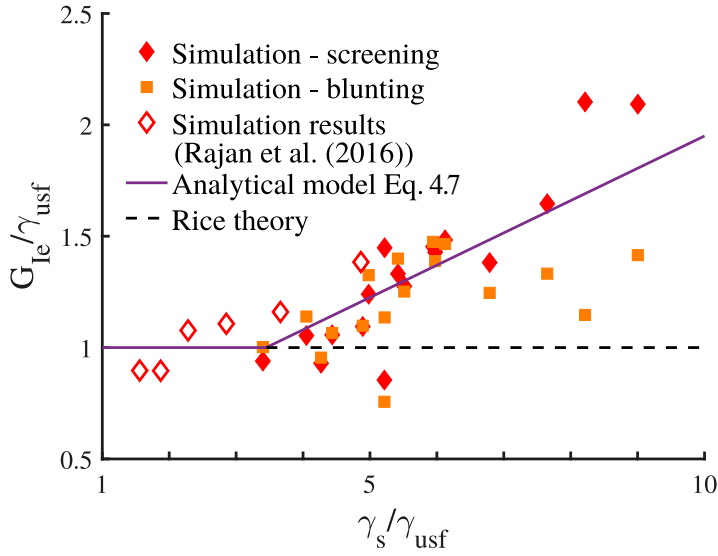


Figure 4.15 – Critical energy release rate G_{Le} as a function of the materials surface energy γ_s normalized by γ_{usf} for all materials studied here; Simulations - screening (red diamonds), Simulations - blunting (orange squares), Simulation results from [132] (open red diamonds), Analytical model Eq. 4.7 (purple line); Rice theory (black dashed line).

4.7 Discussion and concluding remarks

The Rice theory is an elegant, long-standing, and well-accepted model for the approximate analysis of dislocation emission at a crack tip under Mode I loading. However, we have shown that a new model is necessary for three important reasons. First, the Rice theory predictions for K_{Le} and Δ_1^c are inconsistent with detailed molecular simulations: the predicted K_{Le} is too low while the predicted Δ_1^c is too high, and these two deviations cannot be reconciled within the context of the Rice theory. Second, the Rice theory neglects entirely the energy associated with formation of the surface step upon emission, and simulations demonstrate clearly that such a step exists and that the energy cost is high compared to the unstable stacking fault energy. Third, explicit computation of the energy versus shear displacement at the crack tip shows no energy maximum, yet a maximum is required in the Rice analysis since the maximum sets the point of emission.

The new theory is based on the recognition that the crack tip structural unit is impeded from shearing by the energy cost of the step. The nascent dislocation is thus “trapped” by the lattice and can only be emitted when the crack tip structural unit reaches a point of mechanical instability. This instability is fundamentally different from the Rice concept, which envisions a continuous cohesive zone behavior with no “trapping”. We have demonstrated the physical behavior, and rationalized the simulation results, using a Peierls model for the nucleation energy at the crack tip and for the generalized stacking fault energy along the remainder of the slip plane. We can then

compute the critical energy release rate at the emission instability, from which we can find K_{Ie} . The simple Peierls model produces the trends seen in simulations and reduces to the Rice model when the step energy is zero. We have shown that the new theory, a simplified approximation, and an analytic model (Eq. 4.7), are in very good agreement with simulation results across 17 different fcc materials (interatomic potentials).

The present analysis fundamentally changes the dependence of the ductile-to-brittle transition on underlying material properties. A material is brittle when $K_{Ic} < K_{Ie}$. The standard analyses use the Griffith model $K_{Ic} = \sqrt{2\gamma_s\Lambda_{22}^{-1}}$, where Λ_{22}^{-1} is a material property for Griffith cleavage computed from Stroh energy tensor under Mode I, and use the Rice model $K_{Ie} = \sqrt{\gamma_{usf}o(\theta, \phi)/F_{12}(\theta)}$. The new analysis here shows that $\gamma_{s,e}$ (surface energy along the emission plane) also enters into the emission criterion. Using our simple analytic model (Eq. 4.7), the analysis predicts $K_{Ie} = \sqrt{(0.145\gamma_s + 0.5\gamma_{usf})o(\theta, \phi)/F_{12}(\theta)}$ for $\gamma_s/\gamma_{usf} > 3.45$. Thus, decreasing the surface energies of a material decreases both K_{Ic} and K_{Ie} , making embrittlement *less* likely.

The new model recently resolves a discrepancy found between molecular simulations and predictions of the standard brittle/ductile analysis in Mg [58]. In the standard analysis, cases involving slip along the basal plane of hcp Mg are predicted to emit dislocations ($K_{Ic} > K_{Ie}$) but which are observed to cleave in simulations. Although Mg has an hcp crystal structure, with a different elastic anisotropy, and although the fracture planes and slip planes differ, the present model remains applicable. Here, we apply the analytic model of Eq. 4.7 to compute K_{Ie} including the surface energy cost along the slip plane. The necessary energies are reproduced in Table 4.4. Predictions of K_{Ie} using the Rice analysis (see Ref. [58]) and the present model (Eq. 4.7) are also shown in Table 4.4, along with the simulation results for sharp cracks. In contrast to the standard analysis, the new model now correctly predicts all the observed cleavage cases ($K_{Ic} \leq K_{Ie}$), and retains the previous prediction of emission for the case where K_{Ic} is only slightly larger than K_{Ie} . Eq. 4.7 remains imperfect, and the competition between cleavage and emission in Mg is rather subtle, but nonetheless the incorporation of the surface/step energy into the analysis leads to predictions that are consistent with simulations. This demonstrates that the model is valuable for better assessment of brittle vs. ductile behavior.

In summary, a new model for emission based on a local crack tip mechanical instability has been shown to explain, conceptually and quantitatively, the crack tip emission process including the role of step formation at the crack tip. The model has been painstakingly validated across a wide range of fcc materials. Of great practical importance, we have provided an accurate analytic model (Eq. 4.7) that requires only easily-computable material parameters as input. In addition to its new insights into the physical origin of dislocation emission, this model provides a path for (i) designing new materials that exhibit the desired ductile behavior (dislocation emission), which is a necessary precursor to ductile fracture, and (ii) better understanding of chemical embrittlement due to a change in crack tip behavior from emission (ductile) to cleavage (brittle) behavior.

Crack plane	Orientation (m)[l]	γ_s (mJ/m^2)	Slip plane	$\gamma_{s,e}$ (mJ/m^2)	$\gamma_{s,f}$ (mJ/m^2)	K_{Ic} ($MPam^{1/2}$)	$K_{Ic,Rice}$ ($MPam^{1/2}$)	$K_{Ic,New}$ ($MPam^{1/2}$)	Rice prediction	New theory prediction	MD results
Prism I	$(\bar{1}010)[\bar{1}210]$	582	Basal	568	125	0.252	0.236	0.254	Emission	Cleavage	Cleavage
Prism II	$(\bar{1}2\bar{1}0)[1010]$	651	Basal	568	125	0.267	0.262	0.282	Emission	Cleavage	Cleavage
Pyramidal I	$(10\bar{1}0)[\bar{1}210]$	619	Basal	568	125	0.262	0.222	0.239	Emission	Emission	Emission
Pyramidal II	$(11\bar{2}2)[\bar{1}010]$	647	Basal	568	125	0.269	0.250	0.269	Emission	Cleavage	Cleavage

Table 4.4 – Crack tip cleavage/emission competition in magnesium as predicted from (i) Rice theory, (ii) The new theory for dislocation emission, and (iii) as observed in atomistic simulations. The values of material properties and simulations results are taken from [58].

5 New theory for crack-tip twinning in fcc metals

This chapter is extracted from the following publication:

- (1) Andric P, Curtin WA. New theory for crack-tip twinning in fcc metals. *Journal of the Mechanics and Physics of Solids*. 2018 Apr 1;113:144-61.

5.1 Introduction

Metals and alloys having an fcc structure (e.g. Al, Cu, Ni, Ag, Au, Pd, Pt, Ir) are widely used structural materials in different industrial applications. When an fcc metal is intrinsically ductile, a first (leading) partial dislocation nucleates, moves to an equilibrium distance, and leaves a stacking fault extending back to the crack tip (See Figure 5.1a). Ductile or quasi-brittle behavior is then determined by the subsequent crack tip event. The three possible processes are:

- (i) Emission of the trailing partial dislocation, nucleated on the same slip plane as the leading partial. The first and trailing partial dislocations combine to create a full dislocation having no trailing stacking fault, allowing the full dislocation to move far from the now-blunted crack tip (see Figure 5.1b); this behavior is deemed “ductile”.
- (ii) Emission of the twinning partial dislocation having the same character as the first one but occurring on an immediately adjacent plane. This creates a two-layer twin embryo, with both partial dislocations remaining in the vicinity of the crack tip (see Figure 5.1c); this behavior is deemed “quasi-brittle” since the process does not create far-field plasticity.
- (iii) Emission of a partial dislocation having the same character as the first partial dislocation but occurring on a nonadjacent slip plane (see Figure 5.1d). Again, the emitted partial dislocation stays in vicinity of the crack tip, creating a region of two stable stacking faults separated by at least one plane of fcc atoms. This case is rare, and further increase of the applied load leads to another emission event that creates a three-layer twin embryo similar

to what follows from process (ii); this behavior is thus also deemed “quasi-brittle”.

Understanding the fundamental competition between the processes of twinning and trailing partial emission thus provides insights into the controlling material parameters, which then contributes to ensuring ductile behavior when designing new alloys [57].

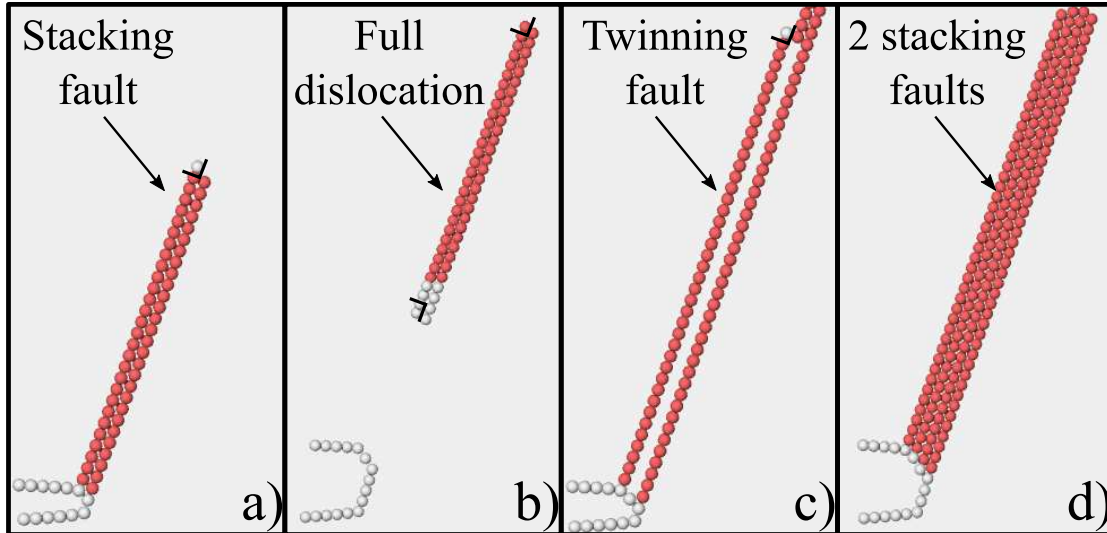


Figure 5.1 – Partial dislocations emitted from a crack tip in a fcc metal: a) First partial dislocation at some equilibrium distance with the stacking fault behind it; b) First and trailing partial dislocation forming the full dislocation with the stacking fault between them; c) Twinning fault formed by the emission of the twinning partial dislocation; d) Region of two stacking faults formed by the second dislocation emission on the nonadjacent slip plane. Only non-fcc atoms are presented and colored according to Common Neighbour Analysis [15]; red for hcp and white for other.

Chapter 3 provides an overview of (i) Rice and (ii) Tadmor-Hai continuum theories for predicting critical stress intensity factors for the emission of the first K_{Ie}^{first} and trailing partial dislocation K_{Ie}^{trail} [50], and twinning partial dislocation K_{Ie}^{twin} [94], respectively. Molecular statics and dynamics simulations have shown that these models are reasonable, but not highly accurate, for predicting the various K_{Ie} . Chapter 4 has demonstrated that the creation of a surface step during the first partial emission was a missing factor in the Rice theory; therefore, we proposed a new theory for computing K_{Ie}^{first} . The Tadmor-Hai model, based on the Rice approach, is quantitatively even less accurate for twinning tendencies. Also, the Tadmor-Hai twinning tendency predicts the emission of the trailing partial prior to twinning in some of materials while molecular statics simulations always show twinning [103]. With the new insights into a completely different mechanism for the first emission process (see Chapter 4), the processes of twinning and trailing emission of the second partial can now be revisited from a different perspective.

Here, we show that there is no creation of a surface step during the emission of the twinning

partial. This suggests that the basic framework of Tadmor-Hai model for twinning is viable. We then show, however, that because the twinning slip plane does not intersect the crack front, the resolved shear stress along that plane at the location of the twin nucleation is lower than the shear stress along the trailing slip plane. Correcting for this difference by relating the far-field applied K_I to the local shear displacement along the twinning plane leads to predictions in excellent agreement with the simulations, rectifying the previous deviations of 20-35%. Using the same local analysis, we show that emission of the trailing partial dislocation is always accompanied by the creation of the surface step. Applying the new theory presented in Chapter 4 to the case of trailing emission, we predict $K_{Ie}^{trail} > K_{Ie}^{twin}$ for all simulations, resolving the discrepancy between previous theory and simulation. Finally, we reveal an alternative mechanism of twinning wherein the crack first advances by cleavage and then emits the twinning partial, such that twinning is controlled by the Griffith cleavage fracture stress intensity K_{Ic} , where $K_{Ie}^{first} < K_{Ic} < K_{Ie}^{twin}$, in agreement with simulations where this process controls twinning. Furthermore, for subsequent emission of twinning partials after the first event, the twinning is often controlled by this alternative mechanism, thus connecting the process of extensive twinning directly to the process of cleavage fracture.

5.2 Tadmor-Hai theory versus atomistic simulations

The accuracy of Tadmor-Hai theory versus molecular statics simulations is examined using the standard "K-test". An fcc crystal is oriented with $X_1 = [\bar{1}\bar{1}2]$, $X_2 = [111]$, $X_3 = [\bar{1}10]$ forming a crack with a slip plane inclined to the angle $\theta = 70.53^\circ$ to the crack and with the Burgers vector angle $\phi_{first} = 0^\circ$. Same crystal orientation is used in Section 4.2.3 since it provides the easiest emission of an edge dislocation along a single slip plane. A traction free crack surfaces is created using "screening"; here we do not use "blunting" since we have shown that "screening" better represents an atomically sharp crack for the emission in Mode I (see Chapter 4). To capture only the crack tip effects without the shielding due to the first partial dislocation we first displace the part of the non-loaded perfect crystal, marked with the red line (see Figure 5.2), along the leading partial slip direction by the partial Burgers vector $b_p = a_0/\sqrt{6}$, where a_0 is a lattice parameter. This method is equivalent to actually nucleating the partial, moving it to infinity by adding a dipole of infinite spacing, and then unloading the crystal to zero load. Since the crack surfaces are already formed by screening of interactions, the crystal is stable in this new initial configuration. We will consider results including the shielding effects later. The crack is loaded in a standard manner by imposing atomic displacement using Eq. 2.19. All other simulation details are as presented in Section 2.4.4.2. We analyze 17 different fcc materials described by EAM interatomic interaction (see Subsection 4.2.1). We terminate the simulation after second partial emission occurs.

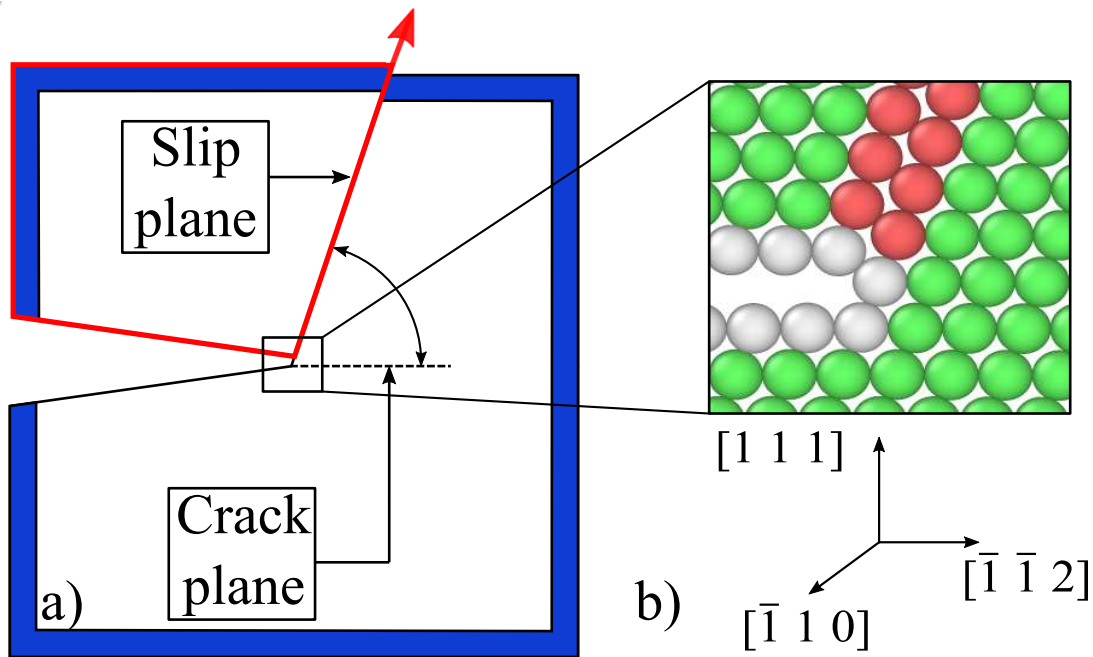


Figure 5.2 – a) Geometry used to simulate second partial dislocation emission using a semi-infinite crack with the first partial dislocation removed to infinity, achieved by displacing the region marked by the red line by the first partial Burgers vector. Blue color indicates boundary atoms. b) Atomic scale crack-tip geometry at zero loading. Atoms are colored based on Common Neighbour Analysis [15]; green for fcc, red for hcp and white for surface.

In every material studied, we observe twinning. In contradiction with the simulations, the Tadmor-Hai theory predicts emission of the trailing partial prior to emission of the twinning partial for Al M, Cr100 and Cr90, both with and without the shielding effect. Since the shielding effect only changes the stress intensity acting on the crack tip, and not the critical values for the two processes, this is not a surprising result. The discrepancy for Al [81] (Al M) was noted by Yamakov et al. [103], as well. Furthermore, the simulations show two different twinning mechanisms. As shown in Figure 5.3b, one mechanism is twinning partial emission by sliding along the adjacent slip plane behind the leading partial slip plane (denoted “back” twinning). As shown in Figure 5.3c, a second mechanism forms the micro-twin by crack advancement of one lattice spacing in direction followed by sliding along the adjacent plane in front of the leading partial (denoted “forward” twinning). The “forward” twinning occurs in Ag, and Cr10-Cr33, while all other materials tested show “back” twinning. These two different twinning modes were first observed in atomistic simulations of Hai and Tadmor [117]. However, the later Tadmor-Hai theory [94] does not distinguish between these two physically different events. Because “forward” twinning resemble Griffith cleavage followed by dislocation emission, the Tadmor-Hai model is essentially a model for “back” twinning.

5.2. Tadmor-Hai theory versus atomistic simulations

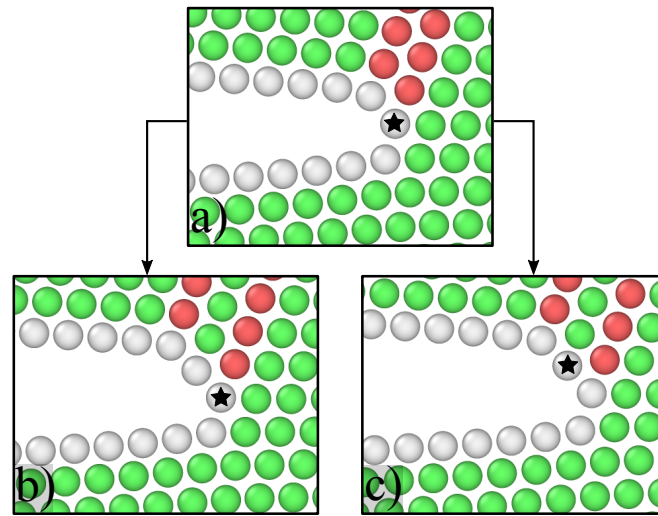


Figure 5.3 – a) Crack geometry in Mode I at the critical load for the emission of the twinning partial dislocation. b) Crack geometry after “back” twinning emission. c) Crack geometry after “forward” twinning emission. The same atom at the original crack tip is indicated in all figures to show the two different mechanisms.

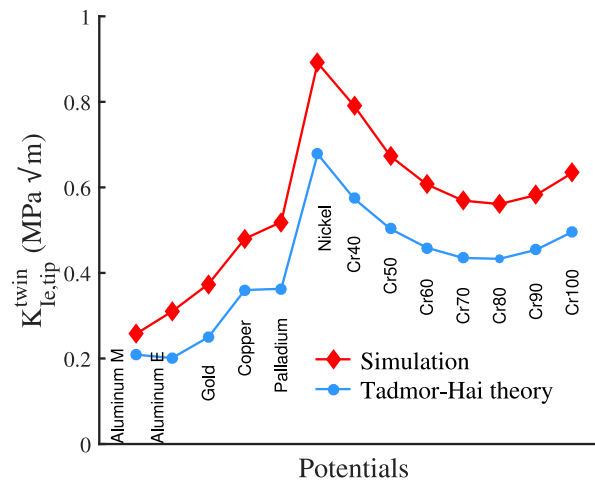


Figure 5.4 – Critical stress intensity factor for emission as observed in the simulations (red diamonds), along with the predictions of continuum theories based on the Peierls model (blue circles) for the “back” twinning partial dislocation .

Figure 5.4 shows the simulated critical stress intensity factor along with the Tadmor-Hai predictions (Eq. 3.8) for all “back” twinning cases. Figure 5.4 shows that the predictions are systematically lower than the simulations by 20-35%. However, the theoretical predictions do follow the trend observed in the simulations, unlike the situation for the first partial dislocation emission (Figure 4.4a). The systematic and significant deviation of the Tadmor-Hai theory requires the development of a new theory. Following our recent discrete analysis of the first partial

emission, below we examine the detailed local processes and location of the actual nucleation event. The analysis reveals both the source of the discrepancy with previous models and motivates a new model that quantitatively captures the observed behavior.

5.3 Energy changes near the crack-tip during second partial dislocation emission

We start by investigating the energy changes during slip in the structural units near the crack tip that are relevant for the emission of twinning and trailing partial dislocation. A schematic of the discrete analysis is shown in Figure 5.5a, showing two adjacent discrete slip planes surrounded by an elastic material containing a crack. The two slip planes are further envisioned to be composed of individual structural units defined by specific triads of atoms, as indicated. Figure 5.5b shows a close-up atomistic view of the crack tip region, and specifically identifies the three structural units that are crucial to our subsequent analysis: one unit directly at the crack tip relevant for trailing partial emission and two units along the nascent twinning plane.

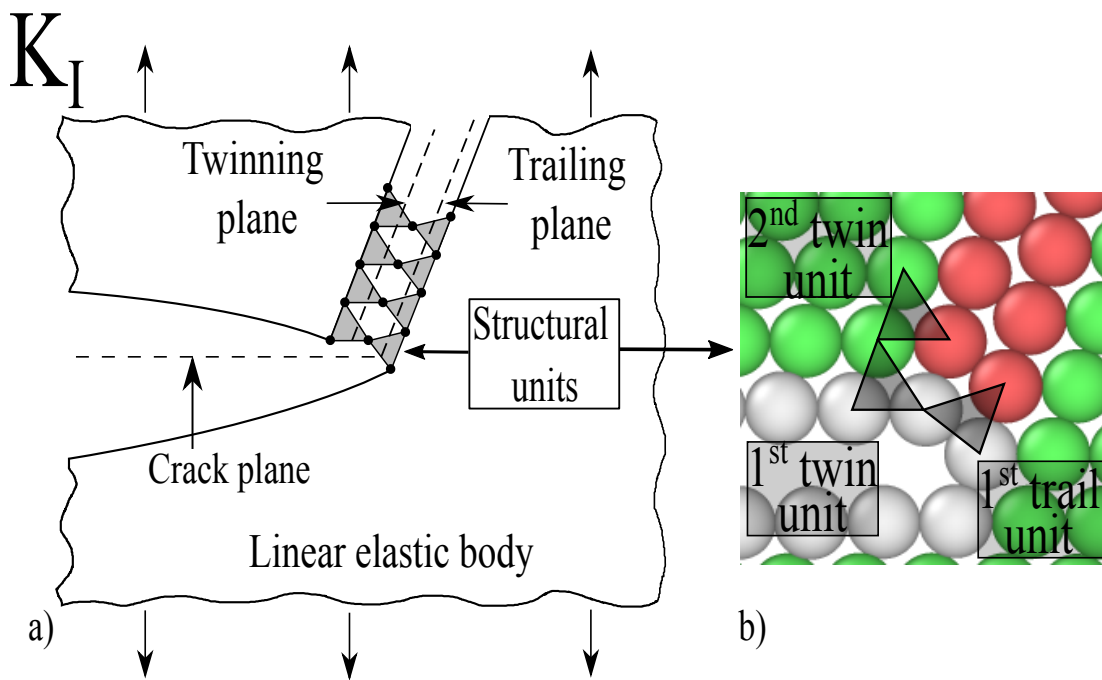


Figure 5.5 – a) Linear elastic body with semi-infinite crack under Mode I loading with embedded slip planes for analysis of the emission of the trailing and twinning partial dislocations. The slip planes are characterized by atomic structural units. b) The three structural units that control emission of the second partial dislocation.

Atom-by-atom energy changes are measured along the two possible slip planes in a manner similar to that introduced in Section 4.3. Identifying such atomic energies are only possible when

5.3. Energy changes near the crack-tip during second partial dislocation emission

using interatomic potentials where the total energy is represented as a sum of atomic energies. More complex approaches would be needed to localize the measured total energy changes when computed using quantum mechanical methods; Zamora et al. [97] have headed in such a direction for the specific problem of step energies. The cell size, orientation, boundary conditions and the minimization procedure are identical to those used in Section 4.3 for computing the nucleation energy for the emission of the first partial Ψ_{first} . The difference is in the initial configuration for which we use the completely relaxed crystal containing a stacking fault (see Figure 9a). We then rigidly slide a portion of the left part of the crystal in the desired slip direction. When the sliding plane is the twin plane, sliding is continued until the full two-layer twinning fault is formed. When the sliding plane is the original stacking fault plane, sliding is continued until the stacking fault is eliminated, which represents the emission of the trailing partial dislocation. During sliding, we compute the energy change of each individual atom in the domain as $\delta E^{atom} = E^{atom}(\Delta) - E^{atom}(\Delta = 0)$, where $E^{atom}(\Delta)$ is the atomic energy at slip displacement magnitude Δ in the slip direction.

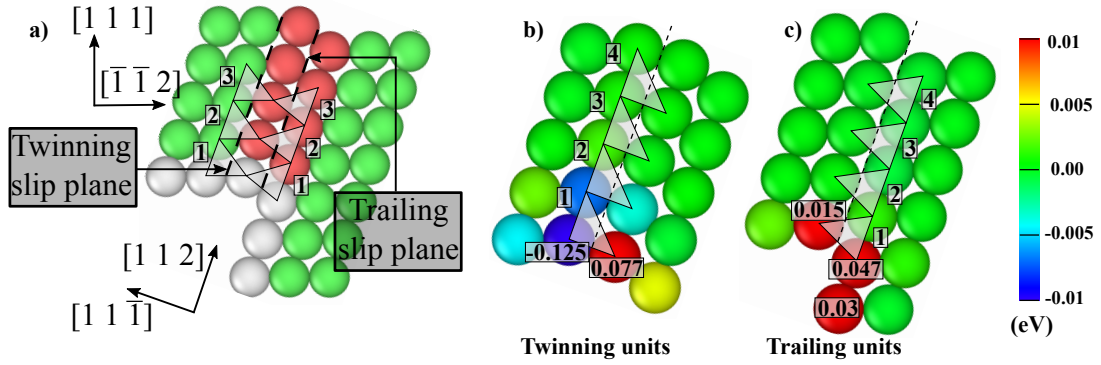


Figure 5.6 – a) Initial configuration of the computational domain used to compute atom-by-atom energy changes due to relative shear displacement along the trailing or twinning slip plane. Energy change per atom after subtraction of the energy changes per atom corresponding to the bulk GSF and GTF energies per atom, showing the energy changes due to surface effects near the crack tip for b) the twinning partial and c) the trailing partial, at relative slip $\Delta = b_p/2$. Atoms in (a) are colored by Common Neighbour Analysis [15] (green for fcc, red for hcp and white for surface); Atoms in (b) and (c) are colored according to energy change shown by the scale. Energies of atoms near the crack tip are off scale, and indicated in each figure.

The crack-tip dislocation emission influences the energies only near the crack tip, for both twinning and trailing partial emission. This is demonstrated by subtracting the atom-by-atom energy changes for the GSF and GTF sliding from the measured $E^{atom}(\Delta)$, as shown in Figure 5.6b and c, at shear displacement $\Delta = b_p/2$. For both twinning partial and the trailing partial emission, (i) the energy change of the crack-tip/surface atoms differs significantly from the response away from the crack-tip/surface and (ii) the energy changes relative to bulk response are almost negligible immediately away from the crack-tip/ surface. The per-atom energy change is crucial, but not sufficient to provide insights into the emission process. Therefore, we examine

the energy change of the basic structural units along the slip plane as indicated in Figure 5.6. We compute the energy change of structural unit i as $\delta E_i^{unit} = \sum_j \delta E_j^{atom}$, where δE_j^{atom} is the contribution of atom j belonging to unit i , with the total energy change of atom j shared equally between units to which it belongs. The energy due to one surface atom adjacent to the first crack-tip trailing unit must also be added to the energy of that first unit (see Figure 5.6c). The slip energy per unit sliding area is then obtained as by dividing by the area per structural unit in the $[112] \times [\bar{1}10]$ slip plane, $\delta E_i^{unit}/(\sqrt{3}a_0^2/4)$. The author is taking an opportunity to point out to a minor typo that has appeared in the original paper where lattice parameter a_0 to the power of two was accidentally omitted.

The energies to shear each structural unit along the twinning and trailing slip planes, denoted as Ψ_i^{twin} and Ψ_i^{trail} ($i = 1, 2, \dots, n$), are shown in Figure 5.7. Both $\Psi_1^{twin}(\Delta)$ and $\Psi_1^{trail}(\Delta)$ are notably different than all other units, $\Psi_{i \geq 2}^{twin}(\Delta)$ and $\Psi_{i \geq 2}^{trail}(\Delta)$. Furthermore, all other units exhibit essentially the bulk response $\Psi_{i \geq 2}^{twin}(\Delta) \approx \Psi_{gtf}^{twin}(\Delta)$, and $\Psi_{i \geq 2}^{trail}(\Delta) \approx \Psi_{gsf}^{trail}(\Delta)$. The $\Psi_2^{trail}(\Delta)$ is slightly different than the $\Psi_{gsf}^{trail}(\Delta)$ presented in Figure 3.1 because there are small additional contributions to $\Psi_{gsf}^{trail}(\Delta)$ from the next two planes of atoms just above/below the two planes of atoms immediately adjacent to the slip plane. Thus, the energy change along the slip plane is in fact nearly $\Psi_{gsf}^{trail}(\Delta)$ but this is slightly underestimated by only considering the energy change $\Psi_2^{trail}(\Delta)$ of the atoms in the as-defined second structural unit; this difference has no effect on our main results. Several important features emerge from Figure 5.7. First, the energy of the first structural unit for the twinning process is much smaller than for the bulk twinning process, $\Psi_1^{twin}(\Delta) \ll \Psi_{gtf}^{twin}(\Delta)$. Thus, during twin partial emission, there is no creation of the step and in fact a decrease in the local surface energy due to atomic rearrangements. The first twinning unit is therefore very easily sheared. Emission of the twin partial requires, however, continued shearing further along the twin plane, and this shearing is controlled by $\Psi_{i \geq 2}^{twin}(\Delta) \approx \Psi_{gtf}^{twin}(\Delta)$. Second, the energy for slip of the first trailing unit is always accompanied by additional step energy and so, as for the first partial, is far above the bulk GSF energy, $\Psi_1^{trail}(\Delta) \gg \Psi_{gsf}^{trail}(\Delta)$. The step energy for the trailing partial is smaller than that for the first partial (see Figure 4.6) because the trailing partial has a screw component along the crack front that does not contribute to step formation (see also Schoeck [123]), but it remains significant and cannot be neglected. Note that zero energy for these cases corresponds to the crystal with the stacking fault (after emission of the first partial dislocation) and so, since the trailing dislocation annihilates the stacking fault, the final energies are lowered and $\Psi_{gsf}^{trail}(\Delta = b_p) = -\gamma_{ssf}$. Due to the smaller step energy and $\Psi_{gsf}^{trail} < 0$ for $\Delta < 3b_p/4$, Ψ_1^{trail} does have a maximum value but well above the γ_{usf} . Third, the final value of $\Psi_1^{trail}(\Delta = b_p)$, denoted as γ_{step}^{trail} , is $\gamma_{step}^{trail} = (0.35 \pm 0.03)\gamma_s$ for all materials tested; this value is one-half the step energy for first partial emission $\gamma_{step}^{first} \approx 0.7\gamma_s$. All the above properties are shown for the particular case of Ni in Figure 5.7 but are observed in all other materials studied here.

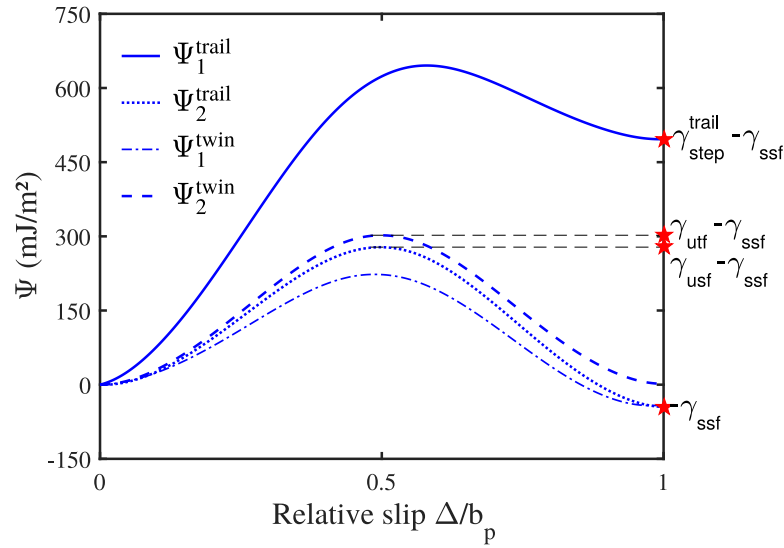


Figure 5.7 – Slip energy change (per unit area) vs. shear displacement of the first trailing unit (solid line), first twinning unit (dashed-dotted line), second twinning unit (dashed line), and second trailing unit (dotted line), computed for fcc Ni [81]. The second twinning unit and second trailing unit are negligibly different from the bulk GSF and GTF energies.

The above observations reveal the mechanisms for the second partial emission, as follows. Emission of the twinning partial dislocation is controlled not by the very soft first twin unit but by the *second* twinning unit, which responds like the bulk $\Psi_{gtf}^{twin}(\Delta)$ with no step energy. Thus, the Tadmor-Hai theory can be applied for predicting K_{Ie}^{twin} but with a modification because the second crack tip unit *is not at the crack tip*. Second, emission of the trailing partial dislocation is similar to emission of the first partial, being controlled by the mechanical instability at high step energies and reducing to the Rice criterion for low step energies. These mechanisms then motivate a new theory for twin emission and use of the theory presented in Chapter 4 for trailing emission, as discussed below.

5.4 New theory for crack-tip twinning

The energy analysis in the previous section shows that it is the second twinning unit that controls the emission of the twinning partial dislocation. However, this key unit is not at the crack tip, and so the Tadmor-Hai theory cannot be applied directly. The Tadmor-Hai theory assumes that the driving force for emission is K_I , just as for the first partial and trailing partial, and neglects the fact that the twinning plane does not intersect the crack tip. In fact, the stresses acting on the twinning plane differ from those acting on the stacking fault plane, and this difference must be incorporated into the theory.

Specifically, to use the Tadmor and Hai model to predict $K_{Ie,tip}^{twin}$ we must relate the far-field

Chapter 5. New theory for crack-tip twinning in fcc metals

applied K_I to the *local stress* acting on the *second twinning unit*. Assuming linear elasticity, at any applied K_I the ratio of the shear displacement on the trailing unit (at the crack tip) to the shear displacement on the second twinning unit is some constant that depends only on the elastic constants C_{ijkl} ,

$$\frac{\Delta_1^{trail}}{\Delta_1^{twin}} = f^{(1)}(C_{ijkl}). \quad (5.1)$$

For all the fcc materials studied here, and $\theta = 70.5^\circ$, we find $f^{(1)}(C_{ijkl}) = 1.3 - 1.42$ where the superscript “1” denotes the first twinning emission (see below). For other crystal orientations we find that the parameter $f^{(1)}(C_{ijkl})$ varies only slightly, as shown for Ni in Appendix A.6. Therefore, to achieve the necessary critical displacement $\Delta_{2,c}^{twin}$ for twinning at the second structural unit requires an applied stress intensity that is a factor $f^{(1)}(C_{ijkl})$ larger than the stress intensity required to attain the same displacement *at the crack tip*. The critical stress intensity for twinning at the second structural unit is thus larger than that predicted by Tadmor and Hai by the factor $f^{(1)}(C_{ijkl})$. The new criterion for the applied stress intensity for twinning is then simply

$$K_{Ie,tip}^{twin} = f^{(1)} \sqrt{(\gamma_{utf} - \gamma_{ssf})o(\theta, \phi_{first})/F_{12}(\theta)}. \quad (5.2)$$

Figure 5.8 shows the predictions of Eq. 5.2 for all materials exhibiting “back” twinning, and excellent quantitative agreement is found. The accuracy of the new theory for different slip plane inclination angles is further examined in Appendix A.6; very good agreement is again obtained.

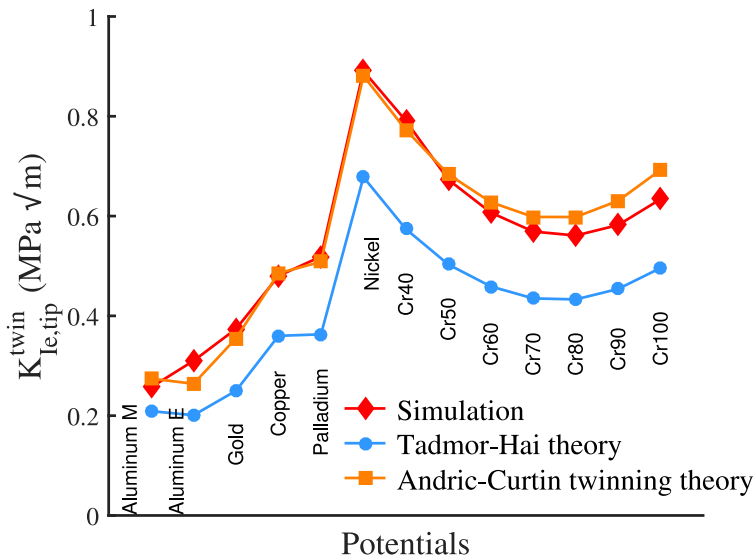


Figure 5.8 – Critical stress intensity factor for emission as observed in the simulations (red diamonds), along with the predictions of continuum theories based on the Peierls model (blue circles), and the Andric-Curtin theory (orange squares) for the “back” twinning partial dislocation.

The above analysis neglects the shielding effect due to the first partial dislocation emission. The

5.5. Trailing partial emission: why twinning is observed in all simulations

shielding by the first partial negative contribution (shielding) adds to the applied stress intensity to give the total crack tip stress intensity. The above crack tip analysis remains valid for controlling the emission process. Therefore, in the presence of the first partial, the remote applied stress intensity factor for “back” twinning is

$$K_{Ie}^{twin} = f^{(1)} \left(\sqrt{(\gamma_{utf} - \gamma_{ssf})o(\theta, \phi_{first})/F_{12}(\theta) + k_I^d + \frac{F_{22}(\theta)}{F_{12}(\theta)}k_{II}^d} \right). \quad (5.3)$$

We have simulated the emission of the second partial dislocation in the presence of the first partial dislocation. The position of the first partial as a function of the applied stress intensity is an outcome of the simulation. Figure 5.9 shows the predictions of Eq. 5.3 against the simulation results for all materials showing “back” twinning, and excellent agreement is again obtained. Note that there is no result for Al E [124], because this potential switches from “back” to “forward” twinning in the presence of the first partial dislocation. A possible reason for this change is discussed in Section 5.6. The results in Figure 5.9 reaffirm the accuracy of the detailed local crack-tip analysis of the twinning process.

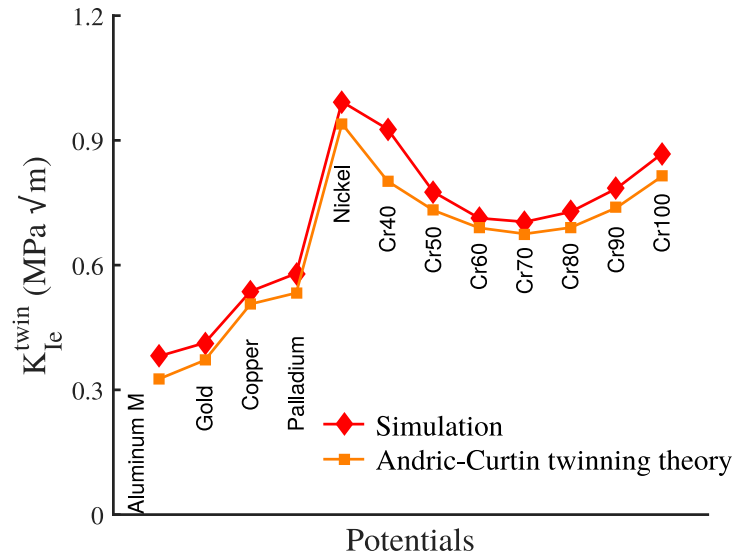


Figure 5.9 – Critical stress intensity factor for the emission of the “back” twinning partial dislocation including the effect of shielding due to the first partial dislocation, as observed in the simulations (red diamonds) and as computed by the new twinning theory (orange squares).

5.5 Trailing partial emission: why twinning is observed in all simulations

We now address why simulations show that twinning is always preferred when $\phi_{first} = 0$. Twinning occurs when $K_{Ie}^{twin} < K_{Ie}^{trail}$. Above we predicted K_{Ie}^{twin} accurately, and therefore we must now assess K_{Ie}^{trail} . The energy analysis in Figure 5.7 shows that the step energy during

Chapter 5. New theory for crack-tip twinning in fcc metals

trailing emission is significant, and this necessitates the application of the new theory for crack-tip dislocation emission (see Chapter 4) for predicting K_{Ie}^{trail} .

Material	Twinning partial $K_{Ie,tip}^{twin}$ (MPa \sqrt{m})	Trailing partial $K_{Ie,tip}^{trail}$ (MPa \sqrt{m})	Ratio $\gamma_s/(\gamma_{usf} - \gamma_{ssf})$
Al [81]	0.274	0.358	39.06
Al [124]	0.264	0.377	39.06
Au [126]	0.355	0.406	8.66
Ag* [126]	0.382	0.474	5.29
Cu [125]	0.485	0.608	10.54
Pd [126]	0.508	0.615	10.05
Ni* [81]	0.881	1.035	6.73
Cr10* [127]	1.142	1.443	3.86
Cr20* [127]	1.002	1.240	4.69
Cr33* [127]	0.842	0.997	6.22
Cr40 [127]	0.772	0.896	7.26
Cr50 [127]	0.684	0.789	9.42
Cr60 [127]	0.628	0.722	12.42
Cr70 [127]	0.598	0.677	16.74
Cr80 [127]	0.598	0.660	21.73
Cr90 [127]	0.630	0.671	25.03
Cr100 [127]	0.692	0.705	25.22

Table 5.1 – Predicted critical stress intensities for twinning (Eq. 5.2) and trailing (Eq. 5.5) partial dislocation emission, for 17 fcc materials. The ratio of surface energy to unstable minus stable stacking fault energy is shown, and the Rice theory is applicable when this value is below 6.9, as indicated for those materials marked by an asterisk.

We first recall the analytical expression for G_{Ie}^{first} (Eq. 4.7). Furthermore, the step energy is sufficiently high, $\gamma_{step}^{trail} \ll (\gamma_{usf} - \gamma_{ssf})$ (see Table 5.1), in most materials studied and $\gamma_{step}^{trail} = \gamma_{step}^{first}/2$. We thus substitute this latter expression into Eq. 4.7 and also replace γ_{usf} by $\gamma_{usf} - \gamma_{ssf}$ in Eq. 4.7, leading to

$$G_{Ie}^{trail} = \begin{cases} 0.0725\gamma_s^e + 0.5(\gamma_{usf} - \gamma_{ssf}), & \gamma_s^e > 6.9(\gamma_{usf} - \gamma_{ssf}) \\ (\gamma_{usf} - \gamma_{ssf}), & \gamma_s^e < 6.9(\gamma_{usf} - \gamma_{ssf}) \end{cases} \quad (5.4)$$

The critical stress intensity factor for the emission of the trailing partial dislocation K_{Ie}^{trail} is then easily computed as

$$K_{Ie,tip}^{trail} = \sqrt{G_{Ie}^{trail} o(\theta, \phi)/F_{12}(\theta) \cos \phi_{trail}} \quad (5.5)$$

Using Eq. 5.5 to predict K_{Ie}^{trail} , we find $K_{Ie,tip}^{twin} < (K_{Ie,tip}^{trail})_{new}$ for all materials showing “back” twinning, in a perfect agreement with simulations (see Table 5.1). Note that Eq. 5.4 also captures the correct limit with respect to the ratio $\gamma_s/(\gamma_{usf} - \gamma_{ssf})$, where the Rice theory for K_{Ie}^{trail} is applicable for materials with a low step energy. Since emission of the trailing partial never

happens at $T=0K$, we cannot prove the quantitative accuracy of Eq. 5.5 but it is consistent with all simulations. As for the analysis of twinning, careful attention to the local crack-tip energetics provides crucial insights for understanding of the mechanics of the crack-tip dislocation emission.

5.6 Forward twinning and twin thickening in fcc metals

Both the Tadmor-Hai theory and the new theory for crack-tip twinning are appropriate for predicting K_{Ie}^{twin} when “back” twinning occurs. As noted earlier, the process of “forward” twinning can occur by crack advancement by one lattice spacing followed by sliding along the twin plane at the new crack tip (see Figure 5.3c). At $T = 0K$, the crack growth process requires attainment of the Griffith critical stress intensity K_{Ic} for cleavage. “Forward” twinning thus occurs for materials where $K_{Ic} < K_{Ie}^{twin}$, with K_{Ie}^{twin} computed via Eq. 5.2. That is, before “back” twinning can occur, the crack cleaves and the stress intensity is sufficient to nucleate the twinning dislocation at the new crack tip ahead of the original stacking fault plane. Figure 5.10a shows that Ag, Cr10 and Cr20 satisfy the criteria for “forward” twinning and these are indeed all cases where forward twinning is observed. The Cr33 material also shows “forward” twinning in simulations even though $K_{Ic} > K_{Ie}^{twin}$, but the difference is quite small and discrepancies may arise due to non-linear effects that are absent from our models. The standard Tadmor-Hai is unable to distinguish between “back” and “forward” twinning, and predictions using Eq. 3.8 yield $K_{Ic} > K_{Ie}^{twin}$ for all materials, indicating that “back” twinning would be expected in all cases. The ability to distinguish between two different twinning modes provides additional support for the qualitative and quantitative accuracy of the analysis and models (Eqs. 5.2 and 5.3) presented in this chapter.

The recognition of the different processes of “back” and “forward” twinning now changes our understanding of further crack-tip twinning, after the first twin partial emission, as follows. “Back” twinning for the second twin partial, thickening the twin by one additional layer, would occur by nucleation even further from the crack tip than for the first “back” twin nucleation. Being further from the crack tip necessitates a higher applied K_I to reach nucleation even though the underlying process remains the same. In other words, the scaling factor $f^{(2)}(C_{ijkl})$ for second “back” twin partial emission is larger than the value $f^{(1)}(C_{ijkl}) = 1.3 - 1.42$ for the first “back” twin partial. Each subsequent “back” twinning partial thus requires further increases in applied K_I . At some point, the applied K_I reaches K_{Ic} , after which the twin process changes to thickening by the “forward” twinning mechanism. Assuming that the sharp crack cleavage value of K_{Ic} applies independent of the evolving shape of the crack tip as the twin thickens, and ignoring for the moment the shielding effects of the twinning dislocations, the “forward” twinning occurs at the n^{th} twin emission for which

$$f^{(n)}(C_{ijkl})\sqrt{(\gamma_{utf} - \gamma_{ssf})o(\theta, \phi_{first})}/F_{12}(\theta) > K_{Ic} \quad (5.6)$$

Since the $f^{(n)}$ grow rapidly ($f^{(1)} \sim 1.4$; $f^{(2)} \sim 1.7$; $f^{(3)} \sim 2.0$), the onset of “forward” twinning is expected after only a few “back” twinning events. Figure 5.10b shows the Griffith

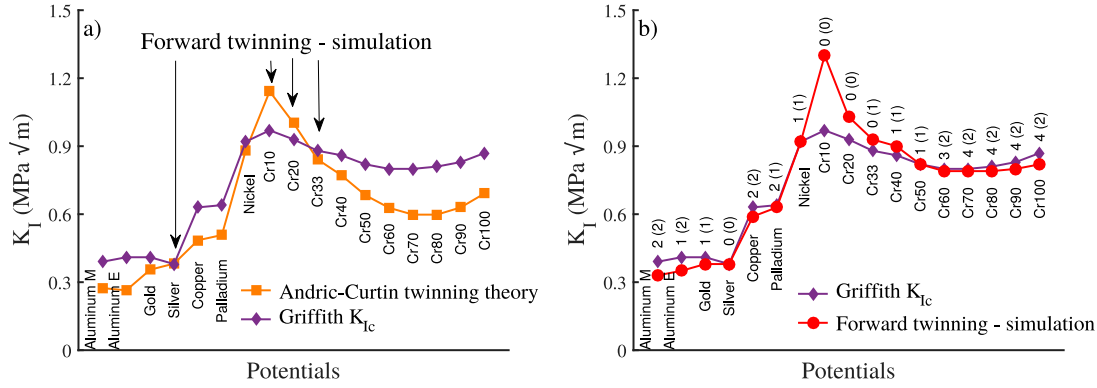


Figure 5.10 – a) Critical stress intensity factor for Griffith cleavage K_{Ic} (purple diamonds) and predicted “back” twinning partial emission $K_{Ic,tip}^{twin}$ (orange squares); forward emission is predicted when $K_{Ic} < K_{Ic,tip}^{twin}$ and the cases where forward twinning is observed in simulations are indicated. b) Critical stress intensity factor for Griffith cleavage K_{Ic} (purple diamonds) and simulated value of the critical stress intensity at the onset of “forward” twinning (red circles), showing that forward twinning starts at K_{Ic} . The number of “back” twinning events prior to “forward” twinning is indicated for each material, as observed in simulation and, in parentheses, as predicted by Eq. 5.6

value for cleavage along with the simulation stress intensity factor at which “forward” twinning occurs, without shielding effects due to previously-emitted partial dislocations. The onset of “forward” twinning occurs at an applied K_I very close to the Griffith cleavage K_{Ic} . The only exception is the Cr10 material where “forward” twinning occurs high above K_{Ic} ; this is due to some rearrangement of crack-tip atoms that delays “forward” twinning emission although the cleavage process starts developing at K_I very close to K_{Ic} . Figure 5.10b also indicates the number of “back” twinning partial dislocations prior to “forward” twinning as observed in the simulations and as estimated by Eq. 5.6 (given in parentheses). The predictions are in a very good agreement with the simulations for most of the materials studied here. The number of “back” twinning partials observed in the Cr70-Cr100 materials is larger than estimated via Eq. 5.6; this discrepancy may arise because of changes to the crack tip geometry being more important for these materials. These results confirm that our analysis captures the change from “back” to “forward” twinning with good accuracy.

As noted earlier, previously-emitted partial dislocations act to shield the crack tip. This shielding occurs for both emission and cleavage processes. Ignoring mix-mode cleavage, the onset of “forward” twinning can be estimated to occur at the n^{th} twinning event, where n satisfies

$$f^{(n)}(C_{ijkl}) \left[\sqrt{(\gamma_{utf} - \gamma_{ssf})o(\theta, \phi_{first})}/F_{12}(\theta) + \sum_{i=1}^n \left(k_I^d + \frac{F_{22}(\theta)}{F_{12}(\theta)} k_{II}^d \right) \right] > K_{Ic} + \sum_{i=1}^n k_I^d$$

(5.7)

for any twin dislocation array, $k_{II}^d \propto k_I^d$ while $f^{(n)} > 1$. Therefore, the onset of “forward” twinning should occur sooner (smaller n) in the presence of the shielding that exists in the real situation.

After the cleavage event, the “forward” twinning process is similar to the first emission process, involving step creation. The “forward” twinning should be slightly easier, $K_{Ie}^{forward} < K_{Ic}$, since the process eliminates the stacking fault in favour of the twinning faults rather than creating a stacking fault. Therefore, since the first partial emission necessarily satisfies $K_{Ie}^{first} < K_{Ic}$, the entire twinning process is ultimately controlled by the conditions established for first partial emission. The brittle/quasi-brittle transition is then truly determined by the conditions for the first partial emission, even though increasing applied stress intensity factors are required to drive subsequent twinning! And, the quasi-brittle domain actually intimately involves the cleavage process – the crack begins to cleave but then is able to immediately emit another twinning partial dislocation, leading to additional shielding.

Finally, crack tip cleavage may require local crack tip stress intensities that differ slightly from K_{Ic} . Cleavage above K_{Ic} at $T = 0K$ can occur due to lattice trapping [79]. Probably of more importance is that, as twinning (or trailing partial) emission evolve, the shape of the crack tip changes and this changes the stresses acting around the crack tip. The influence of the crack shape on at the atomic scale was first analysed by Gumbsch [55]. The twinning process leads to the development of a wedge shape, which then involves stress concentrations at the two corners and a differently-oriented crystal in the twinned region. If the cleavage process requires local stresses different than those for the sharp crack, then this factor must be embedded into an effective value of K_{Ic} to be used in the analyses discussed here.

5.7 Concluding remarks

A new theory for predicting the critical stress intensity factor for crack-tip twinning in fcc metals has been presented. The discrete analysis of energetic changes where the actual nucleation takes place is again shown to be the key to the development of a predictive theory. It has been shown that the emission of the twinning partial dislocation is not accompanied by the surface step creation, but rather with energetic decrease near the crack-tip. The following conclusion is that the Tadmor-Hai theory applies but additional modifications need to be introduced. The new theory is based on a recognition that the twinning partial emission is controlled by the second twinning unit along the twinning plane. The shearing energy change of the second twinning unit is controlled by the bulk GTF energy. However, the stress acting at the second twinning unit is lower than that at the crack tip. The lower stress is accounted through a new parameter $f(C_{ijkl})$ which is then incorporated in the new analytical formulation. Predictions for the K_{Ie}^{twin} are shown to be in excellent agreement with simulations. The analytical model for predicting the critical stress intensity factor for a trailing partial dislocation emission K_{Ie}^{trail} , which involves

Chapter 5. New theory for crack-tip twinning in fcc metals

step creation, is based on the theory presented in Chapter 4. Comparison between K_{Ie}^{twin} and K_{Ie}^{trail} across wide range of fcc metals show why twinning is always preferred at $T = 0K$. Finally, we find a new mode of “forward” twinning, which starts after only a few (0-4) “back” emission events and is responsible for further twin thickening. “Forward” twinning is closely connected to Griffith cleavage, and our analysis demonstrates that the twinning versus cleavage competition is then fully determined by the competition for the very first partial dislocation emission.

6 Stress-dependence of generalized stacking fault energies

This chapter is extracted from the following publication:

- (1) Andric P, Yin B, Curtin WA. Stress-dependence of generalized stacking fault energies. *Journal of the Mechanics and Physics of Solids*. 2019 Jan 1;122:262-79.

6.1 Introduction

The Generalized Stacking Fault Energy (GSFE) Ψ_{gsf} is one of the most important properties for understanding dislocation phenomena in crystalline materials [133]. The GSFE governs the dissociation distance of fcc partial dislocations, the distribution of Burgers vector across the core of a dislocation, and is used in the classic Peierls-Nabarro model to compute these physical features [43]. The GSFE is also recognized as a crucial material property for describing nanoscale plasticity, especially dislocation nucleation processes such as dislocation emission (i) from a crack tip [50, 75], (ii) from a grain boundary [134, 135], (iii) during nanoindentation [136], and (iv) to create crack-tip twinning [94, 91].

For a given slip plane and slip direction in a crystal, the GSFE is the energy associated with an imposed shear displacement Δ_s between two non-sheared crystalline blocks. The standard measurement is performed allowing displacements of all atoms normal to the slip plane, and thus full relaxation of the normal stress (or traction) T_n throughout the cell, leading to $\Psi_{gsf}(\Delta_s, T_n = 0)$. The normal relaxation gives rise to changes in the inter-planar spacings around the fault; we denote the total inelastic normal displacement as Δ_n ¹. The changes in planar spacings are often neglected. In some early mechanics works, computations held the two blocks rigidly at the unstrained lattice constant of the crystal and then minimized the energy by relaxing the normal displacement across only the two planes of atoms on either side of the fault plane [130]. In this case, Δ_n is slightly different than in the more-general case and is localized to the fault plane, but

¹ Δ used in Chapters 4 and 5 corresponds to Δ_s used in this chapter. Opening displacement Δ_n is not considered in the new theories presented in Chapters 4 and 5.

again this is often neglected.

In fcc metals, the focus here, favorable sliding occurs along the $[112]$ crystallographic direction. The GSFE has a local minimum at $\Delta_s = b_p$ where $b_p = a_0/\sqrt{6}$ is the magnitude of the partial dislocation Burgers vector for fcc lattice parameter a_0 . The GSFE at this point is the stable stacking fault energy γ_{ssf} . Prior to reaching the stable stacking fault, the GSFE has maximum corresponding to the unstable stacking fault energy with energy γ_{usf} . The quantities γ_{ssf} and γ_{usf} are primary fault energies used to understand various dislocation phenomena in metals. Typical GSFE curves for Al [81], with full normal relaxation and relaxation only across the slip plane, both at $T_n = 0$, are shown in Figure 6.1. The difference between the two methods is indeed small in this case, largely justifying the prior neglect of the differences between the two methods.

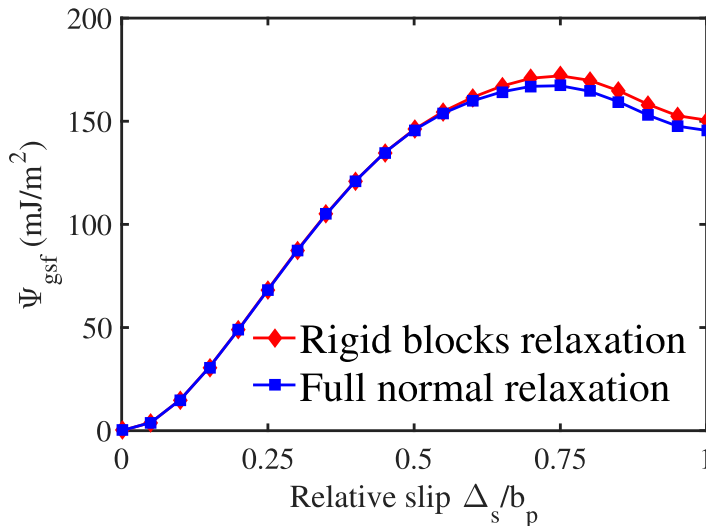


Figure 6.1 – Generalized stacking fault energy with full normal relaxation (blue squares) and relaxation only across the slip plane (red diamonds) computed in Aluminum [81] at $T = 0K$.

The high stresses often associated with nanoscale phenomena suggest that the normal stress dependence of the GSFE, and in particular of γ_{ssf} and/or γ_{usf} , are important. Rice and collaborators postulated that γ_{usf} decreases under a high tensile stress T_n , facilitating crack tip dislocation emission [50, 130]. Such “opening softening” was estimated to decrease the critical energy release rate for crack-tip dislocation emission by up to 30% in fcc metals [130]. Subsequently, the notion of “opening softening” was invoked in different contexts but without a quantitative analysis of its effects in each particular problem [119, 120]. The need for quantification motivated several computational studies of the stress effects on the GSFE using molecular statics simulations [129, 137] and first principle calculations [138, 139]. All of these studies reported “opening softening”. The prior computational studies were performed under displacement boundary conditions, which we show below can be problematic. In addition, the Rice theory for dislocation emission is typically somewhat lower than detailed simulation studies (see Chapter 4) and so “opening softening” would lead to further deviations between theory and simulation. In addition,

our analysis for a crack-tip dislocation emission and twinning, presented in Chapters 4 and 5, agrees very well with simulations of the critical stress intensity factor without including any “opening softening” effect. These factors motivate us to revisit the measurement/computation of the stress dependence of the GSFE more thoroughly than in earlier works.

GSF calculations under an applied stress can be envisioned in principle through two thermodynamic interface quantities, (i) a generalized stacking fault (potential) energy GSFE, and (ii) a generalized stacking fault enthalpy (GSFH, consistent with the standard thermodynamic notation for the enthalpy as $H = E + PV$). The GSFE $\Psi_{gsf}(\Delta_s, \Delta_n)$ is a local surface constitutive law associated with shearing Δ_s and normal displacement Δ_n . However, the total inelastic normal displacement observed under applied normal stress $\Delta_n(\Delta_s, T_n)$ extends over several atomic planes around the stacking fault and so is non-local. A Δ_n cannot easily be imposed since there are actually individual internal variables $\Delta_n^{(i)}$ for successive planar spacings $i = 0, \pm 1, \pm 2, \dots$. By changing variables from normal displacement to normal traction, we can define $\Psi_{gsf}(\Delta_s, \Delta_n(T_n)) \equiv \Psi_{gsf}(\Delta_s, T_n)$ also as the GSFE (potential energy). Under normal traction, not all interatomic planar spacings $\Delta_n^{(i)}$ are accessible; only those corresponding to the imposed traction T_n can be measured. As noted above, the standard GSFE is precisely $\Psi_{gsf}(\Delta_s, \Delta_n(T_n = 0)) \equiv \Psi_{gsf}(\Delta_s, T_n = 0)$ and the value of $\Delta_n(\Delta_s, T_n)$ is not usually reported. Here, we apply a normal traction T_n and directly measure $\Psi_{gsf}(\Delta_s, T_n)$ and $\Delta_n(\Delta_s, T_n)$. The GSFE $\Psi_{gsf}(\Delta_s, T_n)$ generally increases, or remains nearly constant, over a wide range of tractions approaching normal decohesion levels; there is no “opening softening”.

Under an applied traction normal to the fault plane, the relevant thermodynamic quantity for the entire system is the enthalpy. Subtracting the enthalpy of the reference perfect crystal yields the GSFH, $\Psi_{gsf}^{enth}(\Delta_s, T_n) = \Psi_{gsf}(\Delta_s, T_n) - T_n \Delta_n(\Delta_s, T_n)$. When the normal opening is positive, this quantity can decrease under increasing normal stress. Previously reported “opening softening” results are essentially calculations of Ψ_{gsf}^{enth} [129, 137, 138, 139] (aside from detrimental finite size effects). However, the term “enthalpy” was never used, and the quantity was often reported as the GSFE (potential energy) under stress. The distinction between GSFE and GSFH is important. While Ψ_{gsf}^{enth} is the proper thermodynamic quantity for the entire system under a traction normal to an infinite fault plane, this quantity cannot easily be used in general mechanics problems and, if used improperly can lead to spurious conclusions.

The importance of defining and distinguishing the various thermodynamic quantities in mechanics problems is thus highlighted here in two applications: (i) fcc partial dissociation under applied normal stress, and (ii) crack-tip dislocation emission under mixed Mode II/I loading. We show that a precise use and/or understanding of $\Psi_{gsf}(\Delta_s, T_n)$ and $\Delta_n(\Delta_s, T_n)$ enables quantitative understanding of explicit molecular statics simulations of these two problems. In particular, for crack-tip dislocation emission, we demonstrate that there is no “opening softening” as previously reported and the simulations are entirely consistent with the underlying $\Psi_{gsf}(\Delta_s, T_n)$ and $\Delta_n(\Delta_s, T_n)$.

6.2 GSFE under normal stress: simulation methods

We compute the GSFE under applied normal stress using interatomic potentials (and the LAMMPS code [87]) and first principles density-functional theory (DFT) calculations (VASP code [140, 141]) in molecular statics. The GSFE for relative sliding of two crystalline blocks of material is computed in the standard manner (see Figure 6.2). At relative shear displacement Δ_s , the GSFE is computed as

$$\Psi_{gsf}(\Delta_s, T_n) = [E(\Delta_s, T_n) - E(\Delta_s = 0, T_n)]/A \quad (6.1)$$

where $E(\Delta_s = 0, T_n)$ is the potential energy of a perfect crystal under stress T_n , $E(\Delta_s, T_n)$ is the potential energy of the simulation cell at relative slip displacement Δ_s , and A is the area of the simulated fault. Note that in the above, the work done by the applied stress is not included, so that Eq. 6.1 is the desired potential energy.

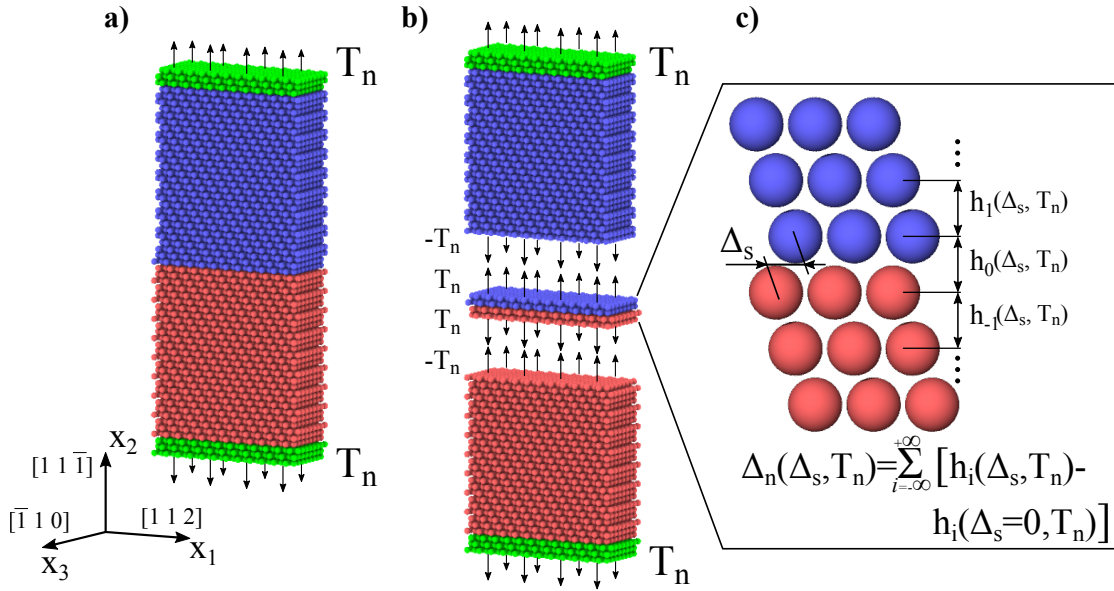


Figure 6.2 – a) Typical simulation cell for computing the GSFE under applied normal stress, with the lower and upper domains indicated by red and blue, and atoms on which forces are applied indicated in green. b) Stacking fault region for describing the local constitutive behavior for rigid block sliding under applied tractions T_n . c) Inter-planar spacing around the stacking fault for a given shear displacement Δ_s and applied tractions T_n . Atoms are visualized using OVITO [15].

In the interatomic potential computations, we first define a rectangular simulation cell oriented with $X_1 = [112]$, $X_2 = [11\bar{1}]$ and $X_3 = [\bar{1}10]$, and dimensions $6\sqrt{6}a_0 \times 20\sqrt{3}a_0 \times 2\sqrt{2}a_0$. We set periodic boundary conditions along the X_1 and X_3 direction in the plane of the fault, and traction boundary conditions in the X_2 direction normal to the fault. The simulation cell length in the X_2 direction is sufficient to prevent any interaction between the upper and lower surfaces and the stacking fault. The desired stress along the $X_2 = [11\bar{1}]$ direction is created by applying

forces to atoms within (r_c = cut-off distance of the interatomic potential) of the top and bottom X_2 boundaries (see Figure 6.2a). At a given applied normal stress $\sigma_{22} = T_n$ we compute initial atomic positions and the initial energy $E(\Delta_s = 0, T_n)$ by minimizing the total energy using the “fire” method [88]. Under an applied load T_n , the cell sizes along X_1 and X_3 are held fixed; thus lateral loads σ_{11} and σ_{33} develop as T_n is increased. However, in finite-length simulation cells, allowing relaxation of the total lateral stresses includes a compensation for lateral stresses due to the fault itself; this leads to erroneous stresses away from the fault, and changes in stored elastic energy that are then attributed to the fault only. Thus, it is best to use fixed cell sizes along X_1 and X_3 with periodic boundary conditions; the GSFE under uniaxial stress is shown in Appendix A.7 for comparison and differences are negligible. After the initial minimization, the upper half of the crystal in the $[112]$ slip direction is displaced relative to the (fixed) lower half by the displacement Δ_s . The applied normal stress is held fixed for all shear displacement values. As with standard GSF computations, atomic relaxation is allowed only in the X_2 direction normal to the slip plane and the minimum energy computed. We perform calculations in fcc Nickel, Copper and Aluminum using the Mishin et al. EAM interatomic interactions [81, 125].

First principle DFT calculations of the GSFE in Cooper, Aluminum and Magnesium are performed as follows. The exchange-correlation functional is treated within the generalized gradient approximation (GGA) with the Perdew-Burke-Ernzerhof (PBE) parametrization [142]. Core electrons are replaced by the projector augmented wave (PAW) pseudopotentials [143]. The cutoff energy of the plane wave basis set is 800eV for Cu, 500 eV for Al, and 400 eV for Mg, respectively. Simulation of the GSFE is accomplished using the tilted-cell method [144]. We start with a simulation cell in the fully-periodic bulk crystal structure with the $X_1 - X_3$ plane parallel to the desired stacking fault plane. The (non-orthogonal) cell has lattice vectors (a_1, a_2, a_3) . A new periodic simulation cell with lattice vectors $(a_1, a_2 + \Delta_s t, a_3)$ is then defined where t is a unit vector lying in the $X_1 - X_3$ slip plane and in the direction of the slip. The change in periodicity thus introduces an initial atomistic fault across the $X_1 - X_3$ periodic boundary of the cell. All atoms are then permitted to relax in the X_2 direction normal to the fault and the length of the cell normal to the fault plane is also allowed to relax such that the normal stress is the desired applied stress, $\sigma_{22} = T_n$. This procedure is appropriate for computing the GSFE when atoms undergo no in-plane relaxations, which is true by symmetry for the fcc stable stacking fault position and is generally valid for fcc and hcp basal fault planes (see [145] for notable exceptions for other hcp slip planes). We use 12 atomic layers normal to the fault, which is just about sufficient to avoid SF-SF interactions of the periodic images for the close-packed planes in Cu, Al, and Mg. Our results for the stable stacking fault energies are then close to those reported in other work [145] using different methods and different cell sizes. Other details of the DFT parameters and geometry setup can be found in Ref. [145].

We now introduce few technical points that are crucial for achieving accurate DFT results. First, the force convergence criterion must be selected carefully. In some cases, it must be smaller than the value of $10^{-3} \text{eV}/\text{\AA}$ typically used in DFT studies. The smaller value is necessary due to energy contributions arising from the corresponding uncertainty in the stress state when stress boundary conditions are used. For an uncertainty in stress of $d\sigma$, the uncertainty in the

energy is $dE = \frac{V}{2C}(d\sigma^2 + 2\sigma d\sigma)$ assuming linear elasticity, where C is the plane-strain elastic modulus for loading along the x_2 direction. Taking Mg as an example ($C_{33} = 63.6\text{GPa}$, atomic volume 22.9\AA^3 , 12 atoms in the supercell), in the stress-free state ($T_n = 0$) force convergence at 10^{-3}eV/\AA corresponds to $d\sigma \sim 7 \cdot 10^{-3}\text{GPa}$ and $dE \sim 7 \cdot 10^{-7}\text{eV}$, which is negligible. However, at a stress $T_n = 5\text{GPa}$, the error is $dE \sim 0.9\text{meV}$. Since the GSFE energy is calculated by subtracting two supercell energies, this uncertainty in the supercell total energy can cause a large uncertainty in the computed GSFE, with uncertainty of $\sim 3\text{mJ/m}^2$ for Mg. Here, we choose 10^{-4}eV/\AA ($\sim 0.7 \cdot 10^{-3}\text{GPa}$) for Al and Mg, reducing the total error in energy to $\sim 0.09\text{meV}$ and thus good accuracy in the computation of the GSFE. For Cu, the effective elastic constant C is approximately four times larger than that of Mg so that a force tolerance of 10^{-3}eV/\AA leads to an error of 0.3meV at 5GPa , and hence only an error of 1.3mJ/m^2 in the GSFE. Difficulty in converging of ionic relaxations in Cu limits the force tolerance to 10^{-3}eV/\AA and so it is not possible to reduce the error further. This discussion also shows that a smaller number of layers introduces less error. But too few layers lead to spurious interactions among the periodic images of the SF. We find that 12 layers of atoms is satisfactory for avoiding both problems.

6.3 GSFE under normal stress: results

Figure 6.3(i) shows the GSFE $\Psi_{gsf}(\Delta_s, T_n)$ as computed for Ni, Cu, and Al using interatomic potentials for a range of applied normal tensile stresses up to $T_n = 15\text{GPa}$. In Ni and Cu, the entire GSFE curve increases with applied normal tensile stress; the increases in Ψ_{gsf} up to 10GPa are fairly small, however. Similar trends are generally found in Al but the GSFE does decrease for the highest stress and large shear displacements, $\Psi_{gsf}(\Delta_s > 0.7b_p, T_n = 7.5\text{GPa})$, where the normal stress is approaching the material cohesive stress (maximum sustainable normal stress in the material). Focusing on the most important points of the GSFE, the unstable and stable stacking fault energies γ_{usf} and γ_{ssf} , Figure 6.4 shows γ_{usf} and γ_{ssf} normalized by their values at $T_n = 0\text{GPa}$. In Ni and Cu, γ_{usf} is fairly insensitive to stress up to $\sim 10\text{GPa}$, while γ_{usf} increases more rapidly in Al. In contrast, γ_{ssf} varies more rapidly with stress, especially in Al and Cu. Al does show “opening softening” (normalized values below unity) at $T_n > 6\text{GPa}$. Overall, the trend for all materials is “opening hardening”.

Studies using EAM potentials enable us to analyze atom-by-atom energy changes around the fault. For all shear displacements, the energy contributions to the GSFE are localized to two (Ni and Cu) or three (Al) atomic planes on each side of the slip plane. Figure 6.5 shows examples at the unstable and the stable stacking fault displacements for Ni. This is fully expected since the GSFE is the energy change of the atoms due to the presence of the planar fault, and deviations from perfect crystal behavior are well-known to extend only a few layers of atoms from the defect plane even for much more drastic planar defects such as free surfaces and grain boundaries.

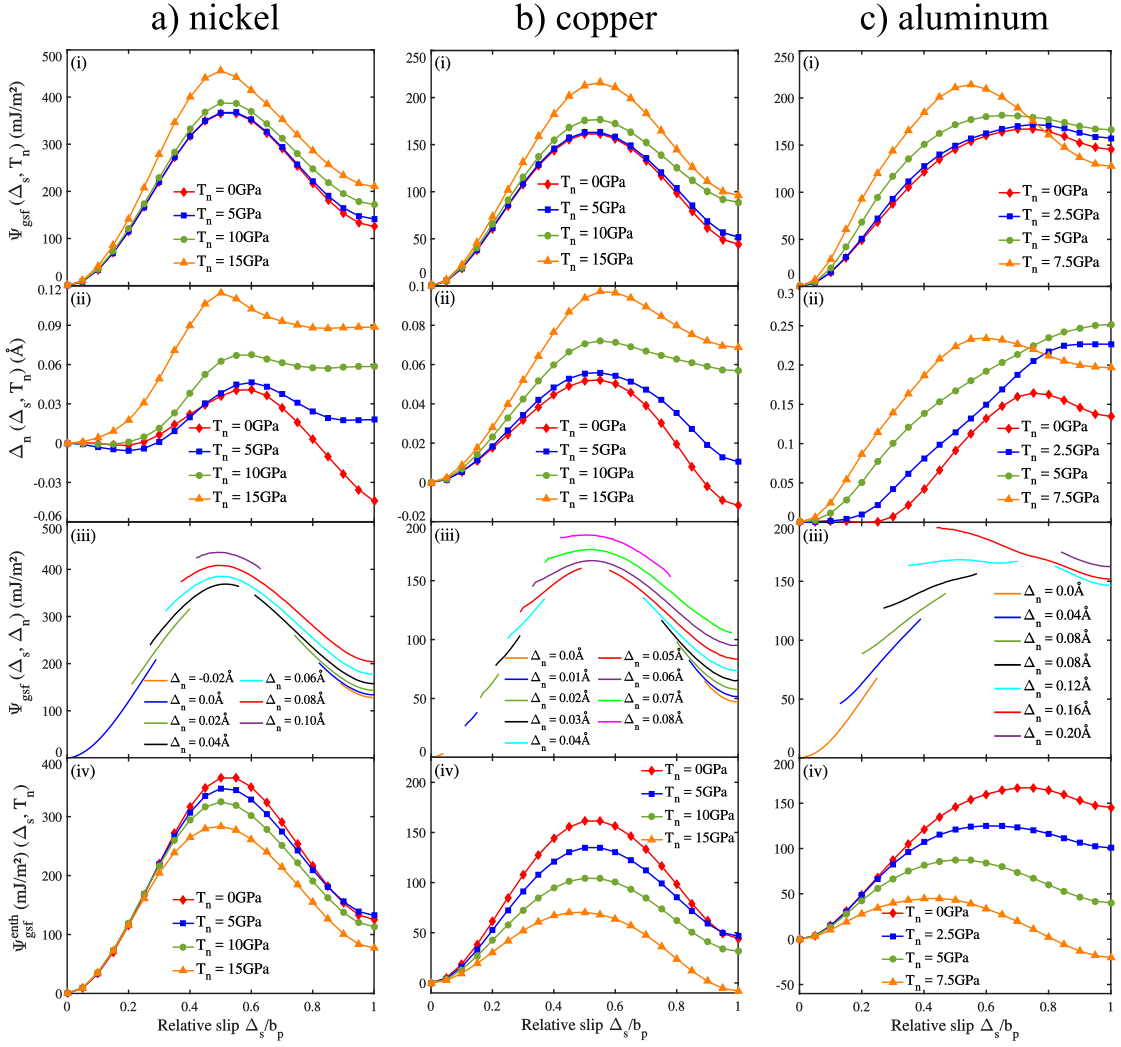


Figure 6.3 – (i) The GSFE Ψ_{gsf} , and (ii) total inelastic normal displacement Δ_n across the slip plane for different applied normal stresses T_n ; (iii) The GSFE Ψ_{gsf} for different applied inelastic displacements Δ_n ; (iv) GSFE versus shear displacement Δ_s for different applied normal stresses T_n . All values are computed with interatomic potentials at $T = 0K$ in a) nickel, b) copper and c) aluminum.

Figure 6.6(i) shows the GSFE versus applied normal stress as computed via first-principles for Al, Cu, and the basal plane in Mg (which is very similar to fcc). In all three materials, the qualitative trends are similar to those obtained using interatomic potentials. There is no “opening softening”. For the stresses considered here, the DFT-computed GSFE is nearly constant in Cu and Mg and increases in Al. Quantitative differences between DFT and interatomic potentials are expected, with the DFT being the reference, but the differences are not significant relative to our main points. These results also show that the GSFE typically increases with applied stress. There is no “opening softening”, in contrast to prior concepts and results in this literature. This is the first main result of this paper.

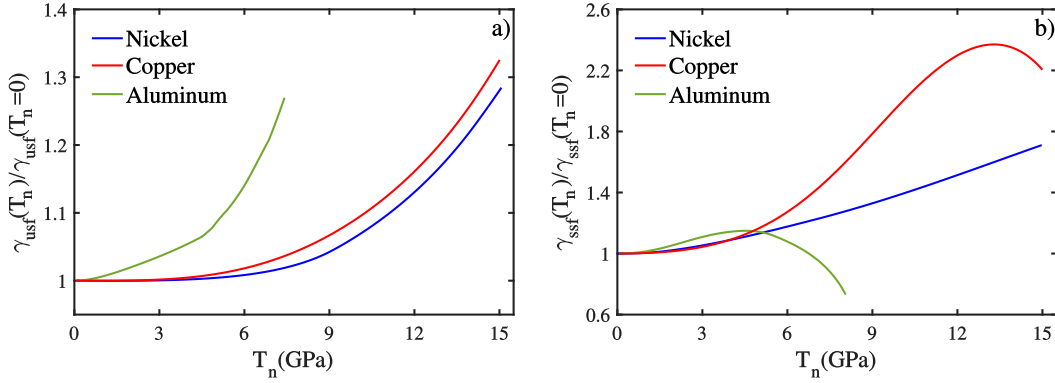


Figure 6.4 – Normalized stable γ_{ssf} and unstable stacking fault γ_{usf} energies in Ni (blue color), Cu (red color) and Al (green color) versus applied normal tensile stress.

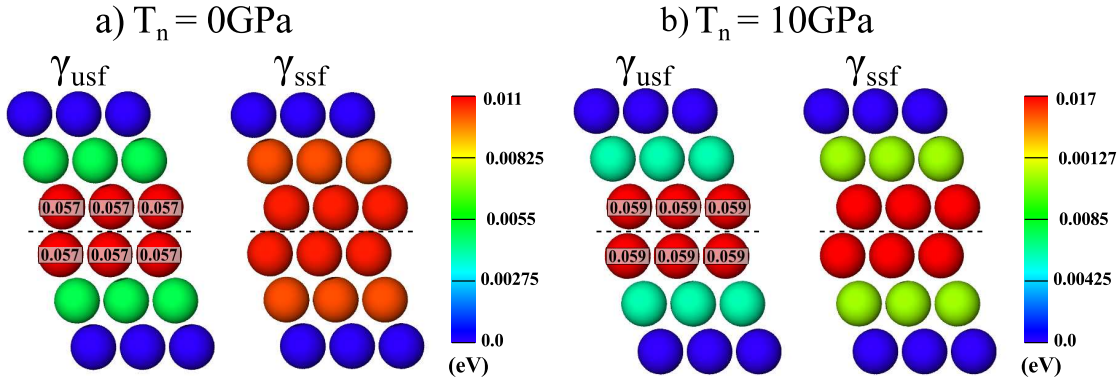


Figure 6.5 – Atom-by-atom energy change during rigid block shear displacement at the point of the unstable stacking energy γ_{usf} and stable stacking fault energy γ_{ssf} in fcc Ni under a) zero applied stress, and b) at the applied stress $T_n = 10$ GPa. Note that contributions to the energy are confined to a few layers of atoms around the fault. Energies of atoms exceeding the energy scale are indicated.

We further examine the inelastic normal displacement under applied normal stress. The $\Delta_n(\Delta_s, T_n)$ represents a total change in atomic planar spacings, over several atomic layers around the stacking fault, due to the change in local atomic environment away from the perfect strained crystal. Defining h_i as the atomic inter-planar spacing perpendicular to the slip plane between the $(i-1)^{th}$ and i^{th} planes (see Figure 6.2c), $\Delta_n(\Delta_s, T_n)$ is computed as

$$\Delta_n(\Delta_s, T_n) = \sum_{i=-\infty}^{+\infty} [h_i(\Delta_s, T_n) - h_i(\Delta_s = 0, T_n)] \quad (6.2)$$

Non-zero inelastic displacements are always found over the three atomic plane spacings (central plane and one on either side of the fault $-1 \leq i \leq 1$) (Figure 6.2c) but can extend up to five plane spacings $-2 \leq i \leq 2$ in some cases as computed by first principles methods. We note that in DFT

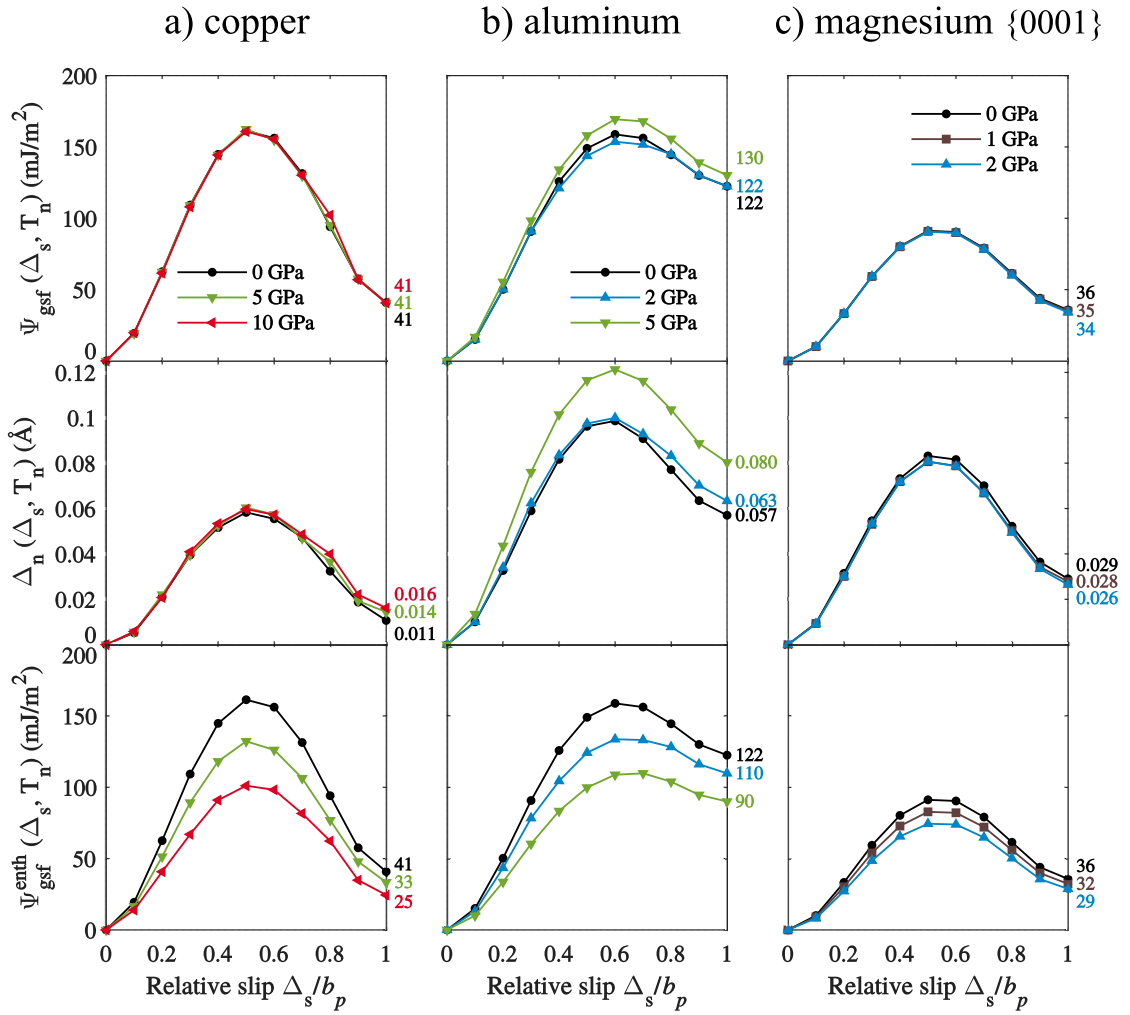


Figure 6.6 – (i) The GSFE Ψ_{gsf} , (ii) total inelastic normal displacement Δ_n across the slip plane, and (iii) GSFEH versus shear displacement Δ_s for different applied normal stresses as computed in DFT in a) copper, b) aluminum and c) magnesium {0001}.

computations there are very small variations in interplanar spacing throughout the entire cell due to non-zero forces below the DFT tolerance level; these are numerical noise and arise even in simulations of the stressed perfect crystal. Figure 6.3(ii) shows the total inelastic normal displacement $\Delta_n(\Delta_s, T_n)$ computed via interatomic potentials for Ni, Cu, and Al at the various normal stresses T_n . Δ_n generally increases with increasing applied stress. Only in Al at high shear displacement and high normal stress does the opening decrease. Figure 6.6(ii) shows similar trends in Δ_n obtained from the first principle calculations, with no decreases in Δ_n observed in any materials. Overall, the inelastic normal displacements follow the same trends with stress as the GSFE.

From the results in Figures 6.3(i,ii), we can compute the GSFE $\Psi_{gsf}(\Delta_s, \Delta_n)$ for different magnitudes of the inelastic normal displacement Δ_n over certain ranges of displacement as shown

in Figures 6.3(iii). Only those inelastic normal displacements corresponding to equilibrium conditions at the imposed normal stresses are accessible but the trends are clear. Figure 6.3(iii) clearly demonstrates an “opening hardening” trend: the GSFE increases with increasing Δ_n . The physical origin of the “opening hardening” is not clear. At high stresses where the effect is largest, the entire material is deforming non-linearly and the inelastic normal displacements also vary with applied load. Hence, we have not been able to attribute the small total energy changes (that ultimately lead to increases in the fault energy) to a single specific mechanism.

The GSFE and the total inelastic normal displacement then allow for the computation of the generalized stacking fault enthalpy (GSFH) as

$$\Psi_{gsf}^{enth}(\Delta_s, T_n) = \Psi_{gsf}(\Delta_s, T_n) - T_n \Delta_n(\Delta_s, T_n) \quad (6.3)$$

Figures 6.3(iv) and 6.6(iii) show the GSFH versus shear displacement Δ_s and normal stress T_n for all cases studied here. The GSFH always decreases when $T_n > 0$, although Δ_n is not always positive, and the decreases can be a significant fraction of the zero-stress energy. Incorporating this apparent “opening softening” directly into mechanics problems as a replacement for the GSFE is, however, not quite accurate. The GSFH is measured only when the planar fault extends entirely across the area of the system. Geometry effects in mechanics problems differ, and thus the use of GSFH is not appropriate in all cases. The combination of $\Psi_{gsf}(\Delta_s, T_n)$ and $\Delta_n(\Delta_s, T_n)$, or the use of $\Psi_{gsf}(\Delta_s, \Delta_n)$ is more general, as we will show below.

6.4 GSFE under normal applied loading: boundary conditions and size effects

Direct use of stress boundary conditions leads to clear results and insights about the GSFE and the inelastic normal displacement $\Delta_n(\Delta_s, T_n)$, from which the GSFH can be computed. Previous computations reporting “opening softening” used displacement boundary conditions [129, 137, 138, 139]. The enthalpy change associated with a localized planar defect in a material can be computed using either stress or displacement boundary conditions at infinity, and so in principle boundary conditions should not matter. However, only the enthalpy is obtained and simulations, especially DFT studies, are not performed on infinite systems, leading to size-dependent differences. For the stacking fault problem under an imposed normal displacement, the inelastic normal displacements lead to relaxation of the stresses throughout the entire simulation cell so as to maintain the imposed displacements on the cell. The relaxed stresses lead to relaxed elastic energies far from the stacking fault that are included into the calculation of the fault energy. The result is not the GSFE nor the GSFH, but asymptotically approaches the GSFH for large sizes.

The analysis of finite-sized cells under displacement control is simple because the planar fault problem is essentially one-dimensional in the X_2 dimension only. In a cell of length L_2 with imposed total displacement u_2 , the strain in the reference calculation at zero shear displacement

6.4. GSFE under normal applied loading: boundary conditions and size effects

is $\epsilon_{22} = u_2/L_2$. The total stored elastic energy in the cell of volume V is then

$$E_{elastic} = \frac{1}{2}C\epsilon_{22}^2V \quad (6.4)$$

and the normal traction is $T_n = C\epsilon_{22}$, where C is the plane-strain elastic modulus for loading in the $X_2 = [11\bar{1}]$ direction. At shear displacement Δ_s , with inelastic normal displacement $\Delta_n(\Delta_s, T_n)$ across the cross-section of the cell, the total displacement is unchanged but now given by $u_2 = \Delta_n + \epsilon_{22}L_2$. The elastic strain is thus decreased to $\epsilon_{22} - \Delta_n(\Delta_s, T_n)/L_2$. The stored elastic energy in the system is then

$$E_{elastic} = \frac{1}{2}C[\epsilon_{22} - \Delta_n(\Delta_s, T_n)/L_2]^2V \quad (6.5)$$

The elastic energy released upon introduction of the shear displacement is the difference between Eqs. 6.4 and 6.5. Dividing by the area A , with $V = AL_2$, leads to

$$\begin{aligned} \frac{E_{elastic}(\Delta)}{A} &= -C\epsilon_{22}\Delta_n(\Delta_s, T_n) + \frac{1}{2}C\frac{\Delta_n^2(\Delta_s, T_n)}{L_2} = \\ &= -T_n\Delta_n(\Delta_s, T_n) + \frac{1}{2}C\frac{\Delta_n^2(\Delta_s, T_n)}{L_2} \end{aligned} \quad (6.6)$$

The change in total energy, including the actual change in potential energy $\Psi_{gsf}(\Delta_s, T_n)$ of the fault, is then

$$\begin{aligned} \Psi_{gsf}^{disp}(\Delta_s, T_n) &= \Psi_{gsf}(\Delta_s, T_n) + \frac{E_{elastic}(\Delta)}{A} = \\ &= \Psi_{gsf}(\Delta_s, T_n) - T_n\Delta_n(\Delta_s, T_n) + \frac{1}{2}C\frac{\Delta_n^2(\Delta_s, T_n)}{L_2} \end{aligned} \quad (6.7)$$

This result is neither the GSFE nor the GSFH, although it approaches the GSFH as $L_2 \rightarrow \infty$. The rate of approach to the GSFH depends on $\Delta_n(\Delta_s, T_n)$, which is unknown in advance and is both traction-dependent and material dependent. Computations using a single simulation cell size for different tractions and/or different materials thus introduce uncontrolled errors in spite of appearing to be systematic.

We demonstrate the convergence issue explicitly using interatomic potentials under displacement boundary conditions as follows. We use same rectangular simulation cell ($X_1 = [112]$, $X_2 = [11\bar{1}]$, $X_3 = [\bar{1}10]$) and later cell dimensions ($L_1 = 6\sqrt{6}a_0$, $L_3 = 2\sqrt{2}a_0$) with periodic boundary conditions in X_1 and X_3 . We consider X_2 lengths between 10 and 240 $[11\bar{1}]$ atomic planes. For a desired applied normal stress T_n , the corresponding applied normal strain ϵ_{22} is computed from Hooke's Law. The atomic positions are initialized by linearly displacing all atoms at x_2 by $x_2\epsilon_{22}$ in the $[11\bar{1}]$ direction. The initial total energy $E(\Delta_s = 0, \epsilon_{22})$ is computed by relaxing all the non-boundary atoms using the "fire" method [88], while the boundary atoms (atoms within r_c of the X_2 boundaries at $x_2 = 0$ and $x_2 = L_2$) are held fixed at the imposed displacements corresponding to the applied strain ϵ_{22} (see Figure 6.2a). We then rigidly slide the

upper half of the crystal in $[112]$ slip direction, holding the X_2 positions of the boundary atoms fixed and allowing all other atoms to relax in the X_2 direction normal to the slip plane. The total energy of the simulation cell $E(\Delta_s, \epsilon_{22})$ versus slip displacement is then computed for all three studied materials. The apparent energy change is then calculated using Eq. 6.1.

Figure 6.7 shows the normalized values of γ_{usf} and γ_{ssf} at the applied strain of $\epsilon_{22} = 0.045$ as a function of the X_2 dimension (number N of $[11\bar{1}]$ atomic layers). This applied strain corresponds to an applied stress of ~ 15.8 GPa in Ni, ~ 9.8 GPa in Cu, and ~ 5.1 GPa in Al. Since all other points on the GSFE curve follow a similar evolution we do not present them. Figure 6.7 shows that at least 100 $[11\bar{1}]$ atomic layers are needed for reasonable converged results $\Psi_{gsf}^{disp} \sim \Psi_{gsf}^{enth}$ at this applied strain. In addition, since we do not control either the normal traction nor the inelastic normal displacements, and since the material might be nonlinearly elastic at high strains, the simulation results in Figure 6.7 may not be corrected simply by using Eq. 6.7.

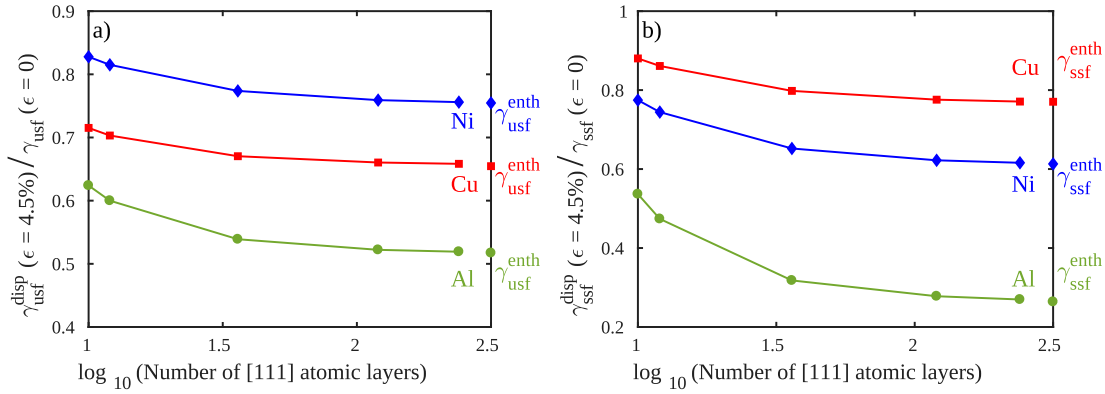


Figure 6.7 – The size dependence of a) γ_{usf}^{disp} and b) γ_{ssf}^{disp} using displacement boundary conditions along with γ_{usf}^{enth} and γ_{ssf}^{enth} computed using Eq. 6.3 and shown on the right axis, at the applied strain of $\epsilon_{22} = 0.045$ in nickel (blue diamonds), copper (red squares) and aluminum (green circles).

The use of displacement boundary conditions in DFT has further been studied in Cu for the stable stacking fault energy γ_{ssf} . The displacement boundary conditions are as described above, but using the tilted cell method and a cell length of 12 atomic layers. Table 1 shows γ_{ssf} and Δ_n computed using stress boundary conditions along with γ_{ssf}^{enth} , computed using Eq. 6.3, and γ_{ssf}^{disp} computed using displacement boundary conditions for different applied normal stresses. With increasing applied stress, there is a difference between γ_{ssf}^{disp} and γ_{ssf}^{enth} , with $\gamma_{ssf}^{enth} < \gamma_{ssf}^{disp}$ as expected. The difference here is not large because $\Delta_n(\Delta_s, T_n)$ in Cu is particularly small (see Figure 6.6(ii)) but the trend is clear. Larger errors would be found in the other materials using the same cell size. Thus, obtaining converged results in DFT using displacement boundary conditions is not attractive since (i) the inelastic normal displacement $\Delta_n(\Delta_s, T_n)$ is not known a priori, (ii) the size needed for convergence is not clearly established a priori, and (iii) the direct application of stress on much smaller cells, as done here, provides all the necessary information

with far less computational effort.

T_n (GPa)	γ_{ssf} (mJ/m ²)	Δ_n (Å)	γ_{ssf}^{enth} (Eq. 6.3) (mJ/m ²)	γ_{ssf}^{disp} (mJ/m ²)
0	40.9	0.011	40.9	41.0
5	40.6	0.014	33.6	34.6
10	40.7	0.016	24.7	27.7

Table 6.1 – Stable stacking fault energy γ_{ssf} and inelastic normal displacement Δ_n computed in copper via DFT using stress boundary conditions along with the stable stacking fault enthalpy γ_{ssf}^{enth} computed using Eq. 6.3, and γ_{ssf}^{disp} computed using displacement boundary conditions.

6.5 Applications of the GSFE

Section 6.3 has clearly highlighted that the GSFE and GSFH are the two thermodynamic quantities that arise during GSF calculations under an applied normal stress. In addition, the crucial feature above is the inelastic normal displacement Δ_n across the stacking fault plane that enters in both Ψ_{gsf} and Ψ_{gsf}^{enth} . Here, we examine which thermodynamic quantity is most appropriate to use for describing different mechanics problems.

6.5.1 GSFE: An analysis based on the Eshelby method

The stacking fault induces normal inelastic displacements Δ_n of the atomic planes just around the fault plane (Figure 6.2b and 6.2(ii)). The local nature of Δ_n suggests that stress dependence of the stacking fault can be derived using an Eshelby-type analysis [24] where the inelastic normal displacement is treated as an “eigenstrain” ϵ^T associated with an “inclusion” confined to the stacking fault region. Any finite length stacking fault must be bounded by partial dislocations but here we first outline the general Eshelby analysis and then in Sec. 6.5.2 we apply it to the prediction of the fcc Shockley partial dissociation distance under applied normal stress.

Following standard analysis, consider a body with no inclusion that is subjected to external surface tractions \mathbf{T}^A applied over the boundary S . The total free energy of the body, which is the generalized enthalpy, is

$$F_1 = \frac{1}{2} \int_V \boldsymbol{\sigma}^A : \boldsymbol{\epsilon}^A dV - \int_S \mathbf{T}^A \mathbf{u}^A dS \quad (6.8)$$

where $\boldsymbol{\sigma}^A$, $\boldsymbol{\epsilon}^A$ and \mathbf{u}^A are the stress, strain, and displacement due to the applied load \mathbf{T}^A . The first term is the elastic energy stored in the volume V and the second term is the work done by the applied tractions \mathbf{T}^A on S . Now consider the insertion of an inclusion of area A having the same elastic moduli as the body but having a chemical energy change $\Psi_{gsf}A$ and undergoing

some eigenstrain ϵ^T . The enthalpy of the system is then

$$F_2 = \frac{1}{2} \int_V (\boldsymbol{\sigma}^A + \boldsymbol{\sigma}) : (\boldsymbol{\epsilon}^A + \boldsymbol{\epsilon}) dV - \int_S \mathbf{T}^A (\mathbf{u}^A + \mathbf{u}) dS \quad (6.9)$$

where $\boldsymbol{\sigma}$, $\boldsymbol{\epsilon} - \boldsymbol{\epsilon}^T$ and \mathbf{u} are additional and unknown stress, *elastic* strain, and displacement fields, respectively, generated by the inclusion that undergoes some eigenstrain $\boldsymbol{\epsilon}^T$. Using integration by parts, Gauss law, and some simple algebraic manipulations (for more details see [24, 146]) the enthalpy can be written as

$$F_2 = \frac{1}{2} \int_V \boldsymbol{\sigma}^A : \boldsymbol{\epsilon}^A dV - \int_S \mathbf{T}^A \mathbf{u}^A dS - \frac{1}{2} \int_V \boldsymbol{\sigma} : \boldsymbol{\epsilon}^T dV - \int_S \mathbf{T}^A \mathbf{u} dS + \Psi_{gsf} A. \quad (6.10)$$

The third and fourth terms are elastic energy stored in the body only due to the inclusion eigenstrain and an interaction energy corresponding to the external work done by the deformations caused by the inclusion, respectively. The change in enthalpy is then

$$\Delta F = -\frac{1}{2} \int_V \boldsymbol{\sigma} : \boldsymbol{\epsilon}^T dV - \int_S \mathbf{T}^A \mathbf{u} dS + \Psi_{gsf} A. \quad (6.11)$$

Our computational results above shows that the Ψ_{gsf} itself is stress-dependent, but this can be folded into Eq. 6.11 by self-consistently computing the actual stress inside the inclusion. This does not change the main features of our analysis.

The analysis presented above is rather general and does not depend on the inclusion shape. Now, consider a plate-like inclusion that extends across the entire crystal. This corresponds to the stacking fault configuration used to compute the GSFH (see Sec. 6.2 and Figure 6.2). The first term in Eq. 6.11 then disappears since the inclusion is not constrained by the surrounding elastic material and therefore generates no additional stress ($\boldsymbol{\sigma} \rightarrow 0$). Thus, the change in crystal enthalpy becomes

$$\Delta F = -T_n \Delta_n A + \Psi_{gsf} A \quad (6.12)$$

where $2\mathbf{u} \equiv 2u_2 = \Delta_n$ on the body's outer boundary ($u_2/2$ displacements on the top and bottom surfaces normal to the fault). Dividing Eq. 6.12 by the stacking fault area leads to

$$\frac{\Delta F}{A} = -T_n \Delta_n + \Psi_{gsf} \quad (6.13)$$

which is precisely the GSFH. Note that Eq. 6.13 is only valid when the stacking fault region exists across the entire crystal. When the stacking fault region is confined, e.g. surrounded by elastic material (Shockley partial dislocations in fcc metals, dislocation emerging from a grain boundary, etc.), the change in crystal enthalpy is given by Eq. 6.11.

Further integration of Eq. 6.11 using Gauss law leads to the alternative expression

$$\frac{\Delta F}{A} = -\frac{1}{2A} \int_{V_I} \boldsymbol{\sigma} : \boldsymbol{\epsilon}^T dV - \frac{1}{A} \int_{V_I} \boldsymbol{\sigma}^A : \boldsymbol{\epsilon}^T dV + \Psi_{gsf} \quad (6.14)$$

The two volume integrals are non-zero only within the inclusion volume V_I because ϵ^T exists only inside the inclusion, regardless of the inclusion shape. Often, the first term is small because the additional stress caused by the inclusion eigenstrain is proportional to ϵ^T and so this term is second order in ϵ^T . The second term is similar to the contribution $-T_n \Delta_n$ but is not exactly the same. From Eq. 6.14, it is clear that, even for an infinite elastic space subject to traction boundary conditions, the GSFH emerges only as a special case for a specific geometry (the infinite fault), although the overall free energy change has an “enthalpy-like” nature to it (due to the second term in Eq. 6.14).

6.5.2 Shockley partial dislocation dissociation under applied normal stress

The analysis presented in the previous section can be applied to analyze the stress dependence of fcc partial dislocation spacing. In fcc metals, it is energetically favorable for a perfect dislocation of Burgers vector $\frac{1}{2}\langle 110 \rangle$ to dissociate into two Shockley partial dislocations with Burgers vectors of the $\frac{1}{6}\langle 112 \rangle$ type [43]. The slip in between the two partial dislocations, along the $\langle 112 \rangle$ direction between closed-packed $\{111\}$ atomic planes, generates a stacking fault with energy cost (per unit area) $\gamma_{ssf} = \Psi_{gsf}(\Delta = b_p, T_n = 0)$. The elastic interactions between the two partials are repulsive and so the partial dislocations have an equilibrium separation that balances the elastic and stacking fault energies.

At zero applied normal stress, the analysis is standard; we use isotropic elasticity to enable clear analytic expressions. We consider an infinitely long edge dislocation lying along the $\xi = \hat{x}$ and dissociated into two parallel partials with a stacking fault between them (Figure 6.8). The partial Burgers vectors \mathbf{b}_1 and \mathbf{b}_2 lie at angles $\theta = 60^\circ$ and $\theta = 120^\circ$ with respect to the dislocation line ξ . At partial separation d , the crystal energy (per unit length) is

$$F = W_1 + W_2 + W_{12} + \gamma_{ssf}d \quad (6.15)$$

where W_1 and W_2 are the elastic self-energies of the partial dislocations, and W_{12} is the elastic interaction energy between the two partial dislocations [43]

$$W_{12} = -\frac{\mu(\mathbf{b}_1 \cdot \xi)(\mathbf{b}_2 \cdot \xi)}{2\pi} \ln \frac{d}{|\mathbf{b}|} - \frac{\mu}{2\pi(1-\nu)} [(\mathbf{b}_1 \times \xi) \cdot (\mathbf{b}_2 \times \xi)] \ln \frac{d}{|\mathbf{b}|} \quad (6.16)$$

with μ and ν the shear modulus for sliding along $\langle 110 \rangle$ direction and Poisson’s ratio, respectively. The self-energies of each partial dislocation do not depend on the partial separation and so do not influence the equilibrium separation. Therefore the equilibrium distance minimizes $W_{12} + \gamma_{ssf}d$, leading to the well-known result

$$d = \frac{\mu b_p^2}{8\pi\gamma_{ssf}} \frac{\nu + 2}{1 - \nu}. \quad (6.17)$$

Using material properties for fcc Ni and Al as described by the EAM potential [81] (see Appendix B), the dissociation distances are and $d_0 = 16.3\text{\AA}$, $d_0 = 10.1\text{\AA}$, respectively. A full anisotropic

analysis for Ni yields 19.1\AA , but anisotropy does not affect the major findings below.

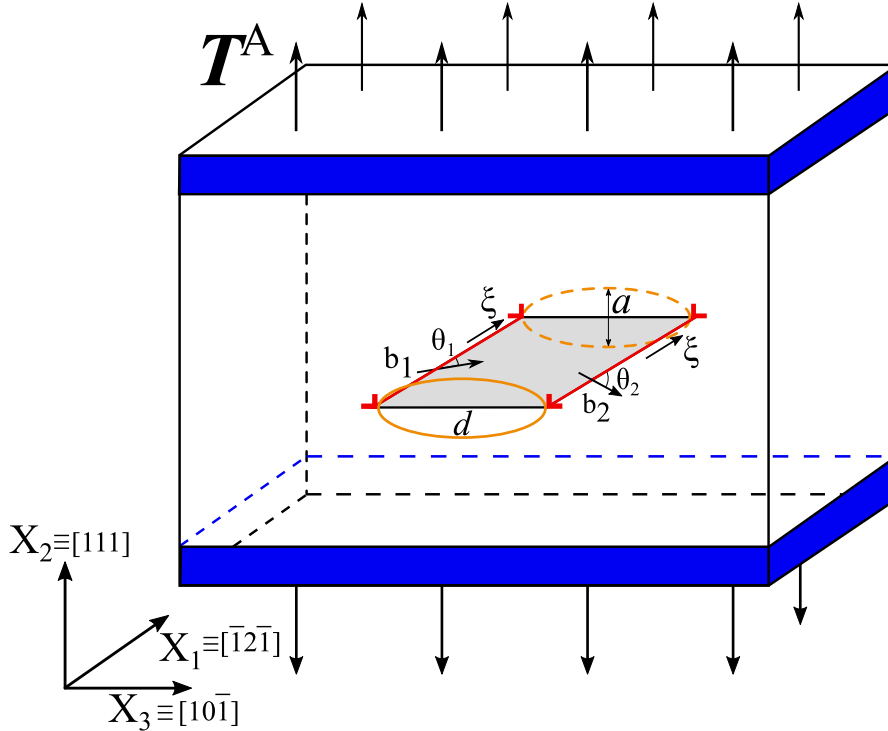


Figure 6.8 – Geometry used to simulate the equilibrium separation d between Shockley partial dislocations under normal stress applied that is perpendicular to the slip plane (along x_2 axis). Red color indicates partial dislocations and dislocation lines along x_1 axis, while the grey color represents the stacking fault. Orange color indicates the elliptic cylinder that undergoes some eigenstrain $\epsilon^T = \epsilon_{22}^T = \Delta_n(\Delta_s, T_n)$. Blue color indicates boundary atoms.

We now examine the partial dislocation dissociation distance with increasing applied stress perpendicular to the slip plane $T^A = T_2 = T_n$. Eq. 6.17 suggests that applied normal stress nominally affects the stable stacking fault energy. Because the stacking fault defect is completely surrounded by linearly elastic material, we treat the stacking fault as a defect with an eigenstrain using the analysis of the previous section (Eq. 6.14), as follows. The inelastic normal displacements exist over several atomic planes around the fault plane. We thus consider the stacking fault as an elliptic cylindrical inclusion having major axis length d (the stacking fault length) and minor axis length $a = 3h$ where h is the $\{111\}$ atomic plane spacing (Figure 6.8). The choice of $a = 3h$ is based on the measured inelastic normal displacements in each plane, as shown in Figure 6.9. The total inelastic displacement $\Delta_n(\Delta_s, T_n)$ is the sum over the planes. DFT calculations show inelastic displacements over one additional pair of layers, suggesting $a = 5h$, but this does not influence the main result (see below). The inclusion has the same elastic properties as the matrix and an eigenstrain $\epsilon^T = \epsilon_{22}^T = \Delta_n(\Delta_s = b_p, T_n)/a$. The eigenstrain itself depends on the applied normal stress and so is a non-linear eigenstrain (see Figure 6.9); again, this does not influence the general analysis.

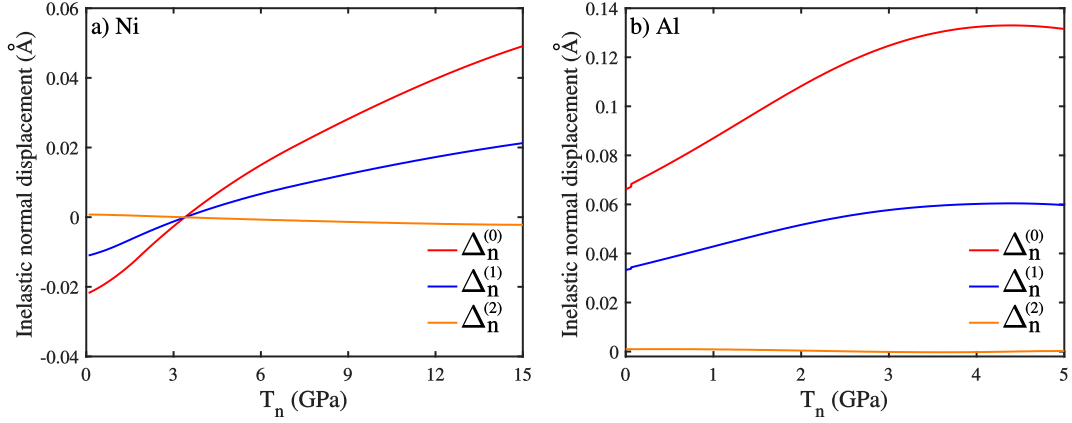


Figure 6.9 – Inelastic vertical displacement at the stable stacking fault position ($\Delta_s = b_p$) in a) Ni and b) Al between atomic planes immediately across the slip plane ($\Delta_n^{(0)}$) (red color), and between atomic planes just above and below the slip plane ($\Delta_n^{(1)}$) (blue color). The inelastic vertical displacement is zero everywhere else, as shown here for ($\Delta_n^{(2)}$) (orange color).

Due to the inclusion with eigenstrain but with no applied stress, there is an additional elastic strain energy contribution per unit length of dislocation of

$$W_I = -\frac{1}{2} \int_{A_I} \boldsymbol{\sigma} : \boldsymbol{\epsilon}^T dA \quad (6.18)$$

where $A_I = ad\pi/4$ is area of the inclusion in the $x_2 - x_3$ plane. The stress inside the elliptical inclusion is constant [24], and given by

$$\boldsymbol{\sigma} = \mathbf{C}(\mathbf{S} - \mathbf{I})\boldsymbol{\epsilon}^T \quad (6.19)$$

where \mathbf{C} is the stiffness tensor, \mathbf{S} the dimensionless Eshelby tensor for an elliptic cylinder [24, 146] and \mathbf{I} the identity tensor. Within isotropic elasticity, $C_{11} = 2\mu(1 - \nu)/(1 - 2\nu)$, $C_{12} = 2\mu\nu/(1 - 2\nu)$ and $C_{44} = \mu$. The elastic energy (per dislocation length) due to $\boldsymbol{\epsilon}^T$ is then simply

$$W_I = -\frac{1}{2} \mathbf{C}(\mathbf{S} - \mathbf{I})\boldsymbol{\epsilon}^T : \boldsymbol{\epsilon}^T A_I \quad (6.20)$$

This contribution is, however, generally negligible. Note also that the interaction energy between the partial dislocations and the inclusion stress field is zero, in isotropic elasticity, because the eigenstrain $\boldsymbol{\epsilon}^T$ has only one non-zero component along x_2 direction and the dislocation stress field is antisymmetric with respect to the $x_1 - x_3$ plane. So, at zero applied traction, the energy remains essentially that of Eq. 6.15 and the dissociation distance that of Eq. 6.15.

When a stress is applied normal to the stacking fault plane, the second energy contribution in Eq. 6.14 must be added to the total energy. For the (elliptical) inclusion with the $\boldsymbol{\epsilon}^T$, this

interaction energy is

$$W_{\sigma} = -\boldsymbol{\sigma}^A : \boldsymbol{\epsilon}^T A_I \quad (6.21)$$

The equilibrium dissociation distance d then minimizes the energy

$$W_{total} = W_{12} + \Psi_{gsf}(\Delta_s = b_p, T_n)d + W_I + W_{\sigma}. \quad (6.22)$$

Since $\boldsymbol{\sigma}^A = \sigma_{22}^A = T_n$, $\boldsymbol{\epsilon}^T = \epsilon_{22}^T = \Delta_n(\Delta_s = b_p, T_n)/a$, $A_I = ad\pi/4$, and W_I is negligible, the energy functional reduces to the simple form

$$W_{total} = W_{12} + d \left[\Psi_{gsf}(\Delta_s = b_p, T_n) - \frac{\pi}{4} T_n \Delta_n(\Delta_s = b_p, T_n) \right]. \quad (6.23)$$

The stress dependence of the GSFE thus appears to reduce the relevant stacking fault energy. The partial separation is then predicted to be

$$d(T_n) = \frac{\mu b_p^2}{8\pi \left[\Psi_{gsf}(\Delta_s = b_p, T_n) - \frac{\pi}{4} T_n \Delta_n(\Delta_s = b_p, T_n) \right]} \frac{\nu + 2}{1 - \nu}. \quad (6.24)$$

There are four contributions to the stress dependence of $d(T_n)$: (i) the interaction energy between two partials, (ii) the change of $\Psi_{gsf}(\Delta_s = b_p, T_n)$ with the applied stress (Figure 6.4), (iii) the coupling of applied stress and inelastic displacement Δ_n , and (iv) the geometrical parameter $\pi/4$ arising because the inelastic displacement is spread over several planes and localized to the dislocation volume, represented by the elliptical geometry. The net result is an increase in the partial dislocation separation with increasing applied normal stress – that is, there is an “opening softening”. However, the direct application of the GSFE as a replacement for the GSFE would not have the factor of $\pi/4$, and thus would predict a larger partial spacing.

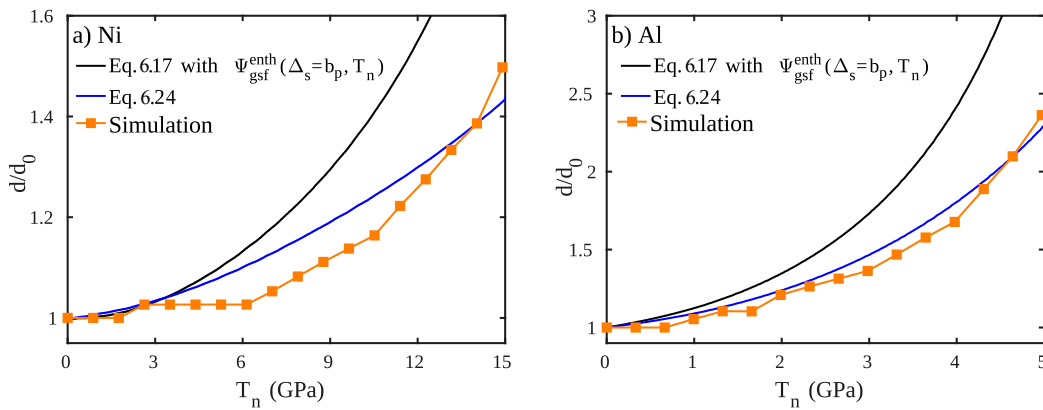


Figure 6.10 – Equilibrium separation between partial dislocations in a) Ni and b) Al at different applied stress that is perpendicular to the slip plane, normalized with its value at zero applied load, as predicted by Eq. 6.17 with γ_{ssf}^{enth} (black line), or by Eq. 6.24 (blue color), and as observed in atomistic simulations (orange squares).

As seen in Figure 6.9, the inelastic normal displacements at small T_n for Ni are negative and are zero at just above $T_n = 3\text{GPa}$. Thus, the theory predicts that the dissociation distance will actually decrease for $T_n < 3\text{GPa}$. In Al, Δ_n is positive for all T_n and much larger than in Ni, and so the dissociation distance is predicted to increase, and more rapidly than in Ni. A subtlety in applying the elasticity analysis at high T_n is that the underlying material becomes nonlinearly elastic. To account for this, we use the tangent modulus $\mu = \mu(T_n)$ and Poisson ratio at the far-field applied stress T_n (see Appendix A.1). This approximation is valid because the problem can be envisioned as first homogeneously deforming the entire material (non-linearly) and then adding a dissociated dislocation into this material. Linearizing around the homogeneously-deformed state enables application of superposition upon addition of the dislocation, similar to the usual introduction of a dislocation into an unstrained (but still non-linear) atomistic material. Figure 6.10 shows the partial spacing versus applied normal stress as predicted using (i) Eq. 6.24, and (ii) Eq. 6.17 with $\Psi_{gsf}^{enth}(\Delta_s = b_p, T_n)$. In both cases we use $\mu = \mu(T_n)$. There are significant quantitative differences between two cases, especially at higher applied loads. Both cases (i) and (ii) do show an “opening softening” effect, although it is almost zero in Ni for $T_n < 3\text{GPa}$ due to the small negative inelastic eigenstrains.

To evaluate the above predictions, we execute simulations using interatomic potentials for Ni and Al. We use the standard methods [147], as follows. The simulation cell is oriented with $X_1 = [\bar{1}2\bar{1}]$, $X_2 = [111]$ and $X_3 = [10\bar{1}]$ (Figure 6.8) with dimensions of $\sim 25 \times 250 \times 600\text{\AA}^3$ (345,400 atoms) that we have verified to be sufficient for converged results. Note that there was a minor typo in the original paper with dimensions along particular directions being ordered incorrectly. We insert a $\{111\}\langle 110\rangle$ edge dislocation by adding a periodic $\{110\}$ plane in the upper half of the crystal that is spread over predicted equilibrium separation distance at $T_n = 0$. Periodic boundary conditions are applied along X_1 and X_3 directions with free surface in X_2 . The system energy is then minimized by the “fire” method with force tolerance 10^{-6}eV/\AA on every atom. The equilibrium distances are then measured as $d_0 = 21.8\text{\AA}$ in Ni, and $d_0 = 13.6\text{\AA}$ in Al; these are slightly higher than predicted by Eq. 6.17 but typical for fcc metals due to the neglect of non-linear effects, spreading of the partial Burgers vector, and the assumption of isotropic elasticity. A normal traction T_n is then applied on the system via vertical forces applied on the boundary atoms within r_c of the X_2 surface boundaries (Figure 6.8). The system energy is again minimized and the equilibrium partial separation measured. The simulated partial spacing d versus applied stress T_n is shown in Figure 6.10 along with the previous predictions. The simulations agree very well with the predictions of Eq. 6.24, which is the complete theory including the multi-plane distribution of inelastic normal displacements represented as an elliptical inclusion. The prediction using simply the enthalpy Ψ_{gsf}^{enth} shows the same trend, but is much larger than observed in both Ni and Al. The simulation results thus confirm the full theory. There is an “opening softening” effect due to the coupling of the inelastic normal displacement to the applied stress, but it is smaller than predicted simply by using the GSFH.

6.5.3 Crack-tip dislocation emission under mixed Mode II/I loading

The previous section has shown a softening effect with applied normal stress for an existing dislocation with existing stacking fault in an infinite elastic medium. Many problems of interest involve dislocation nucleation in which the fault is emerging from some stress concentration and the relevant quantity is the unstable stacking fault energy. Here, we examine the effects of normal stress on one standard problem: emission of a (partial) dislocation from the crack tip of an fcc metal. We use Mode II loading, with an additional Mode I loading to create the normal stress acting on the plane of the dislocation nucleation. This problem cannot be treated using the Eshelby analysis of Sec. 6.5.1 since the partial stacking fault emerges from a crack and so is not surrounded by an infinite elastic medium.

A theory for dislocation emission from a crack tip under Mode II loading, developed by Rice [50], is summarized in Section 3.2 of this manuscript. For a slip plane coplanar with a crack plane, critical Mode II stress intensity factor for dislocation emission K_{IIe} depends on the unstable stacking fault energy $\gamma_{usf} = \Psi_{gsf}(\Delta_s \approx b_p/2)$ and the material elastic properties. Molecular statics simulations showed the Rice theory to be accurate for this crack geometry (see Chapter 4.2.2). For the same crack geometry under mixed Mode II/I loading, there is no exact solution. However, a numerical solution can be obtained by introducing the coupled opening-shear constitutive law $\Psi_{gsf}(\Delta_s, \Delta_n)$ along the slip plane and solving coupled integral equations for the slip displacement of an incipient dislocation emerging from the crack tip [130]. Within this framework, Rice and co-workers showed that K_{IIe} decreases with increasing applied Mode I stress intensity factor K_I . However, the inelastic potential used in that work, which is derived from $\Psi_{gsf}(\Delta_s, \Delta_n)$, had explicit “opening softening” of γ_{usf} ; the predicted softening was thus not due directly to the enthalpy Ψ_{gsf}^{enth} . The full mechanics analysis introduces the coupling of crack-tip stresses and slip along the slip plane through the potential energy $\Psi_{gsf}(\Delta_s, \Delta_n)$. In contrast to the law developed by Rice, the detailed results here show that $\gamma_{usf} = \Psi_{gsf}(\Delta_s \approx b_p/2)$ is nearly independent of the normal opening (see Figure 6.3(iii)), indicating that K_{IIe} should be nearly independent of an applied K_I .

To resolve the discrepancy between results in [130] and results in Figure 6.3(iii), and their presumed consequences on dislocation emission, we perform standard “K-test” simulations using the interatomic potentials for Ni, Cu and Al as described on several places in this document (See Section 2.4). The main difference is that the cracked specimen is simultaneously loaded using both Mode II and Mode I anisotropic displacement field (Eqs. 2.22 and 2.19) in the so-called mixed Mode II/I loading ($K_{II} + K_I$ loading conditions). In each simulation we hold the applied K_I fixed at the desired value and incrementally increase the applied K_{II} until dislocation emission occurs. To create traction free crack surfaces we remove one layer of atoms and artificially delete the atomic interactions across the newly created crack surfaces (see Figure 6.11). Within this crack geometry, emission remains controlled only by the shear response along the slip plane, and no fictitious effects arise near the crack tip that would unduly influence the emission under mixed Mode II/I loading.

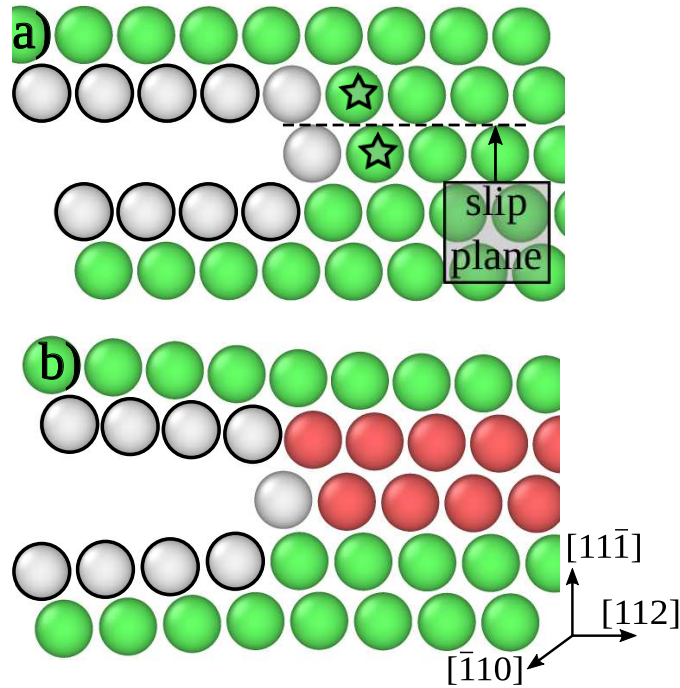


Figure 6.11 – a) Crack geometry in mixed Mode II/I loading formed by removing one layer of atoms and then by artificially canceling the interaction between the atoms marked with black circles. b) Crack geometry after dislocation emission. Opening stress just before the emission is measured between atoms marked with stars. Atoms are colored based on Common Neighbor Analysis [15]; green for fcc, red for hcp and white for surface atoms.

Figure 6.12 shows the simulated K_{IIe} as a function of the applied K_I in Ni, Cu and Al, respectively. There is no “opening softening” observed: the value of K_{IIe} is essential independent of K_I . If there is any effect at all, it is a tendency toward increasing K_{IIe} . The near-crack-tip opening stresses (normal stresses across the slip plane), computed using the average virial stresses on the atoms marked by stars in Figure 6.11a, are shown in Figure 6.12. Due to surface effects, the atomic virial stresses on the crack tip atoms are not reliable; the stresses shown in Figure 6.12 are thus a lower bound. At $K_I = 0 \text{ MPa}\sqrt{\text{m}}$, the near-tip atoms are in normal compression. This is entirely expected because the inelastic normal displacement Δ_n is positive at $\Delta_s \approx b_p/2$. At zero normal stress, the stacking fault cannot expand by Δ_n because of the constraint of the surrounding elastic material. The crack-tip inelastic displacement is then smaller than Δ_n and the normal stress is naturally compressive. With increasing K_I , the near-tip atoms do experience tensile opening stresses (Figure 6.12), as expected, and these stresses can reach levels of 5 – 10GPa. Yet, K_{IIe} remains unaffected by these high normal stresses. This is not surprising since (i) the local unstable stacking fault energy $\Psi_{gsf}(\Delta_s \approx b_p/2)$ is constant or increasing (see Figure 6.4a), and (ii) the work done by T_n over the actual crack-tip inelastic displacement is small/negligible because the crack-tip inelastic displacement is much smaller than Δ_n . Use of the GSFH at the tip would be incorrect because it would include work done by T_n over the Δ_n . We conclude that proper analysis requires the use of $\Psi_{gsf}(\Delta_s, \Delta_n)$ that is derived from $\Psi_{gsf}(\Delta_s, T_n)$ and $\Delta_n(\Delta_s, T_n)$.

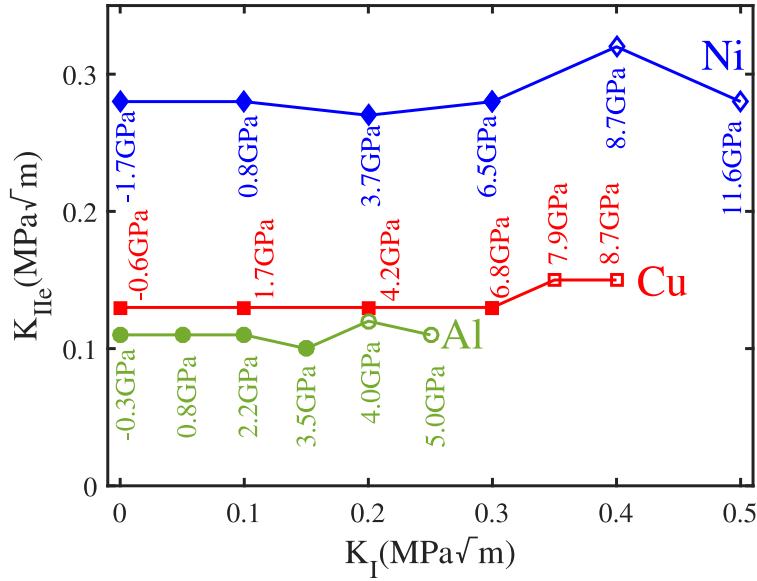


Figure 6.12 – Molecular statics results of the critical stress intensity factor K_{IIe} as a function of the applied K_I in mixed Mode II/I loading in nickel (blue diamonds), copper (red squares) and aluminum (green circles). Crack-tip opening stresses just before the emission are indicated for every applied K_I . Solid symbols correspond to the emission along the upper (initial) slip plane, while the open symbols correspond to the emission along the lower slip plane.

To summarize, no “opening softening” effect is observed in the very well controlled mixed-mode K_{II}/K_I loading test. This is entirely consistent with the absence of “opening softening” in the GSFH measured for these same materials. While the GSFH is the relevant thermodynamic quantity for specific GSF calculations under an applied stress, it is not directly relevant to the crack tip problem. Based on our examinations, reasons for the reported decrease in K_{IIe} with increased K_I in simulations reported in [130] is not due to GSFH but rather due to (i) poorly controlled crack-tip conditions in the simulations leading to spurious effects on emission, (ii) use of a $\Psi_{gsf}(\Delta_s, \Delta_n)$ computed without accounting for the non-linear response of the atomic system, and (iii) subtraction of tension elastic effects assuming only linear response of the system. This test case and the analysis in Sections 6.5.1 and 6.5.2 indicated that mechanics problems are best analyzed using the combination of $\Psi_{gsf}(\Delta_s, T_n)$ and $\Delta_n(\Delta_s, T_n)$ or using $\Psi_{gsf}(\Delta_s, \Delta_n)$, if computable.

6.6 Concluding remarks

Using both interatomic potentials and first principle calculations, we have demonstrated that the generalized stacking fault energy (GSFE) in various metals (Ni, Cu, Al, Mg) generally increases with increasing far-field applied tensile stress normal to the slip plane. There is almost no evidence of “opening softening” that has been envisioned and reported in the literature. An important

additional outcome is that the stacking fault is not a pure-shear defect: shear sliding gives rise to stress-dependent inelastic normal displacements between the atomic planes around the slip plane, leading to a net displacement Δ_n . This net inelastic displacement is typically positive, and does couple to the applied stress, giving rise to a generalized stacking fault enthalpy (GSFH) that does decrease with increasing normal stress. However, the apparent “opening softening” observed in the GSFH does not directly translate to “opening softening” in all mechanics problems involving stacking faults.

The above results are examined via simulation for two canonical problems: the partial dissociation spacing of dislocations in fcc metals and the emission of a dislocation from a crack tip. Theory using the GSFE and opening Δ_n as an eigenstrain shows that the partial spacing does increase with increasing normal stress, consistent with “opening softening”, but not to the degree predicted using the GSFH. Simulations fully support the analysis. Simulations of crack tip emission under Mode II/Mode I loading show no change in the critical Mode II stress intensity for emission due to applied Mode I, and thus no “opening softening”, in spite of normal stresses at the crack tip reaching 5 – 10GPa. This is consistent with the need to analyze mechanics problems using the GSFE and rather than the GSFH directly. In Chapter 4 on crack tip emission in Mode I, we also obtained quantitative agreement with many simulations using an analysis that does not involve any effects of normal stress on the slip behavior.

Overall, the present study provides a fairly complete understanding of the effects of normal stress on stacking fault energies, and demonstrates the consequences for several different situations. “Opening softening” is not a general phenomenon. Analysis of any problem requires consideration of the GSFE and the net inelastic opening displacement Δ_n , and conclusions depend on the specific problem. The results and understanding here thus provide a basis for detailed investigation, or re-investigation, of nanoscale dislocation plasticity phenomena under stresses normal to the slip plane of the dislocations.

7 Conclusion

The continuum Rice and the Tadmor-Hai theories for predicting the critical stress intensity factor for crack tip dislocation emission are well-accepted and widely used in solid-mechanics community. However, atomistic simulations on a wide range of fcc metals have revealed that their predictions are not highly accurate due to various reasons. In this work, two new theories for describing the mechanics of crack-tip dislocation emission and twinning are presented. We now reiterate the main findings presented in this manuscript and discuss future implications of the theories presented.

Atomistic simulations across wide range of fcc metals have revealed that critical shear displacement at the tip Δ_1^c is usually much smaller, while the critical stress intensity factor for the first partial emission K_{Ie}^{first} is higher, than predicted by the approximate Rice theory for Mode I. The present inconsistency appears due to the fact that the first partial dislocation emission is always followed by the surface step creation, a feature completely absent from the Rice theory. An energy cost associated with the step creation then leads to the crack-tip nucleation energy without a maximum. However, the maximum is crucial in the Rice theory since it sets the point for the emission. The new theory presented is fundamentally different from the original Rice theory. The new theory is based on the fact that an incipient dislocation is trapped at the tip by the lattice due to a high energy cost for shearing. As a consequence, *dislocation emission is controlled by the local mechanical instability and nucleation occurs when the crack-tip shear displacement reaches the critical value Δ_1^c* . The physical behavior observed in simulations has been rationalized using a Peierls model for nucleation energy at the crack tip and for the GSF energy further along the slip plane. An approximate analytical expression proposed (see Eq. 4.7) shows an excellent agreement with simulations across 22 different fcc materials described using either EAM or pair potentials. Finally and the most importantly, the new theory naturally reduces to the Rice theory once the step energy becomes negligible.

A similar discrete analysis of the local energetics and deformation in the crack tip vicinity is then used for analyzing the crack-tip twinning. It so happens that the emission of the twinning partial dislocation does not involve step creation and, in fact, there is a decrease in energy near the crack

tip. Twinning is then controlled by the second twinning unit along the twinning plane, which follows the bulk GTF energy. However, the stress acting at the second twinning unit is lower than that at the crack tip. Accounting for this lower stress leads to predictions for the K_{Ie}^{twin} in excellent agreement with simulations. Additional analyses demonstrate why twinning is always observed at $T = 0K$ in all materials studied here. A new twinning mode is reported wherein the crack first advances by cleavage and then emits the twinning partial at the new crack-tip.

Several extensions of the present analysis are necessary. Dislocation nucleation is a thermally activated process at finite temperatures. Computing the energy barrier for nucleation at loads $K_I < K_{Ie}$ is required, and the step energy will contribute an important component to this energy barrier. Furthermore, since the twinning partial emission is not, and trailing partial is, followed by the step creation, the Rice theory is not fully consistent with simulations on predicting the transition from twinning partial emission to trailing partial emission at finite T [103, 104].

The new theory has implications for chemical effects on dislocation nucleation, and it can be extended for predicting the crack-tip dislocation emission in conventional and high entropy alloys. Solutes around at the crack tip can change the step energy, and thus alter the load needed for dislocation emission. The Rice theory accommodates chemistry only through the influence of chemical species on γ_{usf} . Based on the ratio $\gamma_{usf}/\gamma_s = 0.15 \pm 0.05$ for materials studied in this work, the current theory shows that the step energy contributes $\sim 65\%$ of the critical energy release rate, and hence will predict different trends for emission versus specific composition than the standard model.

The role of local chemical transport at the crack tip, and hence kinetic effects, then also becomes important in determining emission just as in cleavage [51]. There is some experimental evidence for hydrogen-enhanced dislocation emission that may be consistent with effects predicted by extension of the present model [62, 148] while coupled Quantum/Continuum methods show that the precise position of an H impurity relative to the slip plane determines whether K_{Ie} is increased or decreased [97]. Thus, behavior at the step will influence chemical embrittlement, i.e. the transition from emission (ductile behaviour) to cleavage (brittle behaviour) in the presence of a chemical environment around the crack.

Finally, the stress dependence of the generalized stacking fault energy (GSFE) has been analyzed. It has been shown that GSFE generally increases with applied far-field stress normal to the slip plane. The observed behavior is in contradiction with the long-standing wisdom that GSFE decreases with applied normal stress. The stacking fault is then shown to be not only a pure-shear defect, but involves inelastic normal displacement across the slip plane Δ_n . The inelastic normal displacement, coupled to the applied stress, gives rise to the generalized stacking fault enthalpy (GSFH). The GSFH does decrease with the applied normal stress since Δ_n is usually positive. However, our mechanics analyses of (i) fcc partial dissociation distance under normal far-field stress, and of the (ii) crack-tip dislocation emission in mixed Mode II/I have shown that GSFH is not useful for general mechanics problems. A nice outcome of the analysis presented in Chapter 6 is that Eshelby inclusion method can be applied for analyzing the atomic scale crystal defects

such as stacking faults. Eventually, the Eshelby method can be employed for evaluating the stress field due to stacking faults in different crystal structures. Stress field due to the stacking fault can have implications on dislocation cross-slip driven by the far-field loading. We will report on this in close future.

A Appendix

The appendices presented are extracted from the following publications:

- (1) Andric P, Curtin WA. New theory for Mode I crack-tip dislocation emission. *Journal of the Mechanics and Physics of Solids*. 2017 Sep 1;106:315-37.
- (2) Andric P, Curtin WA. New theory for crack-tip twinning in fcc metals. *Journal of the Mechanics and Physics of Solids*. 2018 Apr 1;113:144-61.
- (3) Andric P, Yin B, Curtin WA. Stress-dependence of generalized stacking fault energies. *Journal of the Mechanics and Physics of Solids*. 2019 Jan 1;122:262-79.

A.1 Effective elastic constants

Tangent elastic moduli for single crystal Ni [81] (see Sec. 2.4.3.2 and Fig. 2.9) are computed using the following computational method. We define a simulation box, having periodic boundaries, oriented with $X_1 = [1\ 0\ 0]$, $X_2 = [0\ 1\ 0]$ and $X_3 = [0\ 0\ 1]$, and with dimensions in every direction of approximately 50\AA . We set desired stress perpendicular to the $X_2 - X_3$ plane by increasing lattice parameter in X_1 direction, while the lateral lattice parameter is held constant. At a given applied stress we compute C_{11} and C_{12} from the stress-strain response due to applied stress increment of $\Delta\sigma_{11} = 0.1\text{MPa}$, while for estimating C_{44} we apply shear stress of $\tau_{12} = 0.1\text{MPa}$. Fig. 2.9a-c shows the elastic constants as a function of the applied stress. When the crystal orientation is aligned with the cubic axis we find that C_{11} can change up to 30% for the applied stress $\sim 6\text{GPa}$. Furthermore, we use the same method for estimating elastic constant for tension along $[1\ 1\ 1]$ direction as a function of the applied stress. Fig. 2.9d shows that within this crystal orientation elastic constant is less sensitive (up to $\sim 5\%$) and therefore we observe convergence in K_{Ie} for sufficiently big crack (see Fig. 2.17).

In addition, results presented Section 6.5.2 are based on linear isotropic elasticity and thus require

Appendix A. Appendix

proper effective elastic constants input as a function of the normal stress applied. We again employ the molecular statics simulations for calculating the effective isotropic elastic constants as follows. We define a simulation box, having periodic boundaries, oriented with $X_1 = [\bar{1}2\bar{1}]$, $X_2 = [111]$ and $X_3 = [10\bar{1}]$, and with dimension of approximately $35 \times 60 \times 50 \text{\AA}$. We set a desired stress perpendicular to the $X_1 - X_3$ plane by increasing the lattice parameter along $[111]$, while the lateral lattice parameter is held constant. At given applied normal stress we compute the effective shear modulus μ from the stress-shear strain response due to applied shear of $\tau_{23} = 0.1 \text{MPa}$. Then, by relaxing the stress along X_3 direction, we compute the effective Poisson's ratio as $\nu = -\epsilon_{33}/\epsilon_{22}$. Figure A.1 shows the computed effective isotropic tangent moduli as a function of applied stress in Ni and Al. For the applied stresses considered here we find that the shear modulus, in both studied materials, increases with normal tensile stress in part because the Poisson contraction decreases the in-plane atomic spacing which increases the curvature of the energy landscape in shear.

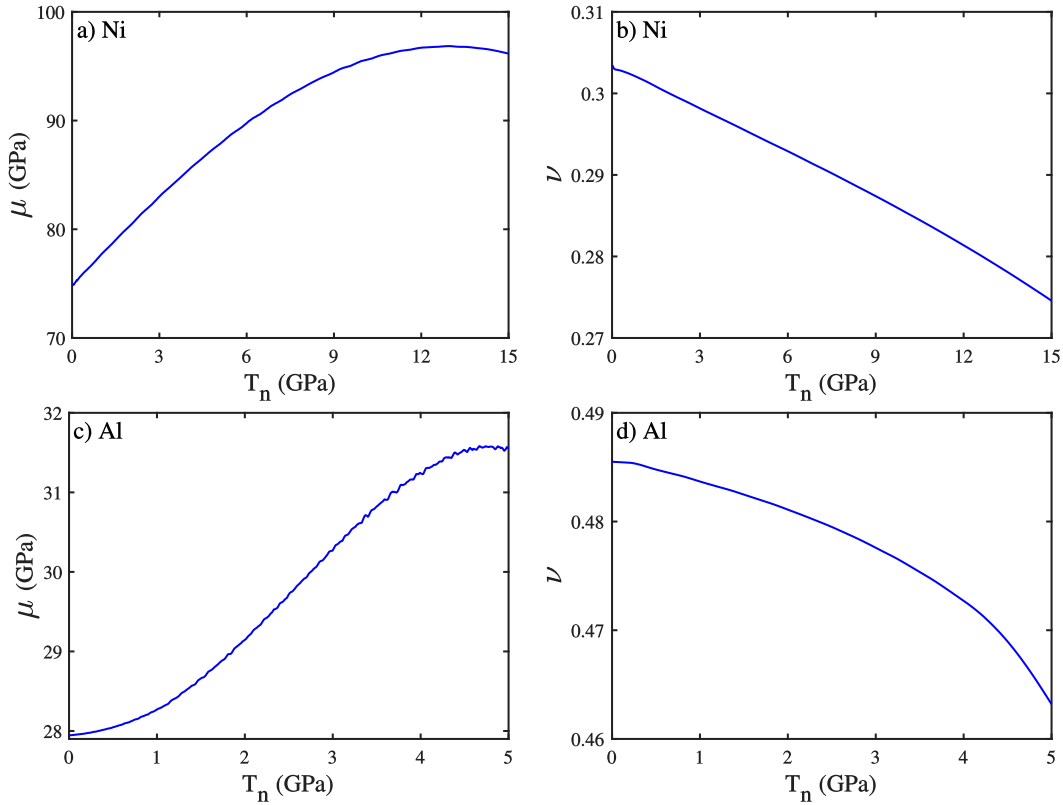


Figure A.1 – Tangent elastic Shear moduli μ and Poisson's ratios ν in Ni and Al computed using molecular statics at $T = 0K$ as a function of the applied far-field normal stress T_n .

A.2 Shearing of the triangular crack tip structural unit

We analyze the shear deformation of triangular structural units along the slip plane. The crack tip dislocation emission is controlled by the local mechanical instability at the crack tip, which is achieved by the critical shear displacement of the crack tip structural unit. The theory presented in Chapter 4 assumes that triangular structural units along the slip plane (see Figure A.2a) are subjected to pure shear deformation. If the structural unit is subjected to pure shear, it will change the shape but not the area (see Figure A.2b). Then, the relative shear displacement of the crack tip unit can be computed as $\Delta_1 = u_s^2 - u_s^1 = u_s^2 - u_s^0 = \Delta'_1$, where u_s is the atom displacement in $[112]$ direction (for fcc materials). This condition is satisfied in the computation of nucleation energies, and in Mode II crack simulations (with some small deviations). In Mode I crack simulations, the K-field introduces normal stresses parallel to the slip plane. Due to normal stresses in the $[112]$ direction, the area of the structural units will be changed (see Figure A.2c). This is an additional energy cost which is not incorporated in the standard nucleation energy. Also, the additional displacement causes that $\Delta'_1 \neq \Delta_1$. This can make a confusion which relative displacement is the representative one. In Mode I simulations studied here, the X_2 coordinate of atoms 2 and 1 is the same, $X_2^2 = X_2^1$ (see the initial geometry in Figure 4.3). Using the initial geometry described above, we conclude that dislocation emission is controlled by the Δ_1 rather than Δ'_1 . However, it is also possible to use Δ'_1 , or an average value, as a measure of the crack tip displacement. This approach will lead to slightly higher predictions than the results presented here (Al M, Al E, Au, Ag, Cu, Pd and Ni potentials). The bigger discrepancy can arise if the crack geometry used changes the vertical position of the crack plane due to surface relaxation effects. We observe this type of behavior in the Cr10-Cr100 materials. As a consequence, we find that Δ'_1 better describes the crack-tip behavior for this particular group of materials. The additional stretching of the structural units is present along the slip plane, as well. We believe that this effect has the more significant effect than the so-called "opening softening". However, it has not been discussed, nor even commented up to date.

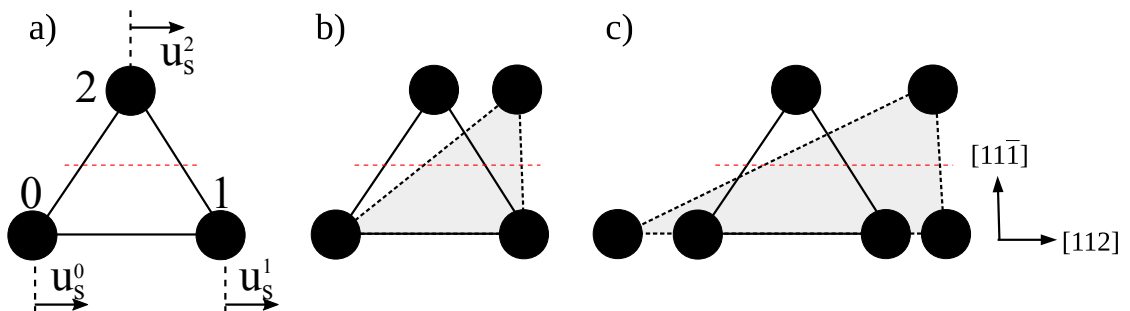


Figure A.2 – Studied crack tip triangular structural unit: a) initial geometry; b) the crack tip unit under pure shear; c) the crack tip unit under shear and normal stresses.

A.3 Comparison of shear displacement profiles in Mode I and Mode II

Both the Rice theory and the theories presented in Chapters 4 and 5 assume that the shear displacement distribution along the slip plane for Mode I, caused by $K_{II}^{eff} = K_I F_{12}(\theta)$, is the same as that for Mode II. In the theory for the emission of the first and trailing partial dislocations, the only difference is that the shear displacement of the crack tip unit is controlled by the nucleation energy rather than the GSF energy. Therefore, the same crack tip shear displacement Δ_1 is achieved at different applied K values for Mode I and Mode II. Nonetheless, for a given crack tip shear displacement Δ_1 , the shear displacements $\Delta_2, \Delta_3, \dots$ should be the same in Mode I and Mode II. We have verified this explicitly via simulation. Specifically, we measure the shear displacements Δ_i ($i = 1, 2, 3, \dots$) along the slip plane for both increasing Mode II K_{II} and increasing Mode I K_I , and obtain the displacements $\Delta_{i,II}(K_{II})$ and $\Delta_{i,I}(K_{II}^{eff})$. We then find the load levels K_{II} and K_{II}^{eff} at which the crack tip shear displacements are equal, $\Delta_{1,II}(K_{II}) = \Delta_{1,I}(K_{II}^{eff})$, and examine the shear displacements $\Delta_{i,I}(K_{II})$ and $\Delta_{i,I}(K_{II}^{eff})$ for $i = 2, 3, \dots$ further along the slip plane. The results for Ni are shown in Figure A.3, where we show the “screening” case for Mode II and the “blunting” case for Mode I so as to add an extra *apparent* level of difference. Figure A.3 demonstrates that the slip distribution along the slip plane is essentially identical for Mode I and Mode II loadings at the same crack tip displacement Δ_1 . The step arising in the Mode I case restrains the crack tip shear displacement $\Delta_{1,I}$, and so a larger applied K_{II}^{eff} is required to obtain the same displacement that would be obtained in Mode II (or in Mode I with no step). This restraint is seen in the graphical analysis of Figure 4.10.

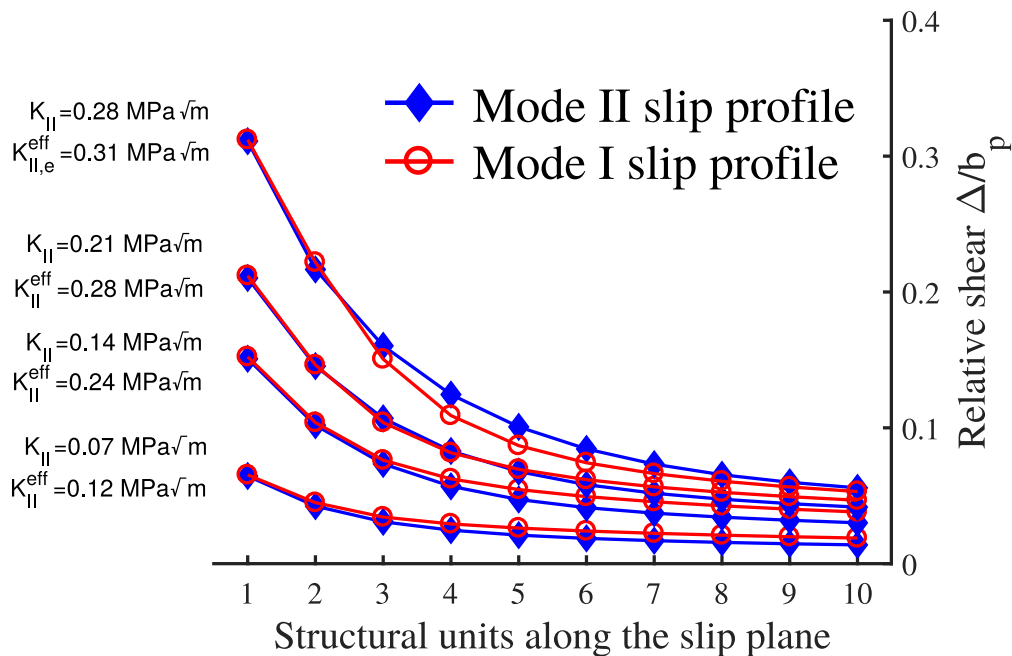


Figure A.3 – The shear displacement distribution along the slip plane in Mode II (screening) and Mode I (blunting) at different far-field K in Ni.

A.4 Computation of the crack-tip parameter β

The crucial parameter in describing the crack tip displacement is the parameter β . Here we present an approximate computational method for finding β . As already discussed in Appendix A.3, at same applied far-field loading we observe different crack tip displacements depending on the step presence. The surface step creation changes the shear resistance of the crack tip structural unit. Within known shear displacements of crack tip unit at same far-field loading $K_{II} = K_{II}^{eff}$, and with known restoring stresses τ_{res} , the slope of the applied stress τ_{app} is uniquely defined. Using this approach we compute the parameter β for 10 fcc materials studied here. We compute $\beta = 1.4-2.3$, as expected. The surprisingly low value in Au is most probably due to high materials anisotropy (see Table A.1). Figure A.4 shows the family of the applied stresses computed in Nickel along with the restoring stresses. Our atomistic simulations reveal that applied stresses τ_{app} are indeed parallel when effects due to non-linearity are negligible.

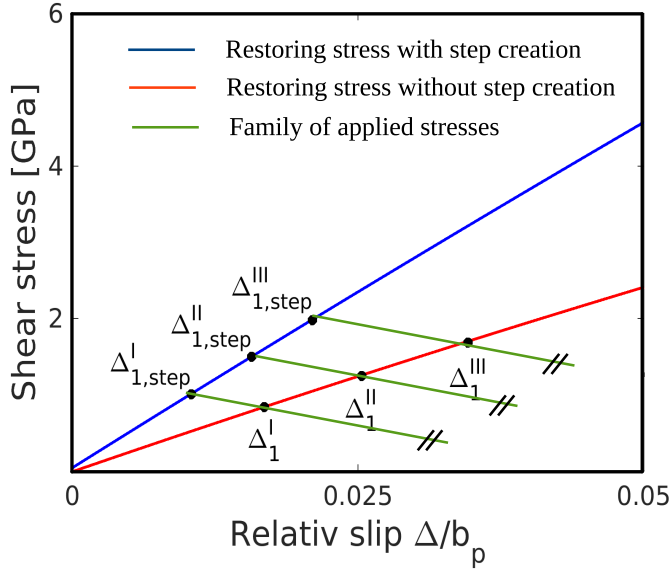


Figure A.4 – Restoring stress τ_{res} of the crack tip structural with the surface step creation (the blue line) and without the surface step creation (the red line) and the family of applied stresses τ_{app} (green lines) for different applied K_I in Nickel.

Material	Parameter β
Cr100 [127]	1.91
Cr50 [127]	2.26
Cr10 [127]	2.36
Al [81]	1.83
Al [124]	1.48
Au [126]	1.23
Ah [126]	1.4
Cu [125]	2.62
Ni [81]	2.15
Pd [126]	1.41

Table A.1 – Values of the parameter β computed in various fcc systems.

A.5 Assessment of the theory for K_{Ie}^{first} and different slip plane orientations

The new theory presented in the paper, and the Rice theory as well, assume that dislocation emission from a crack tip in Mode I is controlled by the effective mode II stress intensity factor K_{II}^{eff} . All differences with respect to the slip plane inclination angle θ are accounted for in K_{II}^{eff} . Here, we examine this assumption in all respects using molecular statics crack simulations at $\theta = 35.3^\circ$, 54.7° , 70.5° and 90° in fcc Ni.

Appendix A. Appendix

First, we show that a slip profile along the sliding plane is independent of the slip plane inclination angle θ . For each inclination angle we find the far field K_I loading that causes the same shear displacement of the crack tip unit Δ_1^i ($i = I, II, III, \dots$)¹ at all orientation angles. We then compare the shear displacements of the structural units further along the slip plane Δ_j^i ($j = 2, 3, 4, \dots$). We find that the slip profiles along the sliding plane are indeed independent of the inclination angle, as shown in Figure A.5a. At the highest testing load, there is a very small deviation along the sliding plane when $\theta = 35.3$ which could be, at this angle, due to the some non-linear effects caused by the larger opening displacement along the sliding plane.

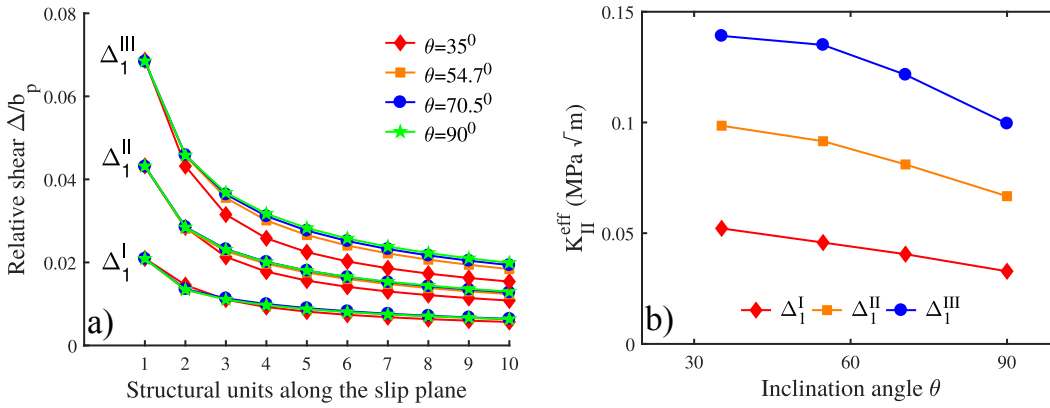


Figure A.5 – a) The shear displacement distribution along the slip plane in Mode I for different inclination angles θ ; b) The effective Mode II stress intensity factor as a function of the inclination angle θ which causes the same crack tip shear displacements.

Second, we compare $K_{II}^{eff} = K_I F_{12}(\theta)$ for the three crack tip shear displacements at each angle, as shown in Figure A.5b. K_{II}^{eff} is nearly independent of θ , but does show a decreasing trend with increasing θ . This could be due to some softening effects caused by the normal stresses (normal and parallel to the sliding plane).

Third, we examine the nucleation energy including the surface step for the different inclination angles. The nucleation energy as a function of the relative slip $\Psi_{nuc}^{first}(\Delta)$ is computed for different inclination angles using the computational method described in Section 4.3. As shown in Figure A.6, the energy and slip resistance are indeed independent of angle for $\theta \geq 54.7^\circ$ and show only small deviations for $\theta = 35.3^\circ$.

Fourth, we present the critical stress intensity factor K_{Ie} observed in the simulations as a function of the slip plane inclination angle as shown in Figure A.7a. The analytical predictions for K_{Ie} of Eq. 4.7 are also shown, and excellent agreement is obtained except at $\theta = 35.3^\circ$, where the analytical model is notably larger. The predictions of the Rice model (which works well for K_{Ie} in Ni) are also shown, and the simulations at $\theta = 35.3^\circ$ fall below the Rice value as well. The low K_{Ie} at $\theta = 35.3^\circ$ emission is facilitated by the presence of two symmetrical slip systems

¹Roman indices used in this notation correspond to different magnitudes of the far-field K_I loading.

A.5. Assessment of the theory for K_{Ie}^{first} and different slip plane orientations

activated. To demonstrate this, simulations at $\theta = 35.3^\circ$ were performed by constraining the first structural unit below the crack plane (unit 1B; see Figure A.7b) to displace according to the elastic K-displacement. With this constraint, dislocation emission along the upper slip plane occurs at a much higher K_{Ie} that is also in excellent agreement with the prediction of Eq. 4.7.

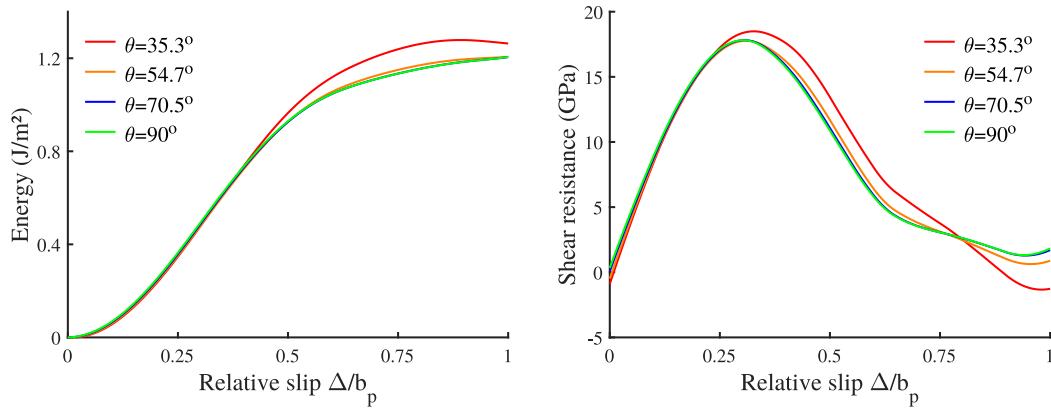


Figure A.6 – a) Nucleation energy as a function of the relative slip for different inclination angles θ ; b) The shear resistance, computed from the nucleation energy, for different inclination angles θ . These curves are computed for fcc Ni.

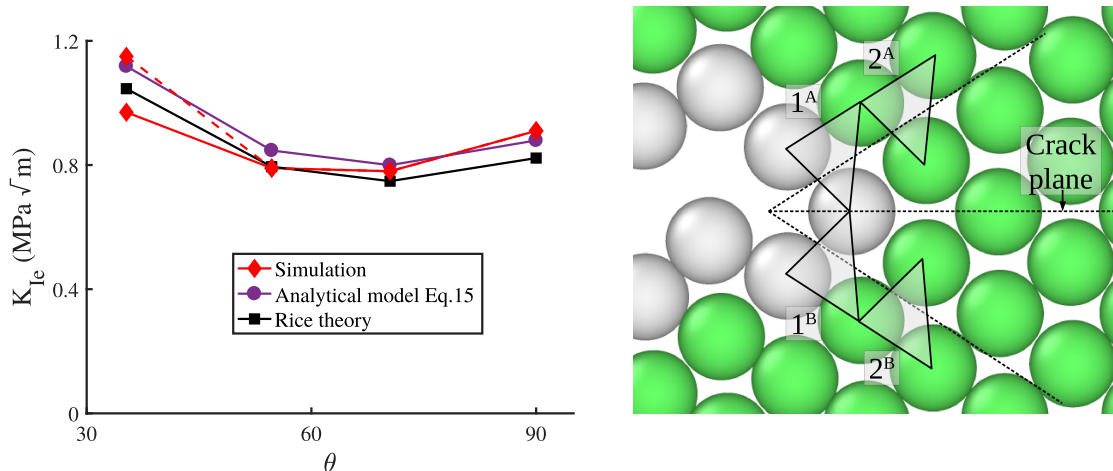


Figure A.7 – a) Critical stress intensity factor for dislocation emission as a function of the slip plane inclination angle θ in fcc Ni; Simulation (red diamonds); Analytical model Eq. 4.7 (purple circles); Rice theory (black squares); dashed line shows the simulation result when constraining deformation of the symmetric slip plane that exists at the lowest angle. b) Crack tip geometry when $\theta = 35.3^\circ$ and definition of the structural units along two symmetric slip planes.

We conclude that there are small differences in precise behavior as a function of inclination angle, with somewhat larger deviations if two symmetrical slip systems are activated; non-linearity and local crack tip geometry will always impart small material-dependent deviations

from theoretical idealizations. However, these differences usually have little impact on the quantitative results, and the predictions of the current model remain generally in good agreement with simulations. This enables application of the theory to make good predictions based on computed or experimental material properties (e.g. unstable stacking fault and surface energies) for systems where interatomic potentials do not exist or are inadequate. We also note that the differences shown in Figures A.5 and A.7 pertain to the Rice theory as well as the present model. The present theory emphasizes the essential role of step creation in determining the major details of dislocation emission, and this important new feature is independent of slip plane inclination angle.

A.6 Assessment of the theory for K_{Ie}^{twin} and different slip plane orientations

The new theory for crack-tip twinning is shown to be in excellent agreement with simulations for the slip plane inclination angle $\theta = 70.5^\circ$ in different fcc metals. We now examine the accuracy of the theory using molecular statics simulations for $\theta = 30.3^\circ$, 54.7° , 70.5° and 90° in the specific case of fcc Ni [81]. We perform standard K-test without the shielding effect, as described above.

First, Table 3 shows that the parameter $f^{(1)}(C_{Ijkl})$ changes very little due to anisotropy and a slightly different position of the twinning unit with respect to the trailing unit. Second, in every case we observe the twinning partial emission, as expected. We then compare the critical stress intensity factors $K_{Ie,tip}^{twin}$ observed in the simulations with the theoretical predictions. We find excellent quantitative and qualitative agreement, except at $\theta = 35.3^\circ$. In this case the new theory for crack-tip twinning is notably higher, despite the fact that we accurately predict the twinning mode (see Table A.2). This discrepancy arises by the presence of the two active symmetrical slip systems that interact slightly. We found similar behavior in the case of the first partial dislocation emission (see Appendix A.5).

For other crack orientations, especially when $\phi_{first} \neq 0$, the theory applies when using the correct component(s) of the Burgers vector(s) that couple to the applied crack tip stress field. Examining all possible cases is far beyond the scope of the present thesis. To conclude, we believe that the work presented here, being an entirely new type of analysis for a long-standing problem, is sufficient for validating the new theory.

A.7 GSFE under uniaxial tension

In Section 6.2 we investigate the GSFE stress dependence when the lateral cell sizes are held fixed. This loading scenario corresponds to the so-called uniaxial strain (imposed with the stress boundary conditions). We now investigate the influence of the lateral stresses on the GSFE by performing an additional set of GSF simulations, in which the relaxation of the lateral stresses is allowed (uniaxial tension). All other simulation details are identical to those presented in

$\theta(^{\circ})$	X_1	X_2	X_3	$f^{(1)}$	$K_{I_e, new}^{twin}$ (MPa \sqrt{m})	$K_{I_e, sim}^{twin}$ (MPa \sqrt{m})	$K_{I_c}^{twin}$ (MPa \sqrt{m})	Predicted mode	Simulated mode
35.3	[001]	[110]	$[\bar{1}10]$	1.22	1.16	0.92	1.06	forward	forward
54.7	$[\bar{1}\bar{1}4]$	[221]	$[\bar{1}10]$	1.29	0.93	0.98	1.01	back	back
70.5	$[\bar{1}\bar{1}2]$	[111]	$[\bar{1}10]$	1.30	0.88	0.89	0.92	back	back
90.0	$[\bar{1}\bar{1}1]$	[112]	$[\bar{1}10]$	1.33	0.99	0.93	0.99	forward	forward

Table A.2 – Critical stress intensity factor for twinning partial dislocation emission for different slip plane inclination angles θ as predicted by the Andric-Curtin twinning theory and as observed in the simulations. The observed and predicted twinning mode is shown, along with the Griffith K_{I_c} and the parameter $f^{(1)}(C_{ijkl})$.

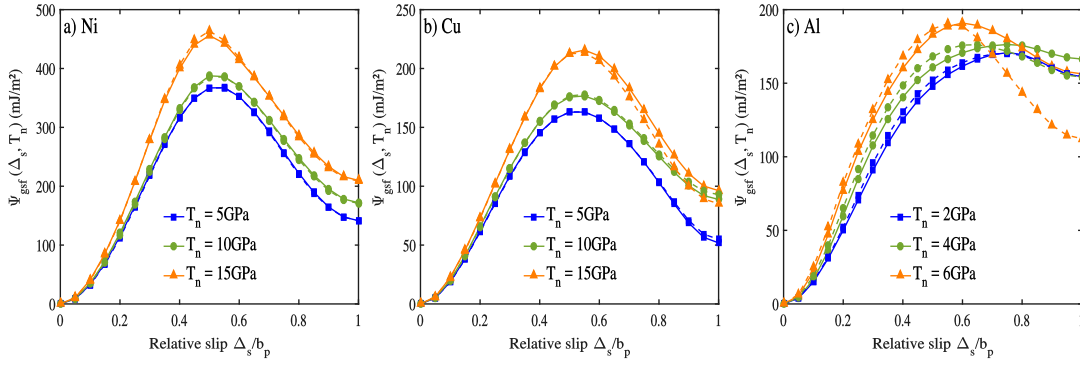


Figure A.8 – GSFE versus slip displacement, for various applied normal tensile stresses under uniaxial strain (solid line) and uniaxial stress (dashed line) as computed using interatomic potentials at $T = 0K$ in a) nickel, b) copper and c) aluminum

Section 6.2. Figure A.8 shows the GSFE curves computed using interatomic potentials for Ni, Cu and Al at different applied normal stresses imposed by the uniaxial strain (solid line) or uniaxial stress (dashed line). We find that lateral loads in Ni and Cu have no significant influence on the GSFE. Furthermore, the GSFE in Al tends to be more sensitive for $\Delta_s > 0.6b_p$ and for applied normal stress above 5GPa. The observed behavior is mainly due to potential which under uniaxial tension becomes unstable for applied stresses slightly above 6GPa.

A.8 Partial dissociation d and stress dependence of isotropic elastic properties

Stress dependence of the materials elastic properties nominally affects only the interaction energy W_{12} between two partials, since the inclusion energy W_I is negligible. Therefore, we investigate how big this effect on predicted dissociation distance d is. Figure A.9 shows the simulated dissociation distance d , along with the predictions of Eq. 6.24 with and without taking into account stress dependence of the elastic properties (see Appendix A.1). Influence of the stress dependent elastic properties on the overall behavior is more emphasized in Ni than in Al. The result sensitivity in Ni is due to similar contribution to the crystal enthalpy from W_{12} and the stacking fault (change in GSFE and inelastic normal displacement with applied normal stress) itself. The stacking fault contribution in Al is bigger than W_{12} (due to very big inelastic displacement (see Figure 6.9)); thus, change in elastic properties only slightly influences predictions on the dissociation distance with increasing applied normal stress.

A.8. Partial dissociation d and stress dependence of isotropic elastic properties

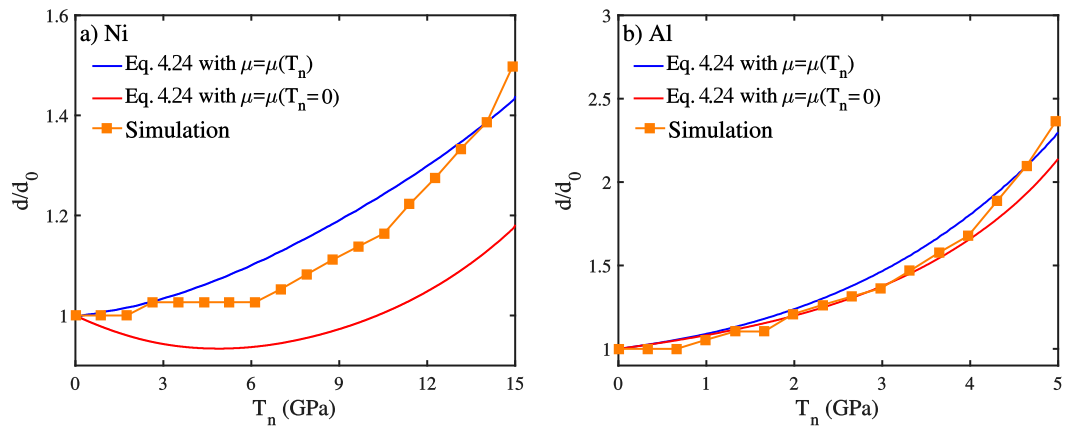


Figure A.9 – Equilibrium separation between partial dislocations in a) Ni and b) Al at different applied stress that perpendicular to the slip plane, normalized with its value at zero applied load, as predicted by equation by Eq. 6.24 when stress dependence of elastic properties is (blue color)/is not (red color) taken into account, and as observed in atomistic simulations (orange squares).

Bibliography

- [1] David Kirkaldy. *Results of an experimental inquiry into the tensile strength and other properties of various kinds of wrought-iron and steel*. Selbstverl. des Verf., 1866.
- [2] William John Macquorn Rankine. On the causes of the unexpected breakage of the journals of railway axles; and on the means of preventing such accidents by observing the law of continuity in their construction. In *Minutes of the Proceedings of the Institution of Civil Engineers*, volume 2, pages 105–107. Thomas Telford-ICE Virtual Library, 1843.
- [3] Alan A Griffith and M Eng. The phenomena of rupture and flow in solids. *Phil. Trans. R. Soc. Lond. A*, 221(582-593):163–198, 1921.
- [4] B Cotterell. The past, present, and future of fracture mechanics. *Engineering fracture mechanics*, 69(5):533–553, 2002.
- [5] E Orowan. Fundamentals of brittle behavior in metals. *Fatigue and fracture of metals*, pages 139–167, 1952.
- [6] GR Irwin. Analysis of stresses and strains near the end of a crack traversing a plate. *Journal of Applied Mechanics*, 1957.
- [7] GR Irwin. Fracture dynamics. *Fracturing of metals*, pages 147–166, 1948.
- [8] Branimir Krstic, Bosko Rasuo, Dragan Trifkovic, Igor Radisavljevic, Zoran Rajic, and Mirko Dinulovic. Failure analysis of an aircraft engine cylinder head. *Engineering Failure Analysis*, 32:1–15, 2013.
- [9] Branimir Krstic, Lamine Rebhi, Nada Ilic, Marjan Dodic, Mirko Dinulovic, Predrag Andric, and Dragan Trifkovic. Failure of mounting bolt of helicopter main gearbox support strut. *Engineering Failure Analysis*, 70:351–363, 2016.
- [10] E Farmand-Ashtiani, J Cugnoni, and J Botsis. Specimen thickness dependence of large scale fiber bridging in mode I interlaminar fracture of carbon epoxy composite. *International Journal of Solids and Structures*, 55:58–65, 2015.
- [11] Yong Zhu, Kenneth M Liechti, and K Ravi-Chandar. Direct extraction of rate-dependent traction–separation laws for polyurea/steel interfaces. *International Journal of Solids and Structures*, 46(1):31–51, 2009.

Bibliography

- [12] Arlette RC Baljon and Mark O Robbins. Energy dissipation during rupture of adhesive bonds. *Science*, 271(5248):482–484, 1996.
- [13] Erik Van der Giessen and Alan Needleman. Discrete dislocation plasticity: a simple planar model. *Modelling and Simulation in Materials Science and Engineering*, 3(5):689, 1995.
- [14] Srinath S Chakravarthy and William A Curtin. Origin of plasticity length-scale effects in fracture. *Physical review letters*, 105(11):115502, 2010.
- [15] Alexander Stukowski. Visualization and analysis of atomistic simulation data with ovito—the open visualization tool. *Modelling and Simulation in Materials Science and Engineering*, 18(1):015012, 2009.
- [16] J Song, M Soare, and WA Curtin. Testing continuum concepts for hydrogen embrittlement in metals using atomistics. *Modelling and Simulation in Materials Science and Engineering*, 18(4):045003, 2010.
- [17] James R Rice. A path independent integral and the approximate analysis of strain concentration by notches and cracks. *Journal of applied mechanics*, 35(2):379–386, 1968.
- [18] JR Willis. A comparison of the fracture criteria of griffith and barenblatt. *Journal of the Mechanics and Physics of Solids*, 15(3):151–162, 1967.
- [19] James R Rice. Mathematical analysis in the mechanics of fracture. *Fracture: an advanced treatise*, 2:191–311, 1968.
- [20] Sun and Jin. *Fracture Mechanics*. Academic press, Boston, 2012.
- [21] Anderson TL. *Fracture mechanics: fundamentals and applications*. CRC press, 2017.
- [22] Gross D and Seelig T. *Fracture mechanics: with an introduction to micromechanics*. Springer, 2017.
- [23] Muskhelishvili NI. *Some basic problems of the mathematical theory of elasticity*. Springer Science and Business Media, 2013.
- [24] John Douglas Eshelby. The elastic field outside an ellipsoidal inclusion. *Proc. R. Soc. Lond. A*, 252(1271):561–569, 1959.
- [25] HM Westergaard. Bearing pressures and cracks. *Journal of Applied Mechanics*, 6(2):A49–53, 1939.
- [26] Ting TC. *Anisotropic elasticity: theory and applications*. Oxford University Press, 1996.
- [27] AN Stroh. Dislocations and cracks in anisotropic elasticity. *Philosophical magazine*, 3(30):625–646, 1958.
- [28] KA Ingebrigtsen and A Tonning. Elastic surface waves in crystals. *Physical Review*, 184(4):942, 1969.

- [29] JR Rice. Stresses due to a sharp notch in a work-hardening elastic-plastic material loaded by longitudinal shear. *Journal of Applied Mechanics*, 34(2):287–298, 1967.
- [30] Allan F Bower. *Applied mechanics of solids*. CRC press, 2009.
- [31] Thomas JR Hughes. *The finite element method: linear static and dynamic finite element analysis*. Courier Corporation, 2012.
- [32] Klaus-Jürgen Bathe. Finite element method. *Wiley encyclopedia of computer science and engineering*, pages 1–12, 2007.
- [33] Grigory Isaakovich Barenblatt. The mathematical theory of equilibrium cracks in brittle fracture. In *Advances in applied mechanics*, volume 7, pages 55–129. Elsevier, 1962.
- [34] Donald S Dugdale. Yielding of steel sheets containing slits. *Journal of the Mechanics and Physics of Solids*, 8(2):100–104, 1960.
- [35] Z Xia, WA Curtin, and BW Sheldon. Fracture toughness of highly ordered carbon nanotube/alumina nanocomposites. *Journal of engineering materials and technology*, 126(3):238–244, 2004.
- [36] J Song, WA Curtin, TK Bhandakkar, and HJ Gao. Dislocation shielding and crack tip decohesion at the atomic scale. *Acta Materialia*, 58(18):5933–5940, 2010.
- [37] Michael Ortiz and Anna Pandolfi. Finite-deformation irreversible cohesive elements for three-dimensional crack-propagation analysis. *International journal for numerical methods in engineering*, 44(9):1267–1282, 1999.
- [38] Nicolas Richart and Jean-François Molinari. Implementation of a parallel finite-element library: test case on a non-local continuum damage model. *Finite Elements in Analysis and Design*, 100:41–46, 2015.
- [39] Mathias Wallin, WA Curtin, Matti Ristinmaa, and Alan Needleman. Multi-scale plasticity modeling: Coupled discrete dislocation and continuum crystal plasticity. *Journal of the Mechanics and Physics of Solids*, 56(11):3167–3180, 2008.
- [40] E Van der Giessen, VS Deshpande, HHM Cleveringa, and A Needleman. Discrete dislocation plasticity and crack tip fields in single crystals. *Journal of the Mechanics and Physics of Solids*, 49(9):2133–2153, 2001.
- [41] Viggo Tvergaard and John W Hutchinson. The relation between crack growth resistance and fracture process parameters in elastic-plastic solids. *Journal of the Mechanics and Physics of Solids*, 40(6):1377–1397, 1992.
- [42] Yueguang Wei and John W Hutchinson. Steady-state crack growth and work of fracture for solids characterized by strain gradient plasticity. *Journal of the Mechanics and Physics of Solids*, 45(8):1253–1273, 1997.

Bibliography

- [43] JP Hirth and J Lothe. *Theory of Dislocations*, 2nd. Ed.: John Willey & Sons, 1982.
- [44] VS Deshpande, A Needleman, and E Van der Giessen. Discrete dislocation plasticity modeling of short cracks in single crystals. *Acta Materialia*, 51(1):1–15, 2003.
- [45] VS Deshpande, A Needleman, and E Van der Giessen. Discrete dislocation modeling of fatigue crack propagation. *Acta materialia*, 50(4):831–846, 2002.
- [46] VS Deshpande, A Needleman, and E Van der Giessen. Scaling of discrete dislocation predictions for near-threshold fatigue crack growth. *Acta Materialia*, 51(15):4637–4651, 2003.
- [47] Srinath S Chakravarthy and William A Curtin. New algorithms for discrete dislocation modeling of fracture. *Modelling and Simulation in Materials Science and Engineering*, 19(4):045009, 2011.
- [48] Eleanor Mak and William A Curtin. Paper in preparation.
- [49] James R Rice and Robb Thomson. Ductile versus brittle behaviour of crystals. *Philosophical magazine*, 29(1):73–97, 1974.
- [50] James R Rice. Dislocation nucleation from a crack tip: an analysis based on the peierls concept. *Journal of the Mechanics and Physics of Solids*, 40(2):239–271, 1992.
- [51] James R Rice and Jian-Sheng Wang. Embrittlement of interfaces by solute segregation. *Materials Science and Engineering: A*, 107:23–40, 1989.
- [52] Roger Chang. An atomistic study of fracture. *International Journal of Fracture Mechanics*, 6(2):111–125, 1970.
- [53] Robb Thomson, C Hsieh, and V Rana. Lattice trapping of fracture cracks. *Journal of Applied Physics*, 42(8):3154–3160, 1971.
- [54] Peter Gumbsch and Glenn E Beltz. On the continuum versus atomistic descriptions of dislocation nucleation and cleavage in nickel. *Modelling and Simulation in Materials Science and Engineering*, 3(5):597, 1995.
- [55] Peter Gumbsch. An atomistic study of brittle fracture: toward explicit failure criteria from atomistic modeling. *Journal of Materials Research*, 10(11):2897–2907, 1995.
- [56] Ting Zhu, Ju Li, and Sidney Yip. Atomistic study of dislocation loop emission from a crack tip. *Physical review letters*, 93(2):025503, 2004.
- [57] DH Warner, WA Curtin, and S Qu. Rate dependence of crack-tip processes predicts twinning trends in fcc metals. *Nature materials*, 6(11):876, 2007.
- [58] Z Wu and WA Curtin. Brittle and ductile crack-tip behavior in magnesium. *Acta Materialia*, 88:1–12, 2015.

- [59] R Miller, EB Tadmor, R Phillips, and M Ortiz. Quasicontinuum simulation of fracture at the atomic scale. *Modelling and Simulation in Materials Science and Engineering*, 6(5):607, 1998.
- [60] Diana Farkas, H Van Swygenhoven, and PM Derlet. Intergranular fracture in nanocrystalline metals. *Physical Review B*, 66(6):060101, 2002.
- [61] Johannes J Möller and Erik Bitzek. Fracture toughness and bond trapping of grain boundary cracks. *Acta Materialia*, 73:1–11, 2014.
- [62] Ali Tehranchi and WA Curtin. Atomistic study of hydrogen embrittlement of grain boundaries in nickel: I. fracture. *Journal of the Mechanics and Physics of Solids*, 101:150–165, 2017.
- [63] Ryosuke Matsumoto, Shinya Taketomi, Sohei Matsumoto, and Noriyuki Miyazaki. Atomistic simulations of hydrogen embrittlement. *International Journal of Hydrogen Energy*, 34(23):9576–9584, 2009.
- [64] Shinya Taketomi, Ryosuke Matsumoto, and Noriyuki Miyazaki. Atomistic study of the effect of hydrogen on dislocation emission from a mode ii crack tip in alpha iron. *International Journal of Mechanical Sciences*, 52(2):334–338, 2010.
- [65] Jun Song and WA Curtin. A nanoscale mechanism of hydrogen embrittlement in metals. *Acta Materialia*, 59(4):1557–1569, 2011.
- [66] Jun Song and WA Curtin. Atomic mechanism and prediction of hydrogen embrittlement in iron. *Nature materials*, 12(2):145, 2013.
- [67] Mao Wen, Zhiyuan Li, and Afrooz Barnoush. Atomistic study of hydrogen effect on dislocation nucleation at crack tip. *Advanced Engineering Materials*, 15(11):1146–1151, 2013.
- [68] Erik Bitzek and Peter Gumbsch. Atomistic simulations of dislocation-crack interaction. *Journal of Solid Mechanics and Materials Engineering*, 2(10):1348–1359, 2008.
- [69] X Wendy Gu, Mehdi Jafary-Zadeh, David Z Chen, Zhaoxuan Wu, Yong-Wei Zhang, David J Srolovitz, and Julia R Greer. Mechanisms of failure in nanoscale metallic glass. *Nano letters*, 14(10):5858–5864, 2014.
- [70] Kristopher Learion Baker and DH Warner. An atomistic investigation into the nature of near threshold fatigue crack growth in aluminum alloys. *Engineering Fracture Mechanics*, 115:111–121, 2014.
- [71] Fanchao Meng, Cheng Chen, and Jun Song. Dislocation shielding of a nanocrack in graphene: atomistic simulations and continuum modeling. *The journal of physical chemistry letters*, 6(20):4038–4042, 2015.

Bibliography

- [72] Takashi Sumigawa, Takahiro Shimada, Shuuhei Tanaka, Hiroki Unno, Naoki Ozaki, Shinsaku Ashida, and Takayuki Kitamura. Griffith criterion for nanoscale stress singularity in brittle silicon. *ACS nano*, 11(6):6271–6276, 2017.
- [73] Pasquale Gallo, Yabin Yan, Takashi Sumigawa, and Takayuki Kitamura. Fracture behavior of nanoscale notched silicon beams investigated by the theory of critical distances. *Advanced Theory and Simulations*, 1(1):1700006, 2018.
- [74] Yuemin Sun and Glenn E Beltz. Dislocation nucleation from a crack tip: a formulation based on anisotropic elasticity. *Journal of the Mechanics and Physics of Solids*, 42(12):1905–1932, 1994.
- [75] Predrag Andric and WA Curtin. New theory for mode I crack-tip dislocation emission. *Journal of the Mechanics and Physics of Solids*, 106:315–337, 2017.
- [76] Rubén Pérez and Peter Gumbsch. Directional anisotropy in the cleavage fracture of silicon. *Physical review letters*, 84(23):5347, 2000.
- [77] Peter Gumbsch and Rowland M Cannon. Atomistic aspects of brittle fracture. *Mrs Bulletin*, 25(5):15–20, 2000.
- [78] Gaurav Singh, James R Kermode, Alessandro De Vita, and Robert W Zimmerman. Validity of linear elasticity in the crack-tip region of ideal brittle solids. *International Journal of Fracture*, 189(1):103–110, 2014.
- [79] WA Curtin. On lattice trapping of cracks. *Journal of Materials Research*, 5(7):1549–1560, 1990.
- [80] N Bernstein and DW Hess. Lattice trapping barriers to brittle fracture. *Physical review letters*, 91(2):025501, 2003.
- [81] Y Mishin, Diana Farkas, MJ Mehl, and DA Papaconstantopoulos. Interatomic potentials for monoatomic metals from experimental data and ab initio calculations. *Physical Review B*, 59(5):3393, 1999.
- [82] Ali Tehrani and WA Curtin. Atomistic study of hydrogen embrittlement of grain boundaries in nickel: II. decohesion. *Modelling and Simulation in Materials Science and Engineering*, 25(7):075013, 2017.
- [83] James H Rose, John R Smith, and John Ferrante. Universal features of bonding in metals. *Physical review B*, 28(4):1835, 1983.
- [84] Grigory Isaakovich Barenblatt. The mathematical theory of equilibrium cracks in brittle fracture. In *Advances in applied mechanics*, volume 7, pages 55–129. Elsevier, 1962.
- [85] SM Khosrownejad and WA Curtin. Crack growth and fracture toughness of amorphous Li-Si anodes: Mechanisms and role of charging/discharging studied by atomistic simulations. *Journal of the Mechanics and Physics of Solids*, 107:542–559, 2017.

-
- [86] P Andric and WA Curtin. Atomistic modeling of fracture. *Modelling and Simulation in Materials Science and Engineering*, 27(1):013001, 2018.
- [87] Steve Plimpton. Fast parallel algorithms for short-range molecular dynamics. *Journal of computational physics*, 117(1):1–19, 1995.
- [88] Erik Bitzek, Pekka Koskinen, Franz Gähler, Michael Moseler, and Peter Gumbsch. Structural relaxation made simple. *Physical review letters*, 97(17):170201, 2006.
- [89] I-H Lin and R Thomson. Cleavage, dislocation emission, and shielding for cracks under general loading. *Acta Metallurgica*, 34(2):187–206, 1986.
- [90] James R Rice. Conserved integrals and energetic forces. *Fundamentals of deformation and fracture*, pages 33–56, 1985.
- [91] Predrag Andric and WA Curtin. New theory for crack-tip twinning in fcc metals. *Journal of the Mechanics and Physics of Solids*, 113:144–161, 2018.
- [92] A Ramasubramaniam, WA Curtin, and D Farkas. Fracture in nanolamellar materials: continuum and atomistic models with application to titanium aluminides. *Philosophical Magazine A*, 82(12):2397–2417, 2002.
- [93] Tong-Yi Zhang and JCM Li. Image forces and shielding effects of an edge dislocation near a finite length crack. *Acta metallurgica et materialia*, 39(11):2739–2744, 1991.
- [94] EB Tadmor and S Hai. A peierls criterion for the onset of deformation twinning at a crack tip. *Journal of the Mechanics and Physics of Solids*, 51(5):765–793, 2003.
- [95] William A Curtin and Ronald E Miller. Atomistic/continuum coupling in computational materials science. *Modelling and simulation in materials science and engineering*, 11(3):R33, 2003.
- [96] LE Shilkrot, Ronald E Miller, and William A Curtin. Multiscale plasticity modeling: coupled atomistics and discrete dislocation mechanics. *Journal of the Mechanics and Physics of Solids*, 52(4):755–787, 2004.
- [97] RJ Zamora, AK Nair, RG Hennig, and DH Warner. Ab initio prediction of environmental embrittlement at a crack tip in aluminum. *Physical Review B*, 86(6):060101, 2012.
- [98] RJ Zamora, KL Baker, and DH Warner. Illuminating the chemo-mechanics of hydrogen enhanced fatigue crack growth in aluminum alloys. *Acta Materialia*, 100:232–239, 2015.
- [99] JR Kermode, T Albaret, Dov Sherman, Noam Bernstein, P Gumbsch, MC Payne, G Csányi, and A De Vita. Low-speed fracture instabilities in a brittle crystal. *Nature*, 455(7217):1224, 2008.
- [100] Qing Peng and Gang Lu. A comparative study of fracture in al: Quantum mechanical vs. empirical atomistic description. *Journal of the Mechanics and Physics of Solids*, 59(4):775–786, 2011.

Bibliography

- [101] Erik Bitzek and Peter Gumbsch. Mechanisms of dislocation multiplication at crack tips. *Acta Materialia*, 61(4):1394–1403, 2013.
- [102] Ting Zhu, Ju Li, and Sidney Yip. Atomistic study of dislocation loop emission from a crack tip. *Physical review letters*, 93(2):025503, 2004.
- [103] VI Yamakov, DH Warner, RJ Zamora, E Saether, WA Curtin, and EH Glaessgen. Investigation of crack tip dislocation emission in aluminum using multiscale molecular dynamics simulation and continuum modeling. *Journal of the Mechanics and Physics of Solids*, 65:35–53, 2014.
- [104] Derek H Warner and WA Curtin. Origins and implications of temperature-dependent activation energy barriers for dislocation nucleation in face-centered cubic metals. *Acta Materialia*, 57(14):4267–4277, 2009.
- [105] CH Ersland, IR Vatne, and Christian Thaulow. Atomistic modeling of penny-shaped and through-thickness cracks in bcc iron. *Modelling and Simulation in Materials Science and Engineering*, 20(7):075004, 2012.
- [106] Johannes J Möller and Erik Bitzek. On the influence of crack front curvature on the fracture behavior of nanoscale cracks. *Engineering Fracture Mechanics*, 150:197–208, 2015.
- [107] G Anciaux, T Junge, M Hodapp, J Cho, J-F Molinari, and WA Curtin. The coupled atomistic/discrete-dislocation method in 3d part i: Concept and algorithms. *Journal of the Mechanics and Physics of Solids*, 118:152–171, 2018.
- [108] M Hodapp, G Anciaux, J-F Molinari, and WA Curtin. Coupled atomistic/discrete dislocation method in 3d part ii: Validation of the method. *Journal of the Mechanics and Physics of Solids*, 119:1–19, 2018.
- [109] Jaehyun Cho, Jean-Francois Molinari, William A Curtin, and Guillaume Anciaux. The coupled atomistic/discrete-dislocation method in 3d. part iii: Dynamics of hybrid dislocations. *Journal of the Mechanics and Physics of Solids*, 118:1–14, 2018.
- [110] Max Hodapp, William Curtin, Guillaume Anciaux, and Jean-François Molinari. A lattice green function method for atomistic/continuum coupling: theory and data-sparse implementation. In *European Mechanics of Material Conference*, page 386, 2018.
- [111] Jörg Rottler and Mark O Robbins. Jamming under tension in polymer crazes. *Physical review letters*, 89(19):195501, 2002.
- [112] Michael L Falk and James S Langer. Dynamics of viscoplastic deformation in amorphous solids. *Physical Review E*, 57(6):7192, 1998.
- [113] Ali S Argon. Brittle to ductile transition in cleavage fracture. *Acta Metallurgica*, 35(1):185–196, 1987.

- [114] RW Armstrong. Cleavage crack propagation within crystals by the griffith mechanism versus a dislocation mechanism. *Materials science and engineering*, 1(4):251–254, 1966.
- [115] A Kelly, WR Tyson, and AH Cottrell. Ductile and brittle crystals. *Philosophical magazine*, 15(135):567–586, 1967.
- [116] G Schoeck. Dislocation emission from crack tips. *Philosophical Magazine A*, 63(1):111–120, 1991.
- [117] S Hai and EB Tadmor. Deformation twinning at aluminum crack tips. *Acta Materialia*, 51(1):117–131, 2003.
- [118] SJ Zhou, AE Carlsson, and Robb Thomson. Dislocation nucleation and crack stability: lattice green’s-function treatment of cracks in a model hexagonal lattice. *Physical Review B*, 47(13):7710, 1993.
- [119] J Knap and K Sieradzki. Crack tip dislocation nucleation in fcc solids. *Physical review letters*, 82(8):1700, 1999.
- [120] SJ Zhou, AE Carlsson, and Robb Thomson. Crack blunting effects on dislocation emission from cracks. *Physical review letters*, 72(6):852, 1994.
- [121] G Xu, AS Argon, and M Ortiz. Nucleation of dislocations from crack tips under mixed modes of loading: implications for brittle against ductile behaviour of crystals. *Philosophical Magazine A*, 72(2):415–451, 1995.
- [122] Yu-Min Juan. Ledge effects on dislocation emission from a crack tip: a first-principles study for silicon. *Philosophical magazine letters*, 73(5):233–240, 1996.
- [123] Gunther Schoeck. The emission of dislocations from crack tips: A critical assessment. *Materials Science and Engineering: A*, 356(1-2):93–101, 2003.
- [124] Furio Ercolessi and James B Adams. Interatomic potentials from first-principles calculations: the force-matching method. *EPL (Europhysics Letters)*, 26(8):583, 1994.
- [125] Yu Mishin, MJ Mehl, DA Papaconstantopoulos, AF Voter, and JD Kress. Structural stability and lattice defects in copper: Ab initio, tight-binding, and embedded-atom calculations. *Physical Review B*, 63(22):224106, 2001.
- [126] JB Adams, SM Foiles, and WG Wolfer. Self-diffusion and impurity diffusion of fee metals using the five-frequency model and the embedded atom method. *Journal of Materials Research*, 4(1):102–112, 1989.
- [127] Céline Varvenne, Aitor Luque, Wolfram G Nöhring, and William A Curtin. Average-atom interatomic potential for random alloys. *Physical Review B*, 93(10):104201, 2016.
- [128] Giovanni Bonny, Dmitry Terentyev, RC Pasianot, Samuel Poncé, and Alexander Bakaev. Interatomic potential to study plasticity in stainless steels: the fenicr model alloy. *Modelling and simulation in materials science and engineering*, 19(8):085008, 2011.

Bibliography

- [129] Jonathan A Zimmerman, Huajian Gao, and Farid F Abraham. Generalized stacking fault energies for embedded atom fcc metals. *Modelling and Simulation in Materials Science and Engineering*, 8(2):103, 2000.
- [130] Yuemin Sun, Glenn E Beltz, and James R Rice. Estimates from atomic models of tension-shear coupling in dislocation nucleation from a crack tip. *Materials Science and Engineering: A*, 170(1-2):67–85, 1993.
- [131] Glenn E Beltz, Don M Lipkin, and Lisa L Fischer. Role of crack blunting in ductile versus brittle response of crystalline materials. *Physical review letters*, 82(22):4468, 1999.
- [132] VP Rajan, DH Warner, and WA Curtin. An interatomic pair potential with tunable intrinsic ductility. *Modelling and Simulation in Materials Science and Engineering*, 24(2):025005, 2016.
- [133] Vaclav Vitek. Intrinsic stacking faults in body-centred cubic crystals. *Philosophical Magazine*, 18(154):773–786, 1968.
- [134] Helena Van Swygenhoven. Grain boundaries and dislocations. *Science*, 296(5565):66–67, 2002.
- [135] Helena Van Swygenhoven, Peter M Derlet, and AG Frøseth. Stacking fault energies and slip in nanocrystalline metals. *Nature materials*, 3(6):399, 2004.
- [136] EB Tadmor, R Miller, R Phillips, and M Ortiz. Nanoindentation and incipient plasticity. *Journal of Materials Research*, 14(6):2233–2250, 1999.
- [137] Johannes J Möller and Erik Bitzek. Comparative study of embedded atom potentials for atomistic simulations of fracture in α -iron. *Modelling and Simulation in Materials Science and Engineering*, 22(4):045002, 2014.
- [138] C Brandl, PM Derlet, and H Van Swygenhoven. General-stacking-fault energies in highly strained metallic environments: Ab initio calculations. *Physical Review B*, 76(5):054124, 2007.
- [139] PS Branicio, JY Zhang, and DJ Srolovitz. Effect of strain on the stacking fault energy of copper: a first-principles study. *Physical Review B*, 88(6):064104, 2013.
- [140] Georg Kresse and Jürgen Furthmüller. Efficient iterative schemes for ab initio total-energy calculations using a plane-wave basis set. *Physical review B*, 54(16):11169, 1996.
- [141] Georg Kresse and D Joubert. From ultrasoft pseudopotentials to the projector augmented-wave method. *Physical Review B*, 59(3):1758, 1999.
- [142] John P Perdew, Kieron Burke, and Matthias Ernzerhof. Generalized gradient approximation made simple. *Physical review letters*, 77(18):3865, 1996.

- [143] Peter E Blöchl. Projector augmented-wave method. *Physical review B*, 50(24):17953, 1994.
- [144] S Kibey, JB Liu, Duane D Johnson, and H Sehitoglu. Generalized planar fault energies and twinning in cu–al alloys. *Applied physics letters*, 89(19):191911, 2006.
- [145] Binglun Yin, Zhaoxuan Wu, and WA Curtin. Comprehensive first-principles study of stable stacking faults in hcp metals. *Acta Materialia*, 123:223–234, 2017.
- [146] Toshio Mura. *Micromechanics of defects in solids*. Springer Science & Business Media, 2013.
- [147] Yu N Osetsky and David J Bacon. An atomic-level model for studying the dynamics of edge dislocations in metals. *Modelling and simulation in materials science and engineering*, 11(4):427, 2003.
- [148] SP Lynch. A fractographic study of gaseous hydrogen embrittlement and liquid-metal embrittlement in a tempered-martensitic steel. In *Perspectives in Hydrogen in Metals*, pages 739–750. Elsevier, 1986.

Predrag ANDRIC

Rue de Lausanne 61 | 1020 Renens | Switzerland

+41 76 805 60 76 | predrag.andric@epfl.ch | lammm.epfl.ch

Born on March 25th, 1987 | Serb, B permit | Married, two children



CURRICULUM VITAE

MULTI-DISCIPLINARY | OPEN-MINDED | TEAM-WORKER | COMMUNICATIVE | INDEPENDENT

PROFESSIONAL EXPERIENCE

- 2015 - ... **Doctoral Assistant** | Laboratory for Multiscale Mechanics Modeling, Institute of Mechanical Engineering, EPFL, Switzerland
- Exploring fundamental fracture properties of metals and High Entropy Alloys
 - Atomistic/mechanistic modeling of fracture
 - Finite Element Modeling (FEM) of composites using Ansys
 - Data analysis, Processing and Visualization
 - Expertise in: Fracture Mechanics | Solid Mechanics | Micromechanics | Mechanics of Materials
 - Teaching assistant in *Mechanics of Composites* M. Sc. course (Prof. William Curtin)
- 2013 - 2015 **Teaching Assistant** | University of Defense, Belgrade, Serbia
- Undergraduate courses: Aerodynamics, Flight Mechanics
 - Preparation of class notes
 - Supervision of students in their practical classes
 - Leading students through their personal projects
- 2011 - 2013 **Aircraft Maintenance Engineer** | Serbian Air Force, Belgrade, Serbia
- Chief engineer in B level maintenance of supersonic airplanes
 - Organization and control of periodic airplane inspections
 - Systematic and scientific analysis of atypical aircraft malfunctions

COMPUTER SKILLS

Operative system	LINUX (Ubuntu) environment Windows environment
Writing/Presenting	MS office 2010 (Word, Excel, PowerPoint) LibreOffice LATEX
Scientific computing	MATLAB ANSYS FEMAP LAMMPS (molecular dynamics C++ code)
Programming languages	FORTRAN Python (learning)
CAD software	Autocad CATIA V5

EDUCATION

- 2015 - 2019 **PhD student** | Doctoral Program in Mechanics (EDME), EPFL, Switzerland
(Expected to graduate by April 2019)
Thesis: "The mechanics of crack-tip dislocation emission and twinning"
Advisor: Prof. William A. Curtin
- 2011 - 2013 **Master Degree in Mechanical engineering** | Department for Aerospace Engineering, Faculty of Mechanical Engineering, University of Belgrade, Serbia.
Average success: 9.70 (out of 10.0)
Thesis: "*Application of composite materials in main helicopter rotor blades design*"
Advisor: Prof. Mirko Dinulovic
- 2006 - 2011 **Dipl. Ing. in Mechanical engineering** | Department of Aviation Technical Service, University of Defense, Belgrade, Serbia
Average success: 9.40 (out of 10.0) | **The best student award**
Thesis: "*Stress and strain analysis of a damaged main helicopter rotor blade*"

LANGUAGES

English	Fluent	Serbian	Native
French	Beginner level, A1/A2	Russian	Good understanding

PUBLICATIONS AND PRESENTATIONS

Publications in peer reviewed journals:

- **Andric P**, Curtin WA. Stress-dependence of generalized stacking fault energies. Journal of the Mechanics and Physics of Solids. 2019 Jan; 122:262-79.
- **Andric P**, Curtin WA. Atomistic modeling of fracture. Modelling and Simulation in Materials Science and Engineering. 2018 Nov 16;27(1):013001.
- **Andric P**, Curtin WA. New theory for crack-tip twinning in fcc metals. Journal of the Mechanics and Physics of Solids. 2018 Apr 1;113:144-61.
- **Andric P**, Curtin WA. New theory for Mode I crack-tip dislocation emission. Journal of the Mechanics and Physics of Solids. 2017 Sep 1;106:315-37.
- Krstic B, Rebhi L, Ilic N, Dodic M, Dinulovic M, **Andric P**, Trifkovic D. Failure of mounting bolt of helicopter main gearbox support strut. Engineering Failure Analysis. 2016 Dec 1;70:351-63.

Conference papers:

- Rebhi L, Dinulović M, **Andric P**, Dodić M, Krstić B. On the effective shear modulus of composite honeycomb sandwich panels. Scientific Technical Review. 2016;66(4):59-65.
- Dinulović M, Rasuo B, Krstić B, **Andric P**. Flutter analysis of missile composite folding fins. In6th International Conference on defensive Technologies OTEH 2014.
- Dinulović M, Krstić B, **Andric P**. Application of 3D-random fiber composites for damaged honeycomb panels repair. In5th International Conference on defensive Technologies OTEH 2012 (pp. 6-19).

Conference presentations:

- **Andric P**, Curtin WA. Intrinsic ductility as a precursor to ductile fracture. 22nd European Conference on Fracture (ECF22), Belgrade, Serbia, (2018).
- **Andric P**, Curtin WA. Intrinsic ductility as a precursor to ductile fracture. Invited speaker to Junior THEOS MARVEL seminar series, Jan 2019, EPFL
- **Andric P**, Curtin WA. Stress dependence of generalized stacking fault energies. 10th European Solid Mechanics Conference (ESMC2018), Bologna, Italy, (2018).
- **Andric P**, Curtin WA. New theory for crack-tip dislocation emission and twinning in fcc metals, Deutsche Physikalische Gesellschaft (DGP2018), Berlin, Germany, (2018).
- **Andric P**, Curtin WA. Crack-tip twinning in fcc metals. 14th International Conference on Fracture (ICF14), Rhodes, Greece, (2017).

ADDITIONAL ACTIVITIES AND COMPETENCE

Traveling | Skiing | Hiking

Student representative at the University of Defense – years 2008-2009.

Driving license B

REFERENCES

Prof. William Curtin	PhD advisor Institute of Mechanical Engineering, EPFL, Switzerland Email: william.curtin@epfl.ch phone: 021 69 37366
Prof. Mirko Dinulovic	MSc thesis advisor Faculty of Mechanical Engineering, University of Belgrade Email: mdinulovic@mas.bg.ac.rs phone: +381 11 330 23 66
Prof. ¹⁵² Bosko Rasuo	Professor Faculty of Mechanical Engineering, University of Belgrade Email: brasuo@mas.bg.ac.rs phone: +381 330 22 61

